Numerical and Experimental Investigations on Transpiration Cooling

A thesis accepted by the Faculty of Aerospace Engineering and Geodesy of the University of Stuttgart in partial fulfilment of the requirements for the degree of Doctor of Engineering Sciences (Dr.-Ing.)

by

Dipl.-Ing. Daniel Christopher Albert Prokein

born in Kaiserslautern, Germany

Committee chair: Prof. Dr.-Ing. Jens von Wolfersdorf
Committee member: Prof. Dr.-Ing. Stefan Schlechtriem
Date of defence: 18 October 2021

Institute of Aerospace Thermodynamics
University of Stuttgart
2021

"Tout ce qui est impossible reste à accomplir."

- Jules Verne -

Acknowledgements

This thesis is based on my work during the time as a research associate at the Institute of Aerospace Thermodynamics (ITLR) at the University of Stuttgart. I am very grateful to have been given the opportunity to investigate transpiration cooling for future aerospace applications and I would like to extend my sincere thanks to all who contributed to the success of this endeavour.

My deepest gratitude and appreciation belong to my thesis supervisor Prof. Dr.-Ing. Jens von Wolfersdorf who first sparked my interest in this research field and continuously supported me with excellent advice and guidance. Thank you for always having an open door, reserving time for interesting and productive discussions, and also for giving me the freedom to explore additional scientific questions next to my project work. Furthermore, I would like to thank Prof. Dr.-Ing. Stefan Schlechtriem for taking on the role as co-referee and his interest in my thesis work. Special thanks also go to Prof. Dr.-Ing. habil. Bernhard Weigand who in his role as director of the institute significantly shapes the collegial and supportive working environment at ITLR.

Besides, I would like to express my gratitude to the University of Stuttgart and the Helmholtz Alliance for the support of this research within the frame of the Helmholtz Young Investigator's Group VH-NG-909 'High Temperature Management in Hypersonic Flight'. I absolutely enjoyed the close collaboration with my partners at the German Aerospace Center (DLR) during this project. Many thanks to the entire team not only for the research collaboration but also the great time alongside.

Nürnberg, October 2021

Daniel Prokein

Contents

Contents

Contents

List of Figures

List of Figures

List of Tables

List of Symbols

Latin Characters

Symbol	Description	Unit
A	area	m^2
A_c	transpired surface of porous sample	m^2
$\boldsymbol{a}$	acceleration vector	m/s^2
a_{sf}	specific inner surface of porous structure	m^2/m^3
C_{FD}^*	ratio between form drag and viscous drag	$-$
c_p	specific heat capacity at constant pressure	J/(kgK)
c_s	speed of sound	m/s
c_v	specific heat capacity at constant volume	J/(kgK)
D	diffusion coefficient	m^2/s
DL	dimensionless IR camera output quantity	$-$
e	specific internal energy	J/kg
F	blowing ratio / blowing parameter	$-$
$\boldsymbol{F}$	force vector	N
f	body force per unit mass	N/kg
h	heat transfer coefficient	$\text{W/(m}^2\text{K)}$
h_{st}	specific static enthalpy	J/kg
h_{tot}	specific total enthalpy	J/kg
h_v	volumetric heat transfer coefficient	$\text{W/(m}^3\text{K)}$
$\boldsymbol{I}$	identity matrix	$-$
$\boldsymbol{j}$	diffusion flux vector	$\text{kg/(m}^2\text{s)}$
K_D	Darcy permeability coefficient	m^2

List of Symbols

Symbol	Description	Unit
K_F	Forchheimer permeability coefficient	m
k	thermal conductivity	W/(mK)
k_{tr}	monoatomic thermal conductivity	W/(mK)
κ	turbulent kinetic energy	m^2/s^2
L	thickness of porous sample	m
$L_{t,in}$	turbulent mixing length	m
$\dot{m}$	mass flow rate	kg/s
$\boldsymbol{n}$	surface normal vector	−
p	pressure	Pa
$(\Delta p/L)^*$	normalised pressure drop	Pa/m
$\dot{Q}$	heat flow rate	W
$\dot{q}$	heat flux	W/m^2
R	specific gas constant	J/(kgK)
R_m	universal gas constant	J/(molK)
r	recovery factor	−
$\boldsymbol{S}$	surface vector	m^2
T	temperature	K
TI	turbulent intensity	−
t	time	s
u	velocity	m/s
u_τ	friction velocity	m/s
$\boldsymbol{u}$	velocity vector	m/s
V	volume	m^3
$\sum v_i$	diffusion volume	m^3
W	molecular weight	kg/mol
$\dot{W}_{visc}$	rate of work done by viscous stresses	W
x, y, z	cartesian cordinates	m
Y	mass fraction	−
Δy	shock-generator elevation	m

Greek Characters

Symbol	Description	Unit
α	thermal diffusivity	m^2/s
$\bar{\alpha}$	thermal diffusion coefficient	–
β	wave angle	°
Γ_{HG}	boundary at hot-gas side	–
Γ_{PM}	boundary at coolant-reservoir side	–
γ	heat capacity ratio	–
δ	boundary-layer thickness	m
ε	porosity	–
ϵ	turbulence dissipation	$\mathrm{m}^2/\mathrm{s}^3$
θ	deflection angle	°
Θ	cooling efficiency	–
μ	dynamic viscosity	$\mathrm{kg}/(\mathrm{ms})$
μ_t	eddy viscosity	$\mathrm{kg}/(\mathrm{ms})$
ν	kinematic viscosity	m^2/s
$\nu(M)$	Prandtl-Meyer function	°
ξ_1, ξ_2, ξ_3	system of rectangular coordinates	m
ξ	film cooling parameter	–
ρ	density	kg/m^3
$\boldsymbol{\tau}$	viscous stress tensor	N/m^2
τ_{ii}	normal stresses	N/m^2
τ_{ij}	shear stresses	N/m^2
τ_w	wall shear stress	N/m^2
ψ	molar fraction	–
ω	specific turbulence dissipation rate	$1/\mathrm{s}$

Subscripts

Symbol	Description
∞	free-stream conditions
$*$	reference-state conditions
0	without blowing
b	backside
C/C	Carbon/Carbon
c	coolant

List of Symbols

Symbol	Description
$crit$	critical
D	Darcy
eff	effective
ex	exit / outlet
exp	experiment
F	Forchheimer
f	fluid
fit	fitting range
hg	hot gas / main flow
hyd	hydraulic
in	inlet / reservoir
$insert$	adiabatic wall insert
lat	lateral direction
$layer$	porous transition layer
max	maximum
mod	modified
n	normal
$\parallel$	parallel to fibre orientation
$\perp$	perpendicular to fibre orientation
$pore$	pore / porous channel
r	recovery
ref	reference
res	reservoir condition
s	solid
st	static
std	standard
T	temperature
TC	thermocouple
t	turbulent
tan	tangential
tot	total
tmp	temporary
$visc$	viscous
w	wall
x	axial run length

Superscripts

Symbol	Description
$-$	averaged quantity
$\sim$	Favre mean
$'$	fluctuating quantity
$''$	Favre fluctuation
$+$	dimensionless wall-normal quantity

Dimensionless Quantities

Symbol	Description	Definition
C_f	skin-friction coefficient	$C_f = \tau_w/(1/2\rho u^2)$
CFL	Courant-Friedrichs-Lewy number	$\text{CFL} = |\boldsymbol{u}|\Delta t/\Delta x$
Le	Lewis number	$\text{Le} = \text{Sc}/\text{Pr} = \alpha/D$
M	Mach number	$\text{M} = u/c_s$
Pe	Peclet number	$\text{Pe} = \text{RePr} = uL/\alpha$
Pr	Prandtl number	$\text{Pr} = \nu/\alpha$
Re	Reynolds number	$\text{Re} = uL/\nu$
Sc	Schmidt number	$\text{Sc} = \nu/D$
St	Stanton number	$\text{St} = h/(\rho u c_p)$

Abbreviations

Abbrevation	Description
BC	Boundary Condition
C/C	Carbon/Carbon
C/C-SiC	Carbon/Carbon-Silicon-Carbide
CFD	Computational Fluid Dynamics
CFRP	Carbon Fibre-Reinforced Plastic
CMC	Ceramic Matrix Composite
DLR	German Aerospace Center
DNS	Direct Numerical Simulation
FS	Full scale value
FVM	Finite Volume Method

List of Symbols

Abbrevation	Description
GCI	Grid Convergence Index
IG	Ideal Gas
IR	Infrared Radiation
ITLR	Institute of Aerospace Thermodynamics
LES	Large Eddy Simulation
LTE	Local Thermal Equilibrium
LTNE	Local Thermal Non-Equilibrium
LTS	Local Time Stepping
OF	OpenFOAM / spectraFOAM
OpenFOAM	Open Field Operation and Manipulation
PEEK	Polyether Ether Ketone
PISO	Pressure-Implicit with Splitting of Operators
RANS	Reynolds-Averaged Navier-Stokes
RD	Read value
REV	Representative Elementary Volume
SHEFEX	Sharp Edge Flight Experiment
SIMPLE	Semi-Implicit Method for Pressure Linked Equations
SST	Shear Stress Transport
TVD	Total Variation Diminishing

Abstract

Future challenges in aviation as well as space travel are closely linked to the development of propulsion engines. Enhancing the performance and reusability while reducing emissions constantly increases the demands on the applied materials and cooling technology. In this context, transpiration cooling is of great interest, particularly if applied to modern lightweight composite materials. Several experiments demonstrated the general feasibility of transpiration cooling for rocket engines, combustor elements in (sc-)ramjets, and thermal protection of external surfaces in hypersonic flight. However, the physical processes as well as the modelling of transpiration cooling have still not been conclusively investigated. Moreover, simulation tools for the design and layout of transpiration-cooled structures are lacking. Therefore, developing and validating such a numerical solver has been a primary motivation for the research work summarised in this thesis. At the same time, the combined experimental and numerical approach allowed a detailed analysis of results which contributes to the knowledge of transpiration cooling for CMC materials (ceramic matrix composites) and more complex conditions.

A numerical CFD solver for modelling of transpiration cooling has been developed and integrated into the OpenFOAM software package. It allows the simulation of complex transpiration-cooled structures in non-uniform sub- and supersonic hot-gas flows. An integral approach with full coupling of both domains, i.e. hot-gas flow field and porous structure, is followed. For practical reasons, a volume-averaged method with consideration of local thermal non-equilibrium effects was selected. A three-dimensional Darcy-Forchheimer approach is employed to model coolant through flow. Moreover, the solver is capable of handling the injection of arbitrary coolant gases in a hot main flow of air. A surface-averaged injection model is combined with a modified turbulent boundary condition to represent the transpired porous walls. The solver has been applied to various test cases and validated by means of comparisons to experimental results.

First, unidirectional through-flow experiments are presented for Carbon/Carbon (C/C) structures. The data suggests that the permeability coefficients are independent of the coolant gas used as well as temperature and pressure levels. Additionally, a through-flow experiment with partial sealing of the outlet confirms the proposed superposition principle for multidimensional coolant flow.

Secondly, numerical simulations of a subsonic turbulent channel flow with boundary-layer injection have been performed. The comparison of numerical velocity and temperature profiles to experimental data validates the applied continuous blowing model for microscopic pore openings as well as the numerical models linked to foreign-gas injection.

The main part of the thesis then investigates transpiration-cooled C/C structures in supersonic hot-gas flows. For this purpose, experiments in the institute's supersonic wind tunnel have been conducted using different porous sample geometries, a shock generator, and various coolants. Temperatures were measured on the surfaces as well as within the porous samples by means of thermocouples and in-situ calibrated infrared thermography. Wall pressure measurements and schlieren imaging characterised the supersonic flow field. Transpiration cooling significantly reduces the temperatures on the transpired surface, within the porous sample, and in the wake region. The effect can be correlated to the blowing ratio as well as the coolant properties. A scaling based on the specific heat capacity was found to describe well the cooling efficiency of the porous wall for different coolants. Variations of the sample wall thickness yield locally higher coolant mass fluxes and intensified cooling. A similar effect was found for more complex main-flow conditions exhibiting shock waves and expansion fans. The non-uniform distributions in wall pressure and heat flux affect the local cooling efficiency substantially. Likewise, boundary-layer blowing revealed to have an influence on the supersonic main flow which underlines the importance of coupled simulation approaches.

Concerning the validation of the developed OpenFOAM solver and the applied numerical setup, the simulation results for the different test cases capture all relevant effects well. A good agreement between experiment and simulation was observed for all test cases.

Kurzfassung

Aktuelle und zukünftige Herausforderungen in der Luft- und Raumfahrt sind eng mit der Entwicklung von innovativen Antriebssystemen verbunden. Das Streben nach Leistungssteigerungen und Wiederverwendbarkeit bei gleichzeitiger Reduzierung der Emissionen stellt hohe Anforderungen an die eingesetzten Werkstoffe und Kühltechniken. In diesem Zusammenhang bietet Transpirationskühlung großes Potential, insbesondere in Kombination mit modernen Leichtbau-Verbundwerkstoffen. Verschiedene Experimente haben die generelle Machbarkeit der Kühlmethode für Raketentriebwerke, Brennkammer-Elemente in Staustrahltriebwerken und im Bereich des thermischen Schutzes im Hyperschallflug gezeigt. Die physikalischen Prozesse sowie die Modellierung der Transpirationskühlung bedürfen hingegen weiterer Untersuchungen. Darüber hinaus fehlen Simulationswerkzeuge für den Entwurf und die Auslegung von transpirationsgekühlten Strukturen. Aus diesem Grund stellte die Entwicklung und Validierung eines numerischen Lösers eine primäre Motivation für die vorliegende Forschungsarbeit dar. Ebenso im Fokus der Zielsetzung stand der Erkenntnisgewinn hinsichtlich Transpirationskühlung für CMC-Materialien (ceramic matrix composites) und komplexere Bedingungen.

Ein numerischer CFD-Löser zur Modellierung der Transpirationskühlung wurde entwickelt und in das Softwarepaket OpenFOAM integriert. Er ermöglicht die Simulation komplexer transpirationsgekühlter Strukturen in Heißgasströmungen mit Unter- und Überschallgeschwindigkeit. Ein integraler Ansatz mit vollständiger Kopplung beider Domänen, d.h. Heißgasströmungsfeld und poröser Struktur, wurde bei der Entwicklung verfolgt. Hierbei wurde eine volumengemittelte Methode mit Berücksichtigung lokalem thermischen Nicht-Gleichgewichts gewählt. Zur Modellierung der Kühlmittelströmung innerhalb der porösen Struktur wird ein dreidimensionaler Darcy-Forchheimer-Ansatz verwendet. Weiterhin ist der Solver in der Lage, die Injektion beliebiger Kühlgase in die heiße Hauptströmung abzubilden. Ein flächengemitteltes Einblasmodell wird

mit einer modifizierten turbulenten Randbedingung kombiniert, um transpirierte poröse Wände darzustellen. Der Solver wurde auf verschiedene Testfälle angewandt und durch Vergleiche mit experimentellen Ergebnissen validiert.

Zunächst werden unidirektionale Durchströmungsversuche für Carbon/Carbon (C/C) Strukturen vorgestellt. Die Ergebnisse deuten darauf hin, dass die Permeabilitätskoeffizienten sowohl unabhängig von Kühlgas als auch Temperatur- und Druckniveau sind. Zusätzlich bestätigt ein Durchströmungsexperiment mit partieller Abdeckung des Auslasses das vorgeschlagene Überlagerungsprinzip für mehrdimensionale Kühlmittelströmung. Im zweiten Schritt wurden numerische Simulationen einer subsonischen turbulenten Kanalströmung mit Grenzschichtinjektion durchgeführt. Der Vergleich von numerischen Geschwindigkeits- und Temperaturprofilen mit experimentellen Daten validiert das angewandte Einblasmodell für mikroskopische Porenöffnungen sowie die für die Fremdgasinjektion eingesetzten numerischen Modelle.

Im Hauptteil der Arbeit werden dann transpirationsgekühlte C/C-Strukturen in Überschall-Heißgasströmungen untersucht. Dazu wurden Experimente im Überschallwindkanal des Instituts mit mehreren porösen Probengeometrien, einem Stoßgenerator und verschiedenen Kühlmitteln durchgeführt. Die Temperaturen wurden sowohl an den Oberflächen als auch innerhalb der porösen Proben mit Hilfe von Thermoelementen und in-situ kalibrierter Infrarot-Thermographie gemessen. Wanddruckmessungen und Schlierenfotografie wurden verwendet um das Überschallströmungsfeld zu charakterisieren. Der Einsatz von Transpirationskühlung reduziert signifikant die Temperaturen an der transpirierten Oberfläche, innerhalb der porösen Probe und im Nachlaufbereich. Der Effekt ist vom Ausblasparameter und den Kühlmitteleigenschaften abhängig. Es wurde festgestellt, dass eine Skalierung basierend auf der spezifischen Wärmekapazität die Kühleffizienz der porösen Wand für verschiedene Kühlmittel gut beschreibt. Variationen der Probenwanddicke führen zu lokal höheren Kühlmittelmassenströmen und verstärkter Kühlung. Ein ähnlicher Effekt wurde für komplexere Hauptströmungsbedingungen mit Stoßwellen und Expansionsfächern gefunden. Die ungleichmäßige Verteilung von Wanddruck und Wärmestrom beeinflusst die lokale Kühleffizienz in erheblichem Maße. Ebenso zeigt sich, dass die Grenzschichteinblasung einen Einfluss auf die Überschallhauptströmung hat, was die Bedeutung gekoppelter Simulationsansätze unterstreicht.

Hinsichtlich der Validierung des entwickelten OpenFOAM-Lösers und des verwendeten numerischen Setups zeigt sich, dass die Simulationen alle relevanten Effekte der verschiedenen Testfälle gut abbilden. Eine gute Übereinstimmung zwischen Experiment und Simulation wurde für alle Testfälle beobachtet.

Introduction

Flying has always been a dream of mankind and so the history of aviation dates back more than two thousand years. Following early attempts using gliders and lighter-than-air vehicles such as hot-air balloons or airships, the first powered flights were carried out at the beginning of the 20th century. Since then tremendous advances have been made in aviation and today, a life without air travelling as the fastest form of transportation has become unimaginable. Airplanes connect people around the world and enabled major developments such as the globalisation of our economy. In this context, flight speed has always been an important aspect for passenger travelling as well as the transport of urgently needed goods. Furthermore, the strong increase in the total number of flights and the discovery of man-made climate change have put the reduction of emissions into focus. Both the increase of flight speed and the reduction of emissions are strongly linked to the development of modern aircraft engines. As a consequence, a considerable amount of research aims at increasing the efficiency of gas turbines [124], while several projects investigate new engine concepts for high-speed planes which could reduce international flight times significantly [36].

In a similar manner as flying, the advent of the space age with its preliminary culmination in the lunar landing in 1969 has changed the world profoundly. Pushing the boundaries of the known world and exploring the universe fascinates people and, at the same time, could be vital for the future of humanity. Besides

manned and robotic space exploration, particularly the services of satellites in the areas of communication and navigation improve everyday life on earth. Furthermore, satellite-based earth observation supports the understanding of the planet. Likewise, the monitoring of the climate change from earth orbit provides the information on which grounds global political decisions for environmental protection are made. Therefore, space transportation is of vital importance to society today. Space launches are enabled by rocket technology which is strongly linked to engine development. Enormous amounts of energy are converted within minutes from chemical form into thrust, and eventually kinetic and potential energy. As a consequence of the extreme thermal and structural loads, the complete flight vehicle is typically disposed after a single launch. However, fully-reusable systems have the potential to increase the frequency of launches while simultaneously reduce the associated costs.

The described challenges in aviation as well as space travel are closely connected to the development of propulsion engines. Here in turn, one of the key aspects lies in thermal protection and cooling of the components exposed to high thermal loads. A malfunctioning of the cooling system typically results in catastrophic failure and therefore a reliable and well-understood system is of crucial importance. The research summarised in this thesis focuses on a promising cooling technique applied to modern lightweight composite materials. The investigated method of transpiration cooling offers significant potential regarding increases in cooling efficiency as well as overall cooling potential and is thus of great interest for future aerospace applications.

1.1 Thermal Protection in Aerospace Applications

Thermal protection is an essential aspect in the design and development of aerospace vehicles and their propulsion engines. To improve the thermal efficiency in aircraft engines, the turbine inlet temperature has been continuously increased throughout the past decades which led to more severe requirements on the applied materials and the cooling system [73, 196]. As the hot gas temperatures rise well above the limits of the applied materials, active cooling is required to keep the materials at acceptable temperatures. Besides the more severe temperature levels, also the efficient usage of the coolant fluid is in focus. Typically, fuel or compressed air are employed for cooling. Thus, a reduction of the coolant mass flow rate either increases the amount of fuel generating thrust or reduces the required compression work. Both yield a better engine performance.

In rocket technology, improved cooling and more efficient usage of fuel may yield increased pay load masses. Moreover, reusability has become an important aspect as it has the potential for more frequent launches at lower costs [155, 199]. However, the extreme thermal loads in a rocket engine pose significant challenges to materials as well as state-of-the-art cooling systems. Combustion temperatures of up to $3700\,$K in liquid-fuelled rocket engines require effective cooling techniques to maintain the temperatures below material limits. Additionally, the very large thermal gradients that occur within structural components such as the combustor wall are a limiting aspect.

Besides propulsion engines, also the external surfaces of spacecrafts performing atmospheric reentry are exposed to high thermal loads for the duration of descent flight. As the vehicle is slowed down by the planet's atmosphere and kinetic energy is converted into heat, very high wall temperatures appear on the exposed surfaces. The heat loads are typically reduced by radiation cooling as well as ablation of the external surfaces, i.e. melting and evaporation of the wall substrate. The occurring phase change processes bind large amounts of energy which keep the temperatures at acceptable limits. A significant drawback of this method is that the ablation process wears down the wall substrate. Therefore, parts of the external surfaces have to be renewed if the vehicle is to be flown again. An example for this is NASA's Space Shuttle Orbiter, where a significant number of the ceramic tiles had to be replaced after each flight. Regarding fully-reusable vehicles such as the envisaged space planes, the costly inspection and partial replacement of the thermal protection system would not be practical and increase the turn-around time between flights.

Likewise, future hypersonic aircraft for passenger transport will have to be operated frequently for economical reasons and therefore need to be based upon fully-reusable vehicle concepts (e.g references [21, 176, 178, 179, 197]). This application case is even more challenging as drag is an important aspect. In contrast to reentry spacecrafts (e.g. Apollo command module, Space Shuttle Orbiter, Intermediate Experimental Vehicle) where significant drag occurs and is even desired for aerodynamic breaking, sustained hypersonic flight can only be feasible if drag is kept to an absolute minimum. As a consequence, slender, sharp-edged component designs are selected for leading edges of wings and intakes which yield high heat flux densities and thus complicate the cooling of these structures. In addition to the external surfaces also the combustor parts of the applied airbreathing engines are critical in this regard. Most promising engine concepts for sustained hypersonic flight are ram- or scramjets [36, 166] which expose the internal combustor structures to extremely high thermal loads. With respect to this, not only the inlet and combustor walls but in particular the fuel injection system requires cooling. These devices can

either be wall-bounded or placed within the flow such as strut injectors. The latter-mentioned type significantly improves fuel mixing and is thus beneficial for combustion stability. However, at the same time, the sharp-edged struts are fully exposed to the high-speed flow and thus subject to severe aerothermal heating.

Active cooling techniques

Although progress in the field of material sciences keeps pushing the material limits to higher temperatures, active cooling for all of the mentioned applications is of crucial importance. Different cooling approaches exist which have to be carefully selected with respect to the expected level and duration of thermal loads occurring for the considered application. In the following, three cooling methods are briefly introduced, i.e. convective cooling, film cooling, and transpiration cooling. Figure 1.1 schematically illustrates the cooling techniques.
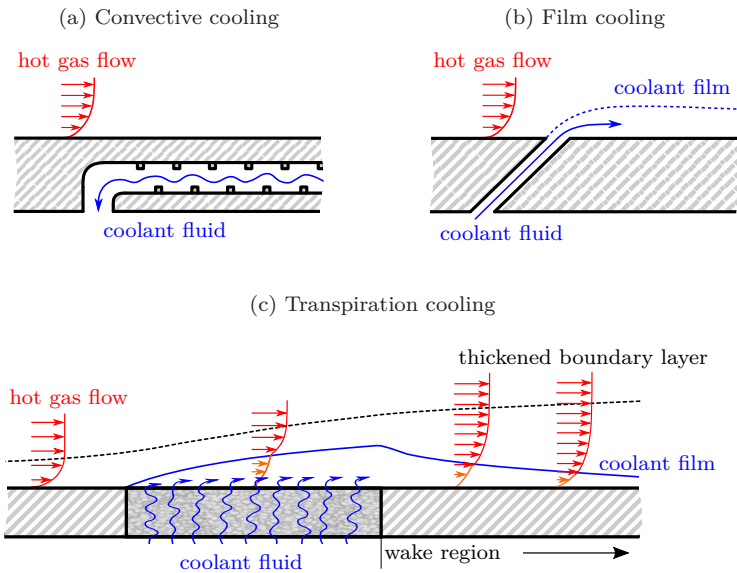
Figure 1.1: Schematic illustration of active cooling methods

In convective cooling, a coolant fluid passes the hot structure on its backside. Heat is first conducted through the wall substrate and then transferred by convection to the coolant. Turbulators and geometrical alterations such as ribs can be used to enhance the heat transfer and to increase the heat exchanging surface [1, 72, 121]. This cooling method is commonly employed in turbojet and liquid rocket engines, where typically air or fuel are employed as coolants. In a rocket engine, the coolant fluid is generally driven by a turbopump and directed through small coolant channels at the backside of the combustion chamber wall. Subsequently the fuel is fed into the injector head and finally the combustion chamber. Since the heat absorbed by the fuel is added to the combustion process again, this type of convective cooling is also referred to as regenerative cooling. Typically, metals such as copper alloys which feature large thermal conductivities are selected for the wall liners.

In both gas turbines and rocket engines, convective cooling is commonly combined with film cooling. This cooling method is based on the injection of a coolant fluid through holes or slots, thus forming a protective coolant-film layer between hot-gas environment and wall. Consequently, the heat flux into the wall is significantly reduced which also decreases the thermal gradients. Although film cooling is very effective in reducing the wall temperatures downstream of the injection location, it requires considerable amounts of coolant fluid. Therefore, the technique is often only applied for cooling of the most critical surfaces. In some rocket engines for example, the combustion chamber is cooled regeneratively while the throat section and the areas close to the injector face plate are additionally film-cooled. Various injection schemes ranging from slot openings over single holes to staggered arrays are employed. Additionally, the shape of film holes, injection angles and velocities are decisive parameters with respect to the resulting cooling efficiency [26, 65, 66]. The cooling effectiveness decreases rapidly as the coolant film is gradually consumed by turbulent mixing and heat conduction from the surrounding hot gas. This effect may even intensify due to secondary flow structures induced by the coolant injection itself. As a consequence, film cooling through a limited number of injection openings will always result in a wall temperature distribution which is non-uniform to some extent [9, 49]. As for regenerative cooling, the transferred heat is retained within the combustion chamber. However, the fuel injected for cooling in the near-wall region does not fully participate in the combustion process, hence resulting in a lower thrust of the engine when compared to a regeneratively-cooled engine.

Similar to film cooling, transpiration cooling introduces coolant fluid into the heated near-wall region. The cooling technique relies on a porous material which provides internal channels that can be used for coolant through flow. It

is based on two mechanisms acting within the porous structure ('internal') and in the main-flow boundary layer ('external'). First, a coolant fluid is provided to the backside of the heated porous wall at low temperature and elevated pressure. The pressure difference between distribution channel and hot-gas side drives a coolant mass flow through the internal porous channels towards the heated side. An intense heat exchange between fluid and solid occurs within the porous structure which reduces the porous wall temperature. Secondly, at the hot-gas side, the exiting coolant is injected into the main-flow boundary layer. As for film cooling, this decreases the net heat flux on the porous wall. In addition to the intense cooling of the transpired surface, the coolant film also protects the downstream region to some extent. In aerospace applications, the selected porous materials are typically dense and provide numerous microscopic pore openings and coolant channels. As a consequence, the fuel is distributed more homogeneously when compared to injection by means of separate film cooling openings. Moreover, the injection velocities are smaller which reduces main flow disturbances and associated thrust losses [97]. As transpiration cooling offers very high cooling potential it becomes particularly interesting if extreme continuous heat loads appear and regenerative cooling cannot be used any more [174]. Examples for this are high-speed aerospace applications such as leading edges of hypersonic vehicles or strut-injectors in scramjet engines. Furthermore, the combustion chamber throat of a reusable rocket engine represents an interesting application case. When applying transpiration cooling to combustion engines, similar as for film cooling, the injection of fuel for cooling purposes reduces the propulsion efficiency of an engine. As a consequence, small coolant flow rates are desirable. On the other hand, sufficient cooling is necessary to ensure structural integrity. Following this, optimising a cooling system using boundary-layer transpiration is a classical design problem. Consequently, a detailed knowledge of the physical processes as well as accurate modelling tools are required to trade engine overall efficiency against cooling.

A comparison of convective-, film-, and transpiration-cooling methods has been performed by Eckert and Livingood [49]. Their analytical study on a flat plate revealed superior cooling efficiencies for transpiration cooling in both laminar and turbulent flow regime when compared to the two other methods. Especially for elevated coolant mass flow rates, i.e. whenever considerable cooling is required, the advantage of transpiration cooling became apparent. Later, this was confirmed by Laganelli [108] for high-speed flows and foreign-gas injection. Additionally, an experimental investigation by Leontiev [119] supports the conclusions.

1.2 Transpiration Cooling

Several early analytical and experimental studies explored the influence of wall transpiration on the main-flow boundary layer for aerospace applications. Already in 1947, Rannie et al. [154] presented a first analytical model to determine the temperature of a transpired wall in a fully turbulent pipe flow. Further fundamental work was carried out in the 1950s using analytical [49, 162] as well as experimental approaches [137, 138]. In the studies, strong reductions in skin friction and heat transfer were detected which can be correlated to the dimensionless blowing parameter (or blowing ratio) defined by

$$F = \frac{\rho_c u_c}{\rho_{hg} u_{hg}} = \frac{\dot{m}_c/A_c}{\dot{m}_{hg}/A_{hg}} = \frac{\text{transpired mass flux}}{\text{hot gas mass flux}} \quad , \tag{1.1}$$

where ρ is density, u is velocity, and $\dot{m}/A$ denotes the area-specific mass flow rate. The subscripts 'c' and 'hg' represent values for coolant and hot gas flow, respectively.

Later, in the 1970s, detailed experimental measurements on porous flat plates in turbulent flow confirmed the earlier found relations [139, 171]. During this period of time, several experiments also demonstrated the potential of transpiration cooling for high-speed applications. These covered both supersonic conditions (M $\approx$ 3) [11, 114, 163] as well as hypersonic conditions (M $\approx$ 8) [207].

Moreover, various coolants were used including light gases (e.g. helium) [114, 145, 207] and heavy coolant gases (e.g. argon, Freon-12) [145, 207]. Numerical calculations extended the list of coolants and additionally investigated the influence of compressibility on transpiration cooling [108, 110]. More recently, additional studies on foreign-gas blowing confirmed the earlier results concerning the substantial effect of the coolant gas properties on transpiration cooling. Meinert et al. [130] performed detailed boundary-layer profile measurements for turbulent channel flow experiments with boundary-layer injection of air, argon, and helium into a subsonic heated main flow. The authors found helium to be most effective in the reduction of skin friction and heat transfer coefficients at the porous wall. Liu et al. [122] studied transpiration cooling applied to a porous nose cone both experimentally and numerically. Again, helium blowing yielded reduced temperatures when compared to heavier coolants with lower specific heat capacities. Additionally, the employed nose cone geometry induced a non-uniform coolant mass flow distribution which significantly affected the local cooling efficiencies. Besides gaseous coolants, also liquid coolants appear to be promising due to their generally higher specific heat capacities when compared to gases. Especially if the coolant undergoes a phase

change, considerable amounts of latent heat are absorbed as demonstrated for water in references [186] and [170]. However, vapour-blockage may adversely affect transpiration cooling and result in non-uniform temperature distributions for certain conditions [84, 194]. Recently, new concepts of self-pumping transpiration cooling were proposed which rely on capillary forces to deliver liquid water to the hot porous surface [85, 91].

In spite of the great potential of transpiration cooling and the mentioned advantages when compared to other cooling methods, a lack of suitable porous materials has prevented wide-spread application up to now. Few materials can cope with the structural loads appearing in combustion chambers or during hypersonic flight and, at the same time, are permeable enough to allow for a sufficient coolant flow rate [153, 185]. However, triggered by the advances in the field of material sciences and the availability of modern porous materials, new interest in transpiration cooling has emerged in the last decades. Besides sintered metal, porous ceramic matrix composites (CMC) are promising materials as they are lightweight, feature little thermal expansion, and are insensitive to thermal shocks. Besides, if protected from oxidation, they withstand high temperatures up to $1800\,\mathrm{K}$ and thus require less cooling compared to most metallic materials [22, 56, 142]. Based on this, several recent studies that investigated transpiration cooling for different application cases are briefly summarised in the following.

Liquid rocket engines

In the field of rocket engine development, transpiration cooling is of particular interest for reusable launch systems. As mentioned before, frequent cyclic loads are one of the limiting aspects for the life time of liquid rocket engines. In this context, transpiration cooling suggests an improved thermo-mechanical behaviour [77, 153]. Furthermore, system studies indicated that transpiration cooling yields a better overall engine performance if the required cooling mass ratio is small [67, 77]. The pressure loss in the coolant channels for a transpiration-cooled engine is significantly reduced when compared to regenerative cooling. The lower requirements on the fuel-supply system can either be transferred to a gain of combustion chamber pressure or a reduction of turbine work. Both aspects yield an increased performance of the overall engine which needs to be evaluated against the reductions in combustion efficiency.[1]

The general feasibility of transpiration-cooled ceramic rocket engines could be demonstrated by means of several experimental test campaigns. Serbest et

---

1   The reduction in combustion efficiency is a consequence of the wall injection of small amounts of fuel which subsequently do not fully partake in the combustion process.

al. [168] conducted hot-firing tests at chamber pressures up to 9 MPa using hydrogen/oxygen combustion at DLR's facilities in Lampoldshausen. In the experiments, the wall temperatures maintained below critical limits for relatively large cooling rates of approximately 10% of the main-stream mass flow rate. However, if transferred from sub-scale test hardware to full-scale application, this corresponds to cooling rates below 1% for which an overall performance gain is expected [77]. Additional life cycle experiments demonstrated a generally good resistance of the tested ceramics to material damage and erosion [168]. Hald et al. [71] and Ortelt et al. [143] summarise on several additional hot-gas and through-flow tests for transpiration-cooled rocket engines while other aspects such as mass, manufacturing costs, reusability, and chemical stability are discussed by Herbertz and Selzer [77]. Regarding the design of a transpiration-cooled thrust chamber, a careful layout of the porous wall liners is required to ensure sufficient cooling of all wall parts while avoiding excessive coolant mass flow rates. This is complicated by the large changes in heat flux and wall pressure along the axial length of a thrust chamber. Especially in the chamber's throat section as well as the thrust nozzle, non-uniform temperature distributions may appear as demonstrated numerically by Ghadiani [63]. In the study, the variation of pressure in combination with a single coolant reservoir let to a deviation from unidirectional coolant flow. The chamber geometry and the appearing cross-flow velocities then yielded a non-homogeneous distribution of coolant flow rate and cooling efficiency.

Reentry flight

With respect to atmospheric entry flights, research work at DLR demonstrated the general applicability of transpiration cooling for thermal protection of external surfaces. Significant temperature reductions were found by Kuhn and Hald [104] for a test series at application-relevant reentry conditions in an arc-heated wind tunnel. Later, this was confirmed by means of a parabolic flight experiment performed in the frame of the project SHEFEX II (SHarp Edge Flight EXperiment II). To evaluate transpiration cooling, one of the external wall panels of the faceted vehicle was replaced by a flat porous Carbon/Carbon (C/C) sample. Despite the relatively modest temperature levels of around 450 K during flight, Böhrk [20] found a significant cooling effect on the transpired surface which extended to the wake region.

Sustained hypersonic flight

Transpiration cooling is also a promising technique for thermal protection of hypersonic flight vehicles as well as their propulsion devices. Here, the

applied materials are exposed to extreme levels of continuous aerothermal loads ($\dot{q} > 12\,\mathrm{MW/m^2}$) while simultaneously enduring considerable structural loads [174, 177]. Considering this, the high maximum service temperature as well as the insensitivity to thermal shocks makes porous CMC materials ideal candidates for application in supersonic hot-gas environments.

Langener et al. [112] experimentally investigated flat plate samples manufactured from C/C material for scramjet-combustor relevant test conditions, i.e. hot gas temperatures of up to 1120 K and a Mach number of 2.1. Based on wall temperature measurements, the authors determined cooling efficiencies for different gaseous coolants and blowing ratios. The coolants' specific heat capacity and the coolant mass flow rate revealed to be decisive influences on the cooling efficiency, while the results were found to be fairly independent from the main-flow total temperature in the tested value range. The measurements show good agreement to a heat-balance model according to Kays et al. [96] after correction for lateral heat conduction apparent in the experiment. Moreover, Langener et al. [112] introduce an analytical relation based on the Darcy-Forchheimer model which is employed to predict the through-flow pressure loss in the hot gas tests.

Huang et al. [83] studied a transpiration-cooled strut injector in a supersonic wind tunnel using methane as coolant. The sintered stainless-steel strut was exposed for a duration of 60 s to a main flow at M = 2.5, $T_{tot} = 1774\,\mathrm{K}$, and $p_{tot} = 1.46\,\mathrm{MPa}$. Highest temperatures were observed at the leading edge where also slight ablation occurred. In spite of this, transpiration cooling proved to be effective as temperatures were significantly reduced when compared to the uncooled model. For slender geometries such as porous leading edges or strut injectors, numerical predictions show a reduced cooling effect in the stagnation point if only a single coolant reservoir is employed [150, 209]. In the considered test cases, this effect originated from either non-uniform external pressure distributions, variations of the porous wall thickness, or a combination of both. Experimentally, Jiang et al. [90] achieved a more uniform cooling efficiency along the length of the strut injector for increasing the injection pressure in the front region reservoir while reducing the pressure in the aft region. Therefore, a strut with two separate coolant reservoirs was manufactured. Reducing the wall thickness of a second modified strut's leading edge as well as adding micro holes at this position to a third strut yielded an even more homogeneous temperature distribution.

Regarding fibre-reinforced ceramics, the anisotropic material properties have an additional effect on transpiration cooling of leading edges. The numerical results by Prokein et al. [150] indicate a significant impact of the inner orien-

tation of fibre-reinforced materials on the temperature levels of sharp-edged structures. For non-favourable material configurations, this effect adds to the previously discussed geometry and pressure influences.

In this context, also the formation of shock waves and expansion fans in high-speed flows is of major importance as both supersonic flow phenomena introduce significant pressure variations. Moreover, significantly increased wall heat fluxes appear due to the complex interaction of shock wave and boundary-layer. Holden and Sweet [79] investigated the interactions of impinging shock waves and transpiration cooling. Their experimental studies at Mach numbers 6 and 8 demonstrated that transpiration cooling is also effective for flow situations exhibiting shock-wave/boundary-layer interaction. The additional thermal loads downstream of the shock impingement could be compensated by relatively small increases in coolant flow rate. Moreover, for the tested conditions, the intensified wall blowing had no significant influence on the size of interaction and separation regions. Recently, a combined numerical and experimental study by Jiang et al. [92] confirmed the slight decrease of transpiration cooling efficiency downstream of the impinging shock wave. Again, applying a higher blowing ratio to the tested sintered bronze plate could compensate for this. Similar results are reported by Strauss et al. for injection of gaseous nitrogen and hydrogen [180, 181]. The observed reduction in the cooling effect is based on a combination of two effects, i.e. a locally increased heat flux and a local rise in wall pressure. The latter yields a smaller pressure difference between transpired surface and coolant reservoir, thus reducing the coolant mass flow rate locally [92, 151]. As the processes within the porous structure and in the main flow are interacting, a conjugate problem arises.

Numerical modelling of transpiration cooling

For the efficient design and layout of transpiration cooling systems, the availability of accurate and reliable numerical tools is of great importance.

Several engineering tools combine analytical or empirical correlations for external flows with the volume-averaged modelling of internal processes in the porous structure [19, 64, 86, 96, 103, 112]. Typically, the models consider the cooling problem as one-dimensional and employ a variant of the Darcy-Forchheimer model for momentum loss of the coolant fluid during through flow [141]. Regarding the energy conservation within the porous structure either a single governing equation or two separate equations are considered for the porous region. Solving only a single energy equation assumes that coolant fluid and porous solid are at the same temperature throughout the porous structure which corresponds to local thermal equilibrium. However, depending

on the considered transpiration-cooling situation, considerable temperature differences between coolant and solid can occur [115, 192]. More detailed approaches thus consider separate energy equations for fluid and solid which are coupled by a volumetric heat exchange coefficient. However, the modelling of the latter as well as the selection of appropriate boundary conditions for the simulation depends on the considered test case and is still uncertain.

Although the engineering methods yield generally good agreement for selected experiments, they are also restricted to well-known flow situations and simple geometries. More complex transpiration cooling cases may exhibit variations in the porous wall thickness or non-uniform hot-gas flow fields. The first-mentioned effect occurs for application cases involving non-flat geometries such as nose cones, strut injectors, or thrust chamber throats. With respect to the main-flow conditions, pressure variations may be introduced for example by flow acceleration or as a consequence of the formation of shock waves and expansion fans [63, 79, 90]. As these effects can hardly be captured by the available correlations, the modelling of transpiration cooling for such applications demands for superior methods such as computational fluid dynamics (CFD).

Several researchers have investigated transpiration cooling using CFD methods [13, 83, 92, 122, 123]. However, only few studies discuss the coupling conditions and their numerical implementation at the transpired interface [33, 37]. Dahmen et al. [37] investigated a subsonic turbulent channel flow with a flat porous C/C wall segment. Their analysis focuses on the external cooling mechanism and evaluates the boundary-layer profiles of velocity and temperature with injection. For this, the authors loosely couple separate solvers for main flow and porous medium by data exchange at the domain boundaries. Cheuret et al. [33] employed a commercial CFD solver to simulate a supersonic transpiration-cooling experiment with a flat porous C/C sample. In their approach, the authors use a single-simulation domain which distinguishes based on the porosity ε between porous structure ($\varepsilon < 1$) and main flow ($\varepsilon = 1$). At the virtual porous interface, the approach applies correction terms for viscous, conductive, and convective terms. As only a single energy equation is solved for the complete domain, local thermal equilibrium (LTE) between coolant and solid phase is assumed.

Recently, also Large Eddy Simulation (LES) as well as Direct Numerical Simulation (DNS) have been performed to resolve turbulence effects for wall injection in more detail [25, 32, 98]. However, these studies focused on the main-flow region only and did not consider the porous wall.

1.3 Motivation and Approach

Transpiration cooling offers great potential for the thermal protection of future combustion engines as well as hypersonic vehicles. As a consequence, a considerate body of research work has focused on different aspects of the cooling technique. In addition to many experimental studies, recently also numerical investigations have emerged. However, the detailed modelling of transpiration cooling as well as the numerical coupling of processes occurring within the porous structure and in the hot-gas main flow field have still not been conclusively investigated. Moreover, numerical tools for the design and layout of transpiration-cooled structures are lacking. This is of particular importance, since the design of aerospace applications increasingly relies on simulation results.

Therefore, within the given thesis work, a numerical CFD solver has been developed that allows the simulation of complex transpiration-cooled structures in non-uniform sub- and supersonic hot-gas flows. The solver is applied to various test cases and validated by means of comparisons to experimental data. Besides the validation of the new solver, the combined numerical and experimental approach aims to enhance the understanding of transpiration cooling for more complex porous geometries and main-flow situations. The main part of the thesis work was embedded in the Helmholtz research project 'High Temperature Management in Hypersonic Flight' which has been conducted in close collaboration between the German Aerospace Center DLR and University of Stuttgart.

Regarding the numerical solver, an integral approach with full coupling of both domains, i.e. hot-gas flow field and porous structure, is followed. For practical reasons, a volume-averaged method with consideration of local thermal non-equilibrium effects was selected. A three-dimensional Darcy-Forchheimer approach is employed to model coolant through flow. Moreover, the solver is capable of modelling the injection of arbitrary coolant gases in a hot main flow of air. Special attention was put on the consideration of anisotropic material parameters which are characteristic for the investigated fibre-reinforced ceramics, i.e. thermal conductivity and permeability. To allow the implementation of own models and solver modifications, the OpenFOAM software package was selected as the framework for the development. Moreover, as OpenFOAM is free of any licensing costs, the open-source software allows for massive parallelisation of simulations.

The developed solver is validated by means of comparison to several transpiration-cooling experiments. Data from literature is employed to validate the modelling of boundary-layer injection through porous walls. Regarding

several other aspects of transpiration cooling, experimental data was found to be sparse and not suitable for the solver's validation. For this reason, several new experiments have been performed in the frame of the given work. The tests cover isothermal through-flow experiments featuring both unidirectional and multidimensional coolant flows. The obtained test data is employed to validate the numerical models regarding the flow behaviour through the pores of fibre-reinforced ceramics. Furthermore, transpiration-cooling experiments in a supersonic wind tunnel have been conducted using different samples, a shock generator, and various coolants. Rather modest temperature levels have been selected to reduce parasitic influences and thus allow for precise measurements. Although the absolute temperatures ($T_{tot} = 500K$) are well below the conditions of real applications, the tests at the ITLR Hot Gas Facility provide a sufficient data base for model development and solver validation. To explore several aspects of transpiration-cooled applications such as mentioned in the introduction, multiple test cases have been studied. Figure 1.2 illustrates the sample geometries and their effects on the flow field schematically.

The 'reference sample' as shown in figure 1.2a on the channel's top wall represents the baseline test case for transpiration cooling. The constant wall thickness in combination with uniform main-flow conditions will result in a rather uniform coolant blowing over the transpired surface. The 'contoured sample' is employed to explore the influence of a variation in the porous wall thickness. The intensity of boundary-layer blowing is expected to change with sample thickness thus yielding a non-uniform coolant flow rate distribution, see figure 1.2b. The effect of pressure variations along the transpired surface is investigated by means of the test cases using a 'shock generator' as shown in figure 1.2c. In the supersonic regime, high-speed flow phenomena such as shock waves and expansion fans may introduce significant pressure variations. Both occur for deflections of the supersonic flow and can thus be triggered by geometrical obstructions. Based on this principle, the shock generator artificially creates a non-uniform flow field to investigate the effect on transpiration cooling. The device is applied in combination with reference sample and contoured sample in the experiments. Lastly, the 'double-wedge sample' given in figure 1.2d combines the effect of wall-thickness variation with a non-uniform main flow field. Due to its non-flat geometry that protrudes into the supersonic flow channel, the porous sample itself creates a system of shock waves and expansion fans. The superposition of effects represents an ideal validation test case for the developed OpenFOAM solver.

Throughout the thesis, a combined numerical and experimental approach is followed to investigate transpiration cooling while validating the new OpenFOAM solver at the same time.

(a) Reference sample

coolant film

boundary layer

(b) Contoured sample

coolant film

boundary layer

(c) Shock generator

shock generator   shock waves

(d) Double-wedge sample

shock wave
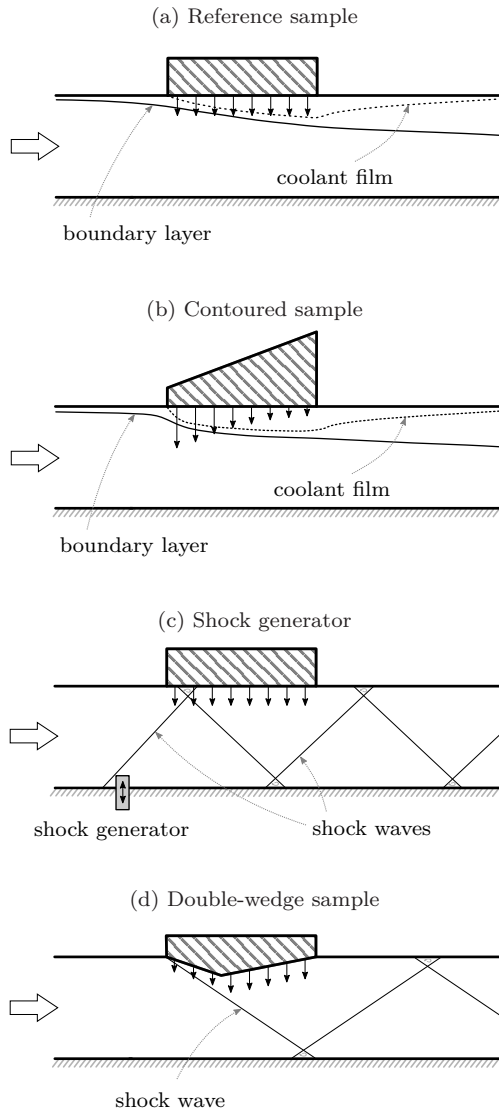
Figure 1.2: Schematic illustration of investigated test cases

1 Introduction

In the following chapters, first, the theoretical background is briefly presented. This concerns the physical fundamentals of compressible high-speed flows and heat transfer as well as the theory of porous media. Subsequently, the experimental setup featuring the supersonic hot-gas channel as well as the different porous samples and the applied measurement techniques are described. The numerical setup and the developed OpenFOAM are detailed afterwards. Besides the numerical methods, an emphasis is placed on the treatment of porous surfaces in the performed simulations. Results on the physical processes within the porous structure, boundary-layer injection into a subsonic turbulent main flow, and transpiration cooling in the supersonic flow regime are presented in chapters 5 to 7. The following table gives an overview of the discussed problems and solution approaches followed.

#	Issue / problem	Approach
5 - 1	**Internal heat transfer**	
	assess situation of internal heat transfer for the here-investigated test cases	evaluate analytical criterion on the deviations between LTE and LTNE
	validate numerical implementation of two-equation energy model	comparison of OpenFOAM simulation to analytical solution
5 - 2	**Unidirectional through-flow behaviour**	
	determination of permeability coefficients for C/C	perform isothermal through-flow tests to obtain Darcy-Forchheimer model coefficients
	evaluate influence of gas properties on the permeability coefficients	perform through-flow tests with different coolant gases
	evaluate influence of fluid temperature and pressure level	analyse hot-gas wind tunnel test data regarding pressure losses (c.f. ch. 7)
	validate OpenFOAM solver with respect to modelling of through-flow processes for various gases as well as different temperature and pressure levels	perform corresponding numerical simulations and compare results to experimental data
5 - 3	**Multidimensional through-flow behaviour**	
	investigate multidimensional through-flow situations within a porous C/C structure	perform through-flow experiments and simulations with partial sealing of outlet area
	validate superposition principle of the 3D-Darcy-Forchheimer approach and its implementation in OpenFOAM	compare integral pressure losses in experiment and simulations

#	Issue / problem	Approach
6	**Boundary-layer injection of various coolants**	
	numerical modelling of boundary-layer injection for various gases and validation of applied models	perform simulations with injection of different gases at isothermal and heated main-flow conditions and compare to test data from literature
	validation of foreign-gas modelling including gas mixtures and diffusion processes	
7 - 1	**Supersonic channel flow without boundary-layer blowing**	
	characterise reference conditions for supersonic flow test case without blowing	perform wind-tunnel experiments and analyse test conditions
	determination of correct numerical setup and validation of OpenFOAM solver for no-blowing test case	perform sensitivity studies on turbulence parameters and compare simulation results to experimental data
7 - 2	**Transpiration cooling in supersonic flow - numerical setup**	
	determination of numerical setup for transpiration-cooling test cases	evaluate resolution of numerical grid based on GCI analysis
		perform sensitivity studies regarding unknown parameters, i.e. turbulent boundary condition at the wall, volumetric heat transfer coefficient, and thermal condition on coolant-reservoir surface
7 - 3	**Reference sample - uniform flow and flat sample**	
	explore transpiration cooling for a flat porous C/C sample in supersonic flow	perform experiments and simulations with reference sample at various blowing rates
	evaluate the influence of lateral heat conduction from the surrounding channel parts into the porous sample	perform simulations for the reference-sample test case with enlarged numerical domain including surroundings
	investigate transpiration cooling with gases other than air and evaluate the influence of coolant gas properties	analyse experimental and numerical results for reference sample test cases using various coolant gases
	validate OpenFOAM solver and numerical setup for transpiration cooling of porous C/C in supersonic flow	compare numerical and experimental results for the reference-sample test cases
	validate OpenFOAM solver w.r.t. foreign-gas modelling and transpiration cooling	compare numerical simulation cases for foreign-gas injection to the respective experimental test data

17

#	Issue / problem	Approach
7 - 4	**Contoured sample - variation of wall thickness**	
	investigate influence of a variation of the porous wall thickness	perform wind-tunnel experiments and complementary simulations with the contoured sample
	validate OpenFOAM solver and setup for more complex transpiration-cooled geometries	compare numerical results for contoured sample 0° and 180° to experimental data
7 - 5	**Shock generator - transpiration cooling in more complex flow fields**	
	explore the effect of considerable non-uniformities in the main flow field on transpiration cooling (i.e. variations of pressure, temperature, and heat flux)	perform experiments and simulations for the reference sample combined with a shock-generator wall insert
	validate OpenFOAM solver and setup for the simulation of more complex main flow fields without and with transpiration cooling	compare numerical and experimental results for shock-generator test cases without and with blowing through the reference sample
	investigate combined effect of non-uniform main flow fields and sample wall-thickness variation	perform shock-generator experiments using the contoured sample and analyse in combination with simulations
7 - 6	**Double-wedge sample - combined effects of geometry and flow field**	
	concluding investigation on test case with non-flat porous sample that combines geometry and main-flow effects	perform transpiration-cooling experiments and simulations for double-wedge sample at various blowing rates and with different coolant gases
	validate OpenFOAM solver for more complex geometries and non-uniform main-flow conditions using different coolants at various blowing rates	compare numerical results to experimental data for porous double-wedge test cases
	validate proposed modified turbulence BC for transpired surfaces of non-flat sample in more complex flow	perform numerical sensitivity study on the choice of BC for the transpired surface of the double wedge

---

Physical Fundamentals

The following chapter briefly introduces the physical background on which the presented investigations on transpiration cooling in sub- and supersonic flows are based. First, the governing equations to describe compressible flows of multiple species are detailed. Certain characteristics of high-speed flows as well as viscous effects are discussed afterwards. Moreover, the basics of convective heat transfer and heat conduction are established with a brief description of the influence of boundary-layer blowing. The fundamentals conclude with an introduction on porous media theory including volume-averaged modelling approaches for through flow and internal heat transfer.

2.1 Governing Equations for Compressible Flow

Fundamental laws of conservation with respect to mass, momentum, and energy apply to any kind of fluid in motion. The resulting governing equations for compressible flows are briefly described in the following and supplemented by the thermal and caloric equations of state. From a mathematical point of view, the set of coupled differential equations can hardly be solved analytically unless several assumption are made. However, numerical methods allow the approximate solution and are thus commonly employed in the simulation of compressible flows.

2.1.1 Conservation of Mass

Mass can neither be created nor destroyed in a closed system. Consequently, the rate of mass change inside a considered control volume equals the net mass flux over the volume's surface. Mathematically this can be expressed by the integral form of the continuity equation (in conservational form):

$$\frac{\partial}{\partial t} \iiint_V \rho \mathrm{d}V + \iint_S \rho \boldsymbol{u} \cdot \mathrm{d}\boldsymbol{S} = 0 \quad , \tag{2.1}$$

where V is the control volume and $\boldsymbol{S}$ is the surrounding surface vector. Applying Gauss' divergence theorem, the differential form for an infinitesimal small volume element is obtained:

$$\frac{\partial \rho}{\partial t} + \nabla \cdot (\rho \boldsymbol{u}) = 0 \quad . \tag{2.2}$$

Equations (2.1) and (2.2) are generally valid and apply to all kind of flows ranging from compressible, incompressible, viscous, or inviscid. However, the given formulation is for a single fluid species or a single fluid mixture only. If multiple species are to be considered, conservation equations for the mass fraction Y_i of each component are required:

$$\frac{\partial}{\partial t}(\rho Y_i) + \nabla \cdot (\rho \boldsymbol{u} Y_i) = -\nabla \cdot \boldsymbol{j}_i \quad . \tag{2.3}$$

In addition to advection, the random motion of molecules leads to species diffusion which is accounted for by the diffusion flux $\boldsymbol{j}$. According to Schlichting and Gersten [164], the diffusion law for a binary mixture reads

$$\boldsymbol{j}_1 = -\rho D_{12}[\nabla Y_1 + \bar{\alpha} Y_1 (1 - Y_1) \nabla(\ln(T))] \quad , \tag{2.4}$$

where the subscripts '1' and '2' indicate the two mixture components and D_{12} is the diffusion coefficient as given in section 2.1.5. In equation (2.4) the first term determines diffusion due to concentration gradients and is also known as Fick's diffusion law [52]. The second term describes diffusion due to temperature gradients and is based on the Soret effect [175]. As diffusion in transpiration-cooling processes is primarily governed by concentration gradients and convective mixing, thermal (mass) diffusion may be neglected in the frame of this thesis by assuming $\bar{\alpha} = 0$. Moreover, also diffusion effects due to pressure gradients and volume forces have been omitted in equation (2.4) as both have a negligible influence in most practical flow problems [62, 129, 206].

To satisfy the continuity equation, the sum of all species mass fractions Y_i equals unity. In numerical simulations, this is commonly reached by the following closure for the last component of the mixture:[1]

$$Y_N = 1 - \sum_{i=1}^{N-1} Y_i \quad . \tag{2.5}$$

2.1.2 Conservation of Momentum

A fundamental principle of physics states that the sum of external forces onto an object is equal to the rate of momentum change that the object experiences. This principle which is also known as Newton's second law is commonly formulated for a body of constant mass as

$$\boldsymbol{F} = \frac{\partial(m\boldsymbol{u})}{\partial t} = m\boldsymbol{a} \quad . \tag{2.6}$$

Different forces may be acting on a fluid particle which can be distinguished into body and surface forces. The first type acts directly on the fluid and thus inside the considered control volume, e.g. gravitational or electromagnetic forces. Surface forces, on the other hand, work on the surface of the fluid volume and comprise a viscous component, i.e. shear and normal stresses, τ_{ij} and τ_{ii}, as well as pressure forces that also apply for inviscid flows. The mentioned forces are equal to the sum of momentum change per time inside the considered volume and the convective momentum transport over the control volume's surface. This can be expressed by the integral form of the momentum equation (in conservational form):

$$\iiint_V \frac{\partial(\rho\boldsymbol{u})}{\partial t} \mathrm{d}V + \iint_S (\rho\boldsymbol{u} \cdot \mathrm{d}\boldsymbol{S})\boldsymbol{u} = \iiint_V \rho\boldsymbol{f}\mathrm{d}V + \boldsymbol{F}_{visc} - \iint_S p\mathrm{d}\boldsymbol{S} \quad . \tag{2.7}$$

Equation (2.7) can be translated into its differential form yielding coupled equations for the three directional components. In honour of the two researchers that independently obtained the set of equations in the first half of the nineteenth century, they are commonly referred to as the Navier-Stokes equations.

---

1   Selecting a component with a rather high mass fraction as species 'N' keeps the associated numerical error small.

Neglecting body forces which do not play a significant role for the present thesis results in the following form:

$$\frac{\partial}{\partial t}(\rho \boldsymbol{u}) + \nabla \cdot (\rho \boldsymbol{u} \otimes \boldsymbol{u}) = -\nabla p + \nabla \cdot \boldsymbol{\tau} \quad . \tag{2.8}$$

Assuming a Newtonian fluid, i.e. shear stress is proportional to shear velocity, and employing Stokes' hypothesis, the viscous stress tensor is given by

$$\boldsymbol{\tau} = \mu \big[\nabla \otimes \boldsymbol{u} + (\nabla \otimes \boldsymbol{u})^T \big] - \frac{2}{3}\mu(\nabla \cdot \boldsymbol{u})\boldsymbol{I} \quad . \tag{2.9}$$

The dynamic viscosity μ is a fluid property which depends on temperature. Values can either be obtained from fluid property databases or through fitted functions as detailed in section 2.1.5.

2.1.3 Conservation of Energy

The first law of thermodynamics states that energy can neither be created nor destroyed and thus the total energy in a closed system is constant. However, energy can be transformed from one form to another, e.g. from kinetic to internal energy. With respect to a fluid volume, the rate of energy change equals the sum of work due to body and surface forces, and the net heat flux into the fluid volume. The latter includes convective energy transport, heat conduction, diffusion, and possibly also volumetric heating of the considered volume. Following this, the integral form of the energy equation is given by

$$\iiint_V \frac{\partial(\rho e_{tot})}{\partial t} \mathrm{d}V + \iint_S \rho e_{tot}\boldsymbol{u} \cdot \mathrm{d}\boldsymbol{S} = \\ \dot{W}_{visc} - \iint_S p\boldsymbol{u} \cdot \mathrm{d}\boldsymbol{S} + \iiint_V \rho(\boldsymbol{f} \cdot \boldsymbol{u})\mathrm{d}V + \dot{Q} \quad . \tag{2.10}$$

For high-speed flows such as investigated in the frame of this thesis, the internal energy stored in the kinetic movement of molecules is significant. Consequently, the total internal energy e_{tot} is used in equation (2.10) instead of the static internal energy e_{st}. The two specific energies are connected by the following relation:

$$e_{tot} = e_{st} + \frac{|\boldsymbol{u}|^2}{2} \quad . \tag{2.11}$$

For the sake of convenience, the static enthalpy may be introduced as $h_{st} = e_{st} + p/\rho$. The total enthalpy is then obtained from $h_{tot} = h_{st} + |\boldsymbol{u}|^2/2$. For an ideal gas mixture consisting of N different species, the static enthalpy per unit mass is defined by

$$h_{st} = \sum_{i=1}^{N} Y_i h_{st,i} \quad . \tag{2.12}$$

Combining these definitions with equation (2.10), the differential form of the total energy equation is obtained:

$$\frac{\partial}{\partial t}(\rho h_{tot}) + \nabla \cdot (\rho \boldsymbol{u} h_{tot}) - \frac{\partial p}{\partial t} = -\nabla \cdot \dot{\boldsymbol{q}} + \nabla \cdot (\boldsymbol{\tau} \cdot \boldsymbol{u}) \quad . \tag{2.13}$$

The heat flux $\dot{\boldsymbol{q}}$ accounts for heat conduction as well as energy transport due to mass diffusion and is given for a binary mixture by

$$\dot{\boldsymbol{q}} = -k\nabla T + (h_{st,1} - h_{st,2})\boldsymbol{j}_1 \quad . \tag{2.14}$$

Radiation effects are assumed to play a minor role in the frame of the present thesis and are thus not considered.

2.1.4 Equations of State

Two additional relations close the system of equations (2.2), (2.8), and (2.13). The thermal state equation connects pressure, temperature, and density. For a pure gas it is given by

$$p = \rho R T \quad , \tag{2.15}$$

with the specific gas constant R. The so-called ideal gas law neglects intermolecular forces which is strictly speaking only valid for gases at comparably low pressure or high temperature. For gas mixtures consisting of multiple species, equation (2.15) can be expressed by

$$p = \rho R_m T \sum_{i=1}^{N} \frac{Y_i}{W_i} \quad , \tag{2.16}$$

where R_m is the universal gas constant, ρ is the mixture density, and W_i are the molecular weights of the individual species.

Furthermore, gases are assumed to be thermally perfect in the given thesis and thus the specific heat capacities c_p and c_v are functions of temperature only. This expresses in the caloric equation of state for a pure gas

$$h_{st} = h_{st,ref} + \int_{T_{ref}}^{T} c_p(T') \, dT' \quad , \tag{2.17}$$

where $h_{st,ref}$ is the specific enthalpy of formation at a reference temperature T_{ref}.

2.1.5 Physical Properties

In the following section, the applied relations and laws used to determine necessary physical properties and proportionality constants are described. A first overview of selected fluid properties of the employed coolant gases at standard reference conditions is given in table 2.1.

Table 2.1: Selected fluid properties of air, helium, argon, carbon dioxide (CO_2), and nitrogen (N_2) at $T = 293.15$ K, $p = 101.325$ kPa [60, 201]

	W $\left[\frac{kg}{kmol}\right]$	ρ $\left[\frac{kg}{m^3}\right]$	c_p $\left[\frac{J}{kgK}\right]$	μ $\left[\frac{kg}{ms}\right]$	k $\left[\frac{W}{mK}\right]$	Pr $[-]$
Air	28.959	1.204	1006.4	$1.821 \cdot 10^{-5}$	0.0259	0.708
Helium	4.003	0.166	5193.0	$1.962 \cdot 10^{-5}$	0.1535	0.664
Argon	39.948	1.662	521.6	$2.231 \cdot 10^{-5}$	0.0175	0.665
CO_2	44.010	1.839	846.1	$1.469 \cdot 10^{-5}$	0.0162	0.765
N_2	28.013	1.165	1041.3	$1.757 \cdot 10^{-5}$	0.0255	0.718

Physical properties of pure gases and gas mixtures

The specific heat capacity of pure gases at a wide temperature range can be calculated from the JANAF/NASA polynomials as provided by Burcat and Ruscic [27]:

$$\frac{c_p}{R} = a_1 + a_2 T + a_3 T^2 + a_4 T^3 + a_5 T^4 \quad , \tag{2.18}$$

where a_1 to a_5 are fluid-dependent coefficients obtained through fitting of experimental data.[2] For a mixture of gases, c_p can be determined from the components' mass fractions Y_i:

$$c_p = \sum_{i=1}^{N} Y_i c_{p,i} \quad .$$

(2.19)

Sutherland's law [182] is used to determine the viscosities of pure gases at a specified temperature:

$$\mu = \frac{A_S \sqrt{T}}{1 + \frac{T_S}{T}} \quad ,$$

(2.20)

where A_S and T_S are the Sutherland constants as given in table 2.2.

To obtain properties for a mixture of several gaseous components, various mixing laws based on kinetic gas theory and empirical findings exist, see for example Poling et al. [149]. With respect to the dynamic viscosity, Sutherland [182] and Wilke [205] suggested the following equation for mixtures of non-polar gases at low pressure:

$$\mu = \sum_{i=1}^{N} \frac{\mu_i}{1 + \frac{1}{\psi_i} \sum_{j=1, j \neq i}^{N} \psi_j \Phi_{ij}}$$

$$\text{with} \quad \Phi_{ij} = \left[1 + \left(\frac{\mu_i}{\mu_j} \right)^{1/2} \left(\frac{W_j}{W_i} \right)^{1/4} \right]^2 \left[8 \left(1 + \frac{W_i}{W_j} \right) \right]^{-1/2} \quad .$$

(2.21)

In equation (2.21), ψ_i denotes the molar fraction of species 'i' and Φ_{ij} is an interaction parameter calculated from the molecular weights W_i and the dynamic viscosities μ_i of the species. Wilke's law has been extensively tested by many authors who found an accuracy of better than 2 % when compared to experimental values, see for example Wilke [205] or Dean and Stiel [39].

---

2 Two sets of coefficients for low and high temperatures are provided to cover the temperature range from 200 K to 6000 K with a switch between both branches at 1000 K.

The thermal conductivity for a pure gas is calculated according to kinetic gas theory by means of the modified Eucken correlation for polyatomic gases [149]:

$$\frac{k}{\mu c_v} = 1.32 + \frac{1.77}{c_v/R} \quad , \tag{2.22}$$

where $c_v = (c_p - R)$ is the specific heat capacity at constant volume.

Similar to the way of calculating the dynamic viscosity of mixtures, Wassiljewa [195] introduced a mixing rule for thermal conductivities. Her findings were later examined by Mason and Saxena [127] who proposed the corresponding interaction parameter A_{ij}. The combination yields

$$k = \sum_{i=1}^{N} \frac{k_i}{1 + \frac{1}{\psi_i} \sum_{j=1, j \neq i}^{N} \psi_j A_{ij}}$$
$$\text{with} \quad A_{ij} = \varepsilon_k \cdot \left[1 + \left(\frac{k_{tr,i}}{k_{tr,j}} \right)^{1/2} \left(\frac{W_i}{W_j} \right)^{1/4} \right]^2 \left[8 \left(1 + \frac{W_i}{W_j} \right) \right]^{-1/2} \quad . \tag{2.23}$$

The interaction parameter A_{ij} is determined from the molecular weights W_i, the monoatomic values of the thermal conductivities $k_{tr,i}$, and the factor ε_k. For the latter different values near unity were found, Poling et al. [149] suggest $\varepsilon_k = 1.0$. Using two relations based on kinetic gas theory for monoatomic gases, i.e. $k/(\mu c_v) = 5/2$ and $c_v = 3/2\,R$, yields $k_{tr,i}/k_{tr,j} = (\mu_i/\mu_j)(W_j/W_i)$. Following this leads to $A_{ij} = \Phi_{ij}$, so that the interaction parameter Φ_{ij} can be applied for both viscosity and thermal conductivity calculation. The general error for non-polar gas mixtures is reported to be less than $3-4\,\%$ [149].

Table 2.2: Model parameters for Sutherland and Fuller-Schettler-Giddings relations [60, 201]

	A_S $\left[\frac{\text{kg}}{\text{ms}\sqrt{\text{K}}} \right]$	T_S [K]	$\left(\sum v_i \right)$ $\left[\text{cm}^3 \right]$
Air	$1.461 \cdot 10^{-6}$	111.00	19.70
Helium	$1.461 \cdot 10^{-6}$	79.44	2.67
Argon	$1.964 \cdot 10^{-6}$	144.00	16.20
CO_2	$1.503 \cdot 10^{-6}$	222.00	26.70
N_2	$1.401 \cdot 10^{-6}$	107.00	18.50

Diffusion coefficients for binary mixtures

The binary diffusion coefficient D_{12} relates diffusion flux to species concentration gradient as described by equation (2.4). The proportionality constant depends on the mixture composition as well as local pressure and temperature. Various equations exist to determine the coefficient for binary gas systems at low pressure, see for example Poling et al. [149]. Due to its accuracy and simplicity, the Fuller-Schettler-Giddings relation [59] was employed for the present thesis work:

$$D_{12} = D_{AB} = \frac{A_D^* \; T^{7/4} \left(\frac{1}{W_A} + \frac{1}{W_B} \right)^{1/2}}{p \; \left\{ \left(\sum v_i \right)_A^{1/3} + \left(\sum v_i \right)_B^{1/3} \right\}^2} \quad , \tag{2.24}$$

with the constant $A_D^* = 3.204 \cdot 10^{-8}$ (s^{3}K$^{1.75}$mol$^{0.5}$)/(m^{3}kg$^{1.5}$) and the diffusion volumes $\left(\sum v_i \right)$ of the binary mixture's components.[3] Relation (2.24) as well as the diffusion volumes for several atoms and simple molecules were obtained through a least-square fitting of experimental data on various binary diffusion systems. The average deviation between calculated diffusion coefficients and experimental data is stated to be 4.2 % [58]. Fuller et al. [60] later updated the diffusion volumes and obtained slightly optimised values which are given for air, helium, argon, carbon dioxide (CO_2), and nitrogen (N_2) in table 2.2.

2.2 High-Speed Flows

Several flow features are characteristic for high-speed flows and have a significant influence on compressible flow fields. Opposed to subsonic flows, the propagation of information in supersonic flows is limited to the downstream direction. This is due to the confined speed at which information is transported within a gas, i.e. the speed of sound c_s. The information propagation is based on the interaction of molecules (e.g. collisions) and is thus governed by the average molecular velocity due to random thermal motion. Consequently, if the bulk velocity of a flow is higher than the speed of sound (within the moving bulk), disturbances cannot travel upstream.

---

3   To obtain the diffusion coefficient D_{12} in m^2/s, values of T, p, W, and $\left(\sum v_i \right)$ have to be inserted in SI units into equation (2.24).

The speed of sound for gases in general and more specifically ideal gases (right-hand side) is defined by

$$c_s = \sqrt{\left(\frac{\partial p}{\partial \rho}\right)_{\Delta s=0}} \overset{IG}{=} \sqrt{\gamma R T} \quad , \tag{2.25}$$

where the partial derivative is taken at constant entropy s and $\gamma = c_p/c_v$ represents the ratio of specific heats [8].

The Mach number gives the ratio of directed flow velocity u_∞ to the speed of sound. It is calculated from

$$M = \frac{u_\infty}{c_s} \quad . \tag{2.26}$$

Based on this definition, compressible flows can be divided into different flow regimes, i.e. subsonic (M < 1), transonic (M $\approx$ 1), supersonic (M > 1), and hypersonic (M $\gtrsim$ 5).

Within an isentropic flow of an ideal gas, the following equations relate static and total values of the state variables for density, pressure, and temperature:

$$\frac{\rho_{tot}}{\rho} = \left(1 + \frac{\gamma - 1}{2} M^2\right)^{\frac{1}{\gamma - 1}} \tag{2.27}$$

$$\frac{p_{tot}}{p} = \left(1 + \frac{\gamma - 1}{2} M^2\right)^{\frac{\gamma}{\gamma - 1}} \tag{2.28}$$

$$\frac{T_{tot}}{T} = \left(1 + \frac{\gamma - 1}{2} M^2\right) \quad . \tag{2.29}$$

In the following, the supersonic flow phenomena which are most relevant for this thesis are briefly discussed.

2.2.1 Shock Waves and Expansion Fans

Since information can only propagate in downstream direction, a supersonic flow has to adapt suddenly to disturbances such as geometrical obstacles. This is in contrast to subsonic flows, where a flow adapts gradually and well upstream to a geometrical change. Consequently, the appearance of shock waves and expansion fans are common phenomena in the supersonic flow regime.
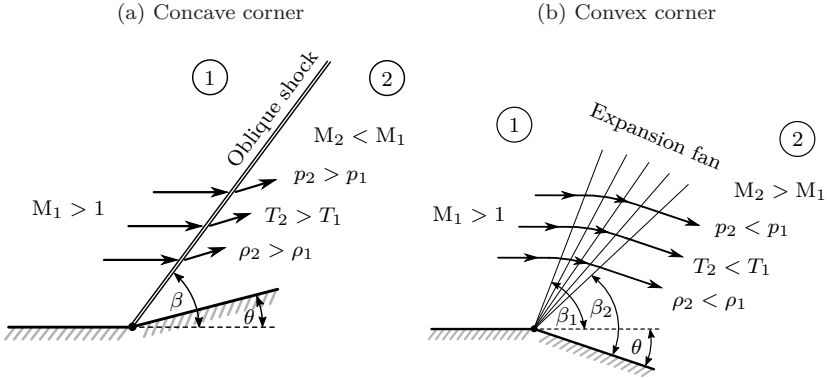
Figure 2.1: Supersonic flow over a corner

An oblique shock forms if a supersonic flow is diverted inwards (e.g. for a narrowing of the flow cross section) such as illustrated in figure 2.1a. The oblique shock wave causes a redirection of the supersonic flow parallel to the wall. Moreover, this is accompanied by an increase of the static values of pressure, temperature, and density. Opposed to this, the Mach number decreases and a loss in total pressure occurs across a shock wave. As the sudden flow adaptation is considered to be adiabatic, the total enthalpy remains constant. The intensity of changes in state variables depends on the strength of the shock, which in turn is dependent on the magnitude of the geometrical change. For an attached oblique shock wave, the wave angle β is a function of the deflection angle θ and the upstream Mach number M_1:

$$\tan \theta = \frac{2}{\tan \beta} \left[\frac{M_1^2 \sin^2 \beta - 1}{M_1^2 \left(\gamma + \cos 2\beta \right) + 2} \right] \quad . \tag{2.30}$$

Equation (2.30) provides two solutions for a given combination of deflection angle θ and upstream Mach number M_1, which are denoted as weak shock solution ($M_2 > 1$) and strong shock solution ($M_2 < 1$), respectively. Which one of the two solutions occurs is determined by the prevailing back pressure. However, the weak solution is preferred by nature and usually obtained if the downstream pressure is not artificially increased.

If the deflection angle exceeds a certain maximum value which depends on the Mach number, i.e. $\theta > \theta_{max}$, no solution exists for equation (2.30). In this case,

the shock detaches from the geometrical obstacle to form a detached, curved shock wave.[4]

To determine the change of state properties across an oblique shock with a wave angle β, the following relations for an ideal gas [8] may be used:

$$\frac{\rho_2}{\rho_1} = \frac{(\gamma + 1)\,M_{n,1}^2}{(\gamma - 1)\,M_{n,1}^2 + 2} \tag{2.31}$$

$$\frac{p_2}{p_1} = 1 + \frac{2\gamma}{(\gamma + 1)}\left(M_{n,1}^2 - 1\right) \tag{2.32}$$

$$M_{n,2}^2 = \frac{M_{n,1}^2 + [2/(\gamma - 1)]}{[2\gamma/(\gamma - 1)]\,M_{n,1}^2 - 1} \tag{2.33}$$

$$\frac{T_2}{T_1} = \frac{p_2}{p_1}\frac{\rho_1}{\rho_2} \quad . \tag{2.34}$$

The downstream values (subscript '2') only depend on the upstream properties (subscript '1') and the normal component of the upstream Mach number

$$M_{n,1} = M_1 \sin\beta \quad . \tag{2.35}$$

In contrast to the normal direction, the velocity component tangential to the shock wave is preserved across a shock, i.e. $M_{tan,1} = M_{tan,2}$.

Using equation (2.33), the downstream Mach number is then calculated from

$$M_2 = \frac{M_{n,2}}{\sin(\beta - \theta)} \quad . \tag{2.36}$$

A normal shock wave represents a special case of an oblique shock (with $\beta = 90°$). Applying the given relations, it is found that $M_2 < 1$ for a normal shock wave, while $M_2 > 1$ for an oblique shock.

---

4 This effect reduces the heat flux on blunt leading edge vehicles during reentry flight on the cost of aerodynamic drag (e.g. Apollo command module, Space Shuttle Orbiter, Intermediate Experimental Vehicle). Viscous dissipation downstream of the normal part of the detached shock heats up the layer of air surrounding the vehicles to extreme temperatures, thus triggering endothermic reactions such as dissociation which reduce the heat flux on the surface.

The limiting case on the other end is a Mach wave which is an infinitely weak oblique shock. The corresponding wave angle is termed Mach angle and can be calculated from

$$\beta = \arcsin\left(\frac{1}{M}\right) \quad . \tag{2.37}$$

In the case that an oblique shock wave hits a wall, it is reflected downstream as shown in figure 2.2. Again, the flow is turned inwards across the shock to be parallel to the wall. As $M_2 < M_1$, the reflected shock wave is weaker when compared to the incident shock. Also, the wave angle β_2 is not equal to β_1 but usually smaller, i.e. $\beta_2 < \beta_1$. Consequently, after an initial shock generation, the reflected shock waves become weaker in strength and show decreasing wave angles in a supersonic channel flow with constant cross section.
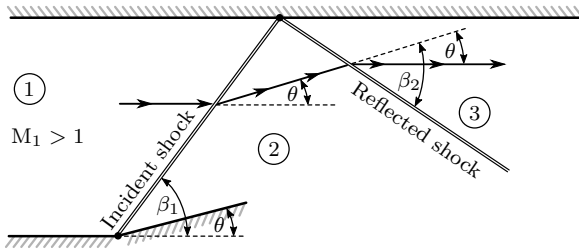
Figure 2.2: Regular reflection of a shock wave from a solid boundary

The counterpart of oblique shock waves are Prandtl-Meyer expansion waves as illustrated exemplarily in figure 2.1b. An expansion fan emerges whenever a supersonic flow is turned outward due to a geometrical expansion. Compared to an oblique shock wave, the effect on the state variables and the Mach number is reversed, i.e. M_2 increases, while ρ_2, p_2, and T_2 decrease with respect to the upstream values. The expansion wave consists of an infinite number of Mach waves resulting in a continuous expansion region which is bounded by the Mach angles β_1 and β_2. Due to the infinitesimal flow deflection at each Mach wave, the changes are smooth and continuously which is opposed to the sudden change across a shock wave. Moreover, the expansion is isentropic and thus total pressure and total enthalpy are conserved.

The Prandtl-Meyer function $\nu(M)$ may be employed to determine the properties downstream of an expansion fan

$$\theta = \nu(M_2) - \nu(M_1) \quad , \tag{2.38}$$

with

$$\nu(M) = \sqrt{\frac{\gamma + 1}{\gamma - 1}} \arctan \sqrt{\frac{\gamma - 1}{\gamma + 1}(M^2 - 1)} - \arctan \sqrt{M^2 - 1} \quad . \tag{2.39}$$

Typically, tabulated values of $\nu(M)$ are used to determine M_2 in dependence of the deflection angle θ. In a second step, the state variables ρ_2, p_2, and T_2 are calculated. As the expansion is isentropic, equations (2.27) to (2.29) may be used for this. When evaluating equation (2.39) for rising Mach numbers, values range from $\nu(M = 1) \equiv 0$ (per definition) to the finite value ν_{max} for $M \to \infty$. Thus, a maximum deflection angle θ_{max} exists for a given upstream Mach number M_1. If exceeded, i.e. $\theta > \theta_{max}$, a shear layer forms between downstream wall and trailing edge of the expansion fan. A further increase of θ then has no influence on the downstream flow.

2.2.2 Viscous Effects

Boundary Layers

Any viscous flow develops a boundary layer when in vicinity of a solid surface. The boundary layer describes the region or layer which relates the undisturbed core flow from free-stream velocity u_∞ to the no-slip condition at the wall, i.e. $u_w = 0$. Generally, it can be distinguished between laminar and turbulent boundary layers. While a developing boundary layer starts as laminar close to the leading edge of a plate, disturbances and instabilities result in a growth of turbulent fluctuations which eventually leads to the transition from laminar to turbulent flow. In this regard, the dimensionless Reynolds number is the characterising parameter as it gives the ratio of inertial forces to viscous forces:

$$Re_x = \frac{\rho u x}{\mu} \quad . \tag{2.40}$$

The characteristic length x is typically chosen to be the run length on a flat plate or the hydraulic diameter of a channel. The point at which the laminar-turbulent transition occurs for a flat plate is estimated from the critical Reynolds number $Re_{x,crit} \approx 5 \cdot 10^5$. For a channel flow, the critical Reynolds number based on

the hydraulic diameter is around 2300 [164]. With respect to the application cases mentioned in the introduction, laminar boundary layers can only be expected at the leading edges of hypersonic flight or reentry vehicles, whereas in combustion engines (e.g. rocket engines, Ram-, or SCRamjets) the flow can be assumed to be fully turbulent in most cases. In accordance with this, only turbulent boundary layers are considered in the given thesis which reduces the complexity of numerical simulations as transition modelling can be omitted.

Within a turbulent boundary layer, random fluctuating motions due to turbulence give rise to an apparent viscosity which is dominating the greater part of the boundary layer (see also section 4.2). The influence of viscous forces is then limited to a thin viscous sublayer directly at the wall. Moreover, irrespective of the main-flow velocity and Mach number, a subsonic part exists within the boundary layer. This gives rise to the phenomenon that even in a purely supersonic core flow, information may travel upstream and alter the flow field such as in boundary-layer separation or shock-wave/boundary-layer interaction. With increasing run length the boundary-layer thickness δ grows. It is commonly specified by means of the wall-normal distance δ_{99} at which the flow velocity reaches $0.99\,u_\infty$. In addition to the run length, also wall temperature and compressibility effects (i.e. the Mach number M) have a significant influence on boundary-layer growth [7]. The major displacement effect that a thick boundary layers can exert on the inviscid outer flow is called viscous interaction.

To estimate the skin friction and drag due to the viscous boundary layer, the wall shear stress

$$\tau_w = \mu_w \frac{\partial u}{\partial n}\bigg|_w \quad , \tag{2.41}$$

or in dimensionless form, the skin-friction coefficient

$$C_f = \frac{\tau_w}{\frac{1}{2}\rho u_\infty^2} \tag{2.42}$$

may be employed. Wall shear stress is typically inversely proportional to the boundary-layer thickness and thus decreases with run length.

Separation of a boundary layer generally results from an adverse pressure gradient which may be present for an incident shock wave or a geometrical obstacle. The point of separation is defined by a vanishing velocity gradient at the wall, i.e. $\tau_w \approx 0$. Due to the strong thickening of the boundary layer occurring in this situation, streamlines leave the wall at a certain angle and thus boundary-layer mass is transported into the outer flow [164].

Shock-Wave/Boundary-Layer Interaction

Shock-wave/boundary-layer interaction is observed when a shock wave hits on a surface and penetrates the boundary layer as illustrated in figure 2.3. The associated pressure rise is transmitted upstream through the subsonic part of the boundary layer and leads to a local thickening of the boundary layer. When sufficiently strong, the adverse pressure gradient triggers a region of separation which exhibits local flow velocities in reverse direction. Upstream of the incident shock, the streamlines are bended away from the thickened boundary layer resulting in several oblique shocks that eventually merge into the stronger separation shock. Additionally, the incident shock is reflected forming a second oblique shock wave. Downstream of this shock the elevated local pressure leads to a bending of the flow towards the wall until it reattaches. The local decrease of δ and the enlargement of the flow passage give rise to a series of expansion waves which are eventually concluded by a compression shock associated with the wall reattachment [7, 166].

If boundary-layer separation appears or not depends on the strength of the incident shock wave and the associated pressure rise. Korkegi [100] proposed an empirical criterion for the critical pressure ratio which, if exceeded, triggers turbulent boundary-layer separation. The model was obtained through summarising experimental data and serves as a first-order estimate:

$$\left(\frac{p_2}{p_1} \right)_{crit} = 1 + 0.3 \mathrm{M}_1^2 \quad \text{for} \quad \mathrm{M}_1 \leq 4.5 \quad . \tag{2.43}$$
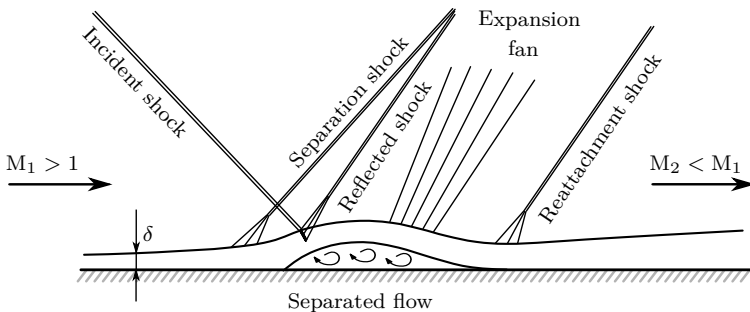
Figure 2.3: Shock-wave/boundary-layer interaction, adapted from reference [166]

With respect to application cases, shock-wave/boundary-layer interactions may lead to extremely severe local heat peaks in the interaction region and are thus particularly important when aerodynamic heating is critical. However, the numerical modelling as well as the complex fluid-dynamic details are still challenging and active topics of research [40, 44, 61, 161, 203].

Similar to the situation illustrated in figure 2.3, also a normal shock interacts with the boundary layer. As an example, this is typically observed in supersonic wind-tunnel testing for the adaptation to ambient pressure at the end of the channel. Matsuo et al. [128] describe this interaction as well as the emerging shock train in detail.

2.3 Heat Transfer

Energy transport in the form of heat occurs whenever a temperature difference between two objects exist. For the case of a fluid overflowing an arbitrary-shaped wall which is at a different temperature, convective heat transfer takes place. The transferred heat is then transported from the surface into the wall by heat conduction. Since both processes are interdependent, a conjugate heat transfer problem arises.

2.3.1 Heat Transfer by Convection

Hot gas heat transfer without blowing

Convective heat transfer depends on several factors such as the driving temperature difference between fluid and wall, the state of the thermal boundary layer, and the fluid properties. Since all these parameters may change with location, also the heat transfer to a certain body usually exhibits local variations. A typical thermal boundary layer for a compressible flow over a flat plate is illustrated in figure 2.4.

In the figure, the cases of an adiabatic and a cooled wall are shown. Far away from the wall, the flow velocity is at its maximum (i.e. u_∞) while the static temperature $T = T_\infty$ is lowest. Viscous forces decrease the velocity towards the wall, where the no-slip condition applies, i.e. $|\boldsymbol{u}| = 0$. The deceleration leads to the conversion of kinetic energy into internal energy of the fluid, which is also referred to as viscous dissipation. For the case of an adiabatic wall, the temperature rises up to a maximum value which is referred to as recovery or adiabatic wall temperature T_r. Due to heat conduction within the boundary
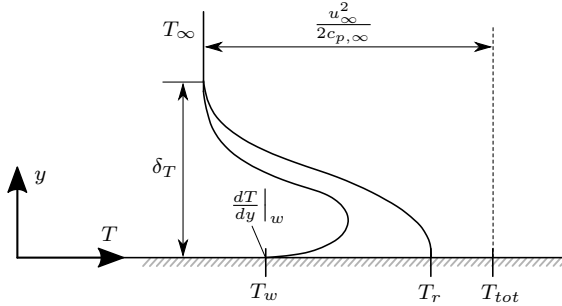
Figure 2.4: Temperature boundary layer in a compressible flow

layer, the total temperature cannot be fully recovered at the wall, and thus $T_r < T_{tot}$. The recovery temperature can be calculated from

$$T_r = T \left(1 + r \frac{\gamma - 1}{2} \mathrm{M}_\infty^2 \right) \quad , \tag{2.44}$$

with the recovery factory r which can be approximated by $r \approx \sqrt{\mathrm{Pr}}$ and $r \approx \mathrm{Pr}^{1/3}$ for laminar and turbulent flows, respectively [96]. Since no heat is transferred at an adiabatic plate, the temperature gradient vanishes at the wall. For the cooled-wall case, the fluid temperature reaches a maximum within the boundary layer before decreasing to the wall temperature T_w. The temperature gradient at the wall and the thermal conductivity of the fluid determine the transferred wall heat flux:

$$\dot{q}_w = -k \frac{\partial T}{\partial n} \bigg|_w = h \left(T_{f,ref} - T_w \right) \quad . \tag{2.45}$$

The form given on the right-hand side introduces the heat transfer coefficient h which relates the heat flux to the temperature difference between wall and fluid, i.e. $\Delta T = T_{f,ref} - T_w$. In this regard, the choice of the reference fluid temperature $T_{f,ref}$ is not trivial. In the case of supersonic flows, the recovery temperature T_r is commonly used.

Moreover, the dimensionless Stanton number can be employed to evaluate convective heat fluxes:

$$\mathrm{St} = \frac{h}{\rho c_p u} = \frac{\dot{q}_w}{\rho c_p u \Delta T} \quad , \tag{2.46}$$

where the free-stream values ρ_∞, $c_{p,\infty}$, and u_∞ are typically used.

Various correlations for the Stanton number and thus the heat transfer coefficient for different flow situations are given in literature, see for example references [96, 201]. Eckert [48] proposed the following correlation for the local Stanton number of a turbulent flow over a flat plate:

$$\text{St} = 0.0296 \, \text{Re}_x^{-0.2} \, \text{Pr}^{-2/3} \quad , \tag{2.47}$$

where the Reynolds number is computed from the run length x with respect to the start of the boundary layer, i.e. $\text{Re}_x = (\rho_\infty u_\infty x)/\mu_\infty$.

Hot gas heat transfer with boundary-layer blowing

Having briefly introduced the characteristics of heat transfer for a non-transpired wall, now the focus is shifted towards heat transfer with boundary-layer blowing. Many early experimental studies explored the influence of transpiration cooling for sub- and supersonic flows, e.g. Leadon and Scott [114], Rubesin [162], and Moffat and Kays [139]. All studies found a strong reduction of heat transfer as well as skin friction for boundary-layer blowing which can be correlated to the blowing ratio $F = (\rho_c u_c)/(\rho_{hg} u_{hg})$.[5] Experiments using various light and heavy coolant gases aside from air additionally revealed a pronounced influence of the coolant's properties [114, 130, 160].

Kays et al. [96] proposed the following relations for the ratios of skin friction and heat transfer with and without (subscript '0') blowing into a turbulent boundary layer:

$$\frac{(C_f/2)}{(C_f/2)_0} = \frac{b_f}{e^{b_f} - 1} \quad \text{with} \quad b_f = \frac{F}{(C_f/2)_0} k_W \tag{2.48}$$

and

$$\frac{\text{St}}{\text{St}_0} = \frac{b_h}{e^{b_h} - 1} \quad \text{with} \quad b_h = \frac{F}{\text{St}_0} k_T^* k_W^* k_C^* \quad . \tag{2.49}$$

In equations (2.48) and (2.49), the modified blowing parameters b_f and b_h account for the influence of fluid properties of the transpired gas. Regarding the correction factors, Kays et al. [96] suggest $k_W = k_W^* = k_T^* = 1$ and $k_C^* = (c_{p,c}/c_{p,hg})^{0.6}$, whereas Meinert et al. [130] obtained different values from fitting their experimental data, i.e. $k_W = (W_{hg}/W_c)^{0.8}$, $k_W^* = (W_{hg}/W_c)^{0.6}$, $k_C^* = 1$, and $k_T^* \approx (T_r/T)^{0.2...0.4}$.

---

5   The blowing ratio $F = (\rho_c u_c)/(\rho_{hg} u_{hg}) = (\dot{m}_c/A_c)/(\dot{m}_{hg}/A_{hg})$ always represents an integral value for the complete transpired area in the frame of this thesis.

From a physical point of view, the reduction in both skin friction and heat transfer can be explained by the injection of coolant gas at low velocity and temperature into the hot-gas boundary layer. This decreases the momentum as well as the internal energy close to the wall or in other terms, the velocity and temperature gradients are reduced when compared to the non-transpired boundary layer. As discussed in section 2.2.2, a vanishing skin-friction coefficient, i.e. $C_f/2 \approx 0$, leads to boundary-layer separation. For large blowing ratios, a blow-off condition is reported by several authors [96, 107, 129]. In this situation, the hot gas flow is fully displaced and the wall is covered by coolant gas (similar to a film-cooling situation). Kays et al. [96] report a blow-off value of $F \gtrsim 1\,\%$ as a rule of thumb for blowing with air into a fully developed turbulent boundary layer.

Despite the simplicity of relations (2.48) and (2.49), both give generally good approximations for simple transpiration-cooling situations. This has also been confirmed in previous studies at ITLR, when Langener [111] and Schweikert [165] found good agreement to their experiments on flat porous CMC plates. However, equations (2.48) and (2.49) are generally limited to one-dimensional coolant flow situations and require the availability of no-blowing values for C_f and St which are difficult to obtain for more complex main-flow conditions.

2.3.2 Heat Transfer by Conduction

Heat conduction inside a solid body (subscript 's') is described by the heat equation

$$\frac{\partial}{\partial t}(\rho c_{p,s} T_s) = \nabla \cdot (\boldsymbol{k_s} \nabla T_s) + \dot{q}_v \quad , \tag{2.50}$$

where $\dot{q}_v$ denotes internal heat sources and $\boldsymbol{k_s}$ is the thermal conductivity tensor of the solid material. While for isotropic materials the thermal conductivity reduces to a scalar, the tensor notation is required for anisotropic materials, i.e. materials for which the thermal conductivity varies with direction.

For an arbitrary rectangular coordinate system ('1,2,3') the symmetrical tensor ($k_{s,ij} = k_{s,ji}$) is given by

$$\boldsymbol{k_s^*} = \begin{pmatrix} k_{s,11} & k_{s,12} & k_{s,13} \\ k_{s,21} & k_{s,22} & k_{s,23} \\ k_{s,31} & k_{s,32} & k_{s,33} \end{pmatrix} \quad . \tag{2.51}$$

The here-considered fibre-reinforced C/C material exhibits orthotropic properties, i.e. has three mutually orthogonal principal axis. Thus, a system of rectangular coordinates (ξ_1, ξ_2, ξ_3) exists for which only the main diagonal tensor entries of $\boldsymbol{k_s}$ are different from zero. The conductivities k_i along these axes are then called the principal conductivities [70]. In the frame of this thesis, the principal coordinate axes (ξ_1, ξ_2, ξ_3) coincide with the Cartesian coordinate axes (x, y, z) yielding

$$\boldsymbol{k_s} = \begin{pmatrix} k_{s,x} & 0 & 0 \\ 0 & k_{s,y} & 0 \\ 0 & 0 & k_{s,z} \end{pmatrix} \quad . \tag{2.52}$$

The heat flux $\dot{q}_n$ normal to a solid surface Γ is obtained from the surface normal vector $\boldsymbol{n}$ and the heat flux vector $\dot{\boldsymbol{q}}$:

$$\dot{q}_n = \boldsymbol{n} \cdot \dot{\boldsymbol{q}} = \boldsymbol{n} \cdot (-\boldsymbol{k_s} \nabla T_s) \quad . \tag{2.53}$$

For an isotropic solid, equation (2.53) reduces to

$$\dot{q}_n = -k_s \frac{\partial T_s}{\partial n}\bigg|_{\Gamma} \quad . \tag{2.54}$$

2.4 Theory of Porous Media

The class of porous media covers various types of materials such as foams, powders, or fibre-reinforced composites to name just a few. Common to all materials is the existence of a void volume which is typically described by the porosity ε computed from the ratio of void to total volume

$$\varepsilon = \frac{V_{void}}{V_{total}} \quad . \tag{2.55}$$

Pore sizes range from very large (e.g. caverns) to the molecular scale, and the openings may be closed or interconnected. It can be distinguished between ordered and disordered materials with isotropic or anisotropic properties. With respect to transpiration cooling, potentially interesting porous materials usually exhibit microscopic pores that add up to rather small porosities ($\varepsilon < 0.4$). This also applies to porous CMC materials such as the here-investigated C/C, i.e. $\varepsilon_{C/C} \approx 10 - 15\%$.

2.4.1 Modelling Approaches

Different modelling approaches may be used to describe the internal processes of coolant gas through flow as well as the heat exchange between coolant and solid within a porous structure.

Ideally, the fluid pores and the solid skeleton are resolved in a numerical simulation of a porous structure. However, depending on the pore size, this may require extremely fine numerical grids which result in high computational costs. Additionally, the detailed structure of the porous material must be known which is often not the case. Consequently, this is not viable for the simulation of most practical transpiration-cooling problems. Instead, typically a volume-averaging approach is employed as described in detail for example by Whitaker [200] or Kaviany [94]. According to this, the real porous medium which consists of two portions (i.e. solid phase and fluid phase) is replaced by two fictitious overlapping continua that fill the complete volume of the porous structure. The general assumption underlying this approach is the existence of a representative elementary volume (REV) that can be used to determine characteristic properties through volume-averaging. The size of the REV has to be chosen in a way that the resulting averaged properties are material characteristics and do not depend on the evaluated location of the homogeneous porous material, as discussed by Bachmat and Bear [10]. The volume-averaged approach which has also been employed in the frame of this thesis introduces several modelling parameters with respect to through flow and heat exchange which need to be determined beforehand.

2.4.2 Through-Flow Behaviour of Porous Structures

In general, the coolant flow through a transpiration-cooled structure is driven by a pressure difference between coolant reservoir and hot-gas side. The material's permeability defines the through-flow resistance and thus relates the pressure drop to fluid velocity or coolant mass flux, respectively. In this regard, the Darcy-Forchheimer model is widely applied to describe the momentum loss occurring for porous flow. A first form given by Darcy [38] was later supplemented by a second term often referred to as the Forchheimer contribution [47, 55]. The resulting Darcy-Forchheimer equation in one-dimensional differential form is given by Nield and Bejan [141] as

$$\frac{dp}{dx} = -\left(\underbrace{\frac{\mu_f}{K_D}u_D}_{\text{Darcy}} + \underbrace{\frac{\rho_f}{K_F}u_D^2}_{\text{Forchheimer}} \right) \ , \tag{2.56}$$

with the fluid's viscosity μ_f, density ρ_f, permeability coefficients K_D and K_F, and the Darcy velocity u_D. In line with the modelling approach, u_D is obtained from volume-averaging the pore velocity u_{pore} over the REV. The Dupuit-Forchheimer relationship [141] connects both velocities by means of the open porosity, i.e. $u_D = \varepsilon\, u_{pore}$.

Equation (2.56) consists of a linear term which is due to viscous drag and a quadratic term related to form drag [109]. While for small through-flow velocities the Darcy term dominates the pressure loss, the Forchheimer contribution is necessary to account for higher flow velocities. The corresponding permeability coefficients K_D and K_F are commonly assumed as material characteristics and may be obtained through experimental determination or theoretical approaches.[6]

The pressure drop over a porous structure with thickness L is obtained through integration of equation (2.56). For a compressible gas and isothermal conditions, the following forms are obtained

$$\left(\frac{\Delta p}{L}\right)^* = \frac{p_{in}^2 - p_{ex}^2}{2 p_{ex} L} = \frac{\mu_f}{K_D} u_{D,ex} + \frac{\rho_{f,ex}}{K_F} u_{D,ex}^2 \quad \text{or} \tag{2.57}$$

$$\frac{p_{in}^2 - p_{ex}^2}{2 L R T} = \frac{\mu_f}{K_D}\left(\frac{\dot{m}_c}{A_c}\right) + \frac{1}{K_F}\left(\frac{\dot{m}_c}{A_c}\right)^2, \tag{2.58}$$

where subscripts 'in' and 'ex' denote the inlet/reservoir and outlet/exit conditions, respectively.

To evaluate the prevailing flow regime, Lage [109] suggests to determine the ratio between form drag and viscous drag which indicates the transition from linear to quadratic flow regime, i.e.

$$C_{FD}^* = \frac{(\Delta p/L)^*_{Forchheimer}}{(\Delta p/L)^*_{Darcy}} = \frac{\rho_f K_D}{\mu_f K_F} u_D = \frac{K_D}{\mu_f K_F}\frac{\dot{m}_c}{A_c} \quad . \tag{2.59}$$

The value of C_{FD}^* approaches zero for flows dominated by viscous drag (Darcy), whereas it tends to infinity for form drag dominated flows (Forchheimer).

---

6 Existing correlations are typically valid only for highly porous, regular, and isotropic materials (see for example Ergun [50]), and are thus not applicable to most CMC materials. For C/C the determination of K_D and K_F has to be performed experimentally, see chapter 5.

The Darcy-Forchheimer equation (or the simpler form neglecting the Forchheimer term) is employed in various fields of research such as geology, petroleum engineering, or resin transfer molding of polymer composites [117, 146, 156]. As many of the considered porous materials exhibit anisotropic permeabilities, a three-dimensional form of equation (2.56) becomes necessary [12, 94, 190]. To account for the anisotropy, the permeability coefficients are provided by symmetrical tensors (i.e. $K_{ij} = K_{ji}$) of the following form:

$$\boldsymbol{K^*_{D/F}} = \begin{pmatrix} K_{D/F,11} & K_{D/F,12} & K_{D/F,13} \\ K_{D/F,21} & K_{D/F,22} & K_{D/F,23} \\ K_{D/F,31} & K_{D/F,32} & K_{D/F,33} \end{pmatrix} \quad . \tag{2.60}$$

Again, the symmetrical tensors can be translated to diagonal forms for orthotropic materials by transformation into the coordinate system of principal axes. For the investigated material C/C, the principal axes coincide with the chosen coordinate system (x, y, z) yielding

$$\boldsymbol{K_{D/F}} = \begin{pmatrix} K_{D/F,x} & 0 & 0 \\ 0 & K_{D/F,y} & 0 \\ 0 & 0 & K_{D/F,z} \end{pmatrix} \quad . \tag{2.61}$$

Employing the inverses of the permeability tensors for easier notation, i.e. $\boldsymbol{D} = \boldsymbol{K_D^{-1}}$ and $\boldsymbol{F} = \boldsymbol{K_F^{-1}}$, the three-dimensional form of the Darcy-Forchheimer equation is obtained

$$\nabla p = - \left(\mu_f \boldsymbol{D u_D} + \rho_f \boldsymbol{F} \ \boldsymbol{u_D^T I u_D} \right) \quad , \tag{2.62}$$

where $\boldsymbol{I}$ is the identity matrix and $\boldsymbol{u_D^T}$ is the transposed Darcy velocity vector.

2.4.3 Thermal Behaviour of Porous Structures

Considering transpiration cooling on the microscopic scale, the solid parts of the porous structure are at a certain temperature T_s while the pores are filled by a coolant at a (typically lower) temperature T_f. Following the volume-averaging approach, fluid and solid phases are overlapping continua with the porosity ε specifying the volume ratio between both phases. Consequently, in addition to heat conduction occurring within the solid, the coolant gases' contribution to heat transfer as well as the interaction between solid phase and fluid phase have to be considered.

The thermal situation of an aerothermally heated porous wall is illustrated in figure 2.5. At the backside of the porous wall, coolant gas is provided at an
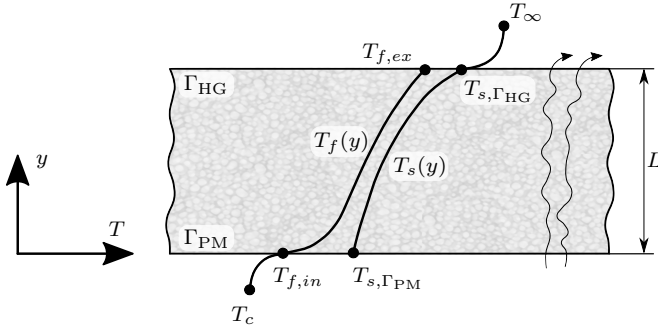
Figure 2.5: Thermal behaviour of an aerothermally heated porous wall

elevated pressure and a certain temperature T_c in the coolant reservoir (also called plenum). Convective heat transfer between the porous backside and the coolant leads to an increased temperature of the entering coolant $T_{f,in}$ when compared to the reservoir conditions. In the following, the temperature distributions of solid and fluid phases are governed by the internal heat exchange within the porous structure. Generally, solid temperature levels decrease due to the heat absorption of the coolant mass flow rate. At the hot-gas side, the coolant exits the porous structure and enters the hot-gas main flow. During through flow, a heat flux of $\dot{q} = \rho_f u_{D,f} c_{p,f} (T_{f,ex} - T_{f,in})$ is transferred by convection from solid skeleton to coolant fluid. Across the porous structure as well as at the hot-gas interface, solid and fluid temperatures may differ, i.e. $T_f(y) \neq T_s(y)$ and $T_{f,ex} \neq T_{s,\Gamma_{HG}}$, respectively.

Following this, two separate volume-averaged energy equations for fluid and solid phases have to be considered:

$$\varepsilon \frac{\partial}{\partial t} (\rho_f c_{p,f} T_f) + \nabla \cdot (\rho_f c_{p,f} u_D T_f) = \varepsilon \nabla \cdot (k_f \nabla T_f) + h_v (T_s - T_f) \quad (2.63)$$

and

$$(1 - \varepsilon) \frac{\partial}{\partial t} (\rho_s c_{p,s} T_s) = (1 - \varepsilon) \nabla \cdot (k_s \nabla T_s) + h_v (T_f - T_s) \quad . \quad (2.64)$$

Equations (2.63) and (2.64) are coupled through a source term representing the internal heat exchange. The latter depends on the temperature difference and the volumetric heat transfer coefficient h_v which may be split into specific inner surface of the porous material and the respective heat transfer coefficient, i.e. $h_v = a_{sf} h$. For a rigid porous structure the specific inner surface a_{sf} is constant, whereas the heat transfer coefficient h depends on several factors such

as the coolant flow field or the properties of the coolant. Various correlations exist to determine h within porous materials, see for example references [2, 4, 13, 53, 54, 57, 210]. However, the relations differ by orders of magnitudes and are generally valid for specific porous materials only. Different limiting cases can be considered with respect to h_v. Complete heat exchange, i.e. $h_v \to \infty$, yields identical temperatures for fluid and solid. This situation is called local thermal equilibrium (LTE) throughout literature and would allow to model fluid and solid phases with a single energy equation. Opposed to this, small h_v-values result in little heat absorption of the coolant and lead to substantial temperature differences between solid phase and fluid phase which is commonly called local thermal non-equilibrium (LTNE). In reality, the thermal situation is between these two limiting cases. In literature, the simplified assumption of a constant h_v-value for the complete porous structure is commonly made [37, 78, 165, 192, 193]. Based on this and a simplified analytical solution that neglects heat conduction in the fluid phase, Wang and Wang [192] developed a criterion to evaluate the influence of LTNE. In addition to the volumetric heat exchange coefficient h_v, also other parameters such as the coolant gases' specific heat capacity $c_{p,c}$, the mass flux $\dot{m}_c/A_c$, or the thermal conductivity of the solid $k_{s,eff} = (1-\varepsilon)k_s$ play an important role. As a result of their analysis, the authors describe the following criterion:

$$\left(\frac{\dot{m}_c c_{p,c} L}{A_c k_{s,eff}} \right) > 0.223 \left(\frac{h_v L^2}{k_{s,eff}} \right)^{0.507} , \qquad (2.65)$$

where L is the through-flow length. If the condition is satisfied, the assumption of LTE leads to an error $\delta_{LTE} = (T_s - T_f)/(T_s - T_c) > 5\%$ in the temperature distributions at the hot-gas side.

Also at the domain boundaries, fluid-phase and solid-phase temperatures may differ. This is a consequence of the significant difference in thermal conductivities of coolant gas and porous solid and the fact that h_v is finite. The volume-averaging approach with two energy equations does not resolve these local effects but yields two (volume-averaged) temperatures at the hot-gas interface of the porous structure. Regarding the conjugated heat transfer problem of transpiration cooling, the two temperatures at the hot-gas side have to be related to a single main-flow temperature at the porous interface [115]. Moreover, also the distribution of the resulting wall heat flux onto the two phases is not trivial as described by several authors [3, 89, 193]. Likewise, different approaches exist for the thermal modelling of the coolant-reservoir side, see for example references [28, 148, 188]. The numerical setup including all selected boundary conditions used in the frame of this thesis is detailed in chapter 4.

CHAPTER 3

Experimental Methods

Verification and validation is an essential part of the development of any new numerical tool. Experiments with well controlled conditions are ideally suited for this task. However, there is only limited experimental data available regarding transpiration cooling in supersonic flows, and even more so for materials such as ceramic matrix composites. Also, transpiration-cooling experiments using gases other than air are sparse. Thus, besides using available literature data, extensive experimental tests have been performed in the frame of this thesis. In addition to the validation of the developed OpenFOAM solver, the results of the combined numerical/experimental approach also contribute to the general understanding of transpiration cooling for CMC materials. The following chapter focuses on the setup of the supersonic wind-tunnel experiments, the investigated porous samples, and the applied measurement techniques.

3.1 Experimental Setup

The following section describes the employed experimental setup consisting of the institute's supersonic hot gas facility, a modular test channel, and a coolant plenum with mounted porous samples.

3.1.1 ITLR Hot Gas Facility

The ITLR Hot Gas Facility which has been employed for the tests is a continuously operating connected tube facility. In the experiments, it provides a constant hot supersonic air flow and allows for long duration tests and measurements at steady-state conditions. An overview of the facility is shown in figure 3.1. First, a screw compressor supplies a continuous flow of air of up to $1.4\,kg/s$ at a maximum pressure of around $1\,MPa$. The air is then fed into an air dryer which reduces the relative humidity to less than 0.5%. Subsequently, three consecutive electrical heater stages (maximum total power consumption $400\,kW$) raise the main flow total temperature to values up to $1350\,K$. The hot gas flow is then directed into the test channel where the main experiment takes place. Depending on the Laval nozzle used, the facility can be operated at different Mach numbers. The total pressure provided by the screw compressor and the total temperature of the air after heating then determine the mass flow rate within the flow channel. For the here-presented steady state experiments the facility was operated at $M = 2.5$, $p_{tot} = 0.5\,MPa$, $T_{tot} = 500\,K$, and $\dot{m}_{hg} = 0.436\,kg/s$. Lastly, after passing through the test section, the flow is exhausted by a chimney into ambience. An auxiliary air supply consisting of four $2\,m^3$ pressure vessels is installed as a standby unit in case of a compressor failure. For cooling investigations, the auxiliary tanks additionally provide air for injection into the test section at a maximum pressure of up to $2\,MPa$. Further test gases such as helium (He), argon (Ar), and carbon dioxide (CO_2) are supplied by means of gas cylinders. The coolant mass flow parameters employed in the here-presented tests are summarised in table 3.1.
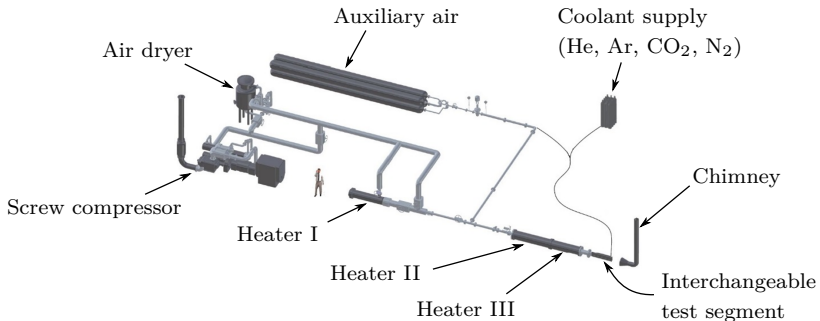
Figure 3.1: ITLR Hot Gas Facility

3.1.2 Modular Test Channel

A new test channel has been designed to investigate transpiration cooling using various porous sample geometries, different coolant gases, and for non-uniform supersonic flow fields exhibiting shock waves and expansion fans. In addition to the sample surface, also the film-cooled wake region is to be evaluated. Special care has been spent on the thermal insulation of the porous sample to avoid parasitic lateral heat conduction as found in previous investigations [111].

As shown in figure 3.1, the test channel is attached downstream of the third heater stage. It is based on a modular design that allows to combine various segments. For the here-presented tests, the setup consists of three modules, see figure 3.2. The heated main flow enters the test channel through the Laval nozzle, where it is accelerated to M = 2.5. Downstream of the Laval nozzle segment, the channel features a constant rectangular cross section of 35.4 mm height and 40 mm width and has an axial length of around 575 mm in total. The flow is assumed to be fully turbulent for most of the channel as indicated by the unit Reynolds number, i.e. $Re_1 = (\rho_\infty u_{x,\infty}) / \mu_\infty \approx 2.3 \cdot 10^7$ 1/m. After passing through the channel, the flow is exhausted into ambience. The flow's recompression to ambient pressure ($p_{ex} \approx 96.4$ kPa) does not affect the measurement section as it occurs close to or directly at the end of the extension module.

The channel is mainly manufactured from stainless steel except for a large top-wall insert made from the high-temperature plastic *Victrex™ PEEK*. For optical access, it features two side-wall windows made from fused silica and a large sapphire window in the bottom plate. Depending on the performed test case, these can be replaced by stainless-steel wall inserts. As the static pressure in the channel flow is below ambience, a complex sealing system is required that consists of a mix of graphite flat gaskets and high-temperature O-ring seals. Since the channel itself is not cooled, the complete section heats up to values close to the recovery temperature of the flow. Regarding this, the PEEK material and the employed O-ring seals limit the permanent operating temperatures to around 500 K. The porous samples used for transpiration cooling are integrated into a coolant plenum. The assembly is then

Table 3.1: Cooling parameters in supersonic flow tests

	Air	Helium	Argon	CO_2
$\dot{m}_c \cdot 10^3 \left[\frac{kg}{s}\right]$	$0.32 - 6.44$	$0.13 - 0.97$	$0.64 - 7.73$	$1.29 - 5.80$
$F [\%]$	$0.05 - 1.00$	$0.02 - 0.15$	$0.10 - 1.20$	$0.20 - 0.90$
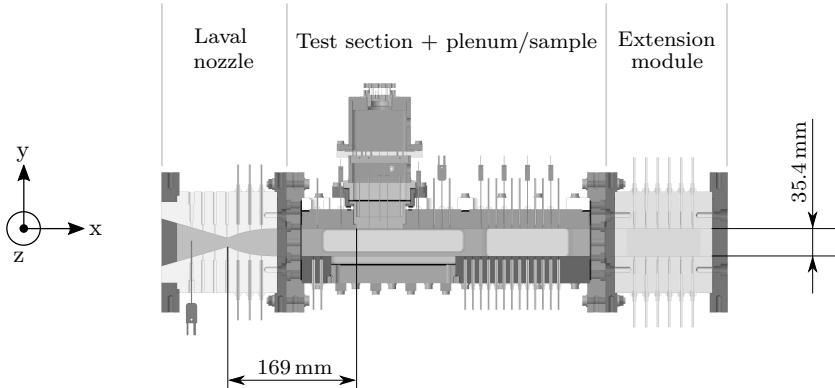
Figure 3.2: Slice view of modular test channel

attached as a single part to the test section's top wall. After installation, the surface of the sample is flush with the top wall (except for the double-wedge sample). The sample extends over the full channel width of 40 mm and has a length of 60 mm in streamwise direction. It is positioned between $0.169\,\mathrm{m} < x < 0.229\,\mathrm{m}$, while the origin of the axial coordinate coincides with the Laval-nozzle throat. To avoid a significant influence of parasitic lateral heat fluxes, the ceramic sample is surrounded by the thermally low-conducting PEEK material ($k_{PEEK} = 0.25\,\mathrm{W/(mK)}$). This reduces the heat flux from the uncooled channel walls into the porous sample considerably albeit not completely (see section 7.3.2). In addition to the thermal insulation of the sample, the top wall made from PEEK allows the measurement of nearly adiabatic wall temperatures in the film-cooled wake region. As the experiments are performed in the supersonic flow regime, the manufacturing tolerances of all components were chosen very small in order to avoid steps at transitions and junctions which would lead to the formation of shocks and disturb the measurements. This is evaluated in section 7.1 based on the measured pressure distribution and schlieren images.

In addition to the tests using the channel configuration as illustrated in figure 3.2, validation experiments with an artificially-modified, non-uniform flow field have been performed. For this purpose, a shock-generator insert has been designed which induces the formation of shock waves. The insert replaces the large window in the channel's bottom plate and features a movable flow barricade which can be continuously elevated into the channel flow. The barricade extends over a width of 35 mm and has been tested up to a maximum elevation position of $\Delta y = 9.7\,\mathrm{mm}$. This corresponds to a channel blockage of around 24%.

Moreover, the insert is equipped with a smaller sapphire window that provides optical access to the sample surface and its direct wake (up to $x \approx 0.26\,\mathrm{m}$). The shock generator is depicted for two positions of the flow barricade in figure 3.3.

(a) $\Delta y = 0\,\mathrm{mm}$ (b) $\Delta y = 9.7\,\mathrm{mm}$
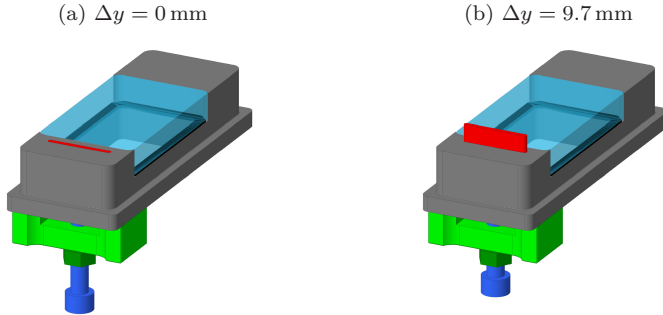
Figure 3.3: Shock generator insert with sapphire window and movable flow barricade (red part)

3.2 Investigated Porous Samples

The employed test samples consist of the porous ceramic material, a galvanised copper layer, and a stainless-steel frame. An exemplary image of the reference sample is given in figure 3.4. The following section briefly describes the porous material C/C, the sample design including mounting frame, and the sample geometries tested in the supersonic hot-gas experiments.
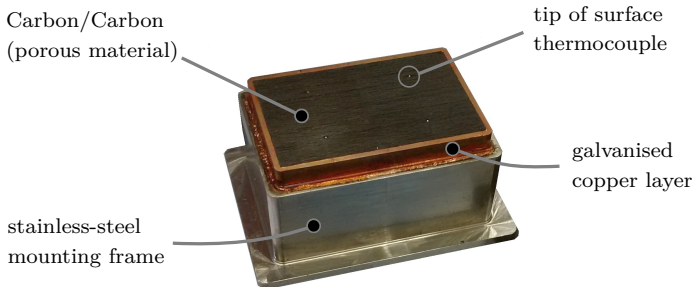
Figure 3.4: Porous sample including mounting frame

C/C material

The investigated material Carbon/Carbon (C/C) is a fibre-reinforced ceramic which has been developed at the Institute of Structures and Design of the German Aerospace Center (DLR). The CMC material is an intermediate product during the Liquid Silicon Infiltration (LSI) process, while the final material is C/C-SiC. The production process is described in detail by Heidenreich [76] whereas only a brief account is given here. First, a green body of carbon fibre-reinforced plastic (CFRP) is formed via autoclave, resin transfer moulding (RTM), or hot pressing techniques using commercially available 0°/90° carbon fabrics impregnated with a phenolic resin. After curing, the green body is pyrolysed in a second step at temperatures of up to 1650°C, which converts the phenolic matrix to amorphous carbon. During cooldown, the volume shrinkage of the matrix and the geometrical stability of the C fibre architecture lead to internal stresses that cause the creation of microcracks in the resulting C/C preform. As a consequence, C/C exhibits a porous microstructure and is suitable for transpiration cooling applications, see figure 3.5.

Due to the fibre component of the material, C/C features anisotropic properties. The lay-up of the here-investigated C/C material are stacked 0/90° twill plies. Two main directions can be identified, parallel and perpendicular directions with respect to the fibre orientation. In the chosen coordinate system, these correspond to the x- and y-axis directions (parallel), and the direction of the z-axis (perpendicular), respectively.
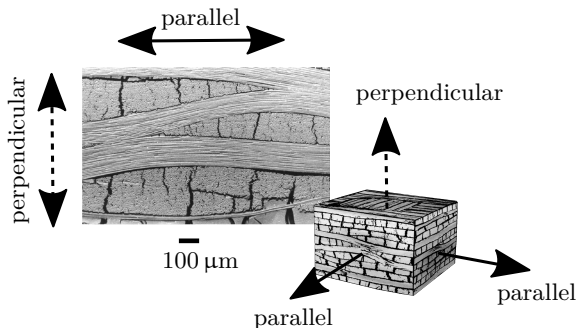
Figure 3.5: C/C microstructure visualised through scanning electron microscopy and isometric view of a C/C-SiC cube to illustrate parallel and perpendicular fibre directions [67]

Using the Archimedes principle [42], DLR Stuttgart determined the material's porosity and density, i.e. $\varepsilon = 10.2\%$ and $\rho_{s,eff} = 1380\,\mathrm{kg/m^3}$, respectively. Moreover, the specific heat capacity of C/C is $c_{p,s} = 750\,\mathrm{J/(kgK)}$, and the effective anisotropic thermal conductivity is $k_{s,eff,\|} = 13.8\,\mathrm{W/(mK)}$ parallel and $k_{s,eff,\perp} = 1.9\,\mathrm{W/(mK)}$ perpendicular to the fibre direction. The corresponding measurements were carried out at room temperature using the *Hot Disk TPS 3500*, which bases on a transient response method. Wagner et al. [189] additionally determined the pore-size distribution of C/C by means of mercury intrusion porosimetry. The measurements yielded peak and median pore diameters ranging between $28 - 30\,\mathrm{\mu m}$ and $11 - 14\,\mathrm{\mu m}$, respectively.

Sample integration concept

The integration of the porous structure into the coolant plenum is realised by means of a mounting frame as shown in figure 3.4. Several steps are required in the manufacturing process. First, the sample is cut from large C/C plates and subsequently manufactured to geometry. In the frame of this thesis, all investigated ceramic samples originate from the same C/C preform. This minimises differences in the material properties between the samples, which may be introduced by slight parameter variations in the production process. In the next step, a surrounding copper layer is galvanised onto the C/C material for the purpose of lateral sealing. The sample is then milled to the defined cross-section of $60 \times 40\,\mathrm{mm^2}$, where the galvanised cooper layer reduces the transpired surface by 1.6 mm from each side. Finally, the porous structure and the copper layer are laser-welded to the stainless-steel frame and then shaped to the final geometry.

Sample geometries

Three different sample geometries have been tested to create multiple validation cases. While the general idea behind the samples has been explained in the introduction chapter, figure 3.6 specifies the dimensions. The drawings additionally indicate the positions of internal temperature measurements, see section 3.3.2 for more details.

The 'reference sample' represents a flat porous wall segment with a thickness of 15 mm, see figure 3.6a. It has a length of 60 mm and a width of 40 mm. However, the galvanised copper layer reduces the transpired surface by 1.6 mm from each side for all samples. The resulting external dimensions as well as the thickness of the copper layer are identical for all investigated samples. Moreover, the component of the transpired surface area that is perpendicular
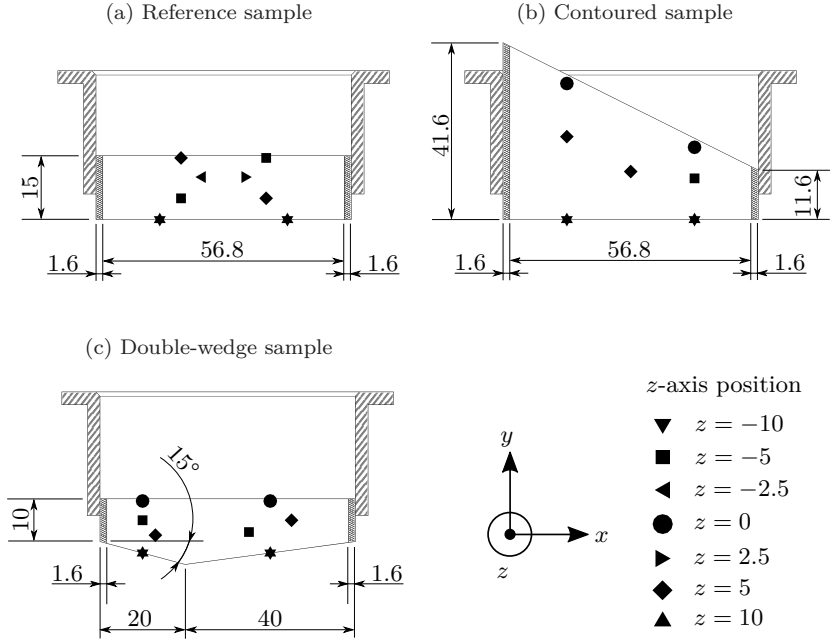
Figure 3.6: Geometry of investigated samples and installation positions of internal thermocouples (units in mm)

to the principal direction of coolant flow (i.e. normal to y-axis) is identical for all samples. This area is employed for the calculation of the blowing ratio, yielding $A_c = 56.8 \times 36.8 \, \text{mm}^2 = 0.00209 \, \text{m}^2$.

The contoured sample depicted in figure 3.6b is flat on the hot-gas side, while its backside surface (towards the coolant reservoir) is at an angle. Thus, the sample's thickness L varies with axial run length of the test channel. Considering only the porous structure available for coolant through flow, L reduces from 40.8 mm to 12.4 mm for the 0° configuration.[1] This configuration is denoted as 'contoured sample 0°' in the following. Alternatively, the sample can be turned by 180° which results in an increasing sample thickness in main-flow direction. This configuration is referred to as 'contoured sample 180°'.

---

1 The dimensions given in figure 3.6b include the copper layer and thus differ.

The third investigated sample is referred to as 'double-wedge sample' and is given in its 0° configuration by figure 3.6c. It exhibits two inclined surfaces which meet at one third of the sample length, i.e. 20 mm. The sample's minimum and maximum thicknesses are 10 mm and 15.36 mm, respectively.

Further test cases result from combining the different porous samples with the shock generator depicted in figure 3.3. Such experiments have been performed with the reference sample and the contoured sample.

3.3 Measurements and Applied Techniques

The following section describes the measurement techniques employed to characterise the transpiration-cooling experiments. Non-intrusive and wall-bounded methods are preferred in supersonic flows as the intrusion of any object results in substantial alterations of the flow field. Moreover, all measurements were taken at steady-state conditions, i.e. after a sufficient settlement time that allowed the channel to reach thermal equilibrium.

3.3.1 Main-Flow Conditions

The mass flow rate of air supplied by the compressor is measured upstream of heater II by combining the measurements of volume-flow rate (Endress+Hauser Prowirl vortex flow meter, accuracy $\pm 0.001 \, \mathrm{m^3/s}$) with temperature (type K, accuracy $\pm 1.1 \, \mathrm{K}$) and pressure (accuracy $\pm 8 \, \mathrm{kPa}$) at the same position. Based on a combined standard uncertainty analysis [16], this yields an uncertainty of $0.008 \, \mathrm{kg/s}$ in the determination of the hot-gas mass flow rate $\dot{m}_{hg}$. Total temperature of the flow is measured after the heater stages and upstream of the Laval nozzle throat by two Electronic Sensors thermocouples (type K, $\varnothing 1 \, \mathrm{mm}$, accuracy $\pm 1.5 \, \mathrm{K}$). Likewise, total pressure is determined before the flow enters the test section by an OMEGA pressure transducer (accuracy $\pm 10 \, \mathrm{kPa}$). Static wall pressure measurements are used to generally characterise the main flow within the test section and to identify the position and strength of shock waves and expansion fans. Therefore, on top and bottom walls of the test section up to 63 static pressure taps are distributed along the symmetry plane of the channel. The pressure measurements are recorded by Scanivalve DSA3016 pressure transducers (accuracy $\pm 400 \, \mathrm{Pa}$). Additionally, four side-wall windows manufactured from fused silica allow for optical access and are used for schlieren photography as detailed in section 3.3.5.

3.3.2 Coolant Plenum and Porous Sample

The coolant mass flow rate is regulated by a Bronkhorst EL FLOW thermal mass-flow controller designed to control mass flows of air, argon, helium, and CO_2. The controller is calibrated to air as the reference gas with an accuracy of $\pm0.5\%$ of the read value (RD) plus $\pm0.1\%$ of the controller's full-scale value (FS), i.e. the maximum mass flow. For other gases than air, it is used with conversion factors which introduce an additional uncertainty. The latter can be calculated from a gas-dependent correlation according to the manufacturer (Ar $\pm3.05\%$ RD, He $\pm3.06\%$ RD, CO_2 $\pm2.66\%$ RD). The mass-flow controller is operated with a constant upstream pressure of 1.67 MPa, whereas the plenum pressure accommodates based on the prescribed mass flow rate and the through-flow resistance of the porous sample. It is recorded through Scanivalve DSA3016 and Omega pressure transducers (accuracy ±400 Pa).

The coolant-reservoir temperature of the fluid is measured by two thermocouples positioned close to the sample's backside (type K, $\varnothing1$ mm, accuracy ±1.5 K, grounded, sheathed).

To record the thermal state of the porous wall, all investigated samples are equipped with ten additional grounded sheathed[2] thermocouples (same type and make). Therefore, bore holes with the size of the thermocouples' diameter are drilled into the C/C structure. Subsequently, the sensors are installed using carbon glue (Aremco Graphi-Bond 669). The measurement positions are spread over the samples' cross section with four and two thermocouples allocated to the hot-gas and coolant-reservoir surfaces, respectively. The remaining four thermocouples are installed at different depths as depicted in figure 3.6. Additionally, two thermocouples are attached to the stainless-steel mounting frame of the samples. The exact measurement coordinates as well as the assumed positioning uncertainties of the employed thermocouples are specified for all samples in appendix B.

3.3.3 Wall Temperature Measurement

Wall temperatures are measured by means of three different methods in the frame of the here-presented experiments: wall thermocouples, an adiabatic wall insert, and infrared (IR) thermography. The two first-mentioned are described in the following, whereas the IR measurements are detailed in section 3.3.4.

---

2 The thermocouples' sheathing material Inconel 600 (2.4816) has a similar thermal conductivity as C/C, i.e. $k_{Inc600} = 14.8$ W/(mK) and $k_{s,eff,\parallel} = 13.8$ W/(mK), respectively.

Wall thermocouples are employed to measure the temperature at nine axial positions distributed over the channel's top wall. Therefore, a total of 13 thermocouples (type K, $\varnothing 1$ mm, accuracy ± 1.5 K, grounded, sheathed) are led through PEEK insert or porous sample and installed flush with the channel's surface, see figure 3.7. Two PEEK surface thermocouples are positioned in a distance of 10 mm left and right of the channel's symmetry plane to check for thermal discrepancies in the cross direction (at fifth axial thermocouple position, marked by ∗). Further measurements using wall thermocouples were performed to determine the thermal state of the channel's bottom wall and to estimate conduction heat fluxes to the channel's surroundings (not indicated in figure 3.7). Although not discussed in detail here, these supported the selection of suitable numerical boundary conditions, see chapter 7.

Besides wall thermocouples, an insulated wall insert designed to measure adiabatic wall temperatures was employed in selected tests. The insert is made from stainless steel and copper, and replaces one of the upstream side-wall windows as displayed in figure 3.8. Three surface thermocouples (Electronic Sensors, type K, accuracy ± 1.5 K) are installed at the backside of the thin
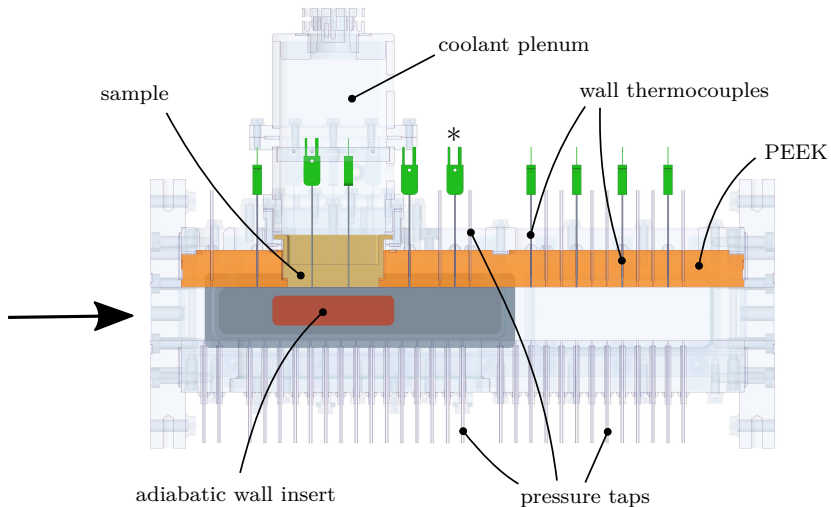
Figure 3.7: Overview of test section and applied wall-measurement techniques
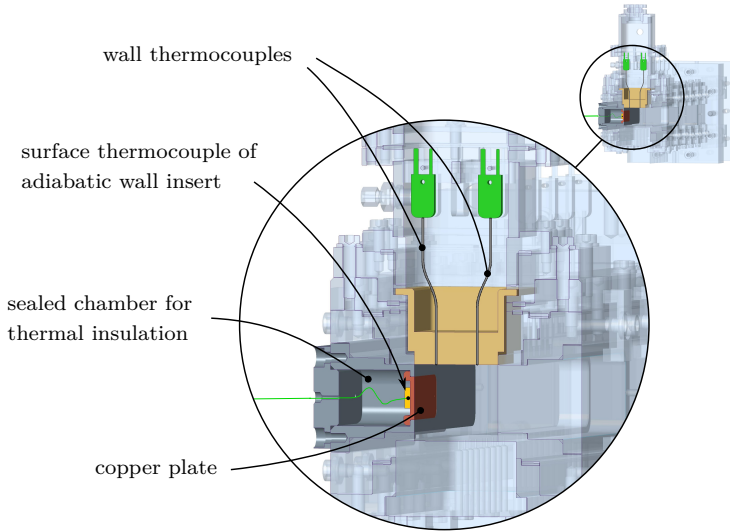
Figure 3.8: Isometric slice through adiabatic wall insert

copper layer (thickness $2\,\text{mm}$). Due to copper's high thermal conductivity ($k_{copper} \approx 380\,\text{W/(mK)}$), the temperature of the thin plate is assumed to be uniform. Opposed to this, a sealed air chamber behind the copper plate thermally insulates the surface thermocouples (and the copper plate) with respect to the outside. Thus, the measured values are expected to be close to the adiabatic wall temperature. Consequently, the insert is denoted as 'adiabatic wall insert' in the following to clearly distinguish between the wall insert's surface thermocouples and the wall thermocouples described above. Due to the defined mounting position, the adiabatic wall insert features negligible positional uncertainties. Moreover, the insulation chamber eliminates the influence of stem conduction [14]. This effect describes undesired heat conduction along the wall thermocouple length which falsifies the measurement. It may become of significance if large thermal gradients are present along the thermocouple. In section 7.1, the influence of stem conduction for the wall thermocouple measurements is evaluated by means of a comparison to the adiabatic wall insert measurement. Although the position of the two measurements differs, i.e. top wall and side wall of the channel, the influence is assumed to be small for the no-blowing case. This is confirmed by the numerical simulations.

3.3.4 Infrared Thermography

Infrared thermography bases on the principle that any body radiates thermal energy which may be transformed in a measurement signal by a suitable IR detector [136]. In the frame of the here-presented study, the non-intrusive measurement method has been employed to assess the spatial temperature distribution on the surfaces of porous sample and surrounding PEEK. For optical access, an IR-transmissive window made from sapphire (thickness 10 mm) replaces a segment of the channel's bottom wall. Moreover, due to the experimental infrastructure and space limitations, an infrared mirror was used to alter the optical flow path, see figure 3.9. The measurements were then taken by means of a FLIR SC7600 infrared camera with a maximum resolution of 640×512 pixels. It detects infrared rays with a wavelength between $1.5 \, \mu m$ and $5.1 \, \mu m$, and thus blends well with the employed sapphire window which offers high transmissivity up to a wavelength of $5 \, \mu m$ [191]. The camera's noise-equivalent temperature difference is specified to be less than 25 mK according to the manufacturer.

The radiation intensity detected by the infrared camera is not limited on the emissions of porous sample and wake region which are to be measured but consists of several further contributions. These originate from the optical path (e.g. infrared window and mirror), reflections (e.g. side walls), or the background. Moreover, the radiation components depend not only on the temperature of the emitting surfaces but also other influences such as surface properties, emissivity, transmissivity, or viewing angles.

As this complicates the quantitative evaluation of the IR measurements, an in-situ calibration has been performed for the here-presented data [24, 111, 126]. The method relates radiation intensities detected by the IR camera to surface temperatures measured by means of wall thermocouples. In the calibration process, the radiation intensity DL in close vicinity of a thermocouple tip ($0.75 \, mm < r < 1.75 \, mm$) is averaged and then assigned to the thermocouple's reading T_{TC}. Moreover, since particularly the temperature reduction for boundary-layer blowing is of interest, a differential calibration method is employed. Consequently, reductions of wall thermocouple measurements, i.e. $\Delta T_{TC} = (T_{TC,F \neq 0\%} - T_{TC,F=0\%})$, are related to reductions of measured radiation intensity, i.e. $\Delta DL = (DL_{F \neq 0\%} - DL_{F=0\%})$. The measurements for the test case without coolant blowing ($F = 0\%$) serve as the reference case here. The applied calibration approach eliminates several non-beneficial influences on the IR measurements. By using differences, parasitic influences present in both blowing and no-blowing cases disappear. This concerns for example the radiation intensities of uncooled components such as the channel's side walls
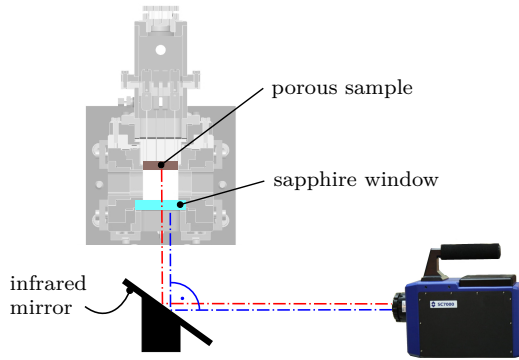
Figure 3.9: IR measurement setup

or the sapphire window which are independent of blowing ratio. Additionally, the narcissus effect [81, 113], which arises from cooling of the camera's sensor to its cryogenic working temperature, is eliminated. In contrast, the effect of transpiration cooling on the porous sample surface and its direct surroundings is captured. A polynomial of second degree is determined from the calibration data set which contains the measurements of various blowing rates. To avoid extrapolation, the data points should include both minimum and maximum temperature levels. Since the surface emissivities (and reflectivities) of C/C and PEEK are different, both regions need to be calibrated separately, resulting in two calibration curves as exemplarily given in figure 3.10.[3] Combining calibration curves, differential IR images, and wall temperature of the test case without blowing, finally results in absolute surface temperature plots.

Figure 3.10: In-situ calibration curves for surface of porous sample and surface of PEEK surroundings for reference sample test case. Left and right ordinates depict temperature reduction and absolute temperature, respectively.
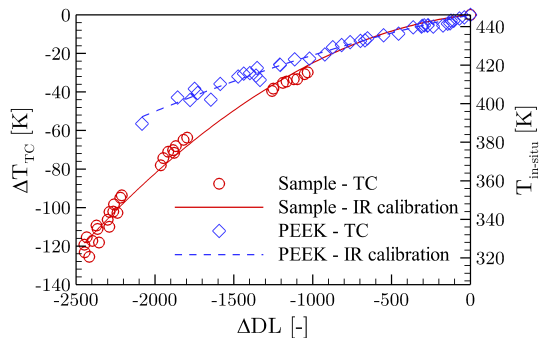
A drawback of the here-proposed calibration method based on differences is that the temperature distribution for the no-blowing case has to be known. For reference and contoured samples, the temperature distribution is assumed to be constant throughout the channel (as shown in chapter 7.1). Thus, $T_{TC,F=0\%}$ is determined as the average of all wall thermocouples. Regarding the double-wedge sample, the observed surface is divided in front and aft surfaces of the porous sample, and PEEK surface. The no-blowing temperature $T_{TC,F=0\%}$ is then determined separately for each surface by averaging corresponding thermocouple measurements. However, since there are moderate local temperature variations on the individual surfaces, the assumption of a constant reference temperature is not entirely correct. Regarding the shock-generator test cases without blowing, substantial temperature differences occur continuously over the porous sample surface. Therefore, absolute values of thermocouple and IR measurements (i.e. T_{TC} and DL) have been used for the in-situ calibration of these test cases.

3.3.5 Schlieren Imaging

Schlieren imaging is applied to visualise the supersonic flow field within the test section. The optical measurement technique captures changes in the refraction index which are directly related to density gradients in the flow. Therefore, the occurrence of shock waves and expansion fans as well as their positions may be determined. Besides, the wave angle indicates the flow Mach number.

The standard schlieren setup employed for the experiments is schematically illustrated in figure 3.11. A white light emitting diode (Philips Luxeon Rebel) and a small aperture ($\varnothing 1\,\mathrm{mm}$) serve as a punctual light source. An achromatic lens ($f = 1000\,\mathrm{mm}$, $d = 100\,\mathrm{mm}$) is employed to parallelise the light beam before it crosses the gas volume between the two side-wall windows of the test section. A second identical achromatic lens focuses the beam onto a horizontal knife edge. The latter blocks all light parts diverted by the changes in the refraction index present between the two lenses. The remaining light beam is captured by a camera (Canon EOS 600D, max. resolution 18 megapixels) yielding one-dimensional schlieren images.

---

3 However, the materials' surface emissivities are not required for the calibration procedure. A flat black finish was applied to the PEEK wall insert to minimise the reflectivity of its surface. The surface absorptivity of a comparable C/C sample was determined to be 0.85 for the temperature range 290 K to 450 K [165].

Side-wall windows made from fused silica allow for optical access at two axial positions (window thickness 15 mm). As indicated in figure 3.2, only the downstream window spreads over the full channel height, whereas the wall-near regions are partially concealed by the window frame for the upstream position (i.e. 2.2 mm at top wall and 6.2 mm at bottom wall).
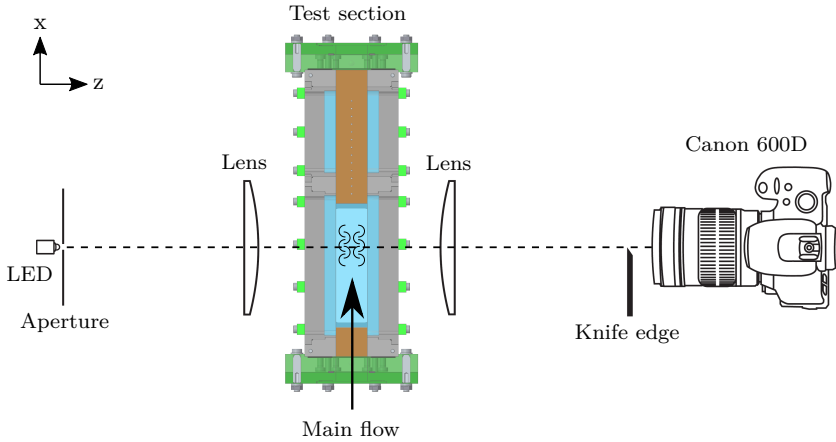
Figure 3.11: Schlieren imaging setup

CHAPTER 4

Numerical Methods

The significance of numerical simulations in the design process of all kinds of engineering application has tremendously increased within the last decades. This has various reasons including economical considerations when compared to extensive experimental test campaigns. Moreover, especially with respect to aerospace applications, numerical methods allow to simulate arbitrary test conditions and flight regimes which may be hard to obtain in a ground-based experiment. In addition, methods such as computational fluid dynamics (CFD) reveal the complete flow field and enable a detailed analysis of physical processes. However, the quality of simulations strongly depends on the applied physical models which therefore require extensive validation. As a consequence, a combined numerical and experimental approach is most promising for many engineering problems.

In the present chapter, the numerical methods and models employed for the simulation of transpiration cooling are described. Starting with an introduction on numerical fundamentals, subsequently the governing equations for main flow and porous structure are discussed. Afterwards, the treatment of porous interfaces and the domain coupling are described. Lastly, the developed OpenFOAM solver is detailed.

4.1 Finite Volume Method

For most practical flow situations, the governing equations presented in section 2.1 have not yet been (or cannot be) solved analytically. Instead, numerical methods such as CFD are employed for flow simulation and analysis. A common approach is to divide the fluid continuum into numerous control volumes by a numerical grid. Flow variables (ρ, $\boldsymbol{u}$, $\boldsymbol{Y}$, p, T) are calculated for discrete positions, e.g. the computational nodes located at the centroids of the respective control volume. Since fluxes leaving a control volume are entering directly a neighbouring volume, the so-called Finite Volume Method (FVM) is conservative. Thus, the solution satisfies the conservation of mass, momentum, species, and energy for any individual control volume as well as for the whole flow domain. To obtain an algebraic equation for a control volume, surface and volume integrals are approximated using quadrature formulae. Consequently, the partial derivates present in the governing equations are discretised using the surrounding cell values. Fluxes between two control volumes depend on the variable values at the surface which separates the cells. Their calculation is based on the numerical interpolation of cell-centred values onto the cell faces. The system of algebraic equations may then be solved by means of different numerical methods.

Solution algorithms

The SIMPLE solution algorithm (Semi-Implicit Method for Pressure Linked Equations) by Patankar and Spalding [147] in combination with relaxation factors is well suited for the simulation of subsonic steady-state problems. The method is based on a predictor-corrector approach which decouples the algebraic operations on pressure from those on velocity. It starts with initial pressure and velocity fields from which an intermediate velocity field is computed. Based on continuity and momentum equations, and with the intermediate velocity field, a pressure correction term is determined. From the updated pressure field, a corrected velocity field is obtained. The sequence is iterated until momentum and continuity equations are satisfied. An extension of the algorithm for unsteady flow problems has been proposed by Issa [87] by means of the PISO algorithm (Pressure-Implicit with Splitting of Operators). It follows a similar procedure to handle the pressure-velocity coupling but employs a second corrector step. Despite being also applicable to supersonic flow problems, the solution algorithms produce spurious oscillations in vicinity of discontinuities in the flow properties, see for example Gutiérrez Marcantonia et al. [69]. Instead, other numerical schemes have proven to be beneficial in high-speed flows featuring local discontinuities because of the formation of shock waves.

Moreover, information transport in compressible flows occurs not only through directed advection but also based on the omnidirected propagation of sound waves. The reconstruction of numerical fluxes typically involves the solution of a Riemann problem which introduces left and right states at each cell face [184]. Besides computationally expensive approximate Riemann solvers such as presented by Roe [159] and Harten et al. [75], the discretisation scheme developed by Kurganov and Tadmor [105] and Kurganov et al. [106] may be employed to solve these algebraic problems. By taking into account the local speed of sound, the central scheme is able to provide accurate non-oscillatory solutions. However, a disadvantage of the scheme typically is the velocity limitation which forecloses viscous flow simulations at low Mach numbers, i.e. M < 0.3. To circumvent this, Kraposhin et al. [101] developed a hybrid scheme combining PISO/SIMPLE method and Kurganov-Tadmor's scheme which is suited for both incompressible and compressible flow regime. As the hybrid scheme has been employed in the frame of this thesis, more details are given in section 4.5.

Numerical errors

The solution of a numerical simulation is only an approximation of the real physical problem. Deviations arise from different error sources which can be classified into the following types:

  1) modelling errors,   2) discretisation errors,   3) iteration errors.

First, the differences between the actual physics involved in the problem and its mathematical representation by equations are denoted as modelling errors. They are mainly due to assumptions and simplifications made during the derivation of conservation equations, e.g. turbulence modelling or volume-averaged porous-structure modelling. Additionally, the applied boundary conditions as well as the coupling conditions between numerical domains may add to the deviations. The modelling error is commonly evaluated by a comparison of simulation results to analytical solutions, accurate experimental measurements, and/or simulation methods of higher quality such as direct numerical simulation. To validate the here-presented numerical simulations, the results are compared to own experimental measurements as well as data given in literature. Although the experimental reference data itself is subject to measurement uncertainties, a good agreement indicates that the simulations represent the physics well within the range of tested conditions.

Secondly, the discretisation error represents the difference between the exact solution of the conservation equations and the exact solution of the system of

algebraic equations. It depends on the applied discretisation schemes as well as the spatial (and temporal) resolution of the simulation domain. Generally, high-order schemes and a fine numerical grid reduce the discretisation error, but increase the computational cost of the simulations. In the frame of this thesis, the geometries of all considered test cases are represented by block-structured grids with hexahedral elements. This concerns fluid, solid, as well as porous domains. To adequately resolve the turbulent boundary layers, the mesh is refined towards the walls using prism layers with growing rates, i.e. h_{i+1}/h_i, set between 1.1 and 1.25. The employed spatial discretisation schemes are of second order. Additionally, in the shock-capturing supersonic simulations, the total variation diminishing (TVD) scheme Minmod is employed [74]. To estimate the spatial discretisation error, Roache [158] established the Grid Convergence Index (GCI) method which represents a widely accepted systematic approach. Following this, the GCI has also been determined in the frame of this study for a generic test case with boundary-layer blowing, see section 7.2.2.

Lastly, the numerical solver approaches the exact solution of the discretised equations iteratively instead of yielding exact solutions. Thus, a residual remains for each of the solved equations which is controlled by a predefined simulation criterion. In the present work, low iteration errors are achieved by ensuring a drop in the residual of at least 4 orders of magnitude for all equations solved. Additionally, the numerical convergence was confirmed through monitoring the change of flow field variables over iterations.

4.2 Turbulence Modelling

Generally, flows can either be laminar or turbulent. While laminar flows are ordered and free from disturbances, turbulent flow on the other hand is associated with random and chaotic fluctuations in space and time. The turbulent motions may be categorised based on their size, ranging from large-scale anisotropic eddies to small dissipative eddies which are commonly assumed as locally isotropic. Although the Navier-Stokes equations as detailed in chaper 2 are valid for all flows including compressible turbulent flow, the extremely small length and time scales related to turbulent fluctuations make the simulations challenging with respect to grid resolution and computational costs. Additionally, the length scale of dissipative eddies decreases with increasing Reynolds number [203]. Consequently, direct numerical simulation (DNS) resolving all turbulent fluctuations has only been feasible for relative simple geometries at low or moderate Reynolds numbers up to now. In contrast, many engineering problems and particularly supersonic flow situations exhibit high Reynolds numbers.

This has led to the existence of various turbulence-modelling approaches. Large eddy simulations (LES) resolve the unsteady and anisotropic large-scale turbulence while using approximations for the smaller eddies. However, the transient and three-dimensional simulations are still computationally expensive. Therefore, the most common method to date is to consider the Reynolds-Averaged Navier-Stokes (RANS) equations where the turbulent fluctuations are time-averaged. Instead of resolving the turbulent motions in detail, only their influence on the main flow field is captured. The averaging process of the flow introduces additional terms and variables which are related to the turbulent motion. The system of equations is then closed by employing one of the various existing turbulence models. Regarding this, the selection of an appropriate model depends on the character and complexity of the flow, the desired modelling accuracy, and the available computational resources.

4.2.1 Reynolds-Averaged Navier-Stokes Equations

Reynolds-averaging is based on the assumption that for a statistically steady flow, the turbulent quantities can be split into a time-averaged and a fluctuating part. Regarding the flow velocity this yields

$$\boldsymbol{u} = \overline{\boldsymbol{u}} + \boldsymbol{u}' \quad , \tag{4.1}$$

with a time-averaged part

$$\overline{\boldsymbol{u}} = \frac{1}{\Delta t} \int_{t_0}^{t_0+\Delta t} \boldsymbol{u} \, \mathrm{d}t \quad , \tag{4.2}$$

where Δt is large in comparison to the typical time scale of fluctuations, and $\boldsymbol{u}'$ is the fluctuating velocity component which satisfies the condition $\overline{\boldsymbol{u}'} = 0$. If compressible flows with multi-component gases (and thus density fluctuations) are to be considered, the governing equations may be simplified by an additional mass-weighted time-averaging, also denoted as Favre-averaging:

$$\boldsymbol{u} = \tilde{\boldsymbol{u}} + \boldsymbol{u}'' \quad , \tag{4.3}$$

where the Favre-averaged velocity $\tilde{\boldsymbol{u}}$ is defined as

$$\tilde{\boldsymbol{u}} = \frac{\overline{\rho \boldsymbol{u}}}{\overline{\rho}} = \frac{\int_{t_0}^{t_0+\Delta t} \rho \boldsymbol{u} \, \mathrm{d}t}{\int_{t_0}^{t_0+\Delta t} \rho \, \mathrm{d}t} \quad . \tag{4.4}$$

Here, the condition $\overline{\rho \boldsymbol{u}''} = 0$ for the fluctuating part arises from the continuity equation.

Applying Reynolds- and Favre-Averaging to the conservation equations in differential form (2.2), (2.3), (2.8), (2.13) yields the following set of governing equations, also denoted as RANS equations:

$$\frac{\partial \overline{\rho}}{\partial t} + \nabla \cdot (\overline{\rho}\tilde{\boldsymbol{u}}) = 0 \quad . \tag{4.5}$$

$$\frac{\partial}{\partial t}(\overline{\rho}\tilde{\boldsymbol{u}}) + \nabla \cdot (\overline{\rho}\tilde{\boldsymbol{u}} \otimes \tilde{\boldsymbol{u}}) = -\nabla \overline{p} + \nabla \cdot \tilde{\boldsymbol{\tau}}_{eff} \quad . \tag{4.6}$$

$$\frac{\partial}{\partial t}(\overline{\rho}\tilde{Y}_1) + \nabla \cdot (\overline{\rho}\tilde{\boldsymbol{u}}\tilde{Y}_1) = -\nabla \cdot \boldsymbol{j}_{1,eff} \quad . \tag{4.7}$$

$$\frac{\partial}{\partial t}(\overline{\rho}\tilde{h}_{tot}) + \nabla \cdot (\overline{\rho}\tilde{\boldsymbol{u}}\tilde{h}_{tot}) - \frac{\partial \overline{p}}{\partial t} = -\nabla \cdot \dot{\boldsymbol{q}}_{eff} + \nabla \cdot (\tilde{\boldsymbol{\tau}}_{eff} \cdot \tilde{\boldsymbol{u}}) \quad . \tag{4.8}$$

Note that the continuity equation remains unchanged, while the transport equations for momentum, species, and enthalpy now contain effective variables which comprise both viscous and turbulent transport. This concept of turbulence modelling is based on the eddy viscosity hypothesis proposed by Boussinesq [23]. It postulates that the turbulent transport acts in a similar way as molecular transport and is linearly proportional to the stress tensor. The three-dimensional nature of turbulence is omitted by the approach. To characterise the transport of momentum due to turbulent motions or eddies, the turbulent eddy viscosity μ_t is introduced. It appears in the effective stress tensor $\boldsymbol{\tau}_{eff}$ which is defined by

$$\begin{aligned}
\tilde{\boldsymbol{\tau}}_{eff} &= \tilde{\boldsymbol{\tau}} + \tilde{\boldsymbol{\tau}}_t \\
&= \mu_{eff}[\nabla \otimes \tilde{\boldsymbol{u}} + (\nabla \otimes \tilde{\boldsymbol{u}})^T] - \frac{2}{3}\mu_{eff}(\nabla \cdot \tilde{\boldsymbol{u}})\boldsymbol{I} - \frac{2}{3}\overline{\rho}\kappa\boldsymbol{I} \quad ,
\end{aligned} \tag{4.9}$$

where $\mu_{eff} = \mu + \mu_t$ is the sum of molecular viscosity and turbulent eddy viscosity. In contrast to its molecular counterpart, μ_t is not a fluid property but a function of the flow. Additionally, equation (4.9) contains the turbulent kinetic energy

$$\kappa = \frac{1}{2}\left(\overline{u_x'^2} + \overline{u_y'^2} + \overline{u_z'^2}\right) \quad , \tag{4.10}$$

which will be discussed in more detail later.[1]

Based on the averaging process, additional terms are also introduced to the species transport equation and the enthalpy equation. In line with the eddy viscosity concept, turbulent species diffusion and heat transport are accounted for by using effective properties

$$\boldsymbol{j}_{1,eff} = -\overline{\rho} D_{12,eff} \nabla \tilde{Y}_1 \quad , \tag{4.11}$$

and

$$\dot{\boldsymbol{q}}_{eff} = -k_{eff} \nabla \tilde{T} + (\tilde{h}_{st,1} - \tilde{h}_{st,2})\boldsymbol{j}_{1,eff} \quad , \tag{4.12}$$

with $D_{12,eff} = D_{12} + D_{12,t}$ and $k_{eff} = k + k_t$. Replacing temperature by enthalpy, equation (4.12) translates to

$$\dot{\boldsymbol{q}}_{eff} = -\overline{\rho} \alpha_{eff} \nabla \tilde{h} - \overline{\rho} \left(D_{12,eff} - \alpha_{eff} \right) \left(\tilde{h}_{st,1} - \tilde{h}_{st,2} \right) \nabla \tilde{Y}_1 \quad , \tag{4.13}$$

with the effective thermal diffusivity defined by $\alpha_{eff} = \alpha + \alpha_t = k_{eff}/(\rho c_p)$.[2]

As for the eddy viscosity, the turbulent variables, i.e. $D_{12,t}$, k_t, and α_t, are no fluid properties but describe the transport due to turbulent motions. The turbulent transport of species and heat may be linked to the previously introduced eddy viscosity μ_t by means of the turbulent Schmidt number and turbulent Prandtl number given by

$$\mathrm{Sc}_t = \frac{\nu_t}{D_t} = \frac{\text{turbulent momentum diffusivity}}{\text{turbulent mass diffusivity}} \tag{4.14}$$

and

$$\mathrm{Pr}_t = \frac{\nu_t}{\alpha_t} = \frac{\text{turbulent momentum diffusivity}}{\text{turbulent thermal diffusivity}} \quad , \tag{4.15}$$

where $\nu_t = \mu_t/\rho$ is the kinematic eddy viscosity.

Both dimensionless numbers are constructed identical to their molecular equivalents $\mathrm{Pr} = \nu/\alpha$ and $\mathrm{Sc} = \nu/D$ which are, however, fluid properties. A simplistic approach which is widely spread in literature employs constant values for Pr_t

---

1 The symbol κ is employed to represent the turbulent kinetic energy to avoid any confusion with the thermal conductivity k.

2 The first term in equation (4.13) represents heat conduction, whereas the second term accounts for energy transport due to diffusion. The latter may have a significant contribution to the enthalpy balance given by equation (4.8) if the (molecular and/or turbulent) Lewis number $\mathrm{Le} = \mathrm{Sc}/\mathrm{Pr} \neq 1$ and the difference between the specific heat capacities of the considered species is large.

and Sc_t. This approach is also followed within the frame of the present work. The choice of the values for turbulent Prandtl and Schmidt numbers is discussed in appendix E.1 and only briefly stated here.

Concerning the turbulent Schmidt number, a value of $\mathrm{Sc}_t = 0.8$ has been applied in all simulations involving species diffusion. With respect to the selection of an appropriate value of Pr_t, a sensitivity study is performed for the supersonic flow test cases discussed in chapter 7. In contrast, for the analysis of the subsonic turbulent channel flow experiments by Meinert [129] (see chapter 6), a constant value of $\mathrm{Pr}_t = 0.87$ as proposed by the author has been used.

Following this approach yields only two remaining unknowns, i.e. turbulent kinetic energy κ and eddy viscosity μ_t. Closure of the equation system is then achieved by using a turbulence model. With respect to this, various models ranging from algebraic relations to more sophisticated two-equation models exist. In the frame of this thesis, Menter's shear stress transport (SST) two-equation model [133] is employed to model turbulence in the main flow. The model as well as the applied near-wall treatment are briefly described in the following sections.

4.2.2 Near-Wall Treatment

The boundary layer relates the free-stream velocity of a flow to the no-slip condition at a rigid wall. In general, turbulent flows exhibit a particular velocity profile which is of universal character. In this context, dimensionless variables for velocity and wall distance are employed:

$$u^+ = \frac{u}{u_\tau} \quad , \tag{4.16}$$

where $u_\tau = \sqrt{\tau_w/\rho}$ is the friction velocity with the wall shear stress $\tau_w = \mu_w \left(\partial u / \partial n \right)|_w$. The dimensionless wall distance is defined by means of u_τ and the wall-normal distance Δy:

$$y^+ = \frac{u_\tau \Delta y}{\nu} \quad . \tag{4.17}$$

Figure 4.1 depicts the 'universal law of the wall' as described for example in references [30, 164, 203]. A turbulent boundary layer consists of inner and outer regions, where the inner region only takes about 10% to 20% of the entire

boundary-layer thickness. It may be further divided into viscous sublayer, buffer zone, and overlap layer. In the viscous sublayer ($y^+ \leq 5$), the flow is laminar and governed by molecular transport processes, whereas mixing is dominated by turbulence in the overlap or log-law layer ($70 \leq y^+$). Both are connected via the buffer layer ($5 \leq y^+ \leq 70$), in which molecular and turbulent transport are approximately in balance.

Different approaches are used in RANS simulations to represent the region in direct vicinity of the wall. These vary in terms of computational effort and range from applying wall functions for the near-wall region to fully resolving the boundary layer through a refined numerical grid [51]. The latter, more general approach, is also denoted as Low-Re-number method and typically yields more accurate simulation results. This particularly applies to complex flow situations and the simulation of heat transfer problems. Following the approach, the first grid cell needs to be placed within the viscous sublayer, i.e. $y_1^+ \leq 1$. As a consequence, wall shear stress and heat flux can be directly computed from the velocity and temperature gradients at the wall, respectively. However, for high Reynolds number flows, the y_1^+ requirement for the first cell leads to small mesh sizes in the wall-normal direction (i.e. $\Delta y_1 \approx 10^{-6}\,\mathrm{m}$) which increases the number of cells and the total simulation time. The Low-Re approach has been employed for all here-presented numerical simulations. Thus, the dimensionless wall distance of the first cell satisfies the condition $y_1^+ < 1$ for all walls while the viscous sublayer is resolved by around 10 cells.
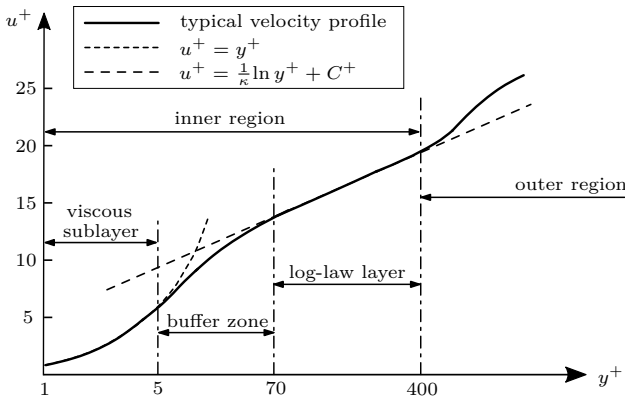
Figure 4.1: Turbulent boundary-layer profile in wall coordinates (von Kármán constant $\kappa \approx 0.41$ and $C^+ \approx 5.0$ for a smooth wall)

4.2.3 Shear Stress Transport Model

The Menter shear stress transport (SST) model combines two widely used turbulence models, namely Jones and Launder's κ-ϵ model [93] and the κ-ω model developed by Wilcox [202]. Both of the models have been applied to numerous test cases and are well validated. However, they exhibit certain strengths and weaknesses depending on the considered flow situations. The κ-ϵ model is based on the transport equations for the turbulent kinetic energy κ and the turbulence dissipation ϵ. From both variables, the eddy viscosity μ_t is then determined. The model has been successfully applied to various flow situations and performs particularly well in turbulent free-shear flows. However, it lacks in sensitivity to adverse pressure gradients and thus delays (or even prevents) separation [131]. Moreover, Low-Re formulations of the model require damping functions since integration through the viscous sublayer is numerically challenging. In contrast to this, the κ-ω model performs significantly better under adverse pressure gradient conditions and may be employed throughout the complete boundary layer without damping functions. Here, transport equations for turbulent kinetic energy κ and specific turbulence dissipation rate ω are solved. A major downside of this model, however, is its strong sensitivity to the free-stream values of ω as demonstrated in reference [132]. In order to combine the advantages of both models while eliminating the disadvantages, Menter [133] suggested the SST model which incorporates a blending function that activates the κ-ω model in wall-near regions and uses the κ-ϵ formulation further away from the wall. For this, the ϵ-equation is transformed into an ω-equation which yields the following two transport equations for turbulent kinetic energy κ and specific turbulence dissipation rate ω:

$$\frac{\partial}{\partial t}(\rho\kappa) + \nabla \cdot (\rho\boldsymbol{u}\kappa) = \tilde{P}_{\kappa} - \beta^* \rho\omega\kappa + \nabla \cdot [(\mu + \sigma_{\kappa}\mu_t)\nabla\kappa] \quad , \qquad (4.18)$$

$$\frac{\partial}{\partial t}(\rho\omega) + \nabla\cdot(\rho\boldsymbol{u}\omega) = \frac{\alpha}{\nu_t}P_{\kappa} - \beta\rho\omega^2$$
$$+ \nabla \cdot [(\mu + \sigma_{\omega}\mu_t)\nabla\omega] + (1 - F_1)\frac{2\rho\sigma_{\omega 2}}{\omega}\nabla\kappa \cdot \nabla\omega \quad , \qquad (4.19)$$

where $P_{\kappa} = \boldsymbol{\tau} : (\nabla \otimes \boldsymbol{u})$ is the rate of turbulent production and $\beta^* = 0.09$ is an empirical coefficient. A limiter is used to prevent the build-up of turbulence in stagnation regions $\tilde{P}_{\kappa} = \min(P_{\kappa}, 10\beta^*\rho\kappa\omega)$. The transition from κ-$\epsilon$ model to κ-ω model is implemented by means of complex blending functions. A coefficient Φ is calculated through $\Phi = F_1\Phi_{\kappa\text{-}\epsilon} + (1 - F_1)\Phi_{\kappa\text{-}\omega}$, where $\Phi_{\kappa\text{-}\epsilon}$ and $\Phi_{\kappa\text{-}\omega}$ represent the coefficients of the κ-ϵ and κ-ω models, respectively. The blending

function F_1 is equal to zero away from the surface and switches to one inside the boundary layer. It is defined by

$$F_1 = \tanh\left(\min\left[\max\left(\frac{\sqrt{\kappa}}{\beta^*\omega y}, \frac{500\nu}{y^2\omega}\right), \frac{4\rho\sigma_{\omega,2}\kappa}{CD_{\kappa\omega}y^2}\right]^4\right) \quad, \tag{4.20}$$

with $CD_{\kappa\omega} = \max\left(2\rho\sigma_{\omega2}\frac{1}{\omega}\nabla\kappa\cdot\nabla\omega, 10^{-10}\right)$ and the distance to the nearest wall y. All further constants of the SST model are specified in table 4.1.

Table 4.1: SST model constants [135]

	β^*	α	β	σ_κ	σ_ω
κ-ϵ	0.09	5/9	0.075	0.85	0.5
κ-ω	0.09	0.44	0.0828	1	0.856

From the solutions of the conservation equations for κ and ω, the turbulent eddy viscosity is calculated via

$$\mu_t = \frac{a_1\rho\kappa}{\max\left(a_1\omega, S\,F_2\right)} \quad, \tag{4.21}$$

where $a_1 = 0.31$, $S = \sqrt{2\boldsymbol{D}:\boldsymbol{D}}$ with $\boldsymbol{D} = \frac{1}{2}\left[\nabla\otimes\boldsymbol{u} + (\nabla\otimes\boldsymbol{u})^T\right]$ is the invariant measure of the strain rate, and F_2 is a second blending function defined by

$$F_2 = \tanh\left(\left[\max\left(\frac{2\sqrt{\kappa}}{\beta^*\omega y}, \frac{500\nu}{y^2\omega}\right)\right]^2\right) \quad. \tag{4.22}$$

Boundary conditions for the SST model in Low-Re formulation are set in line with the no-slip condition for κ and Wilcox' original condition for ω [134, 202]:

$$\kappa = 0 \quad, \tag{4.23}$$

$$\omega_{F=0} = \frac{6\nu_w}{0.075(\Delta y_1)^2} \quad. \tag{4.24}$$

The turbulent kinetic energy κ_{in} of incoming flows may be defined by the turbulent intensity TI

$$\kappa_{in} = \frac{3}{2}\left(u'\right)^2 = \frac{3}{2}\left(\text{TI}\,u_\infty\right)^2 \quad. \tag{4.25}$$

Typically, a turbulent intensity between 2% and 10% is chosen for the simulation of turbulent channel flows. The corresponding inlet condition for the specific dissipation rate is calculated from the turbulent viscosity ratio ν_t/ν

$$\omega_{in} = \frac{\kappa}{\nu} \left(\frac{\nu_t}{\nu}\right)^{-1} \tag{4.26}$$

or the turbulent mixing length $L_{t,in}$

$$\omega_{in} = \frac{1}{C_\mu^{0.25}} \frac{\sqrt{\kappa_{in}}}{L_{t,in}} \quad , \tag{4.27}$$

with $C_\mu = 0.09$.

4.3 Volume-Averaged Porous Structure Equations

Within the frame of this thesis, the porous structure is not resolved on pore level but modelled by means of a volume-averaged approach using several material parameters. The underlying assumption is that the porous material can be considered as homogeneous on the macroscale, see also section 2.4. However, this is only an approximation with respect to the here-considered C/C material. As a consequence of the volume-averaged approach, each cell of the porous domain contains both solid and fluid phases. The volume-averaged conservation equations for the porous domain are given by:

$$\varepsilon \frac{\partial \rho_f}{\partial t} + \nabla \cdot (\rho_f \boldsymbol{u_D}) = 0 \quad , \tag{4.28}$$

$$\frac{\partial}{\partial t} (\rho_f \boldsymbol{u_D}) + \frac{1}{\varepsilon} \nabla \cdot (\rho_f \boldsymbol{u_D} \otimes \boldsymbol{u_D}) = -\nabla p + \boldsymbol{S_{DF}} \quad , \tag{4.29}$$

$$\varepsilon \frac{\partial}{\partial t} (\rho_f c_{p,f} T_f) + \nabla \cdot (\rho_f \boldsymbol{u_D} c_{p,f} T_f) - \frac{\partial p}{\partial t}$$
$$= \varepsilon \nabla \cdot (k_f \nabla T_f) + h_v (T_s - T_f) \quad , \tag{4.30}$$

$$\frac{\partial}{\partial t} (\rho_{s,eff} c_{p,s} T_s) = \nabla \cdot (k_{s,eff} \nabla T_s) + h_v (T_f - T_s) \quad . \tag{4.31}$$

Equations (4.28) to (4.30) represent mass, momentum, and energy equations of the fluid phase, while the solid-phase energy is accounted for by equation (4.31). Coolant momentum loss within the porous structure is considered by means of the Darcy-Forchheimer relation as expressed by the source term in equation (4.29):

$$S_{DF,i} = -\left(\frac{\mu_f}{K_{D,i}} u_{D,i} + \frac{\rho_f}{K_{F,i}} |u_{D,i}| u_{D,i} \right) \qquad \text{for } i = x, y, z \ . \qquad (4.32)$$

4.4 Numerical Treatment of Porous Surfaces

The following section describes the simulation models employed to numerically reproduce the coolant reservoir and the interaction of a transpiration-cooled porous wall with an overflowing hot gas. While the interface between hot gas flow and porous structure is defined by coupling conditions, the coolant flow in the reservoir is not resolved by the numerical grid but only modelled by means of the applied boundary conditions. The section starts with the description of the employed boundary conditions at the coolant-reservoir side Γ_{PM}. Subsequently, the coupling conditions at the interface Γ_{HG} between hot-gas and porous-structure domain are discussed. Figure 4.2 illustrates the two porous surfaces Γ_{PM} and Γ_{HG}.

The presented models are employed for all fully-coupled simulations and are also applied for the single-domain simulations (e.g. only main-flow domain, only porous domain), if not stated otherwise.
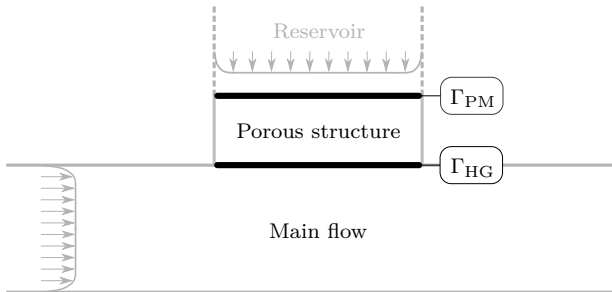
Figure 4.2: Porous surfaces Γ_{PM} and Γ_{HG}

4.4.1 Coolant-Reservoir Side

In a typical transpiration-cooling situation, a porous structure is heated through an overflowing hot gas while a coolant gas at lower temperature enters the porous channels through a reservoir. The surface Γ_{PM} through which the coolant gas enters the porous structure is denoted as 'coolant-reservoir side' in the following. Since the reservoir itself is not included in the simulation, appropriate boundary conditions need to be defined to model its influence.

Pressure-driven mass flow inlet

The coolant mass flow is driven by the pressure difference between coolant reservoir and static pressure at the transpired surface. Due to variations of the hot-gas wall pressure, the driving pressure difference over the sample thickness may locally vary. Besides, also the local coolant-fluid temperature and variations in the porous wall thickness influence the through-flow behaviour. All effects may yield a non-uniform distribution of coolant mass flow rate over the porous inlet and the hot-gas interface. To account for this, the mass flow inlet at the coolant-reservoir side is modelled by a total pressure boundary condition. The condition prescribes a constant value $p_{tot,c}$ over the complete surface Γ_{PM}.

In the frame of the here-presented simulation cases, typically, a target blowing ratio F is to be reached at steady-state conditions. Thus, the boundary condition for total pressure $p_{tot,c}$ has been modified to induce a predefined $\dot{m}_c$ through an iterative process. The boundary condition on Γ_{PM} is mathematically expressed by

$$p_{tot,c}{}^{s+1} = \left[\frac{\dot{m}_c}{\dot{m}_{c,tmp}^s} \right]^j \; p_{tot,c}{}^s \; . \tag{4.33}$$

Here, $\dot{m}_{c,tmp}^s = \sum_i \rho_i^s \boldsymbol{n_i} \cdot \boldsymbol{u}_{\boldsymbol{D,i}}^s A_i$ is the current total mass flow rate at iteration step 's' determined as the sum over all boundary faces 'i' on Γ_{PM}, and $0 < j < 1$ is an appropriate relaxation parameter or function. Thus, the pressure $p_{tot,c}$ incrementally changes while the induced coolant mass flow rate $\dot{m}_{c,tmp}$ asymptotically approaches the target value $\dot{m}_c$.

System-adiabatic coolant reservoir

As the coolant reservoir is not resolved in the simulation, also the thermal behaviour of the incident flow needs to be modelled by the applied boundary conditions. In general, the coolant flow entering the porous structure and

the solid skeleton may be at different temperatures (LTNE). Therefore, two thermal boundary conditions need to be specified at the coolant side, i.e. one for each of the two energy equations (2.63) and (2.64). For the here-presented investigations, the coolant flow approaches the porous structure in normal direction. The respective thermal situation is depicted qualitatively in figure 2.5. Due to the temperature difference over the sample, heat is transported from hot-gas side Γ_{HG} to coolant-reservoir side Γ_{PM}. Since the porous structure at Γ_{PM} is typically at an elevated temperature when compared to the temperature T_c of the coolant fluid in the plenum, heat is transferred from the porous structure to the incident flow. Considering the inflow process on the microscale, the coolant fluid begins to accelerate in direction of the nearest pore at a distance of several times the pore diameter from the porous inlet surface. This small-scale convective heat transfer adds to the heat conduction within the incident flow [125]. Different authors found that the temperature rise due to preheating is not negligible, e.g. references [35, 120]. In the frame of this thesis, a system-adiabatic approach is followed. It assumes that all heat which is transferred from the backside of the porous structure into the coolant reservoir is absorbed by the inflowing coolant gas. Consequently, no energy effectively leaves the porous structure domain.

The resulting boundary conditions on Γ_{PM} may be expressed by the following heat balances:

$$\rho c_{p,f} \boldsymbol{n} \cdot \boldsymbol{u_D}(T_f - T_c) = \boldsymbol{n} \cdot (\boldsymbol{k_{s,eff}} \nabla T_s) \quad , \tag{4.34}$$

$$h_c(T_s - T_c) = \boldsymbol{n} \cdot (\boldsymbol{k_{s,eff}} \nabla T_s) \quad , \tag{4.35}$$

with the coolant-reservoir temperature T_c, the effective solid thermal conductivity $\boldsymbol{k_{s,eff}} = (1-\varepsilon)\boldsymbol{k_s}$, and the local area-specific heat transfer coefficient h_c.[3] Combining equations (4.34) and (4.35) yields the fluid-phase temperature at Γ_{PM}:

$$T_f = T_c + \mathrm{St}_c(T_s - T_c) \quad , \tag{4.36}$$

with the coolant-side Stanton number

$$\mathrm{St}_c = \frac{h_c}{\rho_f c_{p,f} \boldsymbol{n} \cdot \boldsymbol{u_D}} \quad . \tag{4.37}$$

---

3   The fluid-phase heat conduction within the porous solid has been neglected in equations (4.34) and (4.35). As the thermal conductivity of the solid skeleton is generally much higher than the fluid-phase thermal conductivity, the introduced error is small (e.g. $k_s/k_f \approx 350 \dots 550$ for air and C/C in parallel fibre direction).

The condition for the solid-phase temperature gradient at Γ_{PM} is then obtained from equation (4.34), leaving only T_c and St_c as simulation inputs.

Although the above boundary conditions have been used by various authors, e.g. references [28, 35, 123, 188], the choice of the heat transfer coefficient h_c or the Stanton number St_c is not trivial. The intensity of heat exchange depends on the considered test case as well as the employed porous material. Moreover, a dependency of St_c on the blowing ratio exists as shown by Colladay and Stepka [35]. However, since only little experimental data is available (e.g. references [35, 125]), no generalised expression exists to determine neither h_c nor St_c. Instead, a constant value of St_c is typically used which is determined based on sensitivity studies or simply estimated. Regarding this, the condition $\mathrm{St}_c \leq 1$ (i.e. $h_c \leq \rho_f c_{p,f} \boldsymbol{n} \cdot \boldsymbol{u_D}$) ensures that the coolant temperature upon entering the porous structure does not exceed the corresponding solid-phase temperature, i.e. $T_f \leq T_s$ at Γ_{PM}. The opposed limiting case is expressed by $\mathrm{St}_c = 0$ and represents a situation without any preheating of the coolant, i.e. $T_f = T_c$ at Γ_{PM}.

As an alternative, the boundary conditions may also be formulated using the backside solid-phase temperature $T_b \coloneqq T_s$ at Γ_{PM}. If T_c is provided as a second simulation input, equation (4.34) yields the fluid-phase temperature. An advantage of this set of boundary conditions lies in the fact that T_b can be experimentally determined and is then available as an input to a corresponding simulation case. However, in the predictive use of numerical tools, T_b is typically an unknown to be determined from the simulation results. Moreover, this formulation of boundary conditions may lead to unphysical results depending on the employed set of simulation parameters (e.g. h_v, $\boldsymbol{k_{s,eff}}$, $(\rho_f u_D)$, $c_{p,f}$). Lastly, the temperature measurement at the coolant-side boundary itself is challenging and may thus be flawed by measurement uncertainties, e.g. stem conduction effect [14].

4.4.2 Hot-Gas Side

In the here-presented transpiration-cooling simulations, porous structure and hot-gas domains are interacting and are thus treated in a fully-coupled way. Coolant gas exiting the porous domain, is injected into the main-flow boundary layer. Likewise, the static pressure of both domains is linked at the interface. Naturally, also the thermal coupling at the heat-exchanging porous surface is an important aspect in the simulation of transpiration cooling. Subsequently

to kinematic and thermal coupling, the injection of foreign gas into a main flow of air and the modelling of turbulence for a transpired wall are discussed. For the sake of clarity, the subscript 'hg' is used to denote variables of the hot gas flow, while the subscripts 'f' and 's' represent the coolant fluid and solid variables of the porous domain, respectively.

Kinematic coupling

The coolant mass flow rate is driven by the pressure difference between coolant reservoir and static pressure of the main flow at the transpired surface. Likewise, the boundary-layer injection influences the main flow and the pressure distribution on the porous interface Γ_{HG}. As a consequence, both regions are coupled with respect to pressure and mass flow over the interface. This coupling is realised by an internal exchange of variables in the OpenFOAM solver, see section 4.5.

In experiments and real application cases using porous CMC materials, the coolant is injected into the hot-gas boundary layer via numerous microscopic pore openings when exiting the porous structure. For the numerical simulations, however, an injection model using surface-averaging as illustrated in figure 4.3 was selected. This is in accordance with the employed volume-averaging approach for the porous domain. Instead of resolving the individual coolant jets of the single pore openings, the approach prescribes a locally surface-averaged coolant mass flow rate for each boundary face. The model is denoted as 'continuous blowing model' in the following. In a study on a subsonic turbulent channel flow by Prokein and von Wolfersdorf [152], it has been found to be superior when compared to discrete injection models. The latter reproduced the transpired surface by a series of enlarged holes and wall segments without matching the original pore resolution. A brief summary of this study is given in appendix D.
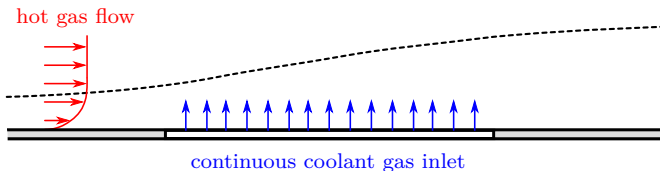
Figure 4.3: Macroscale modelling approach for gas injection through porous walls

The model is applied to all simulation cases including sub- and supersonic main-flow conditions as presented in chapters 6 and 7, respectively. The dominating physical processes are assumed to take place in the thin subsonic layer close to the wall which exists for all viscous flows. Matching cells at the interface in combination with the applied domain coupling ensure that the coolant mass flux exiting the porous domain enters the main-flow domain. This results in the following conditions for pressure and mass flux at the hot-gas boundary Γ_{HG}:

$$p_f := p_{hg} \quad , \tag{4.38}$$

$$\rho_{hg}\boldsymbol{u} := \rho_f \boldsymbol{u_D} \quad , \tag{4.39}$$

with hot gas and Darcy velocities $\boldsymbol{u}$ and $\boldsymbol{u_D}$, respectively.

Thus, not only the patch-normal mass flux is conserved, i.e. $\rho_f \boldsymbol{n} \cdot \boldsymbol{u_D} = \rho_{hg} \boldsymbol{n} \cdot u$, but also possible velocity components in tangential directions. Despite the surface-averaging approach, the resulting injection mass flux is not necessarily uniform over the length and width of the transpired surface. Instead, $\rho\boldsymbol{u}$ may spatially vary as also fluid density ρ_f and local Darcy velocity $\boldsymbol{u_D}$ at the interface are not constant. However, characteristics of the pore distribution such as non–homogeneities on the microscale or structural defects cannot be captured by the continuous blowing model. Moreover, the momentum added to the main flow is reduced when compared to a calculation based on pore velocity which may have an influence on the mixing processes.

Foreign-gas blowing

Transpiration of foreign gases, i.e. other than air, into a main flow of air requires special attention with respect to the porous interface. From a physical point of view, the situation is simple. Coolant gas of a different species exits the porous structure and is injected into the main flow. From the numerical point of view, this would correspond to a mass-flow inlet and should thus be modelled with the condition defined by equation (4.39). However, in the main-flow domain, two species exist which requires the modelling of species diffusion. Thus, an additional boundary condition for the foreign-gas mass fraction Y_1 is to be prescribed at the interface. Moreover, in this case, the foreign-gas species is not only transported into the hot-gas domain through advection but additionally by means of mass diffusion. This is a consequence of the non-uniform mass fraction of foreign gas in the main flow field. It is highest at the porous interface and decreases with wall distance. Thus, the advective mass flux at the porous surface is supplemented by a diffusion mass flux which depends on the

gradient of Y_1 at the wall. The combined mass flux $\dot{m}_c$ is then employed in the calculation of the blowing ratio $F = (\dot{m}_c/A_c)/(\dot{m}_{hg}/A_{hg})$.

In the simulation, two assumptions are made for the porous domain. First, the structure is fully saturated with foreign gas, i.e. no gas mixture is considered within the porous structure. Secondly, no fluid from the main flow enters the porous structure. In contrast to this, the gas in the main-flow domain is treated as a mixture of air and the foreign species as detailed in section 2.1.5. In accordance with this, the species conservation equation is solved, cf. equation (4.7).

As described in section 4.4.2, the coolant mass flux $\dot{m}_i/A_i$ exiting a boundary face 'i' of the porous structure directly enters the hot-gas domain through a matching boundary face. Approaching the interface from the porous-structure side, the mass flux of an individual face 'i' is determined from

$$\left.\frac{\dot{m}_i}{A_i}\right|_{\Gamma_{\mathrm{HG}}-} = \left. Y_1\right|_{\Gamma_{\mathrm{HG}}-}\rho_f \boldsymbol{n}\cdot\boldsymbol{u_D} \quad, \tag{4.40}$$

where Y_1 is the mass fraction of the foreign species, i.e. $Y_1|_{\Gamma_{\mathrm{HG}}-} = 1$ in the porous structure.

Calculating the mass flux from the hot-gas side, the molecular mass diffusion flux $\boldsymbol{j}_1 = \rho D_{12}\nabla Y_1$ adds to the advective mass flux. This results in

$$\left.\frac{\dot{m}_i}{A_i}\right|_{\Gamma_{\mathrm{HG}}+} = \left(\left. Y_1\right|_{\Gamma_{\mathrm{HG}}+}\rho_{hg}\boldsymbol{n}\cdot\boldsymbol{u}\right) + \left(\rho D_{12}\boldsymbol{n}\cdot\nabla Y_1\right) \quad. \tag{4.41}$$

where $Y_1|_{\Gamma_{\mathrm{HG}}+} < 1$ follows from $(\dot{m}_i/A_i)|_{\Gamma_{\mathrm{HG}}-} = (\dot{m}_i/A_i)|_{\Gamma_{\mathrm{HG}}+}$ if $\nabla Y_1 \neq 0$.

A combination of equation (4.39) and a special boundary condition for $Y_1|_{\Gamma_{\mathrm{HG}}+}$ is necessary to inject the correct mass flow rate of the foreign gas into the main flow. Therefore, the so-called Eckert-Schneider boundary condition as described by Schlichting and Gersten [164] is applied to the transpired surface. In line with the introduced definitions, it assumes that the external component, i.e. air (subscript '2'), does not penetrate the porous wall from which the foreign-gas component is transpired. At the interface $\Gamma_{\mathrm{HG}}+$, the diffusion flux of air is defined to be equal in magnitude and opposite in sign to the area-specific mass flow rate of air. This yields a zero net flux over the transpired wall which is expressed by

$$\boldsymbol{n}\cdot\boldsymbol{j}_2 := -\rho_2\boldsymbol{n}\cdot\boldsymbol{u} = -\rho(1-Y_1)\boldsymbol{n}\cdot\boldsymbol{u} \quad, \tag{4.42}$$

where ρ is the density of the gas mixture at the interface of the main-flow domain and $Y_2 = (1 - Y_1)$ is the mass fraction of air.

The diffusion flux of the foreign gas (subscript '1') is obtained from

$$\boldsymbol{n} \cdot \boldsymbol{j}_1 = -\rho D_{12} \boldsymbol{n} \cdot \nabla Y_1 \quad . \tag{4.43}$$

Using the relation $\boldsymbol{n} \cdot \boldsymbol{j}_2 = -\boldsymbol{n} \cdot \boldsymbol{j}_1$, which is valid for a binary mixture, yields the Neumann boundary condition prescribed for the foreign-gas mass fraction:

$$\boldsymbol{n} \cdot \nabla Y_1 = -\frac{1 - Y_1}{D_{12}} \boldsymbol{n} \cdot \boldsymbol{u} \quad . \tag{4.44}$$

Thermal coupling

As for the coolant-side boundary, two thermal coupling conditions are required at the hot-gas side of the porous structure. In the case of transpiration cooling, the convective heat flux $\dot{q}_{hg}^*$ that is effectively transferred from the main flow onto the porous structure is to be distributed between solid and fluid phases, i.e. $\dot{q}_{hg}^* = \dot{q}_s + \dot{q}_f$. With respect to this, several authors proposed various types of coupling conditions, e.g. references [3, 15, 82, 89, 193, 211]. Generally, the approaches can be distinguished based on the weighting used for the distribution of $\dot{q}_{hg}^*$ into fluid-phase heat flux $\dot{q}_f$ and solid-phase heat flux $\dot{q}_s$. Regarding this, the heat-flux ratio is determined either according to the surface ratio, i.e. $\dot{q}_f/\dot{q}_s = \varepsilon/(1-\varepsilon)$, the ratio of thermal conductivities $\dot{q}_f/\dot{q}_s = k_f/k_s$, or a combination of both. For the two first-mentioned conditions, Wang and Shi [193] found unphysical behaviour in their analytical study, i.e. $T_f > T_s$ at Γ_{HG}. Opposed to this, the condition expressed by

$$\frac{\dot{q}_f}{\dot{q}_s} = \frac{\varepsilon k_f}{(1 - \varepsilon)k_s} \quad . \tag{4.45}$$

gave realistic results for all tested conditions. However, due to the large difference between fluid-phase and solid-phase thermal conductivities, i.e. k_f and k_s, the heat flux is mainly transferred to the solid phase. Following this, another possible (and simpler) coupling condition is based on the assumption that the convective heat flux transferred from main flow to porous structure is fully absorbed by the solid phase. This yields the following two conditions on the hot-gas side Γ_{HG} which have been used in the frame of this thesis:

$$\dot{q}_{hg}^* = -\boldsymbol{n} \cdot (\boldsymbol{k}_{s,eff} \nabla T_s) \quad , \tag{4.46}$$

$$0 = -\boldsymbol{n} \cdot (k_f \nabla T_f) \quad . \tag{4.47}$$

Besides the distribution of the main-flow heat flux onto fluid and solid phases of the porous domain, also the temperature of the porous wall at the hot-gas interface demands for further considerations. Based on the LTNE approach, two temperatures from the porous domain, i.e. T_f and T_s, have to be related to a single temperature of the main flow, i.e. T_{hg}. Regarding this, different authors [5, 49, 116] employed the simple condition $T_{hg} = T_s = T_f$ at Γ_{HG}, while others [15, 82, 211] used a surface-averaging approach to determine the main flow temperature at the interface, i.e. $T_{hg} = \varepsilon T_f + (1 - \varepsilon)T_s$. L'Ecuyer and Colladay [115] proposed another model for this situation which has been used in the frame of this thesis. It bases on an infinitesimal transition layer that yields a single averaged temperature T_{layer} for the porous structure domain. Regarding the heat transfer between main flow and porous structure, this temperature then corresponds to the porous wall temperature seen by the hot-gas boundary layer, i.e. $T_{hg} = T_{layer}$ at Γ_{HG}. Accordingly, this temperature is essential in the calculation of the transferred heat flux, i.e. $\dot{q}_{hg} = -\boldsymbol{n} \cdot (k_{hg}\nabla T_{hg})$. The authors introduce an additional parameter for the calculation of T_{layer} which depends on the character of the transition layer. As the choice of this parameter is case-dependent and not trivial, a simplified approach has been used in the present work. It defines the transition-layer temperature to be equal to the solid-phase temperature of the porous domain, i.e. $T_{layer} := T_s$ at Γ_{HG}. Consequently, T_s remains constant in the virtual transition layer, whereas the temperature of the exiting coolant fluid has to increase from T_f up to the solid-phase temperature T_s. This requires a heat flux $\dot{q}_{layer}$ which reduces the convective heat flux $\dot{q}_{hg}$ from main flow to transition layer to the heat flux $\dot{q}_{hg}^* = \dot{q}_s$ that is effectively transferred to the porous structure. By considering this, the transition-layer model satisfies the conservation of energy at the interface Γ_{HG}. The resulting heat-flux balance at the transpired surface is given in the following, while figure 4.4 schematically illustrates the model.

$$\dot{q}_s = \dot{q}_{hg} - \dot{q}_{layer} \quad , \tag{4.48}$$

$$\boldsymbol{n} \cdot (\boldsymbol{k_{s,eff}}\nabla T_s) = \boldsymbol{n} \cdot (k_{hg}\nabla T_{hg}) - \rho_f c_{p,f} \boldsymbol{n} \cdot \boldsymbol{u_D}(T_s - T_f) \quad . \tag{4.49}$$

Besides the discussed thermal aspects, the model also has an influence on the velocity coupling as defined by equation (4.39). Since coolant-fluid temperature T_f and T_{hg} differ while $p_f = p_{hg}$ at Γ_{HG}, also a jump in density occurs in the transition layer. This had to be considered in the numerical implementation of equation (4.39).

Turbulence modelling

As detailed in section 4.2, turbulence in the main flow is modelled by means of the Low-Re formulation of the SST model by Menter. Thus, the turbulent processes are resolved down to the viscous sublayer of the boundary layer. In the simulation setup, a boundary condition needs to be set at all walls. The standard boundary conditions of the κ-ω-model as defined by equations (4.23) and (4.24) are applied for rigid solid walls. Different boundary conditions for transpired porous surfaces have been proposed in literature. Typically, the no-slip condition for the turbulent kinetic energy is applied, i.e. κ = 0. With respect to the specific turbulence dissipation rate ω, three different boundary conditions have been considered in the frame of this thesis and are listed below.

The first approach is to employ the standard boundary conditions for all walls, including the transpired surface. These were specified in section 4.2.3 and are given by

$$\kappa = 0 \quad , \tag{4.23}$$

$$\omega_{F=0} = \frac{6\nu_w}{0.075(\Delta y_1)^2} \quad . \tag{4.24}$$

For surfaces with mass injection (and thus a wall-normal velocity component), Wilcox [204] proposed an alternative boundary condition:

$$\omega_{F>0,std} = \frac{u_\tau^2}{\nu_w} \frac{25}{u_w^+ \left(1 + 5u_w^+\right)} \quad , \tag{4.50}$$
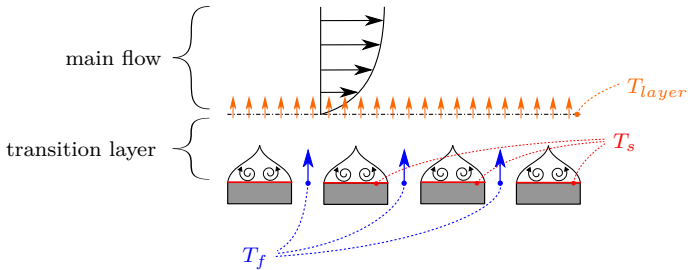
Figure 4.4: Schematic illustration of the transition-layer model at the hot-gas side of the porous interface

where u_τ is the friction velocity and u_w^+ is the reduced wall-normal injection velocity defined by

$$u_w^+ = \frac{u_w}{u_\tau} = \frac{\boldsymbol{n} \cdot \boldsymbol{u_D}}{\sqrt{\tau_w/\rho}} \quad . \tag{4.51}$$

Generally, this relation yields smaller values of the specific turbulence dissipation rate at the wall when compared to equation (4.24). Moreover, the value of ω decreases for more intense boundary-layer blowing, i.e. rising values of u_w^+. Wilcox obtained equation (4.50) through an optimisation of coefficients to match the data of subsonic wind-tunnel experiments by Andersen et al. [6]. The flat porous wall segment used in the experiments was made of sintered bronze material composed of particles with diameters between $17\,\mu m$ and $59\,\mu m$. The material's porosity was around 40% which is rather high when compared to CMC materials used for transpiration cooling applications. In spite of this, the boundary condition has been used in the numerical investigation of a transpiration-cooled C/C wall segment by Dahmen et al. [37].

To consider the influence of smaller porosities (i.e. $\varepsilon < 40\%$), Prokein et al. [151] proposed a slight modification of Wilcox' blowing condition as a third boundary condition. The modified condition is based on the actual injection velocity (or pore velocity) $\boldsymbol{u_{pore}}$ instead of the Darcy velocity $\boldsymbol{u_D}$. Both are connected by the Dupuit-Forchheimer relationship [141] via the open porosity, i.e. $\boldsymbol{u_D} = \varepsilon\,\boldsymbol{u_{pore}}$. Using this relation in combination with the porosity $\varepsilon \approx 40\%$ applicable to the reference experiments by Andersen et al. [6], translates equation (4.50) into the modified blowing condition:

$$\omega_{F>0,mod} = \frac{u_\tau^2}{\nu_w} \frac{62.5\varepsilon}{u_w^+ \left(1 + \frac{2}{\varepsilon}u_w^+\right)} \quad . \tag{4.52}$$

The modified condition is based on the assumption that the enhanced mixing processes at a transpired wall rather depend on the pore velocity $\boldsymbol{u_{pore}}$ than the surface-averaged Darcy velocity $\boldsymbol{u_D}$. Elevated coolant jet velocities on the microscale, i.e. $\boldsymbol{u_{pore}}$, increase the occurring shear forces and trigger an enhanced transport of momentum and heat close to the wall. Regarding this, the porosity ε scales the velocity for a given mass flux (or Darcy velocity), resulting in a higher magnitude of $\boldsymbol{u_{pore}}$ for small porosities. As a consequence, the modified boundary condition yields decreased values of ω at the transpired wall for low-porosity materials. This results in a reduced dissipation of turbulent kinetic energy κ in the near-wall region which leads to enhanced turbulent transport. The new formulation is consistent with Wilcox' original formulation, since equation (4.52) reduces to equation (4.50) for a porosity of $\varepsilon = 40\%$.

4.5 OpenFOAM Solver Development

All numerical simulations presented in the frame of this thesis have been performed with a new CFD solver which has been specifically developed to model complex transpiration-cooling processes. The C++ library OpenFOAM (Open Field Operation and Manipulation) was selected as the basic numerical environment [88, 198]. The software package contains various applications such as CFD solvers and other utilities. OpenFOAM is distributed under the GNU general public license (GPL) and thus, the complete source code is openly accessible. This allows modifications and extensions of the available solvers' capabilities and was an important factor in the decision to use the open-source toolbox. Additionally, the modular design allows to easily add new libraries which can then be loaded and used by various solvers. Since OpenFOAM is free of any licensing costs, highly-parallelised simulations can be performed at the net costs of processor-usage time only.

In line with OpenFOAM nomenclature conventions, the new solver is referred to as *speciesTranspirationFOAM* or short *spectraFOAM*. It has been designed for the simulation of transpiration-cooling processes for arbitrary geometries under sub- and supersonic flow conditions. Further key features are the consideration of local thermal non-equilibrium, multi-dimensional coolant-flow situations, anisotropic material properties, and foreign-gas injection. The solver follows an integral approach and models the complete simulation domain which may include the external main flow, volume-averaged porous structures, and solid regions. The code is organised in two separate parts, one that deals with the main-flow domain and another for all other domains (i.e. porous or solid). Switches are used in the numerical setup to enable or disable the various domains as well as different functionalities of the solver, e.g. the consideration of species diffusion. The numerical development is based on OpenFOAM release 2.3.x and builds upon existing solvers as detailed in the following.

Main flow

The main flow or external flow solver part is based on the compressible solver *pisoCentralFOAM* by Kraposhin et al. [101] which uses a hybrid scheme combining PISO/SIMPLE method [51, 87, 147] and Kurganov–Tadmor's (KT) scheme [105]. Through a blending function depending on the local Mach and acoustic CFL number[4], the solver automatically adapts the applied flux discretisation method. With respect to this, the discretisation method strives towards KT scheme (or more specifically to the version by Kurganov-Noelle-

Petrova (KNP) [106]) with increasing influence of compressibility, whereas it behaves similarly to the standard PISO/SIMPLE method for flows in the low Mach-number regime. The scheme can thus be used for both incompressible and compressible flow regime and was validated for a wide range of Mach numbers, i.e. $0.001 \leq M \leq 3$. This corresponds well to the Mach number regime investigated in the frame of the here-presented thesis. More information on the implementation of the hybrid scheme as well as the validation work of *pisoCentralFOAM* is given in references [101, 102]. For the modelling of transpiration cooling, several modifications and supplements were introduced to the solver apart from the coupling conditions at the porous interface. These include additional thermodynamic libraries for the modelling of gas mixtures as well as modifications with respect to species transport. Regarding the first mentioned, mixing laws for viscosity and thermal conductivity as described in section 2.1.5 are provided by means of an OpenFOAM library. An additional governing equation accounts for species transport in the main flow, see equation (4.7). With respect to this, also the Fuller-Schettler-Giddings relation as given by equation (2.24) was added to the solver. Moreover, an additional term is considered in the solver's enthalpy equation to account for energy transport due to species diffusion. These adaptations as detailed by equations (4.8) and (4.13) have been implemented in the new solver.

Porous and solid regions

The second part of the solver deals with the porous-medium processes and was developed on the basis of the standard solver *chtMultiRegionFOAM*. It supports multi-region treatment for arbitrary numbers of porous and non-porous wall segments, and thus enables the simulation of conjugate heat transfer cases. Depending on the considered problem either the transient or steady-state governing equations are solved by means of the PISO/SIMPLE or SIMPLE methods, respectively. Several adaptations with respect to porous-structure modelling have been implemented. A volume-averaging approach as outlined in section 2.4.1 is employed. To consider LTNE situations (i.e. $T_f \neq T_s$), the porous wall domains are represented by overlapping fluid and solid regions with coupled energy equations. Internal heat transfer between solid skeleton and coolant can be modelled either by using a constant volumetric heat transfer coefficient h_v or heat transfer correlations in dependence of local flow properties.

---

4   The acoustic CFL number is defined by $\text{CFL}_{acoustic} = \frac{(|u|+c_s)\Delta t}{\Delta x}$ where Δx represents the grid spacing and c_s is the local speed of sound. The convective CFL number, i.e. $\text{CFL} = \frac{|u|\Delta t}{\Delta x}$ is related to the numerical stability of explicit time discretisation schemes where the condition $\text{CFL} < 1$ must be satisfied.

Pressure loss for coolant through flow is considered by means of the multi-dimensional Darcy-Forchheimer model as given by equation (2.62). Moreover, the solver takes into account anisotropic material properties with respect to through-flow permeability and heat conduction.

Domain coupling

Kinematic and thermal coupling of both solver parts is performed internally by an exchange of variables at the porous interface. The coolant mass flux vector $\rho \boldsymbol{u_D}$ is transferred from the porous region to the main-flow domain, while the static wall pressure p_{hg} from the external flow field is an input to the porous domain. Thermal coupling is based on the flux forward temperature back method, see for example Verdicchio et al. [187]. Consequently, the interface temperature T_s is provided by the porous domain as a coupling condition for the main flow, whereas the convective heat flux $\dot{q}_{hg}$ from the hot gas flow is transferred in opposite direction. For the here-presented simulations, the grids of coupled domains feature matching cells at the interface which avoids data interpolation. Figure 4.5 depicts a schematic illustration of the coupling between a main-flow region and a porous region, consisting of fluid and solid phases. The solver allows different modes of domain coupling ranging from full to loose coupling at a specified frequency.
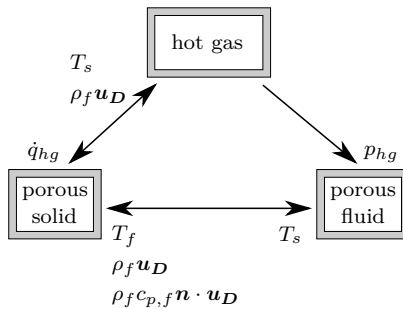
Figure 4.5: Coupling scheme between main-flow domain and porous domain

Local time stepping approach

The main-flow-solver part of *spectraFOAM* uses a transient formulation by design. For stability reasons, the hybrid algorithm is bound by the Courant-Friedrichs-Lewy (CFL) stability criterion based on the local flow velocity [51, 102]:

$$\text{CFL} = \frac{|\boldsymbol{u}|\Delta t}{\Delta x} < 1 \quad , \tag{4.53}$$

where Δt is the time discretisation increment and Δx represents the grid spacing. As a consequence of the high flow velocities in supersonic problems, small values of Δt are required. Additionally, the time scales to reach steady-state conditions in a heat transfer problem are considerably different for main flow and porous structure. Just as for a rigid solid, it requires several seconds to minutes until the temperature distribution within a porous structure is fully established. In contrast, the supersonic flow generally develops a steady-state within fractions of a second. Therefore, large computational run times are required for transient transpiration-cooling test cases. However, when the focus is only on the steady-state solution, a non-uniform (and non-physical) time step may be introduced for the different regions. This results in a local time-stepping (LTS) approach as suggested by Osher and Sanders [144]. The local time step is then determined from the local flow velocity and the parameter $C_{max} < 1$:

$$\Delta t(x) \leq \frac{\Delta x}{|u(x)|} C_{max} \quad . \tag{4.54}$$

Obviously, the time uniformity and temporal accuracy is lost by employing locally varying time steps. Anyhow, if only the steady-state solution is desired, the numerical simulation converges towards this final state considerably faster, see for example Dröske [45]. Moreover, the main-flow region which is solved using the LTS approach can also be coupled to a steady-state simulation of the porous structure. This further reduces the computational costs for conjugate simulations. For all coupled transpiration-cooling simulations presented in chapter 7, the here-described LTS approach has been employed. Subsequent to the calculation of a cell-individual time step $\Delta t(x)$, a damping function as well as a spatial smoothing are applied to the variable. Both limit the change in Δt between iterations and reduce spatial gradients of the local time step which may lead to numerical instabilities.

Porous Structure - Through Flow and Internal Heat Exchange

Having both numerical and experimental setups introduced, now the obtained results and the solver validation are presented. This chapter focuses on the physical processes taking place within a transpiration-cooled porous structure. At the same time, the corresponding numerical models and their applicability to C/C are investigated and validated. First, the internal heat exchange between coolant fluid and the solid skeleton of a porous structure is addressed. Secondly, the through-flow behaviour of porous C/C structures for unidirectional and multi-dimensional coolant flows is discussed. Besides air, other coolant gases are used to explore the influence of fluid properties on internal heat transfer and through-flow resistance. While the internal heat transfer investigation is only theoretical, a combined numerical and experimental approach is employed with respect to the through-flow behaviour. This allows a more thorough analysis and simultaneously validates the applied models.

5.1 Internal Heat Exchange

One of the effect mechanisms of transpiration cooling bases on the internal heat exchange taking place whenever a fluid at a lower temperature flows through a heated porous structure. Regarding this, the intensity of heat exchange is governed by the temperature difference $T_s - T_f$, the internal surface a_{sf} in contact with the coolant, and the state of the thermal boundary layer modelled

by the local heat transfer coefficient h. For a rigid porous structure, the heat-exchanging surface per volume a_{sf} is a constant material property, just like the porosity. Opposed to this, the heat transfer coefficient h may be variable as it depends on the local flow situation as well as local fluid properties. In volume-averaged simulations of porous structures, the two variables are typically combined into the volumetric heat transfer coefficient $h_v = a_{sf}h$. Several authors deduced correlations for the determination of h_v for various porous materials, as discussed in section 2.4.3. However, little work is concerned with CMC materials or similar, see for example Florio et al. [54]. No relation for the here-considered porous material C/C exists to date. Geometrical estimations for the internal (heat-exchanging) surface per volume of the porous material yield values between $10^4 \, \mathrm{m^2/m^3}$ and $10^5 \, \mathrm{m^2/m^3}$ [68, 165]. This suggests large values for h_v between $10^4 \, \mathrm{W/(m^3K)}$ and $10^7 \, \mathrm{W/(m^3K)}$. Due to the lack of available data for C/C, the simplified assumption of a constant h_v-value for all mass flows and coolants and for the complete porous domain has been employed in previous studies using the material, see references [37, 165]. Albeit a simplification, this assumption is also used in the frame of this thesis.[1]

5.1.1 Evaluation of Analytical LTNE Criterion

In this section, the suitability of the LTE assumption is discussed for the test cases investigated in chapter 7. For this, an analytical relation from literature is employed to estimate the modelling error if only a single energy equation is considered for both solid and fluid phases.

Several parameters have a decisive influence on the thermal situation within a porous structure and more specifically the question if a significant temperature difference between solid phase and fluid phase occurs (LTNE) or if both phases are at equal temperature (LTE). Besides the volumetric heat transfer coefficient h_v, also the coolant flow situation, i.e. fluid properties and mass flow rate, as well as porous structure properties are important with respect to this. The criterion by Wang and Wang [192] as defined in equation (2.65) gives a first estimation if LTNE occurs for a certain test case or not. The authors define that the influence of LTNE is non-negligible if the relative difference between hot-gas-side temperatures for LTE and LTNE modelling exceeds 5%. As suggested by their analytical relation, the prediction strongly depends on h_v (which is assumed as constant over the porous sample), the specific heat capacity of the coolant $c_{p,c}$, the solid-phase thermal conductivity $k_{s,eff}$, and the coolant mass

---

1 However, the developed OpenFOAM solver also allows to employ internal heat transfer correlations, if available. In this case, a local h_v is computed for each cell of the simulation domain in dependence of the local values for Re and Pr.

flow rate $\dot{m}_c$ (or blowing ratio F). Additionally, a weak dependency on the run length L exists which is neglected in the following analysis. The contour plot given in figure 5.1 illustrates the h_v-F-parameter range for which the criterion indicates a significant influence of LTNE for the here-investigated test setup and C/C material ($\dot{m}_{hg}/A_{hg} = 307.9 \, \text{kg}/(\text{m}^2\text{s})$, $A_c = 0.00209 \, \text{m}^2$). Regarding this, the areas below the coolant-specific curves represent the parameter range connected to LTNE, whereas areas above the curves correspond to LTE.

It can be noted that the criterion applied to the here-investigated test cases predicts LTNE situations already at moderate blowing ratios. Examining the curve for air as coolant, equilibrium between solid-phase temperature and fluid-phase temperature (LTE) can only be assumed for volumetric heat transfer coefficients higher than $10^7 \, \text{W}/(\text{m}^3\text{K})$ for the highest blowing ratio tested, i.e. $F_{Air} = 1.0\%$. Due to the specific heat capacities of the coolants, LTE requires even higher h_v-values at a given blowing ratio for helium, while lower values are sufficient for CO_2 and argon. Since the value of h_v is estimated to be between $10^4 \, \text{W}/(\text{m}^3\text{K})$ and $10^7 \, \text{W}/(\text{m}^3\text{K})$ for C/C, this suggests that the occurrence of LTNE might be important in the test cases discussed in chapter 7. Thus, the consideration of separate energy equations for fluid phase and solid phase of the porous medium is an essential aspect of the corresponding numerical simulations. Furthermore, although being computationally more challenging, the consideration of both energy equations provides additional flexibility with
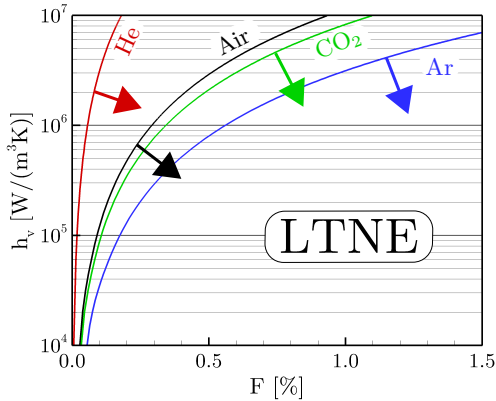
Figure 5.1: Diagram illustrating h_v-F-parameter range for which analytical criterion predicts a significant influence of LTNE (arrows point towards LTNE region)

respect to future application cases of the solver (e.g. higher blowing ratios or coolant gases with high specific heat capacity such as hydrogen).

5.1.2 Solver Validation

In a next step, the numerical implementation of separate energy equations for fluid phase and solid phase and their coupling by means of internal heat transfer is validated. For doing so, the OpenFOAM solver results are compared to a steady-state analytical solution as described in references [123, 188] and given in appendix F. The analytical solution introduces several simplifications to the problem such as incompressibility, constant thermal properties, and negligence of heat conduction within the porous-fluid phase. Consequently, the OpenFOAM solver settings were adapted accordingly to allow for a meaningful comparison. For the validation case, a one-dimensional full porous computational domain of the length $L = 0.01\,\mathrm{m}$ is employed. A system-adiabatic boundary condition according to equations (4.34) and (4.35) is prescribed on the coolant side, while a heat flux on the solid phase is specified at the

$$k_{s,eff}\frac{dT_s}{dx}\Big|_{\Gamma_{\mathrm{PM}}} = h_c\left(T_{s,\Gamma_{\mathrm{PM}}} - T_c\right) \quad k_{s,eff}\frac{dT_s}{dx}\Big|_{\Gamma_{\mathrm{HG}}} = \dot{q}_0$$

$$\rho_f u_D c_{p,f}\left(T_{f,in} - T_c\right) = k_{s,eff}\frac{dT_s}{dx}\Big|_{\Gamma_{\mathrm{PM}}}$$

Table 5.1: Simulation parameters

L	$0.01\,\mathrm{m}$
ε	15%
$\dot{m}_c/A_c$	$0.5\,\mathrm{kg/(m^2 s)}$
$\dot{q}_0$	$100\,\mathrm{kW/m^2}$
$k_{s,eff}$	$1.4\,\mathrm{W/(mK)}$
h_v	$10^5\,\mathrm{W/(m^3 K)}$
ρ_f	$1.18\,\mathrm{kg/m^3}$
$c_{p,f}$	$1004\,\mathrm{J/(kgK)}$
T_c	$300\,\mathrm{K}$
h_c	$10\,\mathrm{W/(m^2 K)}$
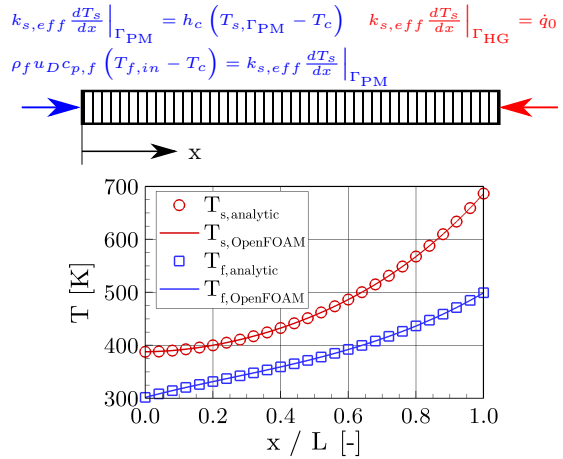
Figure 5.2: Validation test case for internal heat transfer - boundary conditions and simulation results

heated side. Following the results from the previously discussed criterion by Wang and Wang [192], a moderate value of $h_v = 10^5\,\text{W}/(\text{m}^3\text{K})$ is selected for the validation case to ensure the occurrence of LTNE. Further simulation parameters are selected exemplarily as given in table 5.1. Figure 5.2 depicts the analytical (symbols) and numerical (lines) temperature distributions over the sample thickness. An excellent agreement is found between both results which confirms the correct implementation of the LTNE model.

5.2 Unidirectional Flow through Porous Media

The following section details the experimental determination of permeability coefficients based on the Darcy-Forchheimer model. The influence of coolant gases as well as the pressure and mass flux ranges employed for the determination are briefly discussed. Additionally, simulations of the through-flow experiments using the determined permeability coefficients verify the correct implementation of the one-dimensional Darcy-Forchheimer equation in OpenFOAM. Finally, the influence of the coolant gas temperature on through-flow pressure loss is investigated.

5.2.1 Experimental Determination of Permeability Coefficients

Theoretical models for the calculation of permeability coefficients such as proposed by Ergun [50] are not applicable to most CMC materials. As this is also the case for the here-employed material C/C, the coefficients need to be determined experimentally. For doing so, the assembly of coolant plenum and porous sample is used, see figure 5.3. Since only coolant through flow and no main flow is considered, the tests are performed outside of the flow channel.[2] In the test series, the coolant mass flow rate is stepwise increased by means of a thermal mass-flow controller. Simultaneously, static pressure is recorded inside the coolant reservoir p_{in} and for ambient conditions at the outlet $p_{ex} \approx 96.4\,\text{kPa}$. Additionally, the coolant temperature is determined as the average of two measurements within the coolant reservoir. A nearly constant value is recorded during the tests, i.e. $T_f \approx 290\,\text{K}$. Internal thermocouples spread over the sample thickness confirm the isothermal situation of the porous sample. All measurements are taken at steady-state conditions. More details on sensor types and uncertainties are given in section 3.3 and appendix A.

---

2   Identical results are obtained in the fully assembled test channel without main flow, as demonstrated for exemplary blowing ratios. However, testing outside the channel facilitates accessibility and has thus been favoured for the through-flow experiments.
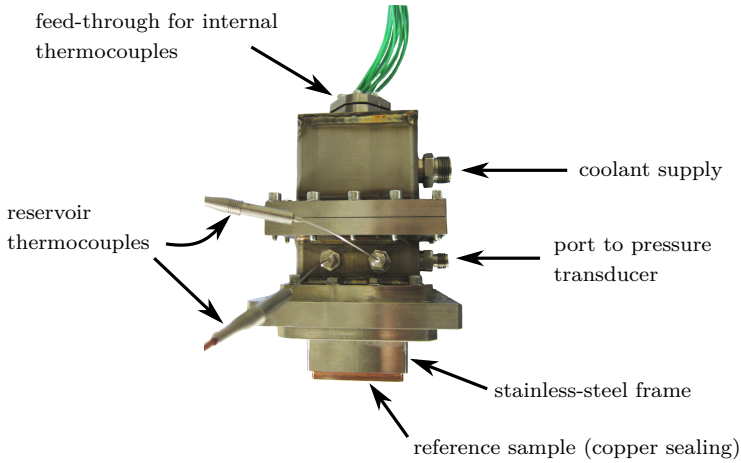
Figure 5.3: Experimental setup for determination of permeability coefficients

Due to the fibre character of the here-investigated C/C, the material's permeability is anisotropic. Consequently, the through-flow resistance differs based on the angle between flow direction and fibre orientation. The following discussion and the here-described determination of permeability coefficients consider only parallel through flow. This is in line with the supersonic transpiration-cooling experiments presented in chapter 7 where the coolant flow is mainly in the parallel-parallel fibre plane.

Figure 5.4 presents the measured through-flow data for the coolant gases air, helium, argon, carbon dioxide (CO_2), and nitrogen (N_2). The pressure loss over the sample (thickness $L = 15\,\text{mm}$) is plotted against mass flux using the form introduced by equation (2.57), i.e. $(\Delta p/L)^* = \left(p_{in}^2 - p_{ex}^2\right)/(2p_{ex}L)$. Error bars resulting from a standard uncertainty analysis [16, 140] are added to the diagram, see also appendix A. The diagram illustrates an increase of pressure loss for rising coolant mass fluxes which strongly depends on the coolant gas properties. The measurements for helium show a significant higher pressure loss for a certain $\dot{m}_c/A_c$ when compared to the other gases. Carbon dioxide exhibits the lowest pressure losses with respect to this. When examining the curves, at first, a linear increase of pressure loss with rising mass flow rate (Darcy regime) is found. At higher mass fluxes, this shifts to a quadratic behaviour (Forchheimer regime).
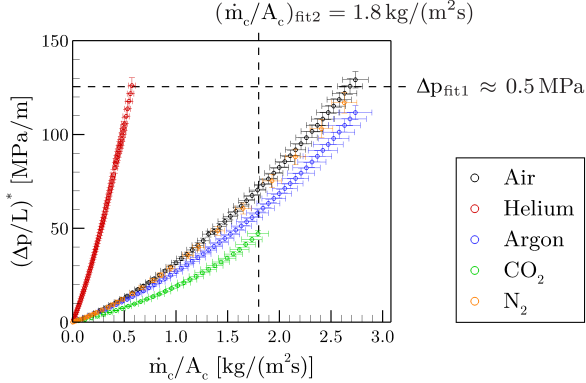
Figure 5.4: Experimental data for normalised pressure loss over air mass flux for through flow parallel to fibre orientation

Based on the experimental data, the permeability coefficients can be determined by a curve-fitting procedure which is based on the Darcy-Forchheimer model:

$$\frac{p_{in}^2 - p_{ex}^2}{2LRT} = \frac{\mu_f}{K_D} \left(\frac{\dot{m}_c}{A_c} \right) + \frac{1}{K_F} \left(\frac{\dot{m}_c}{A_c} \right)^2 \quad . \tag{2.58}$$

This yields a pair of permeability coefficients K_D and K_F for each of the coolant gases included in figure 5.4. Two different fitting ranges were selected for the permeability determination. First, the measured values were evaluated up to a maximum pressure difference of $\Delta p_{fit1} \approx 0.5\,\mathrm{MPa}$. Secondly, the fitting range was confined by a maximum coolant mass flux of $(\dot{m}_c/A_c)_{fit2} = 1.8\,\mathrm{kg/(m^2s)}$. The fitting algorithm takes into account the measurement results, when averaged values are used also the deviation from the average. Additionally, the uncertainties of the employed sensors are considered for the uncertainty calculations. The determination of permeability coefficients is therefore not only based on the mean values, but also takes into account the normal distribution of the measured values contained in the Darcy-Forchheimer equation [167]. The uncertainty in the permeability coefficients is then calculated from a Monte Carlo method as described in reference [17]. Figure 5.5 gives the resulting permeability coefficients including uncertainties.

The determined values for parallel through-flow direction show a fair agreement for the coolant gases N_2, air, argon, and CO_2. This suggests that K_D and K_F are independent of the coolant gas properties in the here-tested range.

(a) Darcy coefficient   (b) Forchheimer coefficient
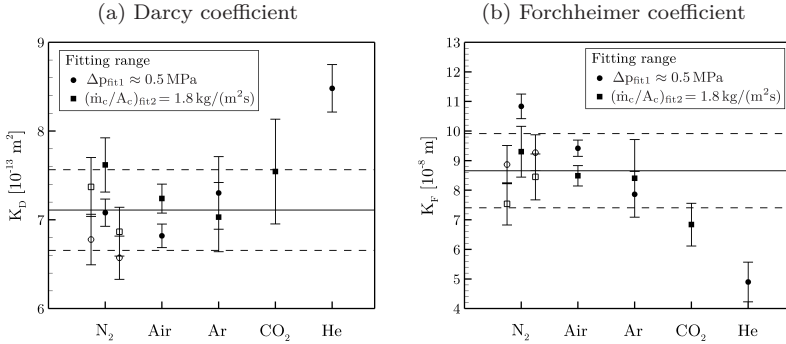
Figure 5.5: Darcy-Forchheimer permeability coefficients for C/C using various coolants and two fitting ranges

Opposed to this, the coefficients determined from the helium measurements show slightly higher deviations which are discussed later. In addition to this, the curve-fitting technique is found to yield similar values of K_D and K_F for both fitting ranges, i.e. Δp_{fit1} and $(\dot{m}_c/A_c)_{\text{fit2}}$. Two additional data points for nitrogen (hollow symbols) are included in figure 5.5 which correspond to earlier measurements before (depicted left of N_2 reference value) and after (depicted right) instrumentation of the sample with thermocouples. The two measurements compare well to the reference data point which is plotted centrally and was taken after exposure to hot-gas channel flow (like the data points for all other gases). The good agreement of all values indicates that neither deterioration nor the instrumentation with thermocouples or the exposure to hot gas flow changed the permeability of the employed C/C material significantly. Leaving the helium coefficients out, the combined mean value of all fits yields $K_{D,\parallel} = (7.11 \pm 0.45) \cdot 10^{-13}\,\text{m}^2$ and $K_{F,\parallel} = (8.66 \pm 1.25) \cdot 10^{-8}\,\text{m}$ as given by solid and dashed lines in the figures.

The deviation for helium may be explained by the prevailing flow regime within the porous structure. With respect to this, the ratio between form drag (Forchheimer) and viscous drag (Darcy) indicates the transition from linear to quadratic flow regime, see also section 2.4.2. The mean values of $K_{D,\parallel}$ and $K_{F,\parallel}$ are used in combination with the maximum mass fluxes $(\dot{m}_c/A_c)_{\text{max}}$ to evaluate the flow regime for the here-described determination of permeability coefficients:

$$C_{FD}^* = \frac{(\Delta p/L)_{Forchheimer}^*}{(\Delta p/L)_{Darcy}^*} = \begin{cases} 1.09 \pm 0.11 & N_2,\,\text{Air},\,\text{Ar},\,CO_2 \\ 0.23 & \text{He} \end{cases} \quad . \quad (5.1)$$

For the gases N_2, air, argon, and CO_2, the equation yields similar C_{FD}^* values which indicates that Forchheimer and Darcy drag contributions are of comparable magnitude for the applied mass fluxes $(\dot{m}_c/A_c)_{\max}$. Opposed to this, the helium value for C_{FD}^* is considerably less because of the low helium mass flux induced by the maximum pressure difference $\Delta p_{\mathrm{fit1}} \approx 0.5\,\mathrm{MPa}$. This suggests that the pressure loss is almost entirely due to viscous drag considered by the linear Darcy term. Therefore, curve-fitting on the basis of the Darcy-Forchheimer equation is not appropriate for the here-presented helium measurements.[3] Consequently, the observed deviation for helium is due to the deviating flow regime. With respect to this, it has to be noted that also the measurements for the other tested gases do not reach the flow regime where the Forchheimer term completely dominates and the Darcy contribution becomes negligible. To carry out such measurements, significantly higher coolant mass flow rates would be required. However, this would also lead to considerably higher pressure differences over the porous sample and thus increase the demands on the test equipment.

An overview of the permeability coefficients K_D and K_F is given in table 5.2. In addition to the determined coefficients $K_{D,\parallel}$ and $K_{F,\parallel}$ in parallel through-flow direction, also the values $K_{D,\perp}$ and $K_{F,\perp}$ for the perpendicular fibre orientation are specified. These have been measured and provided by DLR Stuttgart. Comparing perpendicular and parallel through-flow directions, the permeability coefficients $K_{D,\perp}$ and $K_{F,\perp}$ are lower by a factor of 9 and 15, respectively.

Table 5.2: Permeability coefficients of C/C

Coolant flow orientation	K_D	K_F
parallel	$(7.11 \pm 0.45) \cdot 10^{-13}\,\mathrm{m}^2$	$(8.66 \pm 1.25) \cdot 10^{-8}\,\mathrm{m}$
perpendicular	$(7.81 \pm 0.78) \cdot 10^{-14}\,\mathrm{m}^2$	$(5.86 \pm 0.55) \cdot 10^{-9}\,\mathrm{m}$

5.2.2 Solver Validation

To verify the correct implementation of the one-dimensional Darcy-Forchheimer equation in the OpenFOAM solver, numerical simulations of the previously discussed parallel through-flow experiments were performed. The validation includes the coolant gases air, helium, argon, and CO_2. Each coolant gas and

---

[3] Performing a curve fitting for the helium measurements based on the Darcy equation, i.e. neglecting the quadratic term in equation (2.58), yields a Darcy coefficient of $K_{D,He,\parallel} \approx 6.22 \cdot 10^{-13}\,\mathrm{m}^2$ which is closer to the determined mean value.

applied mass flux correspond to an individual simulation case. All simulations use the permeability coefficients $K_{D,\parallel}$ and $K_{F,\parallel}$ given in table 5.2. A two-dimensional mesh with 15 000 cells and mesh grading towards all boundaries numerically reproduces the reference sample employed for the through-flow experiments. The mesh consists of a single cell layer of the three-dimensional mesh employed for the supersonic simulations discussed in section 7.3. The applied boundary conditions and the grid are illustrated in figure 5.6. Walls are modelled by means of no-slip and adiabatic conditions. The coolant mass flow rate is induced by the modified total pressure boundary condition defined by equation (4.33). The air enters the porous structure at the measured coolant-fluid temperature, i.e. $T_f \approx 290\,\text{K}$, and is exhausted into ambience ($p_{ex} = 96.4\,\text{kPa}$).

$$p_{ex}$$

$$\boldsymbol{u_D} = 0 \qquad\qquad\qquad\qquad \boldsymbol{u_D} = 0$$
$$\nabla T = 0 \qquad\qquad\qquad\qquad \nabla T = 0$$

$$p_{tot,res} = f(\dot{m}_c),\ T_f$$
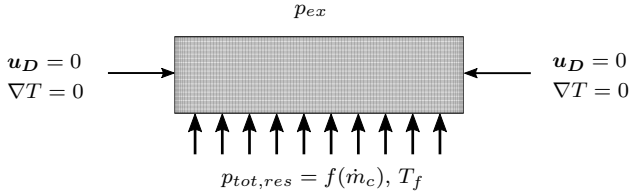
Figure 5.6: Numerical mesh and applied boundary condition for unidirectional coolant flow investigation

Figure 5.7 compares the numerical results to the experimental data. To estimate the influence of the coefficients' uncertainties, additional simulations were performed with minimum and maximum permeabilities resulting from subtracting or adding the specified standard deviations σ_{K_D} and σ_{K_F}, respectively. This adds the areas highlighted in colour to the diagram.

5.2.3 Influence of Coolant Temperature

In the previous analysis, the permeability coefficients K_D and K_F have been found to be independent of the coolant properties in the measured range. However, the pressure loss occurring for the different gases at a certain mass flux varies considerably. This is due to the fluid-dependent properties contained in the Darcy-Forchheimer equation, i.e. viscosity μ_f and density ρ_f. Both properties additionally vary with coolant temperature. For rising temperature
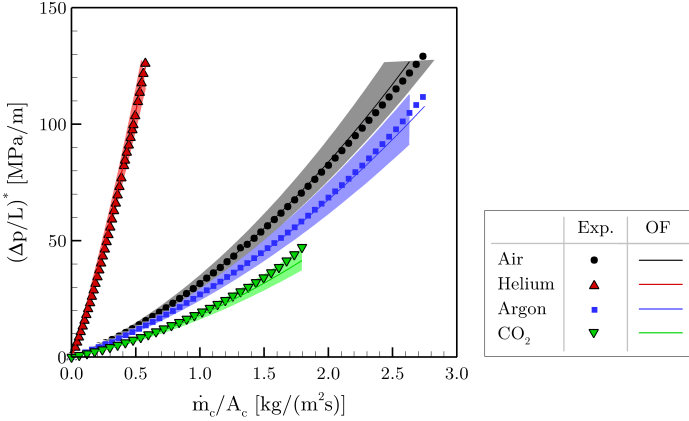
Figure 5.7: Simulation results for normalised pressure drop over mass flux for various gases using the averaged permeability coefficients

levels, μ_f increases while ρ_f decreases. Assuming constant permeability coefficients in the Darcy-Forchheimer equation, both effects should result in an increase of pressure loss for a given mass flux $\dot{m}_c/A_c$. To investigate this effect and for further validation of the OpenFOAM solver's modelling capabilities, the through-flow resistance for heated test cases is addressed in the following. The respective data originates from the supersonic transpiration-cooling experiments and the corresponding numerical simulations presented in chapter 7. However, the analysis given here is concerned with the pressure loss over the sample only, while all cooling related questions are discussed later. In line with the results of the analysis on the LTNE criterion by Wang and Wang [192], a variation of the volumetric heat transfer coefficient h_v between 10^5 W/(m³K) and 10^7 W/(m³K) has been performed in the simulations. As the influence on pressure loss has been found to be small, a value of $h_v = 10^6$ W/(m³K) was selected for the here-presented analysis.

With respect to the previously discussed through-flow tests at cold conditions, i.e. $T_f \approx 290$ K, two variations are introduced: First, the heated test cases exhibit higher coolant-fluid temperatures (due to internal heat transfer) and secondly, the static pressure at the outlet p_{ex} reduces from 96.4 kPa to around 30 kPa. The latter effect is due to the supersonic test conditions in the channel-flow experiments, see chapter 7. As the gas density varies with pressure, an influence is expected. To separate the effects, numerical simulations for all three conditions have been performed. The simulation results thus comprise

data sets for cold conditions and $p_{ex} \approx 96.4$ kPa, and data sets for both cold and heated conditions for $p_{ex} \approx 30$ kPa. In contrast, experimental data is only available for two test conditions, i.e. cold conditions for $p_{ex} = 96.4$ kPa and heated conditions for $p_{ex} \approx 30$ kPa.

The two influences on through-flow pressure loss are considered separately in the following analysis. Before examining the results, it has to be noted that the normalised pressure loss $(\Delta p / L)^* = \left(p_{in}^2 - p_{ex}^2\right) / (2 p_{ex} L)$ chosen for the here-presented result diagrams is sensitive to the outlet pressure p_{ex}. A significant influence on the displayed results is therefore expected. In contrast to this shortcoming, the chosen way of illustration allows to easily determine the inlet pressure for a given mass flux/blowing ratio while representing the mixed linear-quadratic behaviour of the Darcy-Forchheimer equation.

Figure 5.8 depicts numerical and experimental data of the pressure loss $(\Delta p / L)^*$ over mass flux $\dot{m}_c / A_c$ for the different test conditions and the coolants air, helium, argon, and CO_2. Additionally, the blowing ratio is included on the second abscissa to provide a better link to the transpiration-cooling test cases presented in chapter 7.

Regarding the influence of the outlet pressure, a significant increase of $(\Delta p / L)^*$ at a given $\dot{m}_c / A_c$ is found (compare dash-dotted and solid lines). As discussed before, this is partly due to the chosen visualisation and the influence of p_{ex} which scales the normalised pressure loss. Adding to this effect, the generally lower fluid density levels, i.e. $\rho_f = p_f / (RT_f)$, yield higher through-flow velocities u_D and thus increased pressure losses. With respect to the heated test cases, the observed pressure loss for a given mass flux increases further (compare dashed and dash-dotted lines). The additional pressure loss is solely due to the elevated fluid temperature levels during the coolant's flow through the porous structure. In the chosen visualisation, the effect of coolant temperature appears smaller when compared to the influence of the outlet pressure. However, it reveals to be of similar magnitude, if absolute pressure differences are examined, i.e. $\Delta p = p_{in} - p_{ex}$. Good agreement between numerical simulation and experimental results is found for the heated test cases using air, argon, and CO_2 as coolants. For the helium test cases at elevated temperatures, the agreement is less (see also discussion on flow regime in section 5.2.1).

The generally good agreement between simulation and experiment confirms the applicability of the Darcy-Forchheimer model also for the heated test cases. Moreover, the results indicate that the permeability coefficients are independent of fluid temperature and pressure level. This is an important finding which allows to use a single set of K_D-K_F-coefficients for all subsequent simulations. With respect to the numerical validation of porous through flow,

the OpenFOAM solver is able to reproduce the combined effects of increased fluid temperature and reduced outlet pressure.[4]
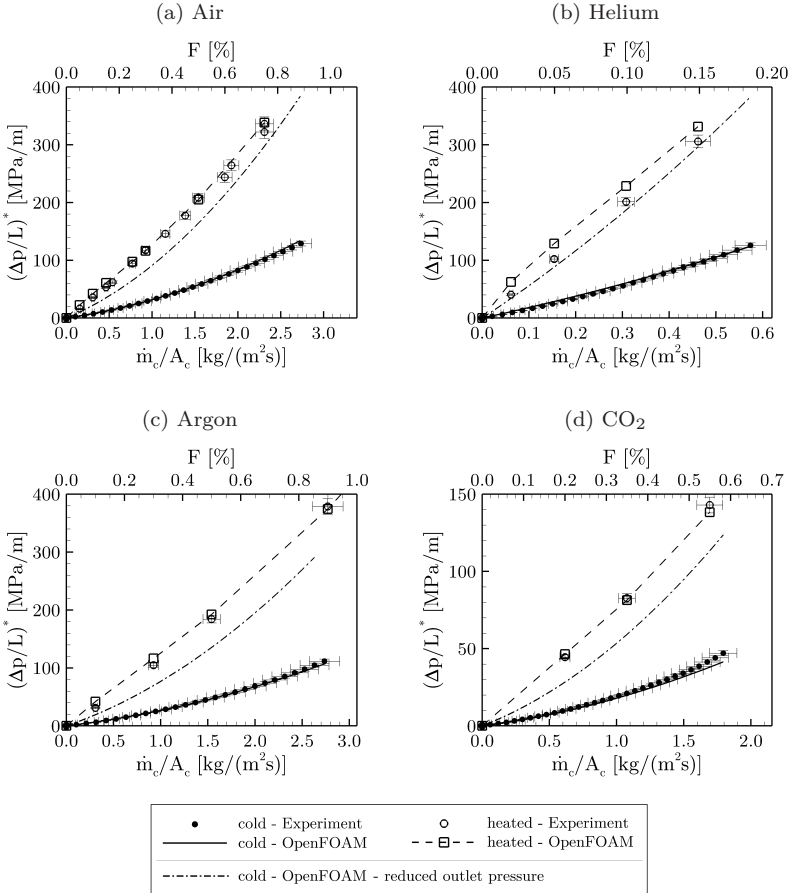
Figure 5.8: Normalised pressure loss over coolant mass flux/blowing ratio

---

4   Additionally, the comparison of experiment and simulation gives a first indication that the temperature of the porous sample (and the internal heat transfer) is generally well captured by the simulation. This is analysed in more detail in chapter 7.

5.3 Multi-Dimensional Flow through Porous Media

In the previous section, unidirectional through-flow behaviour for C/C has been discussed. In general, real application cases will also exhibit coolant flow that is at an arbitrary angle to the carbon fibres and thus not aligned with parallel or perpendicular directions. This is also expected to occur for the supersonic transpiration-cooling experiments discussed in chapter 7. However, due to the fibre lay-up of the investigated C/C samples with 0/90° twill plies, significant cross flow is expected only in the parallel-parallel fibre plane. The corresponding through-flow behaviour is addressed in the following section by means of a validation experiment employing partial sealing of the outlet surface. The purpose of the investigations is to validate the superposition principle postulated by equation (2.62) for arbitrary angles between through-flow direction and fibre orientation. In addition to this, the cross-flow behaviour in the parallel-perpendicular fibre plane is discussed in appendix C by means of a theoretical study as well as OpenFOAM simulations of a porous cone experiment performed at DLR.

5.3.1 Partial-Sealing Experiment

The following validation experiment is designed to induce significant cross flow within the porous structure. Corresponding numerical simulations reveal the coolant flow field within the porous structure. Additionally, the validity of the 3D-Darcy-Forchheimer equation in the parallel-parallel fibre plane is evaluated based on the comparison of integral pressure losses in experiment and simulation.

Experimental setup

For the experiments, a similar setup as for the unidirectional through-flow investigations is employed. Again, static pressures in the coolant reservoir and at ambient conditions are recorded as a function of the applied coolant mass flow rate. Moreover, the temperature of the coolant air is measured for the isothermal tests. To induce coolant cross flow, the outlet surface is partially sealed by a two-component adhesive as shown in figure 5.9. In addition to the illustrated sealing of 25% of the outlet surface, a consecutive measurement series with a sealing of 50% has been performed.

Before starting the through-flow experiment, the applied sealing is examined with respect to leakages at higher reservoir pressure. Due to the experiment's
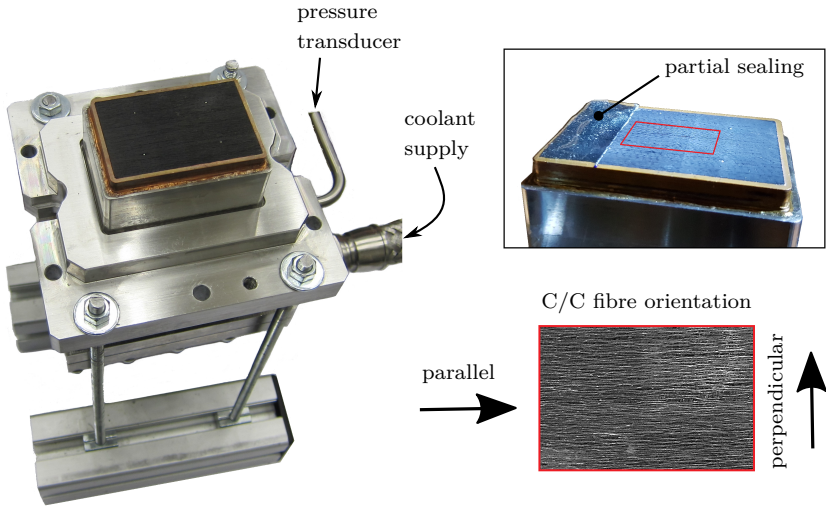
Figure 5.9: Experimental setup for through-flow tests (left) and porous sample with 25% of outlet surface closed (right)

nature involving a porous structure, standard test procedures to detect leakages are not appropriate [41]. Instead, a qualitative analysis based on schlieren images has been performed for through flow of helium at high mass flow rates and high reservoir pressures, respectively. Results of this test cases are given in figure 5.10. In the figures, the adhesive effectively prevents helium to flow over the sealed outlet surface. A pattern of separate coolant jets is observed at the outlet plane of the C/C sample. However, a clear statement on the outflow direction of the coolant is not possible. With increasing distance to the sample, the coolant jets mix with ambient air and among each other.

(a) 0.25% sealing   (b) 0.50% sealing

Figure 5.10: Schlieren images to illustrate outflow behaviour of coolant (here helium) for partial sealing of porous sample (red areas illustrate sealing by adhesive)

Simulation setup

For the simulations, the earlier introduced reference sample (illustrated in figure 3.4) is reproduced by means of a two-dimensional mesh with 15 000 to 18 000 hexahedral cells. Depending on the degree of sealing, i.e. 0%, 25%, or 50%, the numerical outlet is partially replaced by a wall segment to represent the adhesive sealing used in the experiment. The grid features mesh grading towards all boundaries and a refinement of the cell layers close to the transition between outlet and adhesive. The numerical domain and the applied boundary conditions are illustrated in figure 5.11. Walls are modelled by means of no-slip and adiabatic conditions. The air mass flow rate is induced by the modified total pressure boundary condition, see equation (4.33). It enters the porous structure at the experimentally measured coolant-fluid temperature, i.e. $T_f \approx 290\,\text{K}$, and is eventually exhausted into ambience ($p_{ex} = 96.4\,\text{kPa}$). The previously determined permeability coefficients are employed to construct the orthotropic permeability tensor, see table 5.2. Since neither a main-flow domain nor internal heat transfer to the solid-phase of the porous structure need to be considered, only the fluid-phase region is modelled by the solver.

5.3.2 Results and Discussion

The results of the partial-sealing test cases are discussed based on a combined numerical and experimental approach. First, simulation results are presented for different levels of sealing and a constant mass flow rate of $\dot{m} = 1\,\text{g/s}$ (corresponds to $\dot{m}/A_{in} \approx 0.5\,\text{kg/(m}^2\text{s)}$).
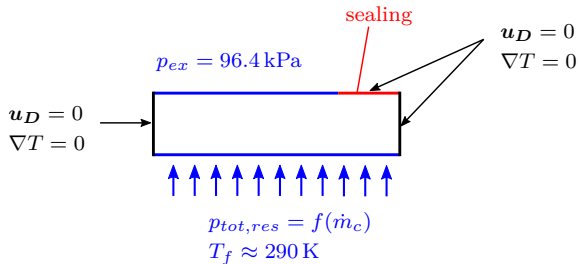
Figure 5.11: Sketch of numerical domain with applied boundary conditions for 25% sealing test case

Figure 5.12 illustrates coolant pressure by means of the greyscale contour, while streamlines coloured by the mass flux indicate the flow direction and transport of coolant mass. The no-sealing test case serves as a reference case with unidirectional coolant flow and straight pressure isolines.

For sealing of the outlet surface, the coolant streamlines below the sealing are forced to change direction which is accompanied by bended pressure isolines. Only streamlines further away from the sealing (i.e. close to the left boarder of the sample) are not affected by this and show an unchanged through-flow behaviour. The cross-flow effect intensifies for the test case with an outlet sealing of 50%. With respect to the coolant pressure, a substantial increase of inlet pressure is found for intensified sealing. Due to the reduced outlet surface, a higher pressure difference between reservoir and outlet is required

(a) 0% partial sealing

(b) 25% partial sealing

(c) 50% partial sealing
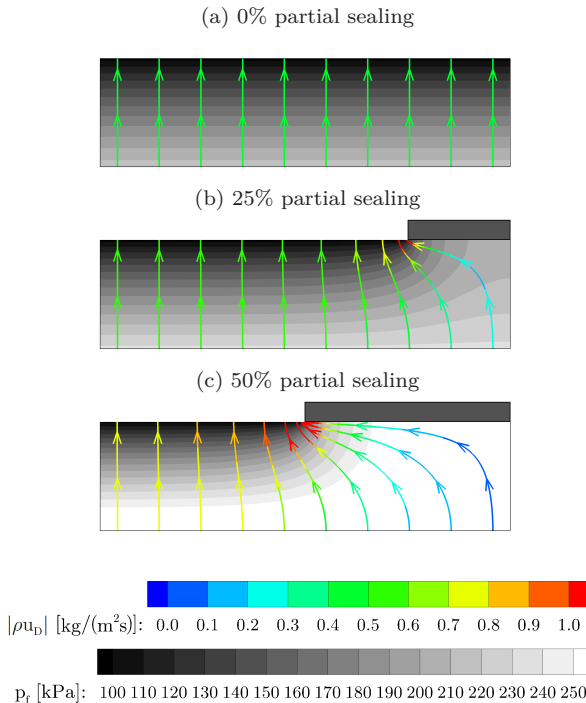
Figure 5.12: Internal pressure distribution and coolant streamtraces for sealing of the outlet surface and $\dot{m}/A_{in} \approx 0.5\,\mathrm{kg/(m^2s)}$

105

to drive the mass flow rate of $\dot{m} = 1\,\mathrm{g/s}$. In line with this, higher mass fluxes occur below the non-blocked outlet. This is indicated by the colour of the streamlines. Comparing the colouring of streamlines below the blocked-outlet area for 25% and 50% test cases, it is found that streamlines further away from the non-blocked outlet transport less coolant mass.

To evaluate the modelling approach, numerical and experimental results for the integral pressure loss $\Delta p = p_{in} - p_{ex}$ over mass flux $\dot{m}/A$ are compared in figure 5.13. In accordance with the determination of permeability coefficients (see section 5.2.1), the value range for the analysis reaches up to maximum pressure differences of $\Delta p = 0.5\,\mathrm{MPa}$. Figure 5.13a illustrates the results with respect to the inlet coolant mass flux. The diagram confirms the previous finding stating higher pressure losses at a given mass flux $\dot{m}/A_{in}$ for sealing of the outlet.

For correlating the pressure loss to the outlet coolant mass flux as shown in figure 5.13b, the stacking of the curves is reversed. While the no-sealing data curve is identical in both diagrams ($A_{in} = A_{ex}$ for 0% sealing), the pressure loss at a given value of $\dot{m}/A_{ex}$ reduces for partial sealing of the outlet. The right-hand diagram thus illustrates the effect of coolant flow in the porous volume below the sealing. If the coolant flow was only unidirectional and no cross flow existed, the curves for 0%, 25%, and 50% sealing would coincide. However, the porous volume below the sealing gives rise to a secondary flow which eventually merges with the primary coolant mass flow (below the non-blocked outlet) before being exhausted into ambience. Although the secondary mass flow is limited in size, it reduces the mass flux below the non-blocked outlet and thus yields lower pressure losses for a given outlet mass flux, i.e. $\dot{m}/A_{ex}$. With respect
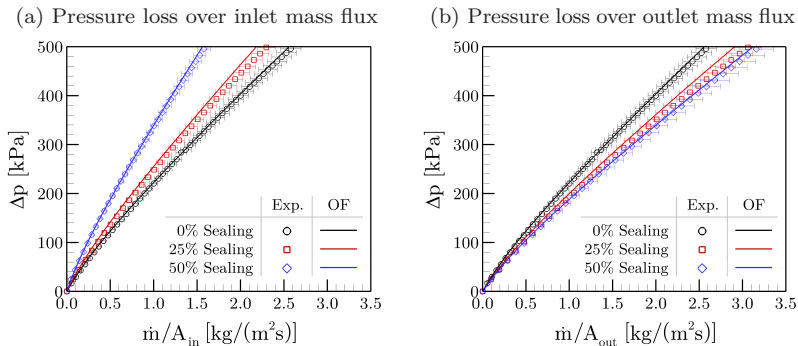
Figure 5.13: Pressure loss over mass flux for partial sealing of the outlet surface

to this, the Δp-reduction from no-sealing to 25% is greater than the additional effect for a sealing of 50% of the outlet surface. This implies that only little additional secondary flow is transported in the enlarged porous volume below the 50% sealing and thus confirms the findings from figure 5.12c. Comparing the simulation results to the measured pressure losses, little deviations are found for all sealing levels and mass flow rates. The generally good agreement suggests the applicability of the superposition principle given by equation (2.62) and thus validates the applied multi-dimensional through-flow approach in the parallel-parallel fibre plane.

5.4 Summary

In the given chapter, the physical processes taking place within a transpiration-cooled porous structure were discussed. At first, the internal heat transfer between coolant and solid skeleton of the porous structure was addressed. A theoretical study based on the criterion by Wang and Wang [192] suggests a non-negligible influence of local thermal non-equilibrium on the transpiration-cooling test cases discussed in chapter 7. This motivates the consideration of separate energy equations for the porous domain throughout the here-presented numerical investigations. Moreover, the solver implementation of the internal heat exchange has been successfully validated based on an analytical solution for a LTNE situation.

In a second step, results with respect to the through-flow behaviour of the porous material C/C were presented. The analysis is split in unidirectional and multi-dimensional coolant flow and combines experimental measurements and numerical simulations. Summarising the permeability investigation for unidirectional flow, the presented measurements confirm the applicability of the Darcy-Forchheimer equation for the modelling of pressure loss within C/C structures. Moreover, the experimental data suggests that the coefficients K_D and K_F for C/C are independent of the coolant gas used and can be considered as material properties in the measured range. The determined values showed to be robust with respect to repetition, also after exposure to hot-gas channel flow. Likewise, the instrumentation with thermocouples has no significant influence on the through-flow characteristics of the C/C sample. However, the results indicate that the flow regime in the experiments employed for the permeability determination has a decisive influence on the resulting coefficients. Additionally, the sensitivity of the pressure loss on the coolant's fluid temperature has been evaluated. As implied by the Darcy-Forchheimer model, the experiment yielded higher pressure losses at elevated temperatures for a given coolant mass flux.

Complementing numerical simulations allowed to separate the effects of higher fluid temperature and reduced outlet pressure present in the experimental data. The simulations verify the correct numerical implementation of the Darcy-Forchheimer model. Moreover, the good agreement to the experimental data confirms the applicability of a single pair of permeability coefficients for all coolants and mass flow rates as well as for varying fluid temperatures and pressure levels.

Subsequently, the multi-dimensional through-flow behaviour in the parallel-parallel fibre plane of C/C was investigated. Regarding this, a validation experiment with partial sealing of the outlet surface has been performed. With increasing level of partial sealing, i.e. 25% and 50%, the pressure loss rises for a given inlet coolant mass flux. The numerical results indicate a significant coolant cross flow below the sealed outlet surface. The generally good agreement of experimental data with the corresponding simulations validates the applied modelling approach based on the superposition principle. Additional validation work given in appendix C confirms the validity of the applied modelling approach also in the perpendicular-parallel fibre plane. However, for the present investigations, only coolant cross flow in the parallel-parallel fibre plane is of importance.

CHAPTER 6

Boundary-Layer Injection of Various Coolants

Subsequent to the porous structure modelling, now the influence of transpiration cooling on the main flow is addressed. Mass injection through a transpired wall particularly alters the main flow in the near-wall region. This manifests in a thicker boundary layer exhibiting smaller velocity and temperature gradients. In line with this, skin friction and wall heat transfer reduce for boundary-layer blowing. Besides the intensity of blowing, the coolant gas properties significantly influence the effects. As described earlier, thermal protection in propulsion engines is one of the main application cases of transpiration cooling. Aside from air, fuel is typically used as coolant in these applications. Similarly, thermal protection of external surfaces in hypersonic flight through transpiration cooling might use other gases than air. As a consequence, the injection of foreign gases into the main flow is an important aspect in the numerical simulation of transpiration cooling. The following validation work focuses on this aspect by investigating boundary-layer blowing of various gases into a non-reactive main flow of air.

6.1 Test-Case Description

For the solver validation, an experimental data set from literature has been selected [129]. In his work, Meinert experimentally investigated a subsonic turbulent channel flow with boundary-layer blowing using various coolant gases.

The subsonic flow velocity allows the measurement of detailed boundary-layer profiles for isothermal and heated test conditions. These are now compared to the results of corresponding numerical simulations. Additionally, the numerical parameters for skin friction and wall heat transfer, i.e. St and C_f, are compared to correlations from literature [96, 130]. A brief account on Meinert's experiments as well as the description of the numerical setup are given in the following.

6.1.1 Experimental Setup

In the wind-tunnel experiments selected as the reference for this validation, a blower supplied a continuous air flow of up to $\dot{m}_{hg} = 1.3\,\text{kg/s}$. The static pressure in the test section was around $100\,\text{kPa}$, while main-flow velocities could be adjusted to values of up to $u_\infty = 160\,\text{m/s}$. For selected test cases, a combination of electrical heater and recuperator was employed to increase the static main-flow temperature up to $T_\infty \approx 550\,\text{K}$. Depending on the considered test case, this results in unit Reynolds numbers $\text{Re}_1 \approx 3.6 - 4.8 \cdot 10^6\,\text{1/m}$ and Mach numbers $\text{M}_\infty \approx 0.21 - 0.34$. The employed measurement section has a constant cross section of $0.114\,\text{m}$ width and $0.1\,\text{m}$ height. At the entrance of the segment, the existing boundary layer is removed by boundary-layer suction ($x = 0$). Thus, a new boundary layer is developing which is tripped artificially downstream at $x = 0.1\,\text{m}$. A porous wall segment made from the stainless-steel packed-bed material SIKA-R5 replaces the wall between the axial positions $0.20\,\text{m} < x < 0.47\,\text{m}$. The material exhibits a porosity of $\varepsilon = 30\%$ and an average pore diameter of $d_{pore} = 10\,\mu\text{m}$. With respect to the latter, SIKA-R5 compares well to porous CMC materials such as C/C which exhibit an average crack size of 11 to $14\,\mu\text{m}$ [189]. However, the porosity of CMC materials is generally lower. In the experiments, coolant gases such as air, argon, and helium are supplied via gas bottles and mass-flow controllers to the coolant reservoir below the porous wall segment.

A combined sensor containing a static-pressure probe, a miniature pitot probe, and a miniature thermocouple is used to measure the boundary-layer profiles. The here-discussed measurements were taken in the middle of the channel at the axial positions $x = 0.342\,\text{m}$ and $x = 0.442\,\text{m}$. The sensor's wall distance was adjusted by a precise positioning system in order to traverse the boundary layer. Based on velocity and temperature profiles, skin friction and wall heat transfer were determined by means of the Clauser method [34]. Moreover, the surface temperature on the porous sample was determined by an infrared pyrometer. All measurements were taken at steady-state conditions, i.e. after

thermal equilibrium was reached. Velocity profiles are calculated from the measured dynamic pressure via Wuest's formula [208]. Meinert et al. [130] point out that the evaluation of measured data for foreign-gas transpiration is challenging due to the significant density variations in the boundary layer. As the concentration profiles were not measured in the experiments, a simplified analogy of momentum transport and diffusion in the turbulent boundary layer was employed in order to determine the required fluid properties of the binary gas mixtures. More information on the experimental setup and the applied data analysis methods can be found in references [129, 130].

6.1.2 Numerical Setup

The corresponding numerical simulations were performed using the OpenFOAM solver described in chapter 4. As the validation is only concerned with the main flow boundary-layer profiles, only this region is considered while the porous domain is neglected in the simulations. However, the mass injection by means of boundary-layer blowing (through the porous structure's outlet) is modelled using the continuous blowing model as detailed in section 4.4.

The computational domain and the applied boundary conditions are shown in figure 6.1. A two-dimensional numerical grid consisting of around 200 000 rectangular cells represents the channel geometry. An air flow with constant area-specific mass flux and constant static temperature is prescribed at the inlet, whereas the outlet is modelled by a fixed pressure boundary condition
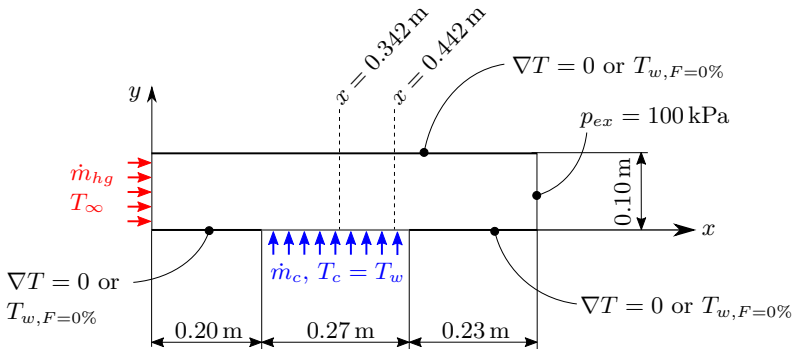

Figure 6.1: Computational domain and applied boundary conditions

of $p_{ex} = 100 \, \mathrm{kPa}$. The channel flow is assumed as fully turbulent, i.e. no laminar-turbulent transition is taken into account. Turbulence modelling is done by means of the Low-Re formulation of the shear stress transport model by Menter [133]. With respect to the inlet conditions, TI = 2% was selected for the turbulent kinetic energy and a mixing length of $L_{t,in} = 4.8\% \cdot d_{hyd}$ is specified for the calculation of the specific dissipation rate ω_{in}. For a good approximation of turbulent behaviour close to the channel wall, a dimensionless wall distance of $y_1^+ < 1$ was obeyed during mesh generation. A turbulent Prandtl number of $\mathrm{Pr}_t = 0.87$ is selected for the simulation of Meinert's test case. Regarding the isothermal test cases, walls are set to be adiabatic, whereas for the heated test cases the experimentally measured temperature is imposed at the porous wall. Since no experimental data on the wall temperature up- and downstream of the porous segment is available, the surface temperature measured on the porous wall for the no-blowing case is applied at these positions. The coolant gas is injected at the measured wall temperature T_w. For the here-considered test cases, the applied continuous blowing model yields an even coolant mass flow rate over the transpired surface and a no-slip condition for the axial velocity component, i.e. $u_y = \dot{m}_c/(\rho_c A_c)$ and $u_x = 0$. Regarding the turbulence settings on the porous wall, the turbulent kinetic energy is set to $\kappa = 0$ while three boundary conditions for the specific dissipation rate ω were proposed in section 4.4. The standard ω boundary condition given by equation (4.24) has been selected for the here-discussed simulations. A brief sensitivity study at the end of this section reviews this choice.

6.2 Injection of Various Coolants into a Main Flow at Isothermal Conditions

The validation on boundary-layer blowing starts by investigating the injection of various gases into a non-heated main flow of air. At first, the injection of air at isothermal conditions, i.e. $T_\infty = T_c = 293.15 \, \mathrm{K}$ is discussed. Figure 6.2 gives velocity distributions over wall distance with varying blowing ratio for simulation (lines) and experiment (symbols). The case of no injection ($F = 0\%$) was evaluated at the axial position $x = 0.342 \, \mathrm{m}$, whereas all measurements with blowing were taken at $x = 0.442 \, \mathrm{m}$. This corresponds to axial positions at the middle and close to the trailing edge of the sample as indicated in figure 6.1.

In a first step, the simulation of the no-blowing case was used as a reference for the determination of inlet conditions. Although the simulation treats the wall flow fully turbulent and does not model the laminar-turbulent transition, the

agreement between numerical and experimental values is very good. This is related to two contrary effects on the boundary-layer growth occurring in the experiment (but not in the simulation). The tripping device has a thickening influence, whereas the laminar boundary-layer growth up to the point of flow transition is weaker when compared to fully turbulent flow. Both effects cancel each other out as already reported by Meinert [129]. Having the main-flow conditions validated, the injection of air at various blowing rates F ranging from 0.0836% to 0.5206% was added to the simulation. Comparing the numerical results to the experimental data points in figure 6.2, a very good agreement is found. The effect of increasing injection rates is well captured in the simulations. It is clearly notable that the boundary-layer thickness increases with rising blowing ratio. Likewise, the velocity gradients at the wall diminish.

Transpiration of the foreign gases argon and helium into a main flow of air requires the modelling of gas mixtures and species diffusion as described in chapter 2. Additionally, the coolant inlet boundary condition (at the porous wall) has to be modelled with special care in order to meet a desired blowing ratio. Regarding this, the Eckert-Schneider boundary condition as detailed in section 4.4 has been employed. Since the injection of heavy (e.g. argon) or light (e.g. helium) gases changes the density within the boundary layer, the velocity profile does not correctly reproduce the deficit in mass and momentum transport in the wall-near region. Instead, the mass flux density ρu_x is employed
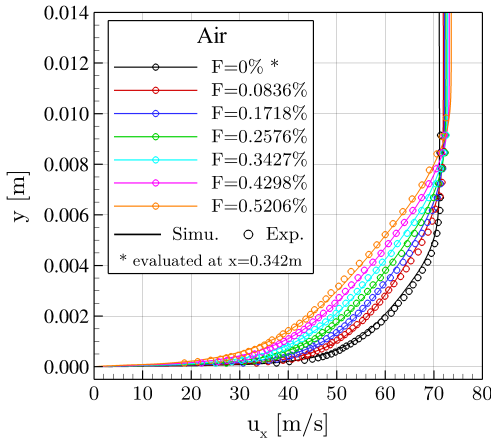
Figure 6.2: Velocity profiles at $x = 0.442$ m for blowing with air into a main flow of air for various blowing ratios at isothermal conditions

for the analysis of foreign-gas transpiration. Figure 6.3 displays the mass flux density over wall distance for argon and helium injection. A very good agreement between simulation and experiments is found for both gases. The boundary-layer thickening as well as the reduced gradients in comparison to the no-blowing case are well represented. It is notable that even comparatively small injections of helium change the mass flux density distribution substantially. This is a consequence of helium's much lower density when compared to air ($\rho_{Air}/\rho_{He} \approx 7$) which decreases the mixture density close to the wall and moreover results in comparatively large transversal velocities. Argon as a heavier gas ($\rho_{Air}/\rho_{Ar} \approx 0.7$) has a reduced effect in this regard. The presented simulation results of argon and helium injection show little deviations to the measured data. Taking into consideration that the experimental results naturally include some measurement uncertainties and are additionally based on analytical diffusion modelling, the agreement is very good.

In addition to the comparison of boundary-layer profiles, the skin-friction coefficient as defined by equation (2.42) allows a detailed analysis of the velocity gradients close to the transpired wall. With respect to transpiration cooling applications, rather the reduction for boundary-layer blowing than the absolute value is of interest. Therefore, the ratio of skin-friction coefficients with and without blowing is determined, i.e. $C_f/C_{f,0}$. Figure 6.4 depicts the results for injection of air, argon, and helium at isothermal conditions and for the axial position $x = 0.442\,\mathrm{m}$. Besides OpenFOAM results (symbols), also the
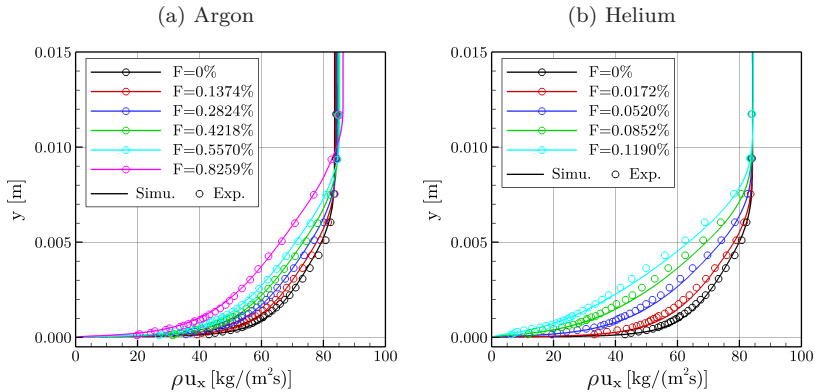
Figure 6.3: Mass flux profiles at $x = 0.442\,\mathrm{m}$ for blowing with argon and helium into a main flow of air for various blowing ratios at isothermal conditions

Figure 6.4: Ratio of skin-friction coefficients with and without transpiration over blowing ratio for air, argon, and helium at isothermal conditions

correlations by Kays et al. [96] and Meinert et al. [130] as given by equation (2.48) are included in the figure (lines). The diagram clearly illustrates the strong reduction of wall shear stress for mass injection. Moreover, a pronounced dependency on the coolant-fluid properties is found. Light gases such as helium reduce the skin-friction coefficient drastically already at low blowing rates. Opposed to this, the influence of the heavier gas argon is less significant. Nonetheless, the highest investigated blowing ratio for argon exhibits a skin-friction coefficient close to boundary-layer blow-off which occurs for $C_f \approx 0$. A very good agreement between simulation results and correlations is found for the transpiration of air, argon, and helium. However, for blowing with foreign gases, the correction factor proposed by Meinert et al. [130] has to be taken into account, i.e. $k_W = (W_{hg}/W_c)^{0.8}$ in equation (2.48).

6.3 Injection of Various Coolants into a Heated Main Flow

Having validated the injection of same and foreign gases at isothermal conditions, boundary-layer injection into a heated main flow is investigated in the following. Numerical simulations using argon and helium as coolants are compared to the corresponding experiments at heated conditions. For the injection of argon, the main flow temperature was $T_{\infty,Ar} = 456\,\mathrm{K}$, whereas for helium injection the experiments were performed at higher temperatures, i.e. $T_{\infty,He} = 550\,\mathrm{K}$. The coolant temperature at injection is set identical

to the measured wall temperature and thus depends on the applied blowing ratio. Besides the temperature dependency of fluid properties, e.g. dynamic viscosity μ and thermal conductivity k, also the effect on the molecular diffusion coefficient (i.e. $D_{12} \propto T^{1.75}$) has to be considered for the heated test cases. Figure 6.5 compares the numerical results to experimental measurements. In addition to the mass flux density, the temperature profile is given on the second abscissa. Again, a very good agreement for the mass flux density is found for both investigated cases. Especially close to the wall, experimental and simulation data coincide nearly perfect, whereas further away from the wall smaller deviations occur. Also the temperature distributions show a fair agreement between experiment and simulation. A clear decrease of temperature gradients close to the wall and a thickening of the temperature boundary layer is found for coolant gas injection. As observed for the mass flux density profiles, the injection of helium at a given blowing ratio F influences the temperature boundary layer more significantly than a comparable argon injection. This is due to the high specific heat capacity of helium ($c_{p,He}/c_{p,Air} \approx 5$) when compared to argon ($c_{p,Ar}/c_{p,Air} \approx 0.5$).

For further analysis, the Stanton number reduction is evaluated for the injection of same and foreign gases. The ratio St/St_0 is determined from the numerical values obtained with and without boundary-layer blowing at an axial position of $x = 0.442\,\mathrm{m}$. Figure 6.6 compares the numerical results to the correlations
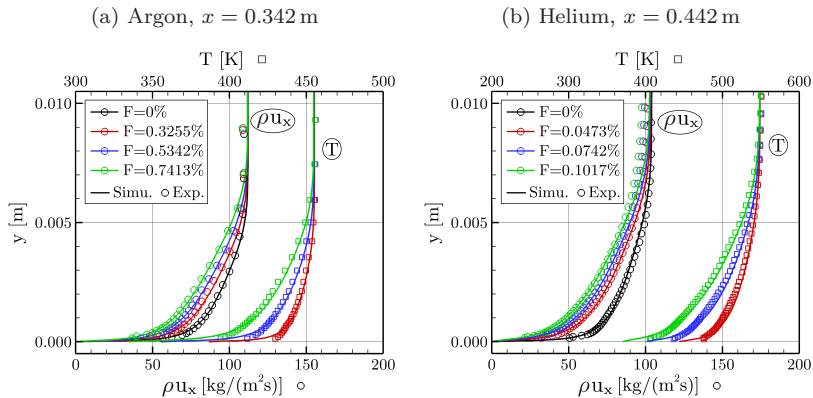
Figure 6.5: Mass flux profiles (x_1-axis, symbol ○) and temperature profiles (x_2-axis, symbol □) at $x = 0.342/0.442\,\mathrm{m}$ for blowing with argon and helium into a heated main flow of air

Figure 6.6: Ratio of Stanton number with and without transpiration over blowing ratio for air, argon, and helium

by Kays et al. [96] and Meinert et al. [130] given by equation (2.49).[1] A distinct reduction of wall heat flux for increased blowing ratios is notable for all coolant gases. For a given blowing ratio, helium is found to have a stronger influence when compared to the other gases. This confirms the previous findings. A good agreement is found for the correlation of Meinert et al., whereas the agreement to the correlation of Kays et al. is less.

6.4 Sensitivity of Turbulence Boundary Condition

The presented results for same and foreign gas injection show a generally good agreement between numerical simulation and experimental data. The standard ω boundary condition given by equation (4.24) was employed at the porous wall in all simulations. To investigate the sensitivity of results on this choice, additional simulations were performed using two further ω boundary conditions for transpired walls, i.e. equations (4.50) and (4.52). As exemplary test cases, an injection of air at isothermal conditions ($F_{Air} = 0.2576\%$), and helium transpiration into a heated main flow ($F_{He} = 0.0473\%$) have been selected.

---

1   The values for St_0 were obtained from separate numerical simulations without blowing while the porous wall temperature was set identical to the value of the respective blowing cases. As a consequence of the weak dependency of St_0 on the wall temperature, the values for St_0 vary slightly for the different test cases.
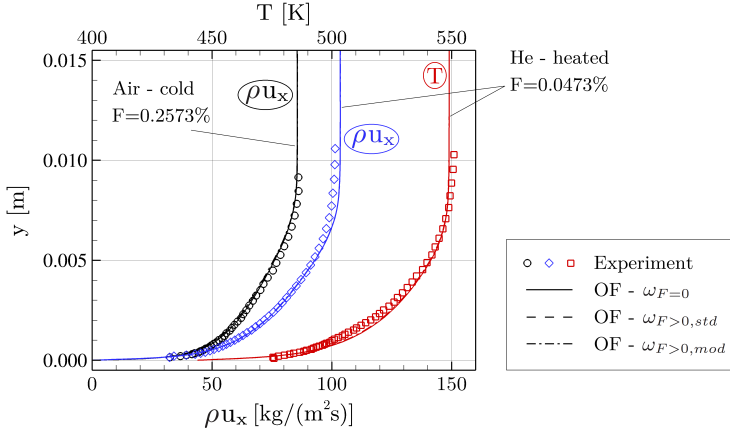
Figure 6.7: Sensitivity study on ω-BC - boundary-layer profiles for selected test cases using air (ρu_x) and helium (ρu_x, T) as coolants

Figure 6.7 illustrates the boundary-layer profiles of mass flux density (air and helium) and temperature (helium only, second abscissa) for the three investigated boundary conditions. The depicted profiles coincide and thus do not indicate any influence of the applied ω boundary condition.

To analyse the wall-near region more closely, the ratios $C_f/C_{f,0}$ and St/St_0 are evaluated at $x = 0.442\,\mathrm{m}$ for non-heated and heated test cases, see table 6.1. The deviations between all boundary conditions for $C_f/C_{f,0}$ and St/St_0 are small. Moreover, the correlations by Kays et al. [96] and Meinert et al. [130] which base on experimental data exhibit uncertainties of similar magnitude, see for example Meinert [129].

Table 6.1: Results of ω-BC sensitivity study for $C_f/C_{f,0}$ and St/St_0

			OpenFOAM			Correlations	
			$\omega_{F=0}$	$\omega_{F>0,std}$	$\omega_{F>0,mod}$	Kays	Meinert
Air	cold	$\frac{C_f}{C_{f,0}}$	0.40	0.47	0.48	0.39	0.39
He	heated	$\frac{C_f}{C_{f,0}}$	0.58	0.61	0.62	-	0.47
He	heated	$\frac{St}{St_0}$	0.72	0.74	0.75	0.76	0.70

Summarising the sensitivity study, only a moderate influence of the ω boundary condition on the results has been found. Regarding the boundary-layer profiles no differences were observed, while slightly larger variations are present in the dimensionless parameters characterising the near-wall gradients. Taking into account the uncertainties present in the experimental data and the correlations, this suggests the applicability of all investigated ω boundary conditions for the here-investigated test cases with same and foreign gas injection. However, it has to be noted that the test cases use Dirichlet boundary conditions at the transpired surface which represent rather hard constraints on the boundary-layer profiles, i.e. $u_x = 0$ and $T = T_w$ for $y = 0$. Thus, a further sensitivity study for a fully-coupled transpiration-cooling test case has been performed and is presented in section 7.2.4.

6.5 Summary

Numerical simulations of a subsonic turbulent channel flow with boundary-layer injection on the basis of an experiment by Meinert [129] have been performed. By comparison of the results to the available experimental data and correlations, the solver has been validated with respect to same and foreign gas transpiration into heated and non-heated main flows. The analysis focused on the boundary-layer profiles of velocity, mass flux density, and temperature as well as the reductions of skin-friction coefficient and Stanton number for blowing.

A generally good agreement was found for all considered test cases. Important effects on the main flow such as the thickening of kinematic and thermal boundary layers and the reduction of gradients close to the wall are accurately represented in the simulations with boundary-layer blowing. Moreover, the influence of the fluid properties of the injected gas is well reproduced. The conformance of results validates several aspects of the simulation setup. First, the continuous blowing model may be applied to represent a transpired wall with microscopic pore openings. Secondly, the models added to the OpenFOAM solver in order to determine fluid properties of gas mixtures and with respect to diffusion modelling (see section 2.1.5) perform well in the simulation of the test cases with foreign-gas injection. In this regard, the applied Eckert-Schneider boundary condition gave good results and may be applied to model the transpiration of foreign gases into a main flow of air. Thirdly, the consideration of the term representing energy transport due to species diffusion is appropriate, see equation (4.13). This is confirmed by the generally well captured heat transfer at the wall.

Summarising this validation work, the OpenFOAM solver and the applied numerical setup perform well in the simulation of foreign-gas injection through a porous wall segment into a subsonic main flow at isothermal or heated conditions. With that in mind, the solver and the numerical models are validated for supersonic main-flow conditions and the ceramic material C/C in the following chapter.

CHAPTER 7

Transpiration Cooling of CMC Structures in Supersonic Flows

The following chapter focuses on transpiration cooling of CMC structures in supersonic main flows. Different porous samples in uniform and more complex supersonic main-flow conditions have been tested experimentally in the ITLR Hot Gas Facility. Corresponding numerical simulations have been performed in parallel. Thus, the developed OpenFOAM solver is validated for different main-flow and transpiration-cooling situations. Moreover, the combined approach enables a more detailed analysis of results since the numerical simulations allow to investigate regions and effects which are not accessible to measurements or cannot be captured experimentally.

The chapter starts with an investigation on the supersonic channel flow without boundary-layer blowing to demonstrate the solver's capabilities to reproduce the correct reference conditions. Subsequently, a sensitivity study for selected transpiration-cooling cases is performed to decide on the final simulation setup. Using the determined simulation parameters, blowing with air and foreign gases through the reference sample is investigated at hot supersonic main-flow conditions. The focus of the investigation is on the temperature levels of the external surfaces and within the porous sample. Moreover, the cooling efficiency is determined for the considered cases. In the following sections, the contoured sample which introduces thickness variations and thus non-uniform coolant blowing is investigated. Besides this geometrical aspect, also modifications of the flow and pressure fields by means of shock generation is considered. The final section deals with the double-wedge sample which combines both effects.

7.1 Supersonic Channel Flow without Boundary-Layer Blowing

The developed OpenFOAM solver is employed to simulate the supersonic wind-tunnel tests performed in the ITLR Hot Gas Facility. In a first step, the heated channel flow without boundary-layer blowing is investigated which serves as a reference for all further test cases. As detailed in chapter 3, the facility allows long-duration testing and thus provides steady-state main-flow conditions for the tests, i.e. $T_{tot} = 500\,\text{K}$, $p_{tot} = 0.5\,\text{MPa}$, and $\dot{m}_{hg} = 0.436\,\text{kg/s}$. The flow is accelerated in the Laval nozzle to M = 2.5, before it enters the test section with a constant cross section of $35.4 \times 40\,\text{mm}^2$.

The simulation domain starts after the heater stages and includes the complete Laval nozzle as well as the constant rectangular test section, see figure 7.1. A Cartesian coordinate system is employed with the channel's symmetry plane corresponding to the x-y-plane. The origin of the x-axis coincides with the Laval nozzle throat and the y-axis origin is defined by the channel's mid height. The positive y-axis direction points from channel mid height to the channel's top wall. With respect to the chosen coordinate system, the mesh covers the axial channel length $-0.20\,\text{m} < x < 0.45\,\text{m}$. A three-dimensional grid is employed for all simulations to capture possible side-wall effects in the channel flow. Additional lateral influences are expected for the transpiration-cooling test cases, since the transpired surface of the porous sample does not extend over the full channel width (due to copper layer with 1.6 mm thickness). The numerical grid used for the simulation reproduces the experimental wind-tunnel geometry with a total of around 7.5 million hexahedral cells.[1] To reduce the mesh size, only a half model is simulated making use of the channel's symmetry plane, i.e. the x-y-plane. In accordance with the selected turbulence model, all walls exhibit a non-dimensional wall distance of $y_1^+ < 1$.

The subsonic inlet is modelled by prescribing both total pressure $p_{tot} = 0.5\,\text{MPa}$ and total temperature $T_{tot} = 500\,\text{K}$. Moreover, turbulence conditions are set using an eddy viscosity ratio of $\nu_t/\nu = 50$ and a constant turbulent intensity TI ranging from 1% to 10%. Conditions of the supersonic outlet are determined from the internal field, i.e. $\nabla p = 0$ and $\nabla T = 0$. Except for inlet and outlet, all boundaries are adiabatic no-slip walls.

---

1 A mesh sensitivity study has been performed for a generic test case with boundary-layer blowing and is presented in section 7.2.2. All parameters such as first-cell height, growing rate, or number of cells have been selected similarly for the here-discussed test case.
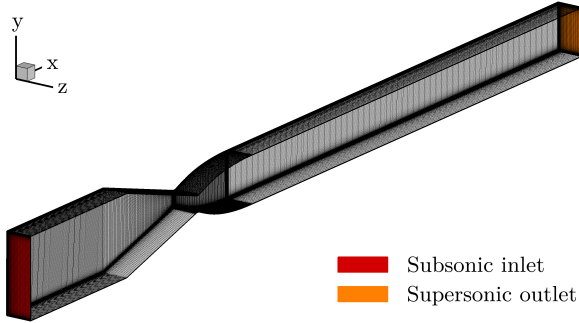
Figure 7.1: Numerical half domain of supersonic flow test channel

7.1.1 Analysis of Flow Field

In the following, the flow field in the test channel without boundary-layer injection is evaluated through experimental and numerical data. Regarding this, the wall pressure over channel length is depicted in figure 7.2. Additionally, a contour plot of the Mach number as well as a slice view of the channel are given in the figure's background.[2]

Examining the diagram, the characteristic pressure drop in the Laval nozzle is found which is due to the flow's acceleration from subsonic ($M \approx 0.15$) to supersonic velocity ($M = 2.5$). In the test section, a nearly constant wall pressure of around $30\,\text{kPa}$ prevails. This value is in line with the isentropic pressure relation for air at a total pressure of $p_{tot} = 0.5\,\text{MPa}$ and $M = 2.5$, cf. equation (2.28). A slight increase of pressure with run length occurs due to the combination of boundary-layer growth and constant channel cross section. Top and bottom wall pressure is coinciding and the even pressure distributions do not indicate the formation of shocks. This attests smooth transitions between modules in the experimental setup. Moreover, no shock train is found for the considered run length, the adaptation to ambient pressure ($p_{ex} \approx 96.4\,\text{kPa}$) takes place downstream of the test section. Comparing simulation results (lines) and experimental data (symbols), a very good agreement is found.

In addition to wall pressure measurements, schlieren images for both side-wall windows have been taken. Figure 7.3 reveals density gradients in the flow

2   Non-porous stainless-steel samples equipped with pressure taps were used for the experimental pressure measurements.
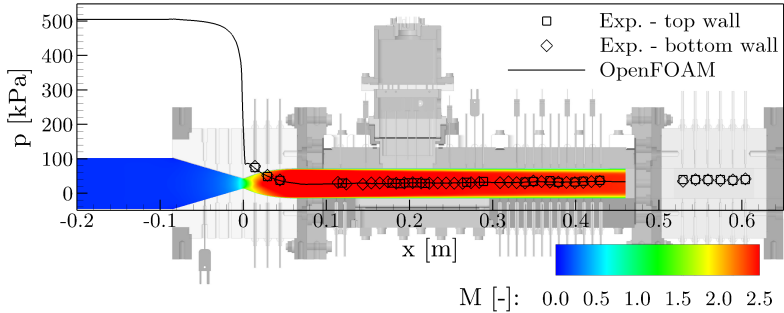
Figure 7.2: Wall pressure distribution and Mach number contour plot for supersonic channel flow

field which are related to Mach lines, i.e. infinitely weak shock waves. For the Laval nozzle's design Mach number $M = 2.5$, the corresponding wave angle is calculated from equation (2.37) to

$$\beta = \arcsin\left(\frac{1}{2.5}\right) = 23.6° \quad . \tag{7.1}$$

It is indicated in the schlieren image by the red-coloured lines, see figure 7.3. The good agreement to the density-gradient lines confirms the channel-flow Mach number of $M = 2.5$.

With respect to the temperature flow field, the total value $T_{tot} = 500\,\text{K}$ is measured in the free stream at a position upstream of the Laval nozzle. Downstream, the flow acceleration results in a significant static-temperature drop in the core flow, i.e. $T \approx 222\,\text{K}$. In the boundary layer, the temperatures increase again up to the recovery temperature T_r due to the flow's deceleration and viscous dissipation, see also chapter 2.
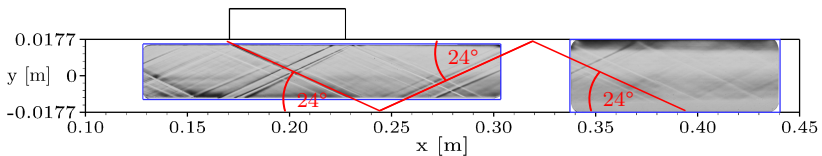
Figure 7.3: Experimental schlieren image of supersonic channel flow without boundary-layer blowing and wave angles for $M = 2.5$

The resulting wall temperature distributions as experimentally measured (symbols) and obtained from OpenFOAM simulations (lines) are given in figure 7.4.

First, the experimental measurements are analysed. The thirteen thermocouples mounted flush with the channel's top wall record a rather uniform temperature distribution along the channel axis, i.e. $T_{F=0} = 446.1 \pm 2.5\,\text{K}$. The deviations of $\pm 2.5\,\text{K}$ from the mean value are within the estimated measurement uncertainty and may be explained by slight differences in the thermocouples' mounting positions along the channel. Moreover, the three thermocouples positioned at different lateral positions ($x = 0.279\,\text{m}$, $z = 0 \pm 0.01\,\text{m}$) measure nearly identical temperatures and do not indicate significant lateral deviations in the temperature field. To measure the adiabatic wall temperature T_r more accurately, a wall insert as detailed in section 3.3 has been employed yielding an averaged temperature of $T_{F=0,\text{insert}} = 446.9 \pm 0.6\,\text{K}$ (side-wall measurements between $0.179\,\text{m} < x < 0.219\,\text{m}$). Although this value is slightly elevated when compared to the wall thermocouples' average, both measurements are in reasonable agreement. This suggests that the wall thermocouple measurements are not significantly affected by stem conduction, i.e. undesired heat conduction along the wall thermocouple length which falsifies the measurement [14].[3]
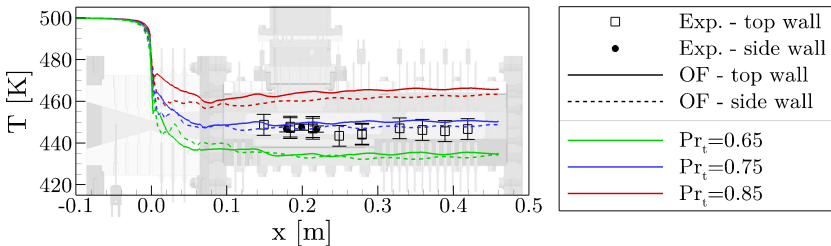
Figure 7.4: Wall temperature distribution for supersonic channel flow

---

3   A theoretical calculation of the recovery temperature for an adiabatic flat plate using $r \approx \sqrt[3]{Pr} = 0.89$, $\gamma_{Air} = 1.4$, and M = 2.5, results in $T_r = 468.9\,\text{K}$. This is around 5% higher when compared to the experimentally measured values. However, the theoretical determination neglects the influences of side-wall boundary layers and corner vortices present in the here-considered rectangular channel flow. In addition to this, the thermal situation of the test channel is not completely adiabatic despite insulation measures such as the employed PEEK material or the wall insert's air chamber. Also, the total temperature within the test section might be slightly reduced when compared to the upstream measurement ($T_{tot} = 500\,\text{K}$) due to heat losses from the non-insulated Laval nozzle segment to the ambience.

Besides experimental data, the numerical results obtained with the new OpenFOAM solver are included in figure 7.4. In the simulations, turbulence is modelled through the two-equation eddy viscosity model κ-ω-SST. As discussed in section 4.2, the choice of the turbulent Prandtl number Pr_t is not trivial. Consequently, a sensitivity study has been performed with respect to this parameter, i.e. $Pr_t \in [0.65, 0.75, 0.85]$. From the results, a significant influence on the numerical results for the adiabatic wall temperature $T_{F=0}$ is found. An increase of Pr_t results in higher wall temperatures which is due to the decreased turbulent transport of heat within the boundary layer. As the heat which originates from viscous dissipation cannot be transported away from the wall into the cooler core flow, the thermal boundary layer becomes thinner and thermal gradients increase.

Comparing the numerical results to experimental data, good agreement is found for $Pr_t = 0.75$ while larger deviations occur for the two other values of Pr_t.[4] Besides the turbulent Prandtl number, also the influence of the turbulent intensity has been investigated by a variation of TI $\in [1\%, 5\%, 10\%]$. However, no influence was found on the wall temperature and thus the results are coinciding with the given curves for the reference value TI = 5%. Besides, no influence of Pr_t or TI on the numerical pressure distribution was detected.

As discussed, the measurement with the adiabatic wall insert indicates similar temperatures as the wall thermocouples and thus confirms the accuracy of the latter. To evaluate the influence of the different measurement positions, numerical wall temperatures have been evaluated for top wall (symmetry plane) and side wall (mid height). The results included in figure 7.4 indicate only small deviations between both positions. This supports the previous statement that the thermocouple measurements are not significantly affected by stem conduction.

7.1.2 Inlet Conditions for Reduced Numerical Domain

To study transpiration-cooling processes with varying blowing intensity and for different porous sample geometries, a reduced numerical domain has been used in order to decrease computational costs. As information is only passed in downstream direction for supersonic flows it is not necessary to simulate the complete channel including the subsonic parts. Instead, flow variables are extracted from the complete channel solution at the position of the reduced domain's inlet plane as indicated in figure 7.5 (i.e. downstream of the Laval

---

4   A brief literature review on the choice of the turbulent Prandtl number in RANS simulations is given in appendix E.1.

u_x [m/s]: 0 100 200 300 400 500 600 700 800
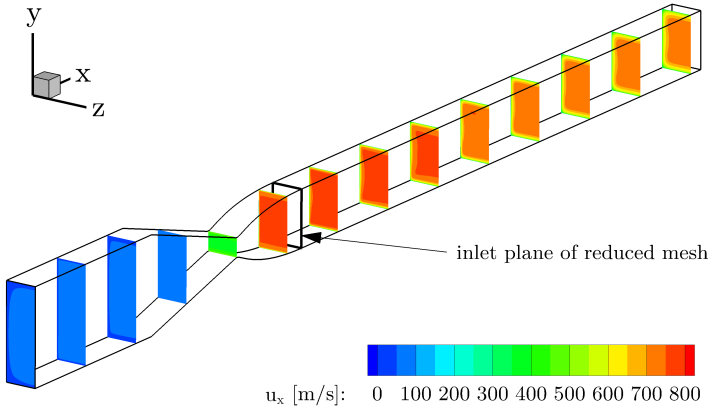
Figure 7.5: Supersonic flow field visualised by means of velocity contour slices

nozzle at $x = 0.064\,\text{m}$). The extracted values are then used as boundary conditions for the reduced mesh simulations. As a consequence, the mesh size reduces to around 4 million cells while the correct inlet flow field and the existing boundary layer are preserved. The resulting boundary conditions on the inlet plane are detailed in appendix E.2.

7.1.3 Summary

The test-channel flow without boundary-layer blowing serves as the reference for all further investigations. The experimental and numerical results indicate a transition from sub- to supersonic flow in the Laval nozzle. Downstream, in the rectangular test section with constant cross section, a completely supersonic flow situation at $M = 2.5$ prevails. Experimentally, a constant wall pressure of around $30\,\text{kPa}$ and an average wall temperature of $446.1\,\text{K}$ were found. While the pressure distribution of the corresponding three-dimensional numerical simulation agrees well with the measurements, a significant dependency on the turbulence settings was found with respect to the wall temperature. In this regard, a sensitivity study suggests that $\text{Pr}_t = 0.75$, $\text{TI} = 5\%$, and $\nu_t/\nu = 50$ accurately reproduce the experimental wall temperature distribution. In summary, the experimental results for the hot-gas channel flow without blowing show a smooth pressure distribution and a rather uniform wall temperature along the channel. Both are well matched by the selected numerical setup.

7.2 Transpiration Cooling - Simulation Setup and Sensitivity Studies

In the following section, the general numerical setup employed for the simulation of transpiration cooling in supersonic flow is described. The choice of different parameters which are unknown or have only been estimated for C/C up to now is evaluated in the frame of sensitivity analyses. Thus, their influences on the simulation results is determined and appropriate values are selected. The sensitivity studies cover the boundary conditions for turbulence on the porous surface Γ_{HG}, the volumetric heat transfer coefficient, and the thermal boundary condition on the coolant-reservoir side Γ_{PM}, where the coolant enters the porous structure. Moreover, the formatting of result figures employed in the corresponding analyses is detailed.

7.2.1 Coupled Simulation Setup

All coupled simulations are performed with a similar numerical setup which only differs slightly in the mesh due to the different experimental test configurations, i.e. the variation of porous sample geometries and the geometrical alteration introduced for the shock-generator cases. The numerical domain for the transpiration-cooling test cases is reduced when compared to the previous simulation without boundary-layer blowing. It starts downstream of the Laval nozzle at an axial position of $x = 0.064\,\mathrm{m}$ and extends over the rectangular test section up to $x = 0.45\,\mathrm{m}$. The three-dimensional domain makes use of the channel's symmetry and can be divided into different regions corresponding to main-flow channel and porous sample.[5] A porous sample is represented by two overlapping numerical grids corresponding to porous-solid and porous-fluid domains. Depending on the test case, the mesh of all regions consists of 5.1 to 6.4 million hexahexdral cells in total. The numerical domain and the applied boundary conditions are exemplarily illustrated for the reference-sample test case with transpiration cooling using air in figure 7.6. The symmetry plane has been blanked for clarity.

At the inlet plane of the domain, values are prescribed through mapping from the reference simulation of the complete supersonic channel, see section 7.1.2. On the channel's top wall, the porous-sample domain is located. Its numerical

---

5 Additional regions are employed for a test case investigating the thermal situation of the porous sample which is presented in section 7.3.2. Here, the sample's surroundings are considered by three solid regions representing PEEK material, the galvanised copper sealing, and the sample's mounting frame made from stainless steel.
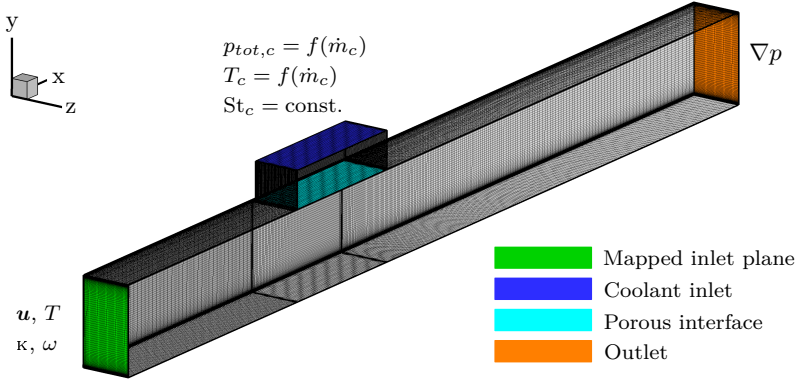
Figure 7.6: Reduced numerical domain and applied boundary conditions for reference-sample test case

grid shares identical cell faces with the main-flow domain on the porous interface. The sample domain covers only the porous material (i.e. C/C) through which the coolant is flowing. The lateral copper sealing as well as the stainless-steel mounting frame are not included in the standard setup. The influence of these parts is investigated in section 7.3.2. Boundary conditions are prescribed at the backside of the porous structure as detailed in section 4.4.1. The coolant fluid temperature T_c is set according to the averaged measurement values from the corresponding experimental test cases and thus varies with blowing ratio. The modified total pressure boundary condition is employed to induce the coolant mass flow rate $\dot{m}_c$. Gaseous air is used as coolant fluid if not stated otherwise. The heat transfer situation at the porous inlet is modelled by the simplified condition of a constant Stanton number and is therefore independent of the applied blowing ratio. A sensitivity study in section 7.2.6 evaluates the influence of St_c and discusses the choice of this parameter. The material anisotropy of the porous C/C samples is considered for all simulations. This concerns the thermal conductivity tensor ($k_{s,eff,\parallel} \approx 7 \cdot k_{s,eff,\perp}$) as well as the permeability tensors ($K_{D,\parallel} \approx 9 \cdot K_{D,\perp}$ and $K_{F,\parallel} \approx 15 \cdot K_{F,\perp}$).

The supersonic outlet is placed sufficiently downstream to avoid any interaction because of recompression to ambient pressure. It can therefore be modelled by a zero-gradient pressure condition. Moreover, as the fluid domain extends up to an axial position of $x = 0.45\,\mathrm{m}$, the film-cooled wake region of the sample can be investigated. All boundary patches except for main and porous inlets are set

to be adiabatic. Kinematic and thermal coupling conditions at the transpired surface are described in section 4.4. A fully-coupled approach between main flow and porous sample is chosen.

7.2.2 Mesh Study

As briefly outlined in chapter 4, assumptions in the physical modelling as well as the numerical solution process itself both introduce errors to the results of a computational simulation. Thus, besides validation by means of comparison to experimental data, also the numerical error of the geometric discretisation has to be addressed. In this regard, the Grid Convergence Index (GCI) method as proposed by Roache [158] and Celik et al. [31] is widely accepted. It is based on Richardson extrapolation [157] applied to the simulation results obtained for three systematically refined numerical grids. The refinement and subsequent extrapolation is to be performed within the asymptotic range which thus yields an 'exact' solution independent of the numerical mesh.

In the frame of this thesis, the procedure as proposed by Cadafalch et al. [29] has been applied to a generic test case with boundary-layer blowing. For this, the main-flow domain as given in figure 7.6 has been discretised in three meshes with 1.15, 3.95, and 13.62 million hexahedral cells (subscripts '3', '2', and '1', respectively). This corresponds to a refinement factor of $r_{12} = r_{23} = 1.51$ for both refinement steps. In the process, the size of the first cell has been scaled while the growing rates h_{i+1}/h_i are kept constant. To comply with the applied turbulence model, a non-dimensional wall distance of $y_1^+ < 1$ has been obeyed during the generation of the three meshes. The medium-sized mesh features the reference resolution which is also employed for the simulations of the transpiration-cooling experiments presented in sections 7.3 to 7.6. Numerical settings have been chosen identical for the generic test case, while boundary conditions are similar but slightly different to the coupled test cases. At the inlet, block profiles are prescribed for the flow variables, i.e. $\boldsymbol{u} = (720\ 0\ 0)$ m/s, $p = 27.5$ kPa, $T = 230$ K, $\kappa = 100$ m^2/s^2, and $\omega = 2 \cdot 10^8$ 1/s. Likewise, the coolant inflow through the porous interface at the top wall is modelled with constant values, i.e. $\boldsymbol{u} = (0\ -5\ 0)$ m/s, $T = 330$ K, $\kappa = 0$, and $\omega = 2 \cdot 10^8$ 1/s. Only the main-flow domain is considered in the GCI analyis, wheareas the porous structure is not included.

Surface values of pressure, temperature, and skin friction in the wake region of the sample (0.229 m $< x <$ 0.450 m) have been selected as the evaluation

variables. The relative local GCI is calculated for the medium-refined mesh according to

$$GCI(\boldsymbol{x}) = \frac{F_s}{r_{23}^{\text{P}} - 1} \left| \frac{f_2 - f_3}{f_1} \right| \quad , \tag{7.2}$$

where f denotes the evaluated variable at $\boldsymbol{x}$, r_{23} is the refinement factor, $F_s = 3$ represents a safety factor, and P is the global observed order of accuracy. The latter is obtained from averaging the local observed order of accuracy $\text{P}(\boldsymbol{x})$ which is defined as

$$\text{P}(\boldsymbol{x}) = \frac{1}{\ln(r_{23})} \ln\left(\frac{f_2 - f_3}{f_1 - f_2} \right) \quad . \tag{7.3}$$

In addition to these values, the percentage of asymptotic as well as oscillatory cells is of interest. The results for the medium-refined mesh have been summarised in table 7.1. The small values given for relative and absolute GCI indicate a sufficient grid resolution of the medium-sized mesh. Moreover, large portions of the cells are converging towards a constant value for grid refinement. However, the asymptotic approximation is not exclusively monotonic but occurs oscillatory for many cells.

Formally, the numerical schemes employed in the simulations are of 2nd order. According to Celik et al. [31], an agreement between formal and observed order of accuracy is an indication of the grids being in the asymptotic range. However, for the investigated case, the observed order of accuracy slightly differs from the formal value, i.e. $\text{P} \neq 2$. As this occurs frequently in practical

Table 7.1: Results of the GCI study for the employed mesh (medium resolution)

	T_{wall}	p_{wall}	$C_f/2$
asymptotic cells [a]	77.4%	57.8%	53.1%
- monotonic asymptotic cells	42.1%	46.9%	37.5%
- oscillatory asymptotic cells	35.3%	10.9%	15.6%
global observed order P [b]	2.66	2.15	1.87
relative local GCI	0 - 0.7%	0 - 4.4%	0 - 18.8%
relative global GCI	0.5%	1.1%	7.5%
absolute local GCI	0 - 2.95 K	0 - 1613 Pa	$0.9 - 18.6 \cdot 10^{-5}$
absolute global GCI	2.05 K	401 Pa	$5.4 \cdot 10^{-5}$

[a] both monotonic and oscillatory asymptotic cells
[b] calculation based on monotonic asymptotic cells [29]

applications of the GCI method, a safety factor of $F_s = 3$ (instead of $F_s = 1.25$) has been employed in the GCI calculation to compensate for the associated uncertainties.

Summing up the results of the mesh sensitivity study, the GCI method reveals no significant numerical error due to the employed geometrical discretisation. The remaining deviations in temperature, pressure, and skin-friction coefficient are considered as small and thus justify the selection of the medium-sized numerical grid for all further simulations.

7.2.3 Reference Test Case

The following section presents the numerical results of a single test case to describe general effects of transpiration cooling as well as the logic of result figures which include experimental and numerical data. For this, a test case using the reference sample and air blowing at $F = 0.50\%$ has been exemplarily selected. Its numerical domain and the applied boundary conditions are given in figure 7.6. Moreover, for the discussion of the example case in this section, simulation parameters are set to $h_v = 10^6 \, \text{W/(m}^3\text{K)}$ and $\text{St}_c = 1$, while the modified blowing boundary condition is applied for the turbulence dissipation rate ω, i.e. equation (4.52). Further test cases for the reference sample with various blowing ratios and different coolant gases are presented in section 7.3.

Figure 7.7 depicts the static temperature contour plot on the symmetry plane and thus gives an overview of the thermal situation for the investigated supersonic transpiration-cooling test cases. Lowest static temperatures occur in the supersonic core flow, while viscous dissipation in vicinity of the walls leads to elevated temperatures in the boundary layer. Besides ordinary boundary-layer growth, an additional thickening is found for the channel top wall where cool air is injected.
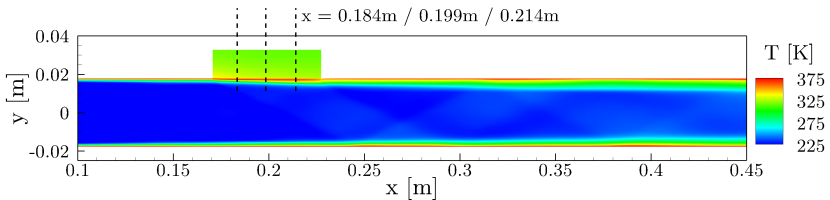
Figure 7.7: Contour plot of temperature for $F = 0.50\%$
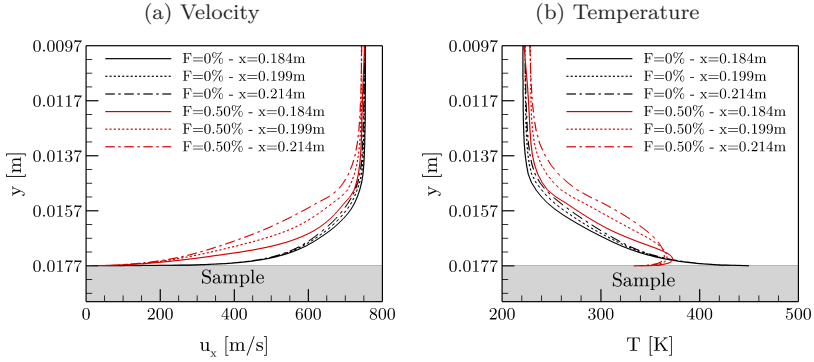
Figure 7.8: Velocity and temperature boundary-layer profiles

Figure 7.8 displays the boundary-layer profiles for axial velocity and temperature at three slice positions, i.e. $x \in [0.184\,\mathrm{m}, 0.199\,\mathrm{m}, 0.214\,\mathrm{m}]$. For the sake of clarity, the ordinate is reversed in the diagrams. Similar to the findings in chapter 6, reduced velocity gradients and an increased boundary-layer thickness is detected when compared to the no-blowing case. Both effects intensify over the transpired surface, i.e. with increasing axial coordinate. Regarding the temperature profiles, typical aspects of wall-bounded supersonic flows are found. The temperature is lowest outside of the boundary layer and increases towards the wall. The transpiration-cooled case corresponds to the cooled-wall case in figure 2.4, whereas the no-blowing case represents the adiabatic-wall case. Boundary-layer blowing yields reduced temperatures directly at the wall ($y = 0.177\,\mathrm{m}$). Moreover, the temperature gradients decrease and the boundary-layer thickness increases over the porous sample, i.e. with rising axial coordinate.

The observed thickening of the boundary layer due to the coolant injection triggers the formation of an oblique shock which may be visualised by schlieren imaging. However, as the flow deflection is small, also the strength of the shock wave is small. Neither the experiment nor the corresponding numerical simulations indicate a significant influence on the axial pressure distribution for the reference-sample test case. More details on this aspect are given in appendix E.3.

The subsequent sections will focus on temperature levels of the investigated porous samples under transpiration cooling. In this regard, it is useful to distinguish between internal and external temperatures, i.e. temperatures within the

porous structure and temperatures on the transpired and non-transpired wall surfaces. The plot logic as well as first results are briefly introduced in the following.

Figure 7.9 illustrates an internal temperature diagram for the reference sample and a blowing ratio of $F = 0.50\%$. Temperature is plotted over the vertical coordinate y, while the position of the reference sample is indicated by the grey area. The sample has a thickness of 15 mm and spreads from $0.0177\,\text{m} < y < 0.0327\,\text{m}$. Numerical temperature distributions are given by solid and dashed lines which represent solid-phase temperature and fluid-phase temperature, respectively. If not stated otherwise, the continuous data is extracted on the sample's centre line, i.e. $x = 0.199\,\text{m}$, $z = 0$. Experimental thermocouple measurements are depicted by filled symbols. Due to the installation of thermocouples as described in section 3.2, the measurement is assumed to correspond to the solid-phase temperature. The simulation equivalent, i.e. the numerical solid-phase temperatures at the thermocouples' positions, are given by hollow symbols. In addition to internal temperatures, also the reservoir temperature averaged from two thermocouples is included in the diagram. In the experiments, both thermocouples were positioned within the coolant reservoir with a distance of around 5 mm to the sample's backside. If applicable, different symbol types and colours are employed to represent the included blowing ratios (e.g. section 7.3). Figure 7.9 depicts the temperature rise from coolant-reservoir side Γ_{PM} ($y = 0.0327\,\text{m}$) to hot-gas side Γ_{HG} ($y = 0.0177\,\text{m}$). It is found that the temperature gradient within the material rises towards the hot-gas side.
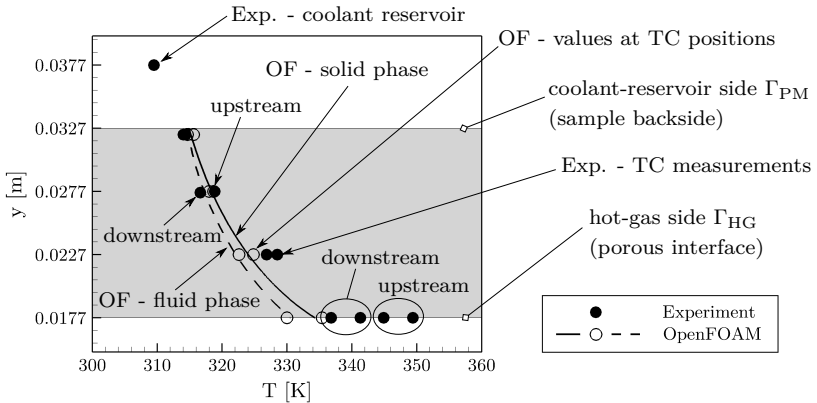

Figure 7.9: Internal temperature distribution for example case $F = 0.50\%$

Moreover, the fluid-phase temperature is only slightly below the corresponding solid-phase values for the applied volumetric heat transfer coefficient of $h_v = 10^6$ W/(m^{3}K). The two thermocouple measurements for a certain sample depth are slightly differing which is due to the respective axial positions (upstream/downstream). The temperatures generally decrease in axial direction due to the coolant film build-up. Additionally, moderate deviations are found for the pairs of surface thermocouples at identical axial position but different lateral positions.[6] Regarding the discrete numerical temperatures evaluated at the thermocouple positions, similar deviations are observed. Again, the lower temperatures for a given sample depth (i.e. y-coordinate) correspond to the downstream positions. However, the differences between slice data (extracted at $x = 0.199$ m, $z = 0$) and discrete numerical values are small. Experimental and numerical results show a generally fair agreement. More detailed analyses and comparisons are given in the following sections.

Besides internal cooling, also the external surface temperatures are reduced through transpiration cooling. Figure 7.10 exemplarily illustrates the corresponding external temperature plot for $F = 0.50\%$. Again, the diagram includes both numerical and experimental data for the channel's top wall. Thermocouple measurements are spread over the channel length and are given by filled symbols. As for the internal temperature plot, numerical values extracted at the thermocouple positions are given by hollow symbols. Moreover, a continuous experimental temperature distribution is obtained from averaging a central strip of in-situ calibrated IR data. For doing so, pixels between -10 mm $< z < 10$ mm are laterally averaged and subsequently plotted as dashed lines. Similar to this, numerical values of the channel's top wall are spanwise-averaged for $|z| < 10$ mm (half domain) and depicted by a solid line. While the field of view is limited for the IR data due to the size of the employed sapphire window, the numerical equivalent extends the continuous temperature distribution further downstream.

The influence of transpiration cooling on the temperature of external surfaces is clearly illustrated in figure 7.10. The blowing ratio of $F = 0.50\%$ yields steeply decreasing temperatures at the beginning of the transpired area and then more slowly over the sample surface. Downstream of the sample, the temperature rises again. However, a cooling effect remains visible for the complete length

---

6   The four surface thermocouples are in good agreement for the no-blowing test case. Additionally, further measurements at $x = 0.279$ m indicate that the thermal flow field in the channel centre (-10 mm $< z < 10$ mm) is not significantly affected by lateral inhomogeneities. The here-observed differences for boundary-layer blowing are also present in the infrared images (see section 7.3) and might be due to non-homogeneous blowing behaviour of the porous sample.
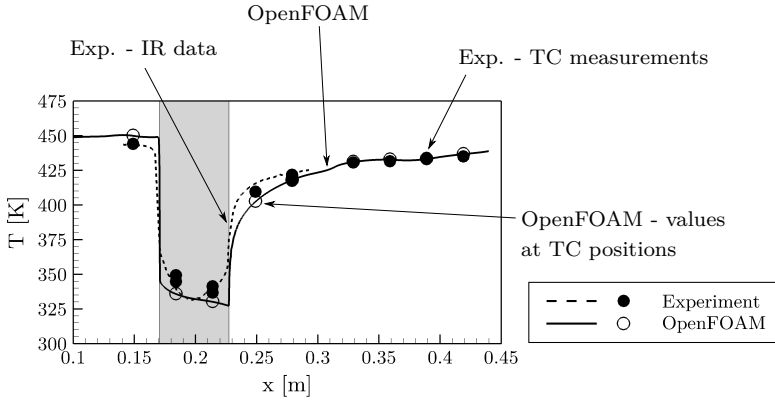
Figure 7.10: External temperature distribution for example case $F = 0.50\%$

observed. The earlier discussed lateral deviations in the thermocouple measurements on the porous surface are also visible here, i.e. at $x = 0.184\,\text{m}$ and $x = 0.214\,\text{m}$. For reasons of clarity, multiple measurements at a given axial coordinate are averaged for the plots in subsequent sections.

As stated earlier, the three temperatures corresponding to main flow T_{hg}, porous solid T_s, and porous fluid T_f are co-occurring at the porous interface Γ_{HG}. The transition-layer model as described in section 4.4.2 is employed to relate the three temperatures. Figure 7.11 illustrates the situation for a slice at $x = 0.199\,\text{m}$ through the symmetry plane. In the figure, the temperature
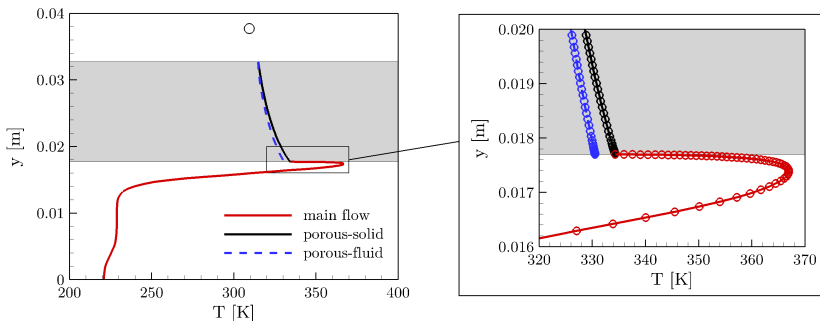
Figure 7.11: Thermal situation at porous interface exemplarily shown for sample's centre line ($x = 0.199\,\text{m}$, $z = 0$)

distribution from channel centre to coolant reservoir is depicted. From low values in the supersonic core flow ($T \approx 222\,\mathrm{K}$), the temperature rises within the boundary layer to a maximum ($T \approx 367\,\mathrm{K}$) before decreasing to the cooled wall temperature ($T \approx 334\,\mathrm{K}$). The latter is prescribed to the main-flow domain as a coupling condition. It originates from the porous region calculation and is equal to the solid-phase temperature at the porous interface. As visible in the detail view, the fluid-phase temperature at the interface is reduced when compared to the other two temperatures ($T_f \approx 330\,\mathrm{K} < T_{hg} = T_s \approx 334\,\mathrm{K}$). In spite of this, the conservation of energy is satisfied across the interface due to the applied transition-layer model. In brief, the convective heat flux from main flow to porous wall is reduced by the amount required to heat up the coolant fluid from $T_f \approx 330\,\mathrm{K}$ to $T_{hg} \approx 334\,\mathrm{K}$.

7.2.4 Turbulence Boundary Condition

The porous surface is modelled by a continuous blowing approach which has to be combined with appropriate turbulent boundary conditions. To determine the numerical settings, three different turbulent boundary conditions for the porous interface are evaluated by comparison to experimental data. Again, the reference test case with a blowing ratio of $F = 0.50\%$ has been selected for the comparison. As described in section 4.4.2, the turbulent kinetic energy is set to $\kappa = 0$ at the interface for all cases, while the specific dissipation rate ω is modelled in different ways as given by equations (4.24), (4.50), and (4.52). All remaining parameters are kept constant for the sensitivity study, i.e. $h_v = 10^6\,\mathrm{W/(m^3 K)}$ and $\mathrm{St}_c = 1$. Figures 7.12 and 7.13 depict the external and internal temperature distributions for the three cases. Compared to the previous diagrams, error bars have been added to the figures (see appendix A for more details on the uncertainty analysis).

The choice of the ω boundary condition on the transpired surface has a significant influence on the temperature levels over the sample surface, whereas the wake region remains unaffected. Comparing to the experimental values, the SST standard boundary condition for non-porous refined walls, i.e. equation (4.24), exhibits the greatest deviations. The blowing modification by Wilcox [204] which is defined by equation (4.50) reduces the value of ω in close vicinity of the wall. This results in a reduced dissipation of turbulent kinetic energy κ which leads to enhanced turbulent transport and thus higher wall temperatures. The results using the modified blowing boundary condition as given by equation (4.52) are closest to the experimental data. The condition is based on
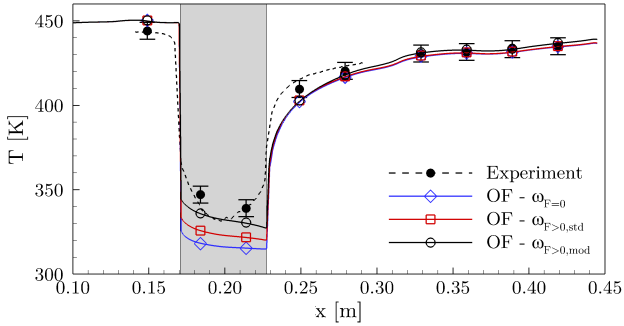
Figure 7.12: Wall temperature over channel length for sensitivity study on ω-BC

Wilcox' suggestion but additionally takes the wall's porosity into account. For the here-employed low-porosity material C/C ($\varepsilon = 10.2\%$), this results in even smaller ω values at the porous interface and thus elevated wall temperatures which are closest to the experimental data.

The findings are supported by the results for the internal temperature distribution given in figure 7.13. From the slope of the three curves, an increase of the wall heat flux $\dot{q}_s$ is notable for Wilcox' blowing condition and even more pronounced for the modified blowing condition. Moreover, the agreement to the experimental measurements is best for this condition, while the largest deviations occur for the standard ω boundary condition.
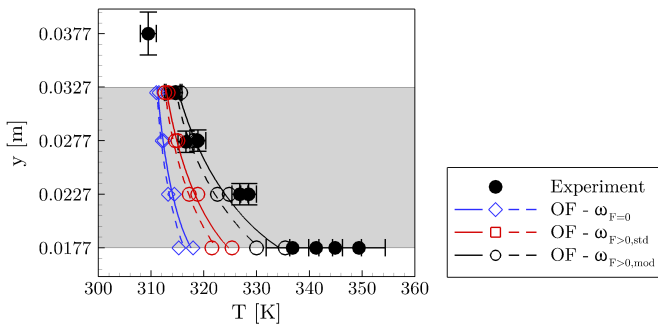
Figure 7.13: Internal temperature over sample thickness for sensitivity study on ω-BC

Summing up the sensitivity study, a strong sensitivity of the sample's surface temperature T_s on the applied ω condition is found. In contrast, the wake region is not affected. Based on the comparison to experimental data, the modified blowing condition given by equation (4.52) is selected for all following simulations. Later, in section 7.6, this finding is confirmed also for non-flat sample geometries and more complex flow conditions.

7.2.5 Volumetric Heat Transfer Coefficient

As discussed in section 5.1, the volumetric heat transfer h_v has not been determined for C/C up to now. To investigate its influence, a sensitivity study is performed based on the reference test case with a blowing ratio of $F = 0.50\%$. For the sensitivity study, all parameters except for h_v are kept constant. With respect to the coolant-side boundary condition, a Stanton value of $\mathrm{St}_c = 1$ is set, while the modified blowing condition $\omega_{F>0,mod}$ is used. A simplified approach assuming a constant volumetric heat transfer coefficient in the complete porous domain is followed. In line with the analysis in section 5.1, the value of h_v is varied between $10^4 \, \mathrm{W/(m^3 K)}$ and $10^7 \, \mathrm{W/(m^3 K)}$. The numerical results (lines) are compared to experimental data (symbols) in figure 7.14. Regarding the simulation data, the diagram depicts the internal temperature distributions for solid phase (solid line) and fluid phase (dashed line) over the porous wall. From the figure, a significant influence on the temperature distributions is found for the variation in h_v. For the two lower h_v-values, i.e. 10^4 and $10^5 \, \mathrm{W/(m^3 K)}$, only little heat is transferred from solid phase to fluid phase.
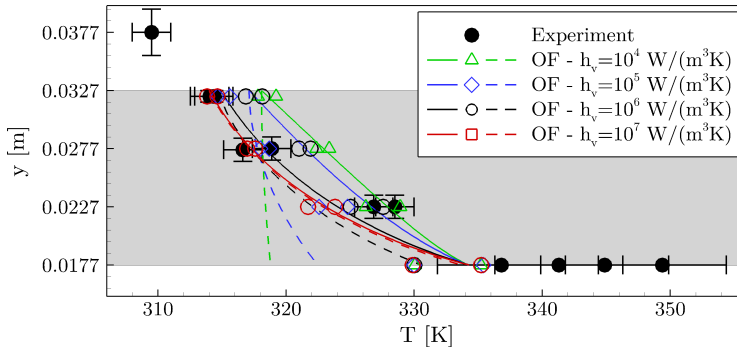

Figure 7.14: Internal temperature over sample thickness for sensitivity study on volumetric heat transfer coefficient h_v

Thus, the increase in coolant-fluid temperature is small when compared to the solid-phase temperature rise over the sample thickness. The two higher h_v-values lead to a more intense internal heat transfer between solid and fluid phases. Consequently, T_f and T_s are rising similarly over the porous wall. Differences between both temperatures are limited to the vicinity of the hot-gas interface Γ_{HG} and nearly vanish for $h_v = 10^7 \, \text{W}/(\text{m}^3\text{K})$. The slope of the temperatures indicates that heat transfer by conduction reduces with increasing distance from the hot-gas side. This is due to the internal heat exchange between solid and fluid phases for the larger h_v-values.

When comparing simulation results to experimental data, good agreement to all thermocouple measurements is found for values $h_v \approx 10^6 \, \text{W}/(\text{m}^3\text{K})$. The solid-phase temperature at the porous interface, i.e. T_s at Γ_{HG}, is equal for all cases. This is a consequence of the employed transition-layer model and the system-adiabatic coolant side, see section 4.4. Thus, the temperature at the hot-gas side, i.e. T_s at Γ_{HG}, is insensitive to the variation of h_v. As this extends to the wake region, the external temperature distribution for all h_v-values is given by the black line in figure 7.12. Regarding the coolant side, different temperatures T_f are found for the coolant fluid entering over the boundary Γ_{PM}. This results from the system-adiabatic boundary condition with $\text{St}_c = 1$ that couples the solid-phase temperature gradient to the rise in fluid temperature, i.e. $(T_f - T_c)$ at Γ_{PM}.

In summary, good agreement is found for $h_v = 10^6 \, \text{W}/(\text{m}^3\text{K})$. This value is selected for the simulations in sections 7.3 to 7.6.

7.2.6 Thermal Boundary Condition on Coolant Side

Similar to the volumetric heat transfer coefficient, also the choice of the thermal boundary condition on the coolant side is not trivial. Within the frame of this thesis, a system-adiabatic boundary condition has been selected as described in section 4.4.1. The condition can be formulated by means of the Stanton number St_c as given by equation (4.36). In the following, the influence of a constant $\text{St}_c \in [0, 0.25, 0.5, 1]$ is investigated. For the study, the volumetric heat transfer coefficient is kept at a constant value of $h_v = 10^6 \, \text{W}/(\text{m}^3\text{K})$ and the modified blowing condition $\omega_{F>0,mod}$ is set at the porous interface.

The internal temperature diagram for the sensitivity study is given in figure 7.15. In general, the internal temperatures show only little dependency on the applied St_c number. The observed deviations are limited to the entrance region in direct vicinity of the coolant side boundary, i.e. $0.0277 \, \text{m} < y < 0.0327 \, \text{m}$. This finding is supported by other studies, e.g. Maiorov [125]. The detail view in figure 7.15
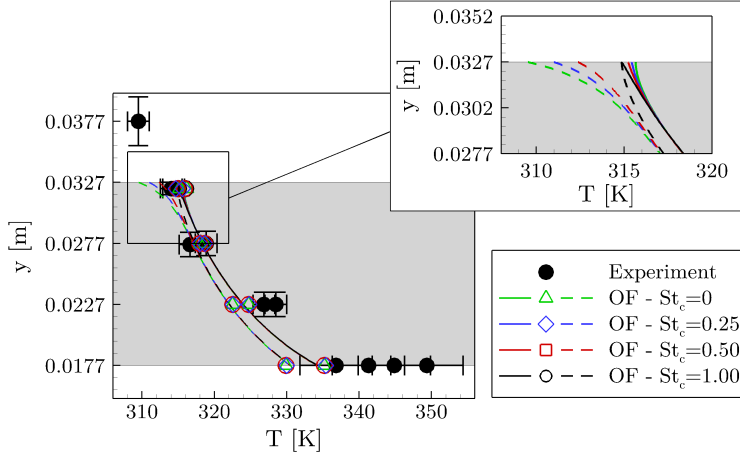
Figure 7.15: Internal temperature over sample thickness for sensitivity study on backside Stanton number St_c

illustrates fluid-phase and solid-phase temperatures in the entrance region more clearly. Based on the prescribed boundary condition, i.e. equation (4.35), the solid-phase temperature gradient $\partial T/\partial n$ at the reservoir side Γ_{PM} results in a heat flux into the coolant plenum. The model equals this heat flux to the temperature rise of the entering fluid, see equation (4.34). For $St_c = 0$ the coolant enters the structure with $T_f = T_c$ at Γ_{PM}, while the solid-phase temperature gradient is zero. However, due to the intense internal heat transfer ($h_v = 10^6\,\mathrm{W/(m^3 K)}$), the coolant fluid is quickly heated within the porous structure. The contrary extreme occurs for $St_c = 1$, where fluid- and solid-phase temperatures are equal at the coolant side, i.e. $T_f = T_s$ at Γ_{PM}. This represents a limiting case, as for values $St_c > 1$ the fluid-phase temperature would rise over the solid-phase temperature which is generally not physical for transpiration cooling. The two remaining values of St_c yield distributions in between the other solutions, i.e. $T_c < T_f < T_s$ at Γ_{PM}. However, for all St_c-values the temperature distributions are coinciding after an accommodation length of around 5 mm. As for the sensitivity study on h_v, the temperatures at the porous interface are found to be equal for all cases. Again, this is a consequence of the applied transition-layer model and results in identical external temperature distributions as given by the black line in figure 7.12.

As a result of the sensitivity study on the Stanton number, only little influence on the solid-phase temperature distribution is found for the investigated test case. The condition $St_c = 1.0$ is selected for all subsequent simulations.

7.2.7 Summary

In this section, the numerical setup for transpiration-cooling cases in supersonic flow has been presented and evaluated with respect to the employed numerical grid as well as several modelling parameters. The mesh study based on the GCI method demonstrated a general independence of simulation results and thus indicates a sufficient resolution of the employed mesh. Following this, sensitivity studies on several modelling parameters have been performed to determine their influence on the simulated test case. Regarding the turbulent boundary condition for the transpired surface, a strong sensitivity of the hot-gas wall temperature (T_s at Γ_{HG}) as well as the slope of the temperature distribution (related to $\dot{q}_s$) was found. The volumetric heat transfer coefficient h_v changes the slope of the temperature distribution but has no influence on the wall temperature of the hot-gas side. In contrast to this, the choice of St_c only influences the entrance region close to the coolant-reservoir side. Based on the comparison to experimental data, the modified blowing condition $\omega_{F>0,mod}$, $h_v = 10^6 \, \mathrm{W/(m^3 K)}$, and $St_c = 1.0$ are selected for all subsequent simulations.

7.3 Reference Sample - Uniform Main Flow and Flat Sample

In the previous sections, the supersonic channel flow without boundary-layer blowing as well as the numerical setup of the transpiration-cooling cases were discussed. Moreover, several simulation parameters were determined based on sensitivity studies. Now, the focus is shifted on transpiration cooling for various test conditions. A combined experimental and numerical approach is followed to analyse the physical processes and simultaneously validate the developed OpenFOAM solver.

The analysis starts with the reference sample which has been tested at supersonic channel-flow conditions, i.e. M = 2.5, $T_{tot} = 500\,\text{K}$, $\dot{m}_{hg} = 0.436\,\text{kg/s}$, and $p_{tot} = 0.5\,\text{MPa}$. After integration into the test section, the flat porous C/C sample is flush with the top wall of the channel and spreads from $0.169\,\text{m} < x < 0.229\,\text{m}$ in the previously defined coordinate system. The analysis of transpiration cooling concentrates on the external and internal temperature distributions as well as the cooling efficiencies. Besides, the influences of blowing ratio and coolant gas properties are investigated. In addition to the transpired surface and the porous sample, also the film-cooled wake region is considered. To validate the developed OpenFOAM solver, a comparison of experimental measurements to corresponding simulations is performed for all investigated aspects. Regarding this, the continuous blowing model which was previously applied to the simulation of subsonic channel flow and a sintered stainless-steel sample is also validated for boundary-layer blowing through C/C in a supersonic main flow. An overview of the simulation parameters applied for all C/C samples is given in table 7.2.

7.3.1 Air Injection

First, the injection of coolant air into the hot main flow of air is investigated. The analysis is divided into external and internal regions which correspond to the transpired and channel-wall surfaces, and the porous wall segment, respectively. Moreover, the discussion focuses on the temperature levels and cooling efficiencies.

Internal temperature distribution

Based on the intense internal heat exchange between porous structure and the through-flowing coolant, the temperature of the porous wall reduces.

Table 7.2: Simulation parameters for supersonic transpiration-cooling test cases

Porosity	ε	[%]	10.2		
Density	$\rho_{s,eff}$	[kg/m^3]	1380		
Specific heat capacity	$c_{p,s}$	[J/(kgK)]	750		
Volumetric heat transfer coefficient	h_v	[W/(m^{3}K)]	$1 \cdot 10^6$		
Permeability coefficients	$\boldsymbol{K_D}$	[10^{-13}m^2]	$\begin{pmatrix} 7.110 & 0 & 0 \\ 0 & 7.110 & 0 \\ 0 & 0 & 0.781 \end{pmatrix}$		
	$\boldsymbol{K_F}$	[10^{-8}m]	$\begin{pmatrix} 8.660 & 0 & 0 \\ 0 & 8.660 & 0 \\ 0 & 0 & 0.586 \end{pmatrix}$		
Thermal conductivity	$\boldsymbol{k_{s,eff}}$	[W/(mK)]	$\begin{pmatrix} 13.8 & 0 & 0 \\ 0 & 13.8 & 0 \\ 0 & 0 & 1.9 \end{pmatrix}$		

Figure 7.16 depicts experimental and numerical temperature distributions over sample thickness for blowing with air at various blowing ratios $F = (\dot{m}_c/A_c)/(\dot{m}_{hg}/A_{hg})$. The experimental data is recorded by means of several thermocouples installed within the C/C samples, see section 3.2. The hot-gas-side surface measurements at identical axial positions are averaged. For the sake of clarity, error bars are omitted, see appendix A for details on the uncertainty analysis. The numerical data is extracted on the sample's centre line ($x = 0.199$ m, $z = 0$). Discrete numerical values at the thermocouple positions are not included in the figure.

The results demonstrate a significant temperature reduction for transpiration cooling already at small blowing ratios. For intensified blowing the internal temperature levels decrease further up to nearly complete cooling for large blowing ratios (i.e. $T \approx T_c$ for $F = 1\%$). In accordance with this, the surface temperatures at the hot-gas side decrease for rising blowing ratio. Differences between measurements at identical y-positions are due to the respective axial positions. Downstream temperature values are reduced due to the build-up of a coolant film. Moreover, a dependency of the measured coolant-reservoir temperature T_c on the blowing ratio is found.

Comparing numerical and experimental results, a generally good agreement is found for all blowing ratios. In general, deviations are small with respect to the measurement uncertainties. However, slightly larger deviations are observed at the entrance region ($y = 0.0322$ m) for small blowing ratios, e.g. $F = 0.10\%$.
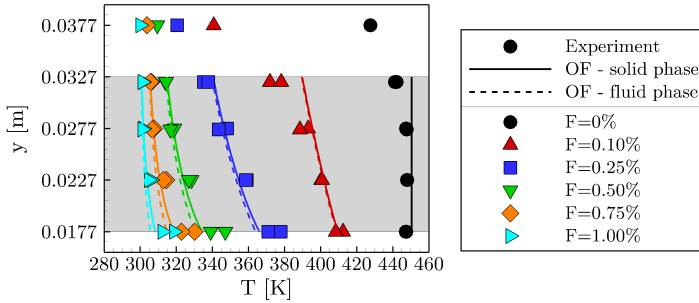
Figure 7.16: Numerical and experimental internal sample temperature for reference sample at different blowing ratios

At this position, the experimental measurement by means of thermocouples is challenging due to the large thermal gradients.

The heat fluxes transferred by conduction from hot-gas side to coolant-reservoir side are visualised by the curves' slopes and can be calculated from the temperature gradients. Neglecting the fluid-phase contribution ($k_f \ll k_s$), this yields $\dot{q}_s = -\boldsymbol{n} \cdot (\boldsymbol{k}_{s,eff} \nabla T_s)$ for the local heat flux over the porous surface. Figure 7.17 depicts the numerical heat flux $\dot{Q}_s/A_c$ surface-averaged for hot-gas side Γ_{HG} and coolant-reservoir side Γ_{PM}.

The heat flux $\dot{Q}_s/A_c$ at the hot-gas side Γ_{HG} varies with blowing ratio F which is due to two counteracting effects. First, a decrease of the wall temperature (as a result of transpiration cooling) increases the driving temperature difference. Secondly, the injection of cool fluid reduces the heat transfer coefficient as
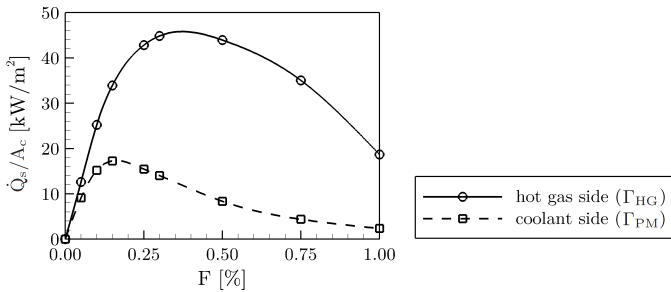
Figure 7.17: Solid-phase heat transfer by conduction

discussed in section 2.3.1. Therefore, $\dot{Q}_s/A_c$ first increases up to a maximum, i.e. $\dot{Q}_s/A_c \approx 46\,\text{kW/m}^2$ for $F \approx 0.35\%$, before decreasing at higher blowing rates. A similar curve is found for the conduction heat flux at Γ_{PM}. The maximum value is observed for $F \approx 0.15\%$, while the heat flux reduces for larger blowing ratios.

External surface temperature

The previous results demonstrated that transpiration cooling significantly reduces the temperature levels within the porous sample. The analysis examined the temperature distribution over the sample thickness and considered the thermal situation one-dimensionally. However, the thermocouple pairs at same depth, i.e. identical y-coordinate, indicated an influence of the axial position. Now, the wall temperature distribution over channel length is assessed for various blowing ratios. Figure 7.18 depicts experimental and numerical wall temperatures for the sample surface and the wake region. Besides discrete thermocouple measurements, IR data and OpenFOAM results are included in the diagram. The two last-mentioned are spanwise-averaged for $|z| < 10\,\text{mm}$.

The diagram confirms the previous findings discussed by means of figure 7.10. A strong temperature reduction at the beginning of the transpired surface is found. The temperature slightly reduces over the porous sample's length due to the effect of the growing coolant film. At the transition to the wake region, the temperature rises again. Still, reduced temperature levels are found for the complete length observed. The temperature reduction intensifies with increasing blowing ratio. However, it can be noted that the additional cooling effect reduces at higher blowing ratios.

Figure 7.18: Numerical and experimental wall temperature for reference sample at different blowing ratios

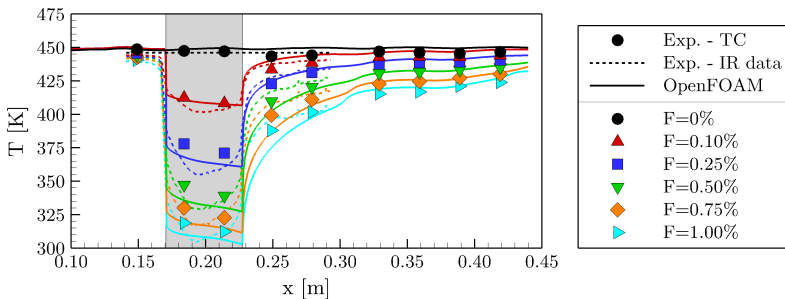A generally good agreement between experimental measurements and numerical simulations is found. The simulation slightly overpredicts the cooling effect on the sample surface and in the direct wake region ($0.229\,\mathrm{m} < x < 0.3\,\mathrm{m}$). Further downstream, the simulation is in good agreement to the experiment. While the simulation's deviations to the discrete thermocouple measurements are moderate, larger differences are found with respect to the spanwise-averaged IR data. The continuous curve reveals a less abrupt temperature drop at the leading edge of the sample. Moreover, in contrast to the simulation results, the temperature rises already on the transpired surface. A possible explanation are parasitic lateral heat fluxes from the surroundings into the sample. The effect intensifies for higher blowing ratios where the temperature difference between cooled sample and uncooled surroundings is larger. Following this finding, the influence of lateral heat-conduction effects is investigated in more detail in section 7.3.2.

For the highest blowing ratios, the temperature curve exhibits a small fluctuation at $x \approx 0.3\,\mathrm{m}$. This is due to the (weak) oblique shock wave caused by boundary-layer blowing. It is reflected at the channel's bottom wall and subsequently hits the top wall at $x \approx 0.3\,\mathrm{m}$. An exemplary schlieren image illustrating this is given in appendix E.3.

Surface temperature distributions

Infrared thermography allows the non-intrusive determination of temperatures on large surface areas. To be able to evaluate the data not only qualitatively but also quantitatively, an in-situ calibration based on surface thermocouples has been performed, see section 3.3.4. The so-obtained IR data has already been used in the previous diagrams to obtain an experimentally measured, continuous temperature distribution. Instead of spanwise-averaged lines, now the two-dimensional wall temperature fields are examined. Figure 7.19 exemplarily illustrates the temperature distribution for air as coolant and two blowing ratios. The contour plots compare experimental (top half) and numerical (bottom half) results. Due to the size of the employed sapphire window, only the sample and the direct wake region (up to $x = 0.285\,\mathrm{m}$) are captured in the IR images.

The contour plots support the previous findings and indicate a significant reduction of temperatures on the transpired surface as well as in the wake region. Regarding the temperature levels, a fair agreement between IR data and simulation is found for the transpired surface while deviations are observed in the wake region. With respect to the sample's surface, the IR images reveal slight
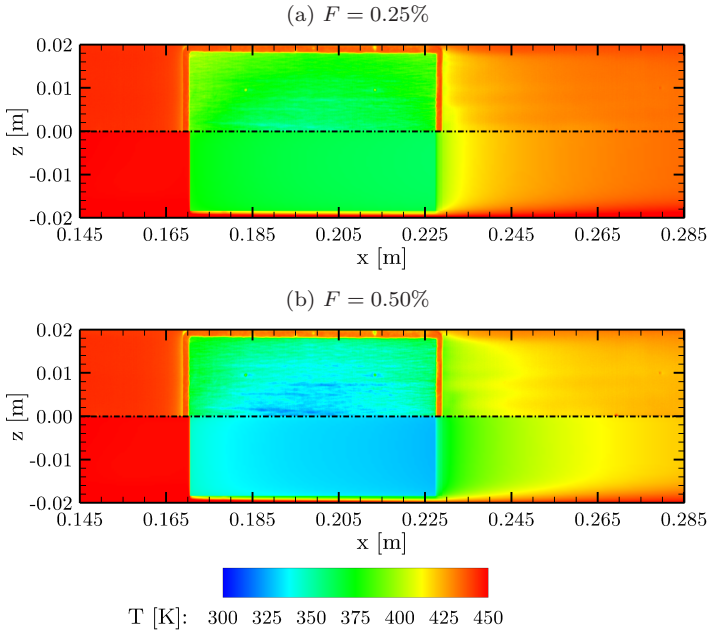
Figure 7.19: Comparison of sample surface and wake region temperatures - in-situ calibrated infrared thermography (top half) and OpenFOAM simulation (bottom half)

non-uniformities in the temperature field which are due to the sample's blowing behaviour. Additionally, the fibre character of C/C and the associated non-uniform surface emissivity become visible. As a consequence of the non-uniform coolant blowing, a weak thermal stratification in the wake region is observed (i.e. hot and cold streaks). These effects are not captured by the volume-averaged numerical simulation approach. Furthermore, the experimentally measured temperature distributions exhibit higher temperatures in the sample's boarder regions whereas the numerical distribution is more uniform. This especially applies to the larger blowing ratio, i.e. $F = 0.50\%$. The higher temperatures close to the leading edge are connected to the non-existent coolant film, and are also slightly visible in the simulation results. However, the temperatures are higher in the experiment which implies the existence of another influencing effect. Likewise, the elevated temperatures in the side-wall and trailing-edge region are not present in the numerical contour plot. Possible explanations are lateral heat conduction into the porous sample and/or a reduced through-flow

permeability close to the sample's boarder and thus less blowing. Also the corner vortices present in the rectangular channel flow may have an influence on the side-wall regions. The first-mentioned effect is investigated by means of a simulation setup including the sample's surroundings in the following section.

7.3.2 Lateral Influences on Thermal Situation of Porous Sample

Different non-desired effects may occur in transpiration-cooling experiments and introduce uncertainties or difficulties in the subsequent analysis of results. Lateral heat conduction from the test channel into the porous sample or vice versa represents such an effect as found by Langener [111]. In his experiments with a water-cooled test section, relatively large heat fluxes were transported from the (typically hotter) porous sample to the cold surroundings, thus altering the measurements which complicated the result analysis. Likewise, for an uncooled test channel as considered in the frame of this thesis, heat fluxes from the hot surroundings into the cold porous sample may occur. To obtain precise temperature measurements and to eliminate this effect to a large extent, extensive efforts have been put into the thermal insulation of the porous sample for the here-presented tests. As described in chapter 3, an insert made from the thermally low-conducting PEEK material ($k_{PEEK} \approx 0.25\,\mathrm{W/(mK)}$) has been employed in the experimental setup. It is completely surrounding the porous sample and is in direct contact with the galvanised copper layer of the sample, see figure 3.4. The thin copper layer is required to seal the porous sample but may introduce heat-conduction effects due to the large thermal conductivity of copper ($k_{copper} \approx 380\,\mathrm{W/(mK)}$). In this regard, the previously discussed axial temperature distributions as well as the IR images revealed some deviations between numerical and experimental results. These could be due to lateral heat fluxes into the sample.

To investigate the effect in more detail, simulations with an enlarged numerical domain as shown in figure 7.20 have been carried out. In addition to the porous C/C material and the main-flow channel, solid regions for PEEK, galvanised copper layer, and stainless-steel mounting frame ($k_{steel} \approx 21\,\mathrm{W/(mK)}$) are included. The simulation is fully coupled, meaning that all interfaces between regions are considered as heat-exchanging surfaces. No thermal contact resistances between solid regions are considered in the analysis. Regarding the boarders of the numerical domain mainly adiabatic conditions have been selected. This corresponds well to the experimental setup where air gaps and cavities reduce the heat fluxes at these surfaces to a minimum. Exceptions to this are the boundary conditions at the top of the steel mounting frame and the bottom surface of the PEEK insert which is in contact with the channel's

$T_{steel} = f(\dot{m}_c)$

PEEK insert

stainless-steel
mounting frame

$T_{PEEK} = 446.1\,\mathrm{K}$
(only overhang)

hot gas channel

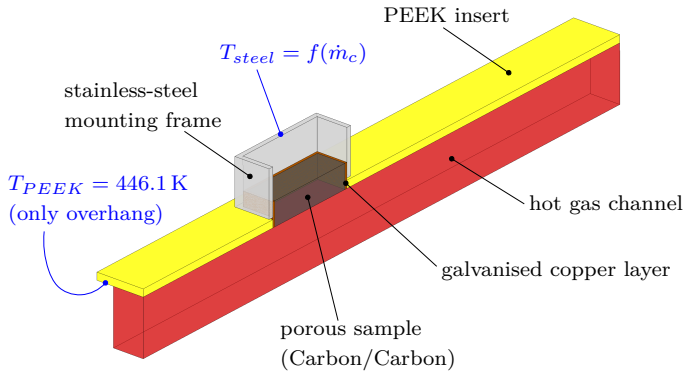galvanised copper layer

porous sample
(Carbon/Carbon)

Figure 7.20: Enlarged numerical domain to investigate lateral heat-conduction
effects (half model)

side wall. The first-mentioned temperature is measured in the experiment by
two thermocouples which are led through the coolant reservoir and attached
to the mounting frame. The averaged value of both is then prescribed as an
input to the numerical simulation. As in the experiment, the temperature
boundary condition for the stainless-steel mounting frame varies with the
applied blowing ratio, i.e. $T_{steel} = f(\dot{m}_c)$. Secondly, the temperature of the
bottom surface of the PEEK which is not in contact with hot gas is set to
the channel wall temperature without blowing which has been measured to be
$T_{PEEK} = 446.1\,\mathrm{K}$.

Figure 7.21 shows a temperature contour plot of the solid and porous regions
for $F = 0.50\%$. The main-flow domain is not included in the plot. In general,
the porous-sample domain, i.e. the C/C material, is at the lowest temperature,
while the highest temperatures occur upstream of the sample and in the side-
wall region ($|z| > 20\,\mathrm{mm}$). From the temperature levels, different heat flow
rates into the porous-sample domain can be identified. In addition to heat flow
rates from PEEK to the porous sample respectively copper layer at front, back,
and side of the sample, a smaller heat flow rate is transported from the top of
the steel mounting into the sample.

Figure 7.22 depicts the external temperature diagram over axial channel length
for different blowing ratios. The plot logic deviates from the previous descrip-
tion. Here, solid lines represent the spanwise-averaged numerical results for
the enlarged domain, whereas the dashed lines give the original results for the
standard-domain simulation (without additional solid regions). Experimental
results are included by means of thermocouple measurements (solid symbols)
and spanwise-averaged IR data (hollow symbols, averaged for $|z| < 10\,\mathrm{mm}$).
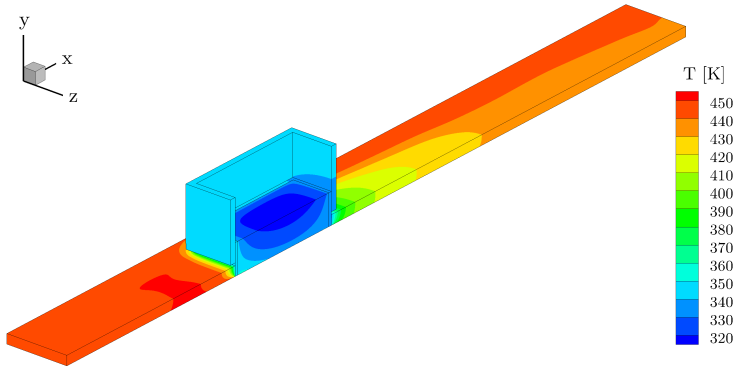
Figure 7.21: Temperature contour plot for enlarged half domain and $F = 0.50\%$

Comparing the numerical results with and without inclusion of the additional solid regions, a moderate influence on the temperature distribution is found. The simulation results for the enlarged numerical domain and the two larger blowing ratios show a slower decrease of temperatures close to the leading edge of the porous sample. Moreover, the numerical temperatures increase towards the trailing edge for $F = 0.50\%$, and more significantly for $F = 1.00\%$. Both effects are also present in the experimental IR data. The deviations between simulations with and without surroundings increase with blowing ratio. This follows from the generally reduced temperature levels of the porous sample at higher blowing ratios which increases the temperature difference that causes heat conduction between uncooled surroundings and sample. Consequently, the influence of lateral heat fluxes on the porous wall temperature is small
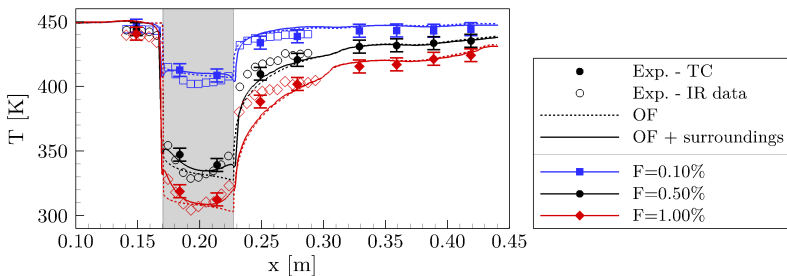
Figure 7.22: Wall temperature over channel length for different blowing ratios, comparison between standard and enlarged numerical domains

for $F = 0.10\%$, whereas a more significant influence is found for the test case with $F = 1.00\%$. However, the temperature increase is limited to the vicinity of the copper layer for all test cases. In contrast, the temperatures in the centre of the porous sample are mostly unchanged. This also applies to the positions of the surface thermocouples which are located close to the centre. Likewise, the surface temperatures in the wake region remain largely unaffected by the consideration of the surrounding solid regions for all blowing ratios tested.

Figure 7.23 exemplarily depicts comparisons of surface temperatures for $F = 0.50\%$. First, numerical simulation and IR image are compared and secondly, the numerical results with and without consideration of the sample's surroundings are shown. Figure 7.23a indicates a better agreement to the experimental data for the simulation using the enlarged domain when compared to the previous analysis for the standard-domain simulation. This concerns the regions close to the sample's leading and trailing edges as well as close to the channel's side wall. However, the deviations in the wake region remain similar. The direct comparison of numerical simulation results given in figure 7.23b highlights the influence of lateral heat conduction into the porous sample. Here, also a change in the wake region is notable.

(a) Infrared thermography (top half) and OpenFOAM with surroundings (bottom half)
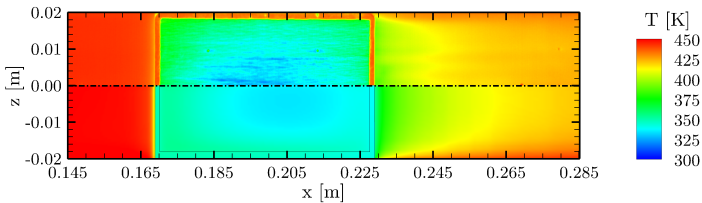
(b) OpenFOAM without (top half) and with (bottom half) surroundings
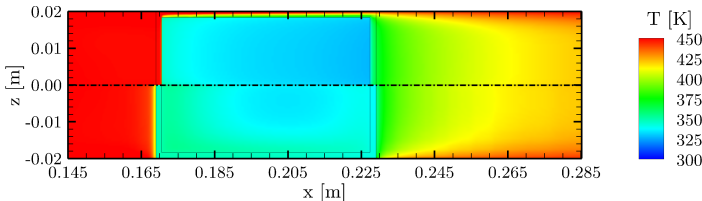
Figure 7.23: Numerical and experimental wall temperature distributions for $F = 0.50\%$
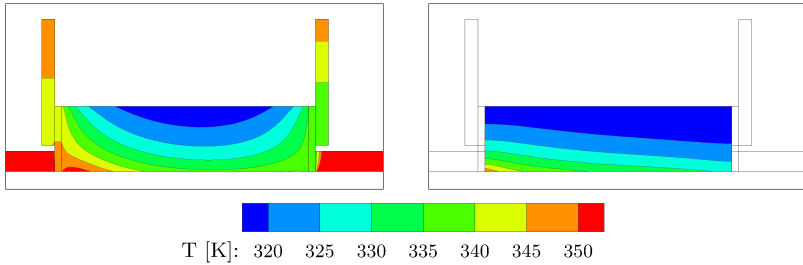
Figure 7.24: Comparison of solid-phase temperature distribution on sample's symmetry plane between simulation with and without surroundings for $F = 0.50\%$

The observed lateral heat fluxes into the C/C sample also change the temperature levels within the porous wall. The solid-phase temperature of the sample with and without consideration of the surroundings is illustrated for $F = 0.50\%$ in figure 7.24. The contour plots demonstrate the higher temperatures close to the copper frame where the lateral heat flow rate is added to the porous sample. As stated before, heat is not only transported from PEEK to the copper frame (and subsequently the sample) but also from the stainless-steel mounting frame. Considering only the sample's central region, both simulation cases show similar temperatures.

This is confirmed by the internal temperature diagram depicted by figure 7.25. In the comparison, the centre line data for both simulation cases is nearly coinciding, thus indicating small deviations at the axial position $x = 0.199\,\mathrm{m}$.
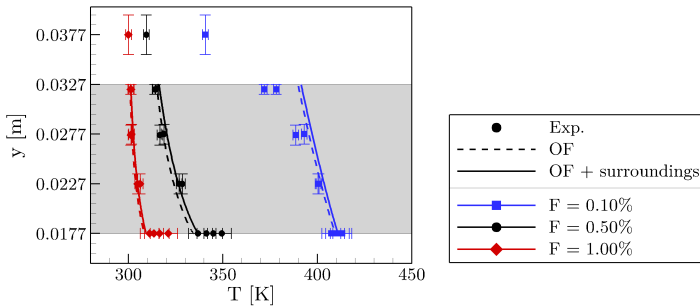
Figure 7.25: Internal temperature diagram for simulation with and without surroundings and $F = 0.50\%$ (data for $x = 0.199\,\mathrm{m}$, $z = 0$)

Summing up the results, lateral heat fluxes are found to have a moderate influence on the thermal situation of the porous sample. Deviations for the simulations with and without surrounding solid regions occur close to the porous sample's boarder, while the central region as well as the wake region remain largely unaffected. The lateral heat conduction leads to higher surface temperatures in vicinity of the copper frame which partly explains the previously observed deviations between IR data and numerical temperature distributions. However, it has to be noted that no thermal contact resistances have been considered in the simulations. Thus, the here-presented lateral heat fluxes and their influence should be less significant in the experiment. In this context, also other effects such as a smaller permeability of the C/C material close to the sample's boarder and thus less intense blowing in these regions could be a possible explanation for the remaining differences.

To reduce the complexity of simulations and the computational costs, it was decided to employ the standard numerical setup (without surroundings) for all subsequent simulations. However, the following points should be kept in mind with respect to the upcoming simulation results. First, the influence of lateral heat fluxes is of minor importance for small to moderate blowing ratios, whereas test cases with higher blowing ratios should be considered more carefully. Secondly, the effects are limited to the boarder regions of the sample while the central region is less affected. There, the temperatures at the surface as well as within the porous wall are similar regardless of the consideration of the additional solid regions. As a consequence, the thermocouple measurements, which are generally taken at central positions, are well suited for comparison to the numerical simulations. Conversely, the continuous experimental temperature distributions obtained through IR data are dropped for the subsequent analyses.

7.3.3 Foreign-Gas Injection

Regarding the application cases of transpiration cooling, various coolants aside from air are of interest. The coolant properties were found to have a significant influence on the heat-transfer reduction for blowing in chapter 6. Therefore, transpiration-cooling experiments in supersonic flow have also been performed with the coolant gases helium, argon, and CO_2. The comparison between numerical simulation and experiment then serves to validate the developed OpenFOAM solver with respect to transpiration cooling using gaseous coolants other than air. Based on findings reported in literature (e.g. references [96, 111]), the specific heat capacity c_p of the coolant is of particular importance in

transpiration cooling. Therefore, in the subsequent comparisons between air and foreign gases, blowing ratios are roughly scaled by the ratio of specific heat capacities. This introduces the modified blowing ratio $F^* = (c_p/c_{p,Air})\, F$. Table 7.3 summarises selected properties of the here-investigated coolants.

Table 7.3: Selected coolant gas properties at $T = 293.15\,\mathrm{K}$, $p = 101.325\,\mathrm{kPa}$ [118]

	ρ $\left[\frac{\mathrm{kg}}{\mathrm{m}^3}\right]$	c_p $\left[\frac{\mathrm{J}}{\mathrm{kgK}}\right]$	$c_p/c_{p,Air}$ $[-]$
Air	1.204	1006.4	1.00
Helium	0.166	5193.0	5.16
Argon	1.662	521.6	0.52
CO_2	1.839	846.1	0.84

Internal temperature distribution

First, the internal temperatures are discussed by means of figure 7.26. In addition to the thermocouple data, numerical results extracted at the domain's centre line ($x = 0.199\,\mathrm{m}$, $z = 0$) are included in the diagram. Each of the test cases for a foreign gas is supplemented by a corresponding test case using air as the coolant, while scaled blowing ratios are applied.
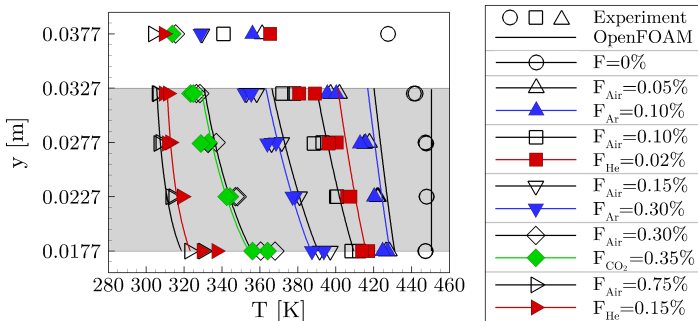
Figure 7.26: Numerical and experimental internal sample temperature for reference sample and different coolant gases

In general, figure 7.26 confirms all of the previously discussed results regarding the internal temperature distribution for transpiration cooling. Additionally, the comparison between the pairs of coolant gases confirms the strong sensitivity of temperature levels on the coolant's specific heat capacity. Similar results for air and foreign-gas transpiration at scaled blowing ratios are found. Compared to air as coolant gas, less (He), comparable (CO_2), or more (Ar) coolant mass flow rate is required to reach equivalent temperature levels. Regardless of the employed coolant gas, the coolant's capacity to absorb heat from the solid skeleton seems to be fully exploited in the test cases. This suggests the occurrence of an intense internal heat transfer for the transpiration-cooled C/C material. The comparison between experiment and OpenFOAM simulation reveals a generally good agreement. The effect of coolant gas properties on the internal temperatures is well captured.

External surface temperature

A corresponding diagram for the external surface temperatures is given by figure 7.27. The same test cases as before with scaled blowing ratios are depicted. The diagram compares thermocouple measurements to spanwise-averaged OpenFOAM results. Again, similar temperature distributions are observed for air and foreign-gas injection at scaled blowing ratios. A good agreement for the considered pairs of test cases is found for the transpired surface. Moreover, the numerical simulation reproduces the experiment well for all coolant gases. Deviations are limited to the previously discussed direct wake region and are more significant for larger blowing ratios (e.g. $F_{Air} = 0.75\%$ or $F_{He} = 0.15\%$).
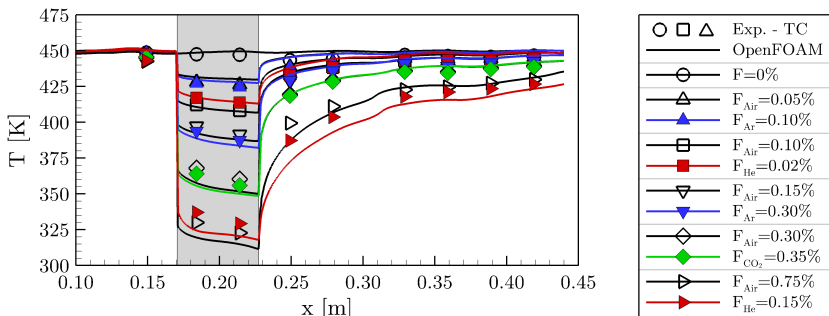

Figure 7.27: Numerical and experimental wall temperatures for reference sample and different coolant gases

In spite of this, the influence of coolant properties is well captured in the simulations.

Downstream of the transpired surface, the produced coolant film protects the wake region. Several film-cooling investigations demonstrated that the cooling efficiency depends on the specific heat capacity of the employed gas for this situation as well, see for example Goldstein [66]. However, the proposed c_p-scaling yields less agreement in the wake region. This particularly applies to the temperature distributions of helium and air, i.e. $F_{He} = 0.15\%$ and $F_{Air} = 0.75\%$. The temperatures for helium blowing are slightly higher on the sample surface, while being lower in the wake region. Thus, helium is more effective in the cooling of the wake region when compared to air. Both experiment and simulation demonstrate this effect. This implies different relationships between specific heat capacity and the cooling efficiencies on the transpired surface and in the wake region. However, the effect is not as significant for the other foreign gases depicted in figure 7.27 which is due to the smaller differences in gas properties, see table 7.3.

Surface temperature distributions

In a next step, numerical and experimental surface temperature distributions are compared in figure 7.28. To explore the wake region effect further, air and helium test cases are selected which are scaled by a factor of 5 which roughly corresponds to the ratio of specific heat capacities. The contour plots feature IR images (top half) and numerical results (bottom half). Comparing numerical and experimental results, a generally fair agreement is found. Deviations close to the sample's boarders for transpiration of air have been discussed in section 7.3.2. Similar differences are now detected for the helium test cases. This suggests that the deviations are not connected to the usage of a particular gas as coolant. Regarding the comparisons between air and helium cooling at scaled blowing ratios, the previous findings are confirmed. The helium test cases exhibit slightly higher temperature levels on the transpired surface, whereas the temperatures in the wake region are reduced. The effect is linked to the different cooling mechanisms for porous sample and wake region: First, the combination of internal heat transport and surface blowing (transpiration cooling) and secondly, the heat-transfer reduction by means of a protective coolant layer in the wake region (film cooling). The two mechanisms are discussed in more detail in the next section.
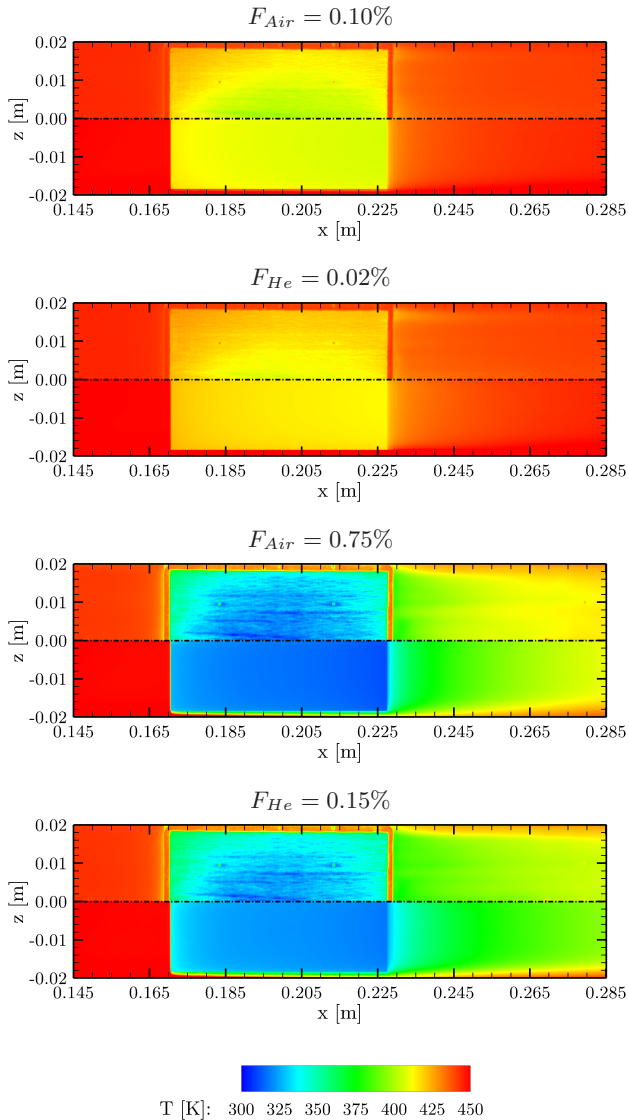
Figure 7.28: Comparison of sample surface and wake region temperatures for air and helium injection - in-situ calibrated infrared thermography (top half) and OpenFOAM simulation (bottom half)

7.3.4 Cooling Efficiency

Previous comparisons between different blowing ratios as well as different coolant gases suffer from the variation of the coolant-reservoir temperature T_c in the test cases, see figures 7.16 and 7.26. To compensate for this, the cooling efficiency is introduced by

$$\Theta = \frac{T_{F=0} - T}{T_{F=0} - T_c} \quad . \tag{7.4}$$

It takes into account the temperatures of the uncooled wall $T_{F=0}$ and the fluid in the coolant reservoir T_c. As it is a measure for the temperature reduction in relation to the maximum possible temperature reduction (i.e. $T_{F=0} - T_c$), it allows for a more meaningful comparison of test cases. Moreover, the dimensionless parameter also facilitates the comparison to further studies from literature with different test conditions.

Transpired wall

Figure 7.29 depicts the cooling efficiency for the transpired surface of the porous sample. The diagram includes experimental (filled symbols, lines) and numerical (hollow symbols) data points for various blowing ratios and all tested coolants. The experimental error bars are based on the differences between the four surface thermocouples (vertical) and the measurement uncertainties in the mass flow rates (horizontal). Numerical values are determined through value-averaging for the transpired surface. The diagram illustrates a strong increase of the cooling efficiency Θ already at low blowing ratios, whereas the behaviour becomes asymptotic for large values of F. Moreover, the analysis confirms the significant dependency on the properties of the coolant gas. Helium is most efficient, followed by air and CO_2 which show similar results. Argon exhibits the worst cooling efficiency for a given blowing ratio. However, a cooling efficiency of around 90% is reached for all coolants at the respective maximum blowing ratios. When comparing experiment and numerical simulation, a generally good agreement for all coolant gases is observed. Deviations slightly rise for increasing blowing ratios, where also the influence of lateral heat conduction showed to be more significant. The previous findings implied similar temperature reductions for blowing ratios scaled by the specific heat capacity of the coolant. Figure 7.30 depicts the data points for Θ over the scaled blowing ratio $F^* = \left(c_p/c_{p,Air} \right) F$.
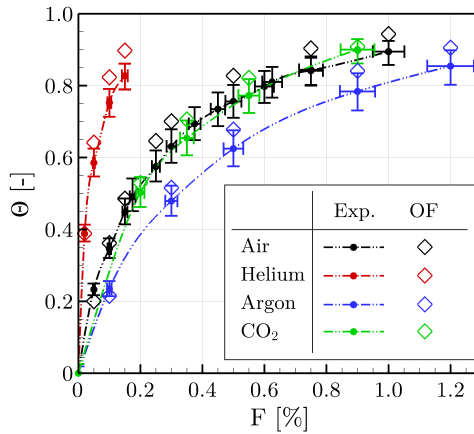
Figure 7.29: Cooling efficiency of the porous wall over blowing ratio for various coolant gases
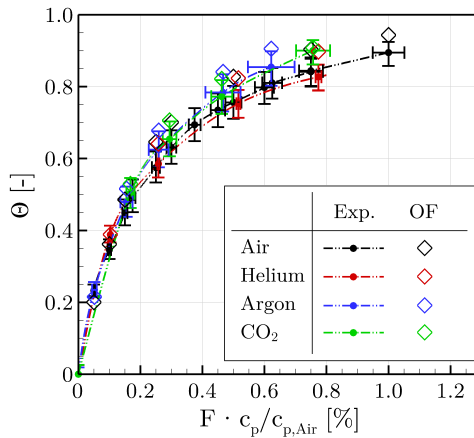
Figure 7.30: Cooling efficiency of the porous wall over scaled blowing ratio for various coolant gases

A good agreement between the curves of all coolant gases is found. This suggests that the cooling efficiency of the porous wall is mainly governed by the coolant's capability to convey energy, i.e. $(\dot{m}_c/A_c)\, c_{p,c}$. Therefore, the intense internal heat transfer between solid skeleton and coolant gas dominates the overall cooling efficiency in the here-discussed test cases. The OpenFOAM results follow the trend well and thus verify the c_p-scaling approach.

Wake region

In the following, the cooling efficiency is also evaluated for the channel's wall surface including the film-cooled wake region. Figure 7.31 depicts the numerically and experimentally determined values of Θ for some of the previously discussed test cases.

As found for the absolute temperatures in figure 7.27, the cooling efficiencies for experiment and simulation compare fairly well. Regarding the pairs of coolant gases at scaled blowing ratios, a good agreement is found for the sample surface which confirms the conclusion drawn from figure 7.30. However, differences are present in the wake region for the comparison between $F_{He} = 0.15\%$ and $F_{Air} = 0.75\%$. Although, the sample surface shows nearly identical results, helium exhibits a substantially higher cooling efficiency in the wake region. In contrast, no significant differences are observed for argon and CO_2 to their equivalent air test cases at scaled blowing ratio. Here, the discrepancies in specific heat capacity and density with respect to air are smaller when compared to helium and air.
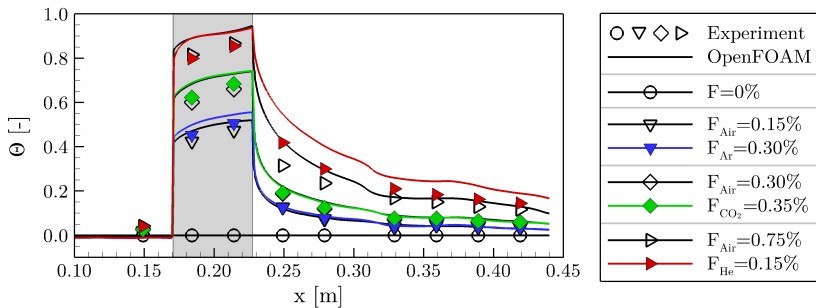
Figure 7.31: Cooling efficiency over axial channel length for various coolant gases

For the transpired surface, the coinciding curves in figure 7.30 demonstrated that similar cooling efficiencies are obtained for different test gases if the modified blowing parameter $F^* = (c_p/c_{p,Air})\, F$ remains constant. The finding was explained by the dominating effect of the internal heat transfer occurring within the porous sample. In contrast, figure 7.31 reveals deviations in the cooling efficiencies of the wake region between test cases at c_p-scaled blowing ratios (cf. $F_{Air} = 0.75\%$ and $F_{He} = 0.15\%$). This suggests a different dependency for the cooling efficiency of the wake region when compared to the transpired surface.

In any case, the numerical and experimental results indicate a considerable influence of the coolant gas properties on the cooling efficiency also for the wake region of the sample. This is in line with film-cooling correlations such as given by Goldstein et al. [65]:

$$
\Theta = \left\{ 1 + \frac{c_{p,\infty}}{c_{p,c}} \left[0.33 \left(4.00 + \xi \right)^{0.8} - 1 \right] \right\}^{-1}
$$

$$
\text{with} \quad \xi = \frac{x'}{F \cdot s} \left(\text{Re}_s \frac{\mu_c}{\mu_*} \right)^{-0.25} \frac{\rho_*}{\rho_\infty} \quad \text{and} \quad \text{Re}_s = \frac{\rho_c u_c s}{\mu_c} \quad ,
$$

(7.5)

where ξ is a dimensionless film cooling parameter with the injection length s and the distance from the injection point x'. The correlation may be used to determine the cooling efficiency in a film-cooled region and is applicable to the injection of same and foreign gases. As it is based on incompressible considerations, the authors used Eckert's reference state method to extend the relations to high-speed compressible flows. A compressibility correction ρ_*/ρ_∞ is included in the definition of ξ, and the fluid properties are evaluated at $T_* = T_\infty + 0.72(T_r - T_\infty)$ with $T_r = T_{F=0}$. Reference [65] describes the derivation in more detail.

7.3.5 Summary

In the given section, transpiration cooling for a flat porous C/C sample and supersonic main-flow conditions has been investigated experimentally and numerically. Boundary-layer blowing was found to cause significant temperature reductions on the transpired surface, in the wake region, and within the porous wall. A strong influence of the applied blowing ratio on the resulting temperature levels was observed. Fully-coupled numerical simulations corresponding to the experimental test cases have been performed using the developed OpenFOAM

solver. The results are in fairly good agreement to the experimental data and captured all relevant effects. These include the substantial temperature drop at the transition to the transpired surface, the build-up of a coolant film along the porous surface, and the rise of temperatures in the non-transpired wake region. The cooling effect remained visible for the complete length observed and depended on the applied blowing ratio. Moreover, the solver allowed to analyse the internal temperature distribution which was found to be in good agreement to internal thermocouple measurements. Deviations between experiment and simulation occurred on the transpired surface, where slight non-homogeneities due to the fibre character of C/C and the sample's blowing behaviour are visible. These effects cannot be captured by the applied volume-averaging simulation approach. Moreover, the regions close to the sample's boarder displayed elevated temperatures in the IR contour plots. These are partly due to heat conduction from the surroundings into the porous sample. This effect could be captured by corresponding numerical simulations with an enlarged simulation domain. The influence of the parasitic conduction heat fluxes was found to be limited to the regions close to the boarders and does not affect the sample's central region or the non-transpired wake region. Therefore, also the locations of thermocouple measurements are not compromised. Moreover, the effect is stronger for higher blowing ratios due to the generally lower temperature levels of the porous sample. As a consequence, subsequent analyses focus on small to moderate blowing ratios and compare simulation results to thermocouple measurements.

The investigation on transpiration cooling using foreign gases revealed a substantial influence of the coolant properties. In particular, a strong sensitivity on the gases' specific heat capacities was detected. Similar temperature levels were obtained for reduced (helium), comparable (CO_2), and increased (argon) coolant mass flow rates.

For a more meaningful comparison between test cases using different gases and blowing ratios, the cooling efficiency was introduced. It is calculated for the transpired surface and takes into account the non-uniform coolant-reservoir temperature and the no-blowing wall temperature. The analysis confirms the significant influences of blowing ratio and coolant gas properties. Furthermore, the cooling efficiency of the porous wall can be described for all gases by a modified blowing ratio that is based on a c_p-scaling. The results indicate a strong internal heat transfer that dominates the overall cooling efficiency of the investigated test cases.

Regarding the non-transpired wake region, a considerable film-cooling effect was observed. Again, an influence of the coolant properties was found which

is, however, different from the dependence found for the transpired surface and the internal temperatures. At scaled blowing ratios, helium injection showed higher cooling efficiencies in the wake region when compared to air as coolant. This was demonstrated by both experiment and corresponding numerical simulations.

Summarising on the numerical validation, the developed OpenFOAM solver was able to capture all relevant effects observed in the transpiration-cooling experiments with the reference sample. Therefore, the continuous blowing model proves to be applicable also to C/C and the supersonic main-flow situation. Moreover, the transition-layer model and the proposed modified blowing boundary condition for the specific turbulence dissipation rate are well suited for the here-presented test cases.

7.4 Contoured Sample - Variation of Wall Thickness

In the previous section, transpiration cooling in supersonic flow using a flat-plate sample has been investigated. Although, a rather uniform temperature distribution was observed, the analysis revealed a reduced cooling effect close to the sample's leading edge. This effect was explained by the non-existent coolant film and to some extent, heat conduction from the upstream part of the channel wall into the sample. Likewise, different more complex application cases, e.g. strut injectors, rocket combustion-chamber throats, exhibit regions of higher wall temperatures where an intensified cooling is desired. In general, increasing the blowing ratio (by means of a higher reservoir pressure) yields a higher cooling efficiency and reduced temperature levels. However, the effect acts on the complete sample whereas possibly only local hot spots require additional cooling. According to the Darcy-Forchheimer equation, the pressure difference to induce a certain coolant mass flow increases with the sample thickness. Vice versa, larger wall thicknesses yield reduced coolant mass flow rates for a fixed pressure difference. Thus, the contouring of porous structures, i.e. the variation of wall thickness, represents a promising approach to locally increase the blowing ratio in transpiration cooling.

In the following, results on transpiration cooling for a porous sample with non-uniform wall thickness are presented. The analysis is focused on the general effect of a wall-thickness variation instead of an optimisation of the cooling in the sense of design improvement. Experimental results for the contoured sample are analysed in combination with complementing numerical simulations. At the same time, the involved comparison of experimental and numerical data further validates the new OpenFOAM solver. The contoured sample is tested using the same experimental setup as before, see also chapter 3. To explore the effect of wall-thickness variations, the sample is tested in two configurations as illustrated by figure 7.32.
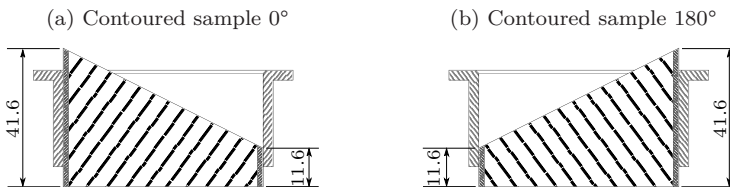
Figure 7.32: Test configurations for contoured sample (units in mm, main-flow direction from left to right)

7.4.1 Wall Temperatures for Injection of Air

In a first step, the general effect of a wall-thickness variation is evaluated. Therefore, surface temperatures recorded by means of IR thermography are depicted in figure 7.33. The plot illustrates experimental data for both configurations of the contoured sample and blowing with air at $F = 0.25\%$ and $F = 0.50\%$.[7] The direct comparison of the two configurations reveals lower temperatures in the sample's front region for the contoured sample 180°. In contrast, the temperatures in the aft region are higher when compared to the contoured sample 0°. In the non-transpired wake region, slightly lower temperatures are observed for the contoured sample 0°. However, the influence is weak when compared to the transpired surface. The IR images clearly demonstrate the effect of a wall-thickness variation on the surface temperatures.
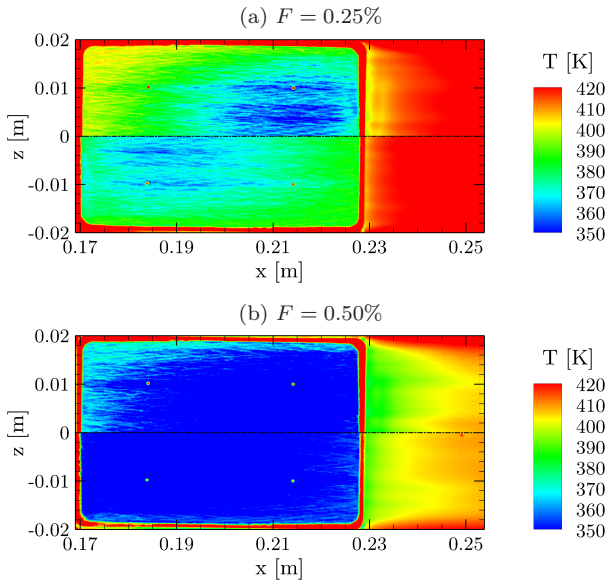
Figure 7.33: Surface temperature distributions from experiment for contoured sample 0° (top) and contoured sample 180° (bottom)

---

7 The field of view is reduced when compared to previous IR images since a smaller sapphire window has been used for the measurements (cf. figure 3.3a).
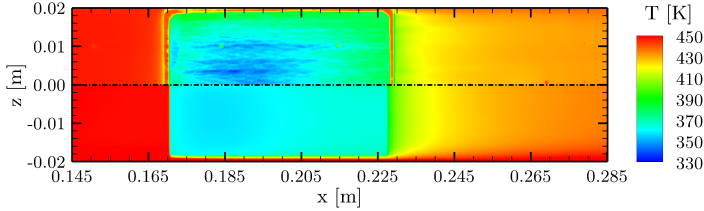
Figure 7.34: Comparison of sample surface and wake region temperatures for contoured sample 180° and F = 0.25% - in-situ calibrated infrared thermography (top) and OpenFOAM simulation (bottom)

Next, the experiment is exemplarily compared to OpenFOAM results for the test case $F = 0.25\%$ in figure 7.34. A generally good agreement is found between simulation and measurement. As for the reference-sample test case, larger deviations are limited to the areas close to the sample's boarders. The simulation captures the effect of reduced temperatures in the front region of the contoured sample 180° where the smaller wall thickness compensates for the non-existent coolant film.

A more detailed analysis may be obtained based on the axial temperature distributions. Instead of the surface temperature, the cooling efficiency is employed for the analysis as it allows for a better comparison between the different test cases and blowing ratios. Figure 7.35 depicts the spanwise-averaged cooling efficiency for both configurations of the contoured sample and the reference sample. The diagram reveals a clear influence of the sample's relative wall thickness on the local cooling efficiency for both simulation and experiment. Compared to the reference sample with a uniform wall thickness, contoured
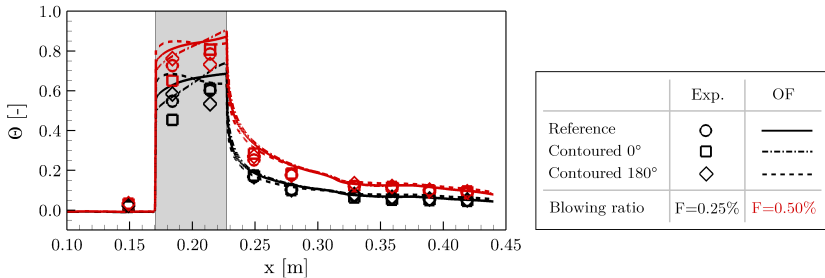
Figure 7.35: Cooling efficiency over axial length for contoured sample in both configurations in comparison to reference sample - numerical and experimental data for $F = 0.25\%$ and $F = 0.50\%$

167

sample 0° exhibits a lower and contoured sample 180° a higher cooling efficiency in the front region, respectively. This changes to the opposite for the aft region of the transpired surface, where the contoured sample 0° shows the highest cooling efficiency. In the wake region, no influence is detected.

The comparison between OpenFOAM results and experimental measurements shows a fair agreement on the transpired surface and a good agreement in the wake region. Trends are well reproduced by the numerical simulation, although deviations are observed regarding the absolute values on the porous surface.

7.4.2 Coolant Mass Flow Distribution and Sample Temperatures

In the analysis of the reference-sample test case, it was shown that an increase in the blowing ratio yields higher cooling efficiencies. Regarding the contoured sample and a single blowing ratio, local variations of the cooling efficiency are observed on the transpired surface. This suggests that the non-uniform wall thickness of the sample triggers local variations of the coolant mass flow rate. To investigate this further, the distribution of coolant mass flow rate and its influence on the internal temperature of the porous sample are evaluated in the following. As the local mass flow rate can hardly be determined experimentally, the through-flow behaviour is analysed by means of numerical simulations.

Figure 7.36 depicts the internal temperature distribution and the coolant mass flux vectors for the symmetry plane of the three test cases at a blowing ratio of $F = 0.25\%$. Confirming the previous results, the leading-edge region exhibits highest temperatures for the contoured sample 0°. Moreover, the temperature isolines suggest heat conduction in axial direction. In contrast, the contoured sample 180° displays lower temperatures in the front region and a generally more homogeneous temperature distribution when compared to the other two samples. The temperature levels for the reference sample are in between the two other test cases. Regarding the through-flow behaviour, the mass flux vectors indicate a locally increased coolant outflow for reduced wall thickness of the samples. Additionally, the curved flow paths demonstrate coolant cross flow for both contoured sample test cases. Opposed to the reference sample, the contoured-sample test cases thus exhibit multi-dimensional coolant flow.

The coolant mass flux distribution over axial length is shown in figure 7.37. The diagram gives the absolute values of coolant mass flux ρu_y for the samples as well as relative deviations with respect to the reference sample. Figure 7.37a displays a variation of $|\rho u_y|$ for both contoured samples while the reference
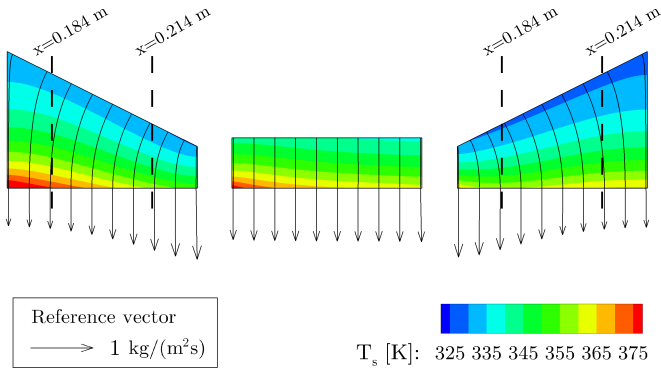
Figure 7.36: Internal temperature distributions and mass flux vectors for contoured
at $F = 0.25\%$

sample exhibits a nearly uniform coolant mass flux. Higher values are linked to smaller wall thickness and vice versa. The non-uniform coolant mass flux may also be considered as a variation of the local blowing ratio and explains the previously discussed temperature variations. The deviations of $|\rho u_y|$ relative to a uniform distribution rise up to around 40% as illustrated by figure 7.37b. Moreover, the non-uniformity is slightly more pronounced for the smaller blowing ratio.
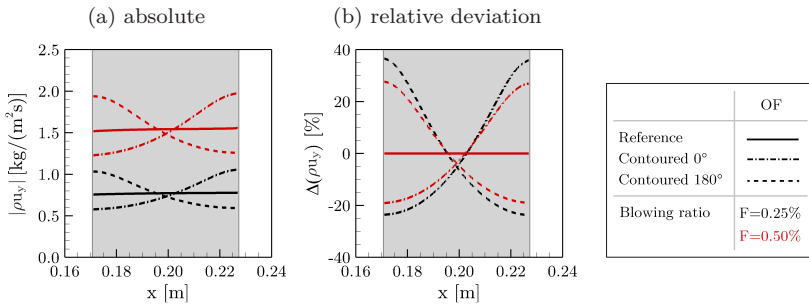
Figure 7.37: Comparison of coolant mass flux distributions for the different samples at $F = 0.25\%$ and $F = 0.50\%$

The internal temperature diagrams given by figure 7.38 allow a more detailed analysis of the thermal situation of the porous structures. Here, numerical results of the OpenFOAM solver are compared to the internal thermocouple measurements for the contoured sample in both configurations. The analysis is split into front region and aft region. The numerical data for solid-phase temperature is extracted on the domain's symmetry plane and the axial positions $x = 0.184\,\text{m}$ and $x = 0.214\,\text{m}$, cf. figure 7.36. Likewise, thermocouple positions are localised close to these axial positions, see figure 3.6b. The diagrams confirm the discussed effect of the wall-thickness variation. Lower temperatures are observed in the region with reduced thickness (and intensified blowing), regardless of whether the sample is in 0° or 180° configuration. Comparing experiment and simulation, a fair agreement is found for all blowing ratios.

(a) Contoured sample 0°

(b) Contoured sample 180°
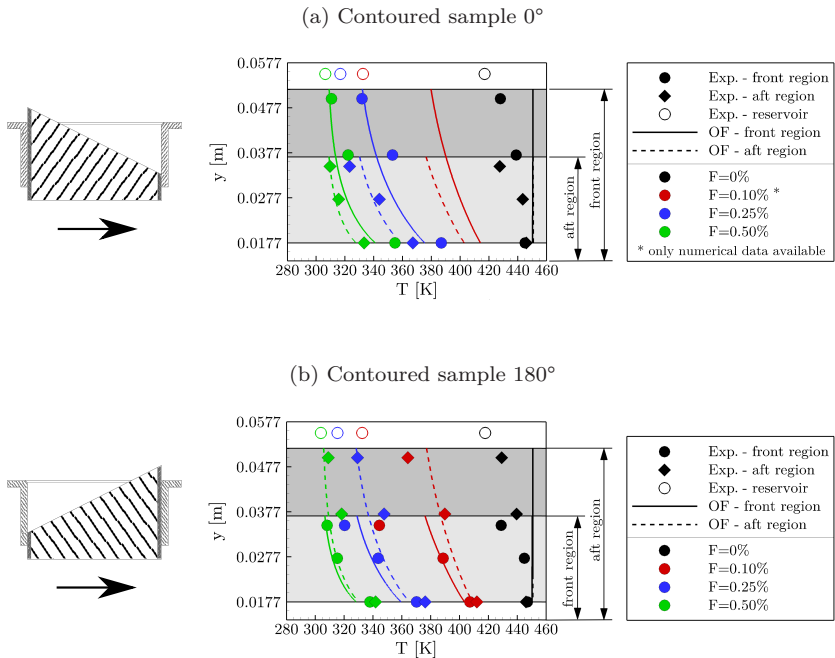
Figure 7.38: Internal temperature distribution for contoured sample 0° and 180° at various blowing ratios

7.4.3 Summary

This section explored the influence of a variation in the sample's wall thickness on transpiration cooling and the achieved cooling efficiency. A significant effect on the surface temperatures was detected in the experiments by means of infrared thermography. Depending on the test configuration, the wall temperatures and cooling efficiencies in the sample's front region are increased or reduced when compared to the reference sample with uniform wall thickness. Higher local wall thicknesses are linked to increased temperatures/reduced cooling efficiencies and vice versa. However, the effect is limited on the transpired surface, no influence on the cooling efficiencies in the wake region was detected. Besides the wall temperatures, also the internal temperature of the porous sample was found to be at elevated levels for the region exhibiting a larger wall thickness. The OpenFOAM solver was able to reproduce all observed effects with a fair agreement to the experiment. Moreover, it allowed to analyse the test cases in more detail, e.g. with respect to the local distributions of coolant mass flux. The simulations revealed locally increased or reduced coolant mass fluxes for the variation of the sample thickness. These non-uniform distributions are the reason for the observed temperature differences between front and aft regions. The wall-thickness variation for the contoured sample 180° counterbalanced the effect of the non-existent coolant film at the beginning of the sample. The latter was found in section 7.3 for the reference-sample test cases and expressed by means of elevated temperatures close to the leading edge.

In summary, the variation in wall thickness yields a non-uniform coolant mass flux distribution which modifies the local cooling efficiencies. The developed OpenFOAM solver reproduces the effects well and was validated by means of a comparison to the experimental data. The contouring of samples proves to be a possible means of controlling local surface temperatures in transpiration cooling. Besides the here-investigated geometrical variation, a similar effect is expected for local variations in the material's permeability. Both design options could be combined to maximise the effect for specific applications.

7.5 Shock Generator - Transpiration Cooling in More Complex Flow Fields

As outlined in the introduction, several application cases for transpiration cooling involve strong pressure variations. Examples for these are the throats of rocket combustion chambers or the combustor parts of ram- and scramjet engines. While for a rocket engine, the substantial acceleration of the flow in throat and nozzle sections causes a pressure reduction, the formation of shock waves and expansion fans introduces pressure variations in the supersonic flow applications. Due to the complexity of the flow field as well as the coupling between porous structure and main flow, the multi-dimensional effects can hardly be captured by available engineering correlations. This underlines the importance of numerical tools such as the here-presented CFD solver.

In the following, the formation of shock waves in supersonic flow is exploited to validate the developed solver and the applied numerical setup for pressure variations on the transpired surface. The shock generator as described in section 3.1.2 is employed to alter the flow field. The insert that replaces the large IR window on the channel's bottom is equipped with a movable flow barricade that introduces an obstruction into the flow field. Thus, an oblique shock forms which can be varied in strength and wave angle by the position of the barricade. First, the flow field and the static wall pressure distribution are examined for the no-blowing test case. Additionally, the influence on the wall temperature and the heat transfer characteristics are analysed. Afterwards, the influence of the more complex flow field on transpiration cooling is explored. Therefore, two shock-generator positions and two porous samples, i.e. the reference sample and the contoured sample 180°, are investigated experimentally and numerically.

7.5.1 Shock-Generator Flow Field without Boundary-Layer Blowing

In a first step, the flow field without boundary-layer blowing is analysed. Schlieren images illustrate the formation of shock waves and expansion fans while corresponding wall pressure diagrams supplement quantitative data.

Figure 7.39 depicts experimental and numerical schlieren images for the shock-generator positions $\Delta y = 5.0\,\text{mm}$ and $\Delta y = 9.7\,\text{mm}$. In contrast to the simulation data, the field of view in the experiment does not extend over the full channel height for the upstream side-wall window. The visualisation reveals a system of shock waves and expansion fans throughout the supersonic channel. As the porous sample is located on the channel's top wall, the analysis focuses on this region. First, the test case for $\Delta y = 5.0\,\text{mm}$ is discussed. Upstream

(a) $F = 0\%$ - $\Delta y = 5.0\,\mathrm{mm}$

(b) $F = 0\%$ - $\Delta y = 9.7\,\mathrm{mm}$
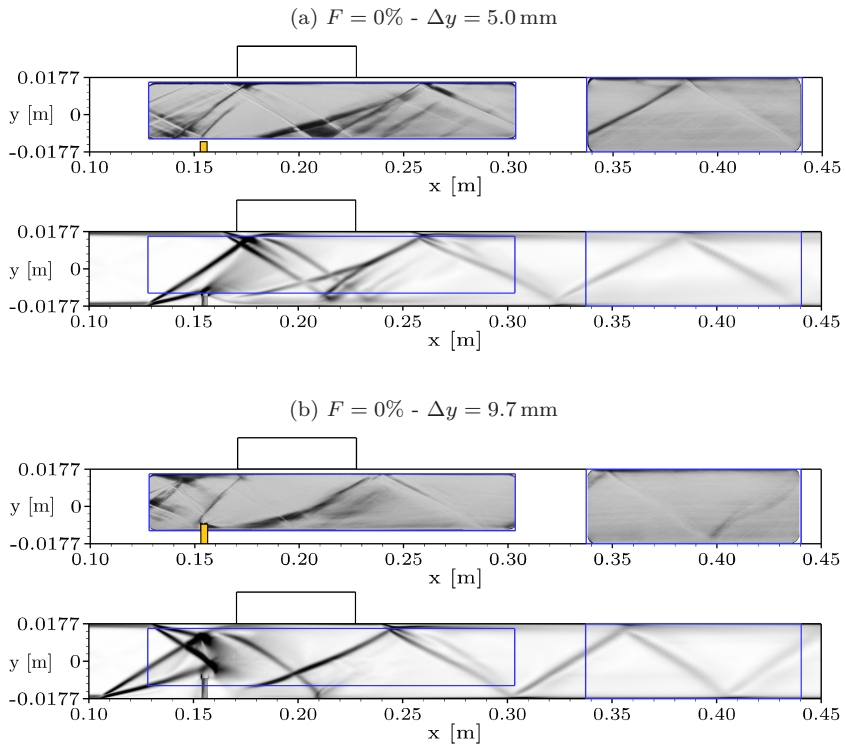
Figure 7.39: Experimental (top) and numerical (bottom) schlieren images for the reference sample without blowing at two shock-generator positions

of the shock generator, an oblique shock wave forms which impinges onto the transpired surface, close to the sample's leading edge. Moreover, a reflected shock hits the channel's top wall in the sample's wake region ($x \approx 0.26\,\mathrm{m}$). Regarding the maximum elevation of the shock generator, i.e. $\Delta y = 9.7\,\mathrm{mm}$, the shock forms further upstream and exhibits a steeper wave angle. Thus, it hits the channel's top wall slightly upstream of the porous sample. Likewise, the reflected shock is shifted in the upstream direction and impinges close to the trailing edge of the sample. Comparing experimental and numerical schlieren images, a very good agreement is found. The numerical simulation is able to reproduce all details of the flow field.

The corresponding static wall pressure distributions for both test cases are given in figure 7.40.[8] The system of shocks and expansion fans considerably alters the pressure distribution. As intended, a significant pressure difference over the sample surface is created. For the shock-generator position $\Delta y = 9.7$ mm, the highest pressure occurs at the leading edge and then continuously decreases by $\Delta p \approx 80$ kPa over the porous sample. In contrast, a local maximum of the wall pressure at an axial position $x \approx 0.19$ m is observed for an elevation of $\Delta y = 5.0$ mm. Downstream, a pressure drop of $\Delta p \approx 60$ kPa follows. Again, a very good conformity between experimental measurements (symbols) and numerical simulations (lines) is observed. This applies to both test cases and the complete length observed. As mentioned before, a strong shock wave and the associated rise in pressure may lead to boundary-layer separation. This is investigated more closely by means of figure 7.41. To estimate the size of recirculation zones, isosurfaces for $u_x = 0$ are indicated in red colour in the figure.

(a) $F = 0\%$ - $\Delta y = 5.0$ mm

(b) $F = 0\%$ - $\Delta y = 9.7$ mm
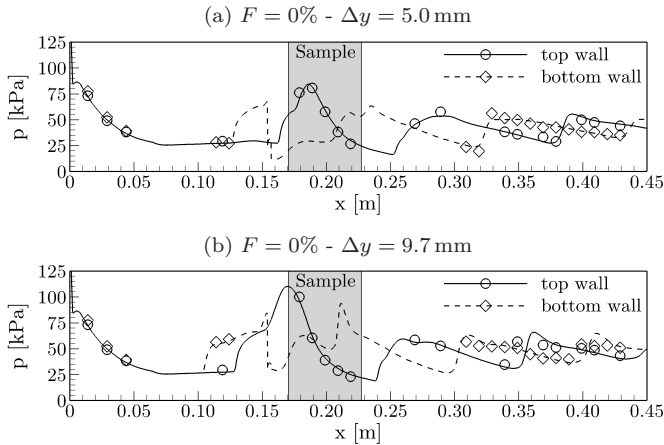
Figure 7.40: Experimental (symbols) and numerical (lines) wall pressure over channel length for the reference sample without blowing at two shock-generator positions

8   For the reduced domain simulations, the numerical pressure distribution in the divergent part of the Laval nozzle (up to $x = 0.064$ m) is supplemented from the full-channel simulation results discussed in section 7.1. Due to the supersonic flow regime, no upstream effect originating from the test section is expected. This assumption has been reviewed and confirmed by means of an exemplary simulation using the full numerical domain.

a) $\Delta y = 5.0$ mm   b) $\Delta y = 9.7$ mm
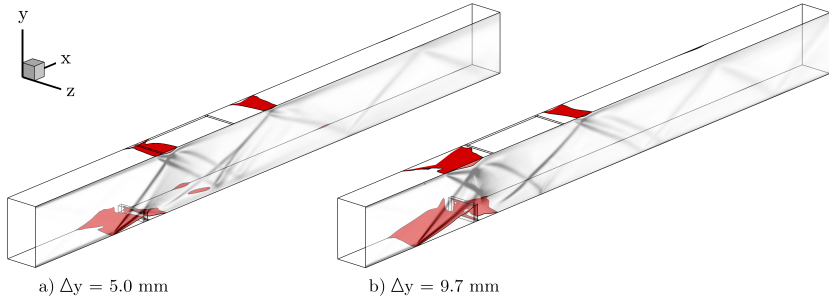
Figure 7.41: Combined visualisation of schlieren image and isosurfaces for $u_x = 0$ indicating recirculation zones for no-blowing case (numerical results, half model)

Regarding the top wall, two recirculation zones are observed. For the test case with $\Delta y = 5.0$ mm, the first separation forms directly at the leading edge of the sample, while the second is positioned in the wake region. The test case with stronger elevation of the shock generator, i.e. $\Delta y = 9.7$ mm, exhibits a larger recirculation zone upstream of the sample's leading edge as well as a second in the wake region. Due to the larger wave angles, both recirculation zones are shifted to an upstream position when compared to the test case with an elevation of $\Delta y = 5.0$ mm. Moreover, the size of the upstream recirculation zone is larger for the test case with $\Delta y = 9.7$ mm. This is confirmed by the schlieren images given by figure 7.39. With respect to the bottom wall, recirculation zones are occurring at both sides of the movable flow barricade of the shock generator.

A simple criterion for the occurrence of boundary-layer separation has been proposed by Korkegi [100] and is defined by equation (2.43). According to the criterion, separation takes place if the pressure ratio exceeds a critical value, i.e. $(p_2/p_1) > 2.9$ for $M_1 \approx 2.5$. Based on the pressure distributions presented in figure 7.40, the criterion predicts two recirculation zones on the channel's top wall. For the test case with shock-generator position $\Delta y = 5.0$ mm, these are located between $0.16\,\text{m} < x < 0.19\,\text{m}$ and $0.25\,\text{m} < x < 0.30\,\text{m}$. The more elevated shock-generator position, i.e. $\Delta y = 9.7$ mm, shifts the positions slightly upstream to $0.13\,\text{m} < x < 0.17\,\text{m}$ and $0.24\,\text{m} < x < 0.26\,\text{m}$. Further downstream, the intensity of reflected shock waves is reduced. Thus, no additional recirculation zones are indicated. The findings based on the Korkegi criterion agree well with the numerical simulation results in figure 7.41.
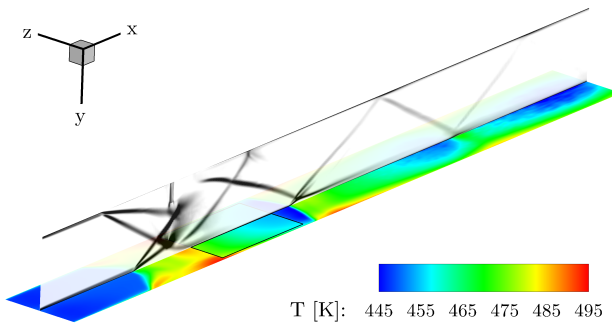
Figure 7.42: Combined visualisation of schlieren image and adiabatic wall temperature distribution for $F = 0\%$ and $\Delta y = 9.7\,\text{mm}$ (numerical results)

The more complex supersonic flow field also alters the temperature flow field and the wall heat flux distribution. To exemplarily illustrate this, figure 7.42 shows the adiabatic wall temperature for a simulation without blowing and a shock-generator position $\Delta y = 9.7\,\text{mm}$. A numerical schlieren image is added and the y-coordinate is inverted to provide a better visualisation. The combined visualisation indicates a significant influence of the shock system on the temperature distribution. Elevated temperature levels are found downstream of the formation point of shock waves as well as in the separation zone. The highest temperatures occur close to the reattachment point at the sample's leading edge.

A comparison to experimental data is given in figure 7.43. The diagram depicts temperature distributions obtained from spanwise-averaged numerical data and wall thermocouple measurements without boundary-layer blowing. Moreover, results for the test cases without shock generator (filled symbols, solid lines)
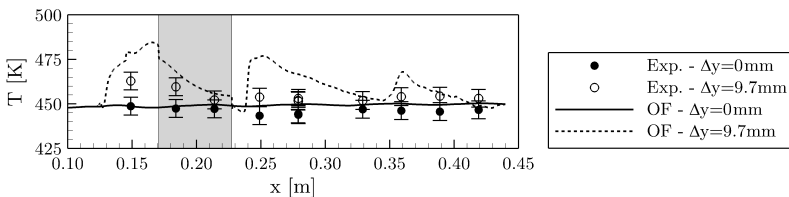
Figure 7.43: Wall temperature distributions for reference sample without blowing and shock-generator positions $\Delta y \in [0,\ 9.7]\,\text{mm}$

and with maximum elevation $\Delta y = 9.7\,\mathrm{mm}$ (hollow symbols, dashed lines) are compared. The figure confirms the previous results and indicates considerable higher wall temperatures for the shock-generator test case. An oscillating temperature distribution is found with minimum values close to the constant wall temperature of the test case without shock generator. Regarding the surface of the porous sample, substantially higher temperatures are observed for the front region of the transpired surface, whereas the values reduce towards the sample's trailing edge. Comparing simulation and experiment for the shock-generator test cases, significant deviations between thermocouple measurements and numerical results are found. In particular, regions of recirculation zones are concerned, where the temperature rise is overpredicted by the numerical solver. Shock-wave/boundary-layer interaction triggers the flow separation as illustrated in figure 7.41. The simulation of this phenomenon is currently still challenging as has been stated by various authors, e.g. Dolling [44]. Commonly, the associated deviations are attributed to the applied turbulence model [40, 161, 183, 203].

To obtain a first estimate of the distribution of heat transfer coefficients on the sample surface, simulations with no blowing and different shock-generator positions are performed. Regarding the thermal boundary condition of the porous surface, both a constant wall temperature condition and an adiabatic wall condition are applied in separate simulations. Figure 7.44a depicts the absolute distributions of the heat transfer coefficient h_0 as well as the adiabatic wall temperature T_r (second ordinate) over sample length. Moreover, the relative deviation to the reference-sample test case without elevation of the shock generator is given in figure 7.44b. As specified before, all numerical data is spanwise-averaged for $|z| < 10\,\mathrm{mm}$.

Figure 7.44a displays a strongly non-uniform distribution of h_0 for the shock-generator test cases which is due to the impingement of shock waves and the occurrence of recirculation zones. The regions of highest heat transfer coincide with the reattachment points after flow separations (cf. figure 7.41). The adiabatic wall temperature is increased for both shock-generator test cases when compared to the test case with no elevation of the flow barricade, i.e. $\Delta y = 0\,\mathrm{mm}$. It decreases along the sample length but remains elevated. With respect to the relative deviations given in figure 7.44b, substantial increases in the heat transfer coefficient of up to 160% are found. Regarding this, the enhancement in h_0 is similar for both shock-generator positions but shifted with respect to the axial position.

This concludes the analysis of the no-blowing test case which serves as the reference in the following investigations.

7.5.2 Transpiration Cooling for Non-Uniform Main Flow Field

As discussed for the no-blowing test case, the introduction of oblique shock waves by means of the shock generator has a significant effect on the distributions of wall pressure, temperature, and heat flux. Based on this, a considerable influence on transpiration cooling is expected.

In contrast, the influence of boundary-layer blowing on the main flow field is small for the shock-generator test cases. Figure 7.45 exemplarily demonstrates this by depicting numerical schlieren images with and without blowing for the shock-generator elevation $\Delta y = 5.0\,\mathrm{mm}$. No significant differences are found for the blowing case. Merely, the recirculation zones at the sample's leading edge and in the wake region (top wall) are marginally larger for the test case with blowing. The corresponding static wall pressure distributions are given in figure 7.46. Likewise, no considerable differences are detected between test cases with and without boundary-layer blowing.

Regarding transpiration cooling, on the other hand, two effects on the coolant mass flow distribution are expected for the test cases with shock generator. First, the combination of constant pressure in the coolant reservoir and a variation of static pressure on the sample surface will result in a non-constant pressure difference over the porous sample. Secondly, the variation in the heat-transfer distribution yields locally higher temperature levels which increase the through-flow resistance (cf. section 5.2.3).
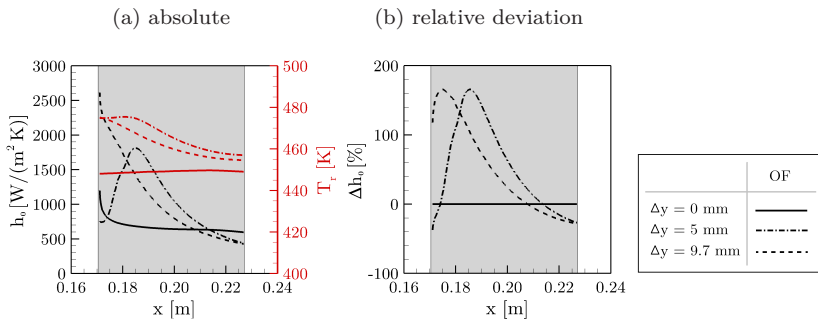
Figure 7.44: Comparison of heat transfer coefficient and adiabatic wall temperature for reference sample and different shock-generator positions

(a) $F = 0\%$ - $\Delta y = 5.0\,\mathrm{mm}$

(b) $F = 0.50\%$ - $\Delta y = 5.0\,\mathrm{mm}$
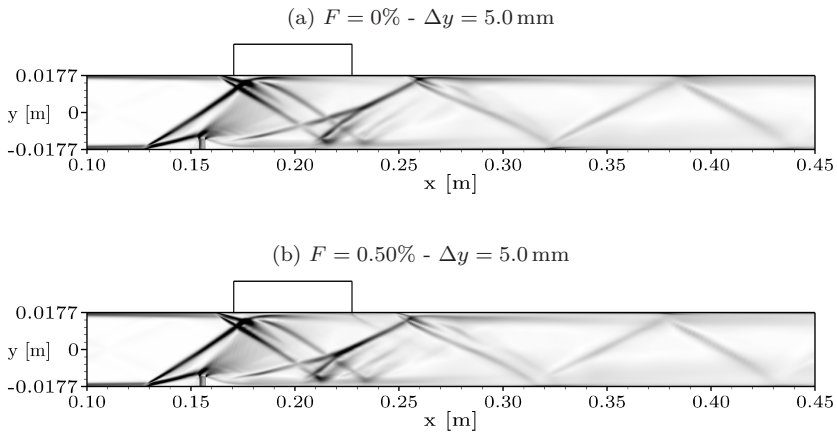
Figure 7.45: Comparison of numerical schlieren images without and with blowing

Figure 7.47a depicts the local coolant mass flow distribution for two blowing ratios and two shock-generator positions. In addition to the absolute values, the relative deviations from the test case without shock generator are given in figure 7.47b. The diagram reveals a non-uniform distribution of the local coolant mass flux $|\rho u_y|$ over sample length. Regions of low coolant mass flux correspond to regions of high static wall pressure and heat flux, compare also figures 7.40 and 7.44. Relative deviations of up to -20% are found with respect to the case without shock generator in figure 7.47b. The effect is stronger for the smaller blowing ratio $F = 0.25\%$ due to the reduced driving pressure difference over the sample when compared to $F = 0.50\%$. Regarding this, the pressure
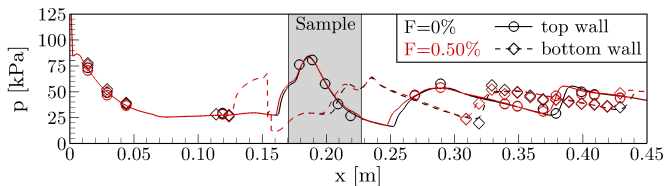
Figure 7.46: Comparison of experimental (symbols) and numerical (lines) wall pressure over channel length without and with blowing for $F = 0.50\%$ and shock-generator elevation $\Delta y = 5.0\,\mathrm{mm}$
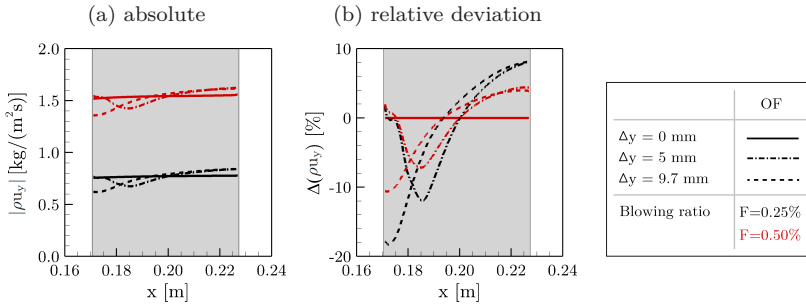
Figure 7.47: Comparison of coolant mass flux distributions for reference sample and different shock-generator positions

difference over the sample thickness has to be related to the pressure variation over the sample surface due to the non-uniform main flow field. The latter remains nearly constant (cf. figure 7.46), while the first changes drastically with blowing ratio. For the two here-discussed blowing ratios, i.e. $F = 0.25\%$ and $F = 0.50\%$, the pressure difference over the porous wall is $\Delta p \approx 316\,\text{kPa}$ and $\Delta p \approx 487\,\text{kPa}$, respectively.

Subsequent to the analysis of the coolant through-flow behaviour, now the resulting surface temperatures as well as the cooling efficiencies are examined. Figure 7.48 depicts surface temperature plots for the blowing ratio $F = 0.25\%$ and three shock-generator positions, i.e. $\Delta y \in [0, 5.0, 9.7]\,\text{mm}$. Each of the contour plots compares experimental measurements to numerical data.

The effect of the flow-field alteration through the shock generator is clearly visible for the transpired surface and the wake region. As suggested by the discussion on local distributions of coolant mass flux and heat transfer, the front region exhibits higher temperatures when compared to the aft region for the two test cases with elevated shock generator. In the wake region, a considerable increase of temperature is detected at the position where the reflected shock impinges. Due to the larger wave angle, the location is shifted upstream for the test case with an elevation of $\Delta y = 9.7\,\text{mm}$. The comparisons between IR thermography and OpenFOAM simulation show a fair agreement for the complete surface observed. Features such as the significant temperature increase on the transpired surface as well as in the wake region are well captured. Moreover, the temperature levels are well represented in general. Exceptions to this are the recirculation zones in the sample's wake as well as close to the leading edge, where the simulation yields higher temperatures.

180

(a) $F = 0.25\%$ - $\Delta y = 0$

(b) $F = 0.25\%$ - $\Delta y = 5.0\,\mathrm{mm}$

(c) $F = 0.25\%$ - $\Delta y = 9.7\,\mathrm{mm}$
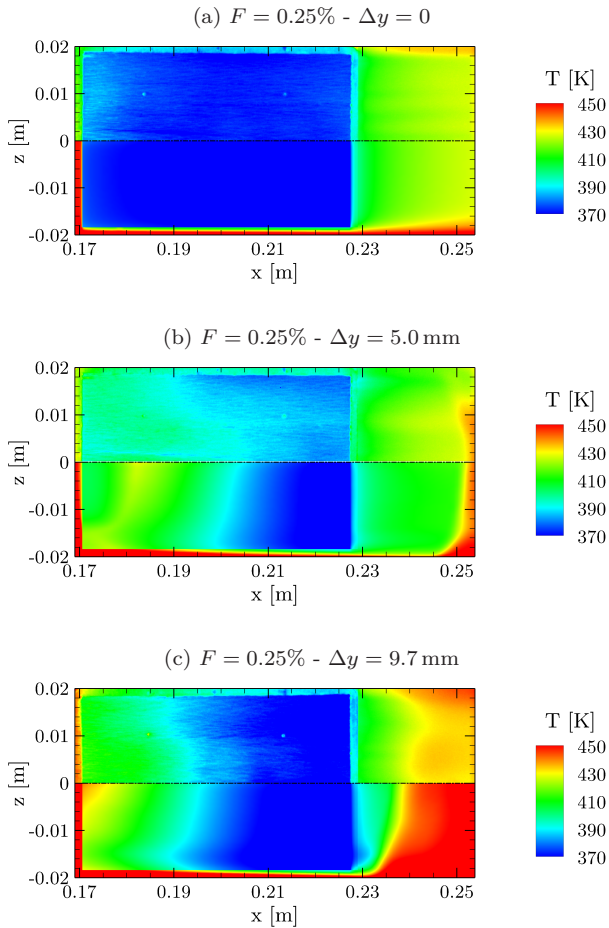
Figure 7.48: Surface temperature distributions from experiment (top) and simulation (bottom) for reference sample at $F = 0.25\%$ and different shock-generator positions

The cooling efficiency as defined by equation (7.4) is employed for a more detailed analysis of the effect of transpiration cooling. As it takes into consideration the no-blowing wall temperature, the influence of the previously discussed numerical modelling error associated to shock-wave/boundary-layer interaction is partly eliminated. Figure 7.49 depicts the cooling efficiency for the blowing ratios $F \in [0.25\%, 0.50\%]$ and shock-generator positions $\Delta y \in [0, 5.0, 9.7]$ mm. The cooling efficiencies of both test cases with shock-generator elevation show low values at the beginning of the samples where the aerothermal load is generally high and the coolant mass flow rate low. The values of Θ increase with sample length for both test cases. However, while Θ increases monotonously for $\Delta y = 9.7$ mm, a local minimum of Θ on the sample is found for the medium shock-generator position. Generally lower cooling efficiencies are observed for the shock-generator test cases except for the rear part of the sample, where the values are similar to the no-shock-generator test cases.

(a) $\Delta y = 5.0$ mm

(b) $\Delta y = 9.7$ mm
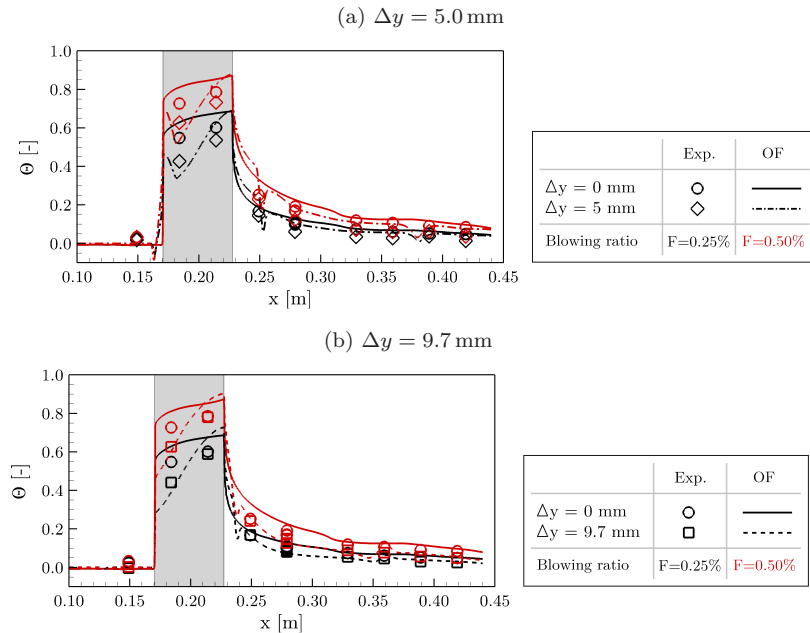
Figure 7.49: Cooling efficiency over axial channel length for blowing ratios $F \in [0.25\%, 0.50\%]$ and different shock-generator positions

For all test cases, a substantial decrease of Θ takes place at the transition to the non-transpired surface. Downstream, in the film-cooled wake region, a reduced cooling effect remains visible for the complete length observed. Here, the influence of the shock generator expresses through a slightly lower value of Θ. The numerical results additionally reveal a decrease of the cooling efficiency at $x \approx 0.25\,\mathrm{m}$ for both shock-generator cases. This is due to the reflected shock wave that impinges on the top wall, see also figure 7.39.

Comparing simulation and experiment, a fair agreement is found. Both experiment and simulation show the described effects associated to the shock generator. However, the differences between test cases with and without shock generator are less pronounced for the experimental measurements when compared to the simulation. This particularly concerns the wake region where the experimental data indicates only a weak influence of the shock generator.

7.5.3 Wall-Thickness Variation in Shock-Generator Flow Field

The non-uniform flow field for the shock-generator test cases triggers the occurrence of local temperature maxima in the regions of highest heat flux. As depicted in figures 7.48 and 7.49, the highest temperature levels or respectively lowest cooling efficiencies are found in the sample's front region. Additionally, the local coolant mass flux $|\rho u_y|$ is at a minimum in this region, see figure 7.47. In section 7.4, the method of sample contouring by means of a variation in the wall thickness proved to be a possible means of counterbalancing local hot spots. In the following, this is explored in context of the here-presented shock-generator test cases.

Due to the locally reduced wall thickness, an elevated coolant mass flux in the front region was found for the contoured sample 180°. However, in the previous analysis, the static wall pressure at the main-flow interface was nearly constant, whereas larger differences were found for the shock-generator test cases. Figure 7.50 depicts the local coolant mass flux $|\rho u_y|$ over sample length for different elevations of the flow barricade, i.e. $\Delta y \in [0, 5.0, 9.7]\,\mathrm{mm}$. In addition to the results of the contoured sample 180°, the previously discussed values for the reference sample are included. The diagram reveals significant higher coolant mass fluxes in the front region for the contoured sample 180° and all shock-generator positions. In contrast, $|\rho u_y|$ is reduced in the aft region. The different shock-generator elevations influence the resulting distribution without changing the general trend. Although the absolute coolant mass fluxes in the front region reduce from $\Delta y = 0\,\mathrm{mm}$ to $\Delta y = 9.7\,\mathrm{mm}$, the relative effect of the wall-thickness variation remains similar. Compared to
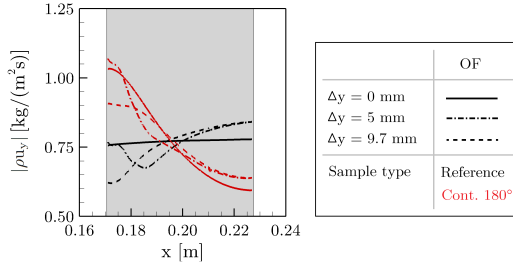
Figure 7.50: Comparison of coolant mass flux distributions for reference and contoured 180° samples at $F = 0.25\%$ and for three shock-generator positions $\Delta y \in [0,\ 5.0,\ 9.7]\,\mathrm{mm}$

the reference-sample test case, up to around 45% more coolant is directed to the front region. Here, also the highest heat fluxes are acting as demonstrated earlier by figure 7.44. The resulting cooling efficiencies for maximum shock-generator elevation and two blowing ratios are compared to the reference-sample test case in figure 7.51. The diagram indicates a more homogeneous cooling efficiency for the contoured sample 180°. Compared to the reference sample, slightly higher values are found in the front region, while Θ is smaller in the aft region. The effect on the transpired surface is visible in both experiment and numerical simulation. Conversely, no effect is notable for the wake region. This confirms the earlier finding, stating that the total coolant mass flow rate is decisive for the cooling of the wake region, while the local distribution of coolant injection is not of importance for the investigated test cases. However, also for the transpired surface, the effect of the locally reduced wall thickness is limited. The substantial increase of aerothermal loads in the front region
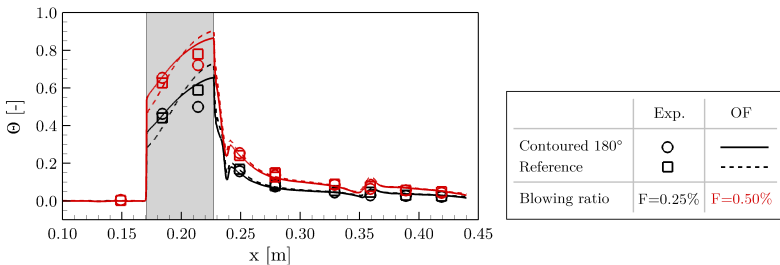
Figure 7.51: Comparison of cooling efficiency over axial channel length for reference and contoured 180° samples for shock-generator position $\Delta y = 9.7\,\mathrm{mm}$

due to the shock-generator flow field dominates the cooling efficiency and the temperature levels. As a consequence, the front region exhibits significant lower cooling efficiencies than the aft region, even for the contoured sample 180°. This seems reasonable when comparing the relative deviations in the heat transfer coefficient and local coolant mass flux, i.e. +160% and +40%, respectively. The agreement between simulation and experiment is good in the wake region and fair on the sample surface. The effect of the contoured sample 180° for the transpired surface is well captured, although some deviations in the absolute values are present.

Concluding the study of this test case, the method of variable wall thickness proves to be effective in the reduction of local hot spots also for more complex flow fields such as present in the shock-generator test cases. However, the non-uniform distribution in coolant mass flux for the contoured sample 180° was found to be not sufficient to achieve uniform cooling efficiency over the sample surface. For this, a stronger variation in the wall thickness, a generally less-permeable porous material, or a grading in the permeability would be necessary.

7.5.4 Summary

The shock-generator test cases introduced the formation of shock waves and expansion fans to the flow field. The strength of these flow-field modifications depended on the position of the movable flow barricade that represents the geometrical obstruction. Two shock-generator positions were analysed in this section, i.e. $\Delta y = 5$ mm and $\Delta y = 9.7$ mm, which resulted in pressure differences over the sample surface of around 60 kPa and 80 kPa, respectively. The more complex flow field yielded areas of increased wall temperature and heat flux. Moreover, due to the impingement of shock waves and the interaction with the boundary layer, flow separation and recirculation zones occurred upstream and downstream of the sample at the channel's top wall. With respect to this, the OpenFOAM results were confirmed by the empirical Korkegi criterion.

Regarding transpiration cooling, the change of the flow field due to the shock generator has a significant influence on the distribution of coolant mass flux over the porous surface which was found to be non-uniform in the test cases. The observed variation depended on blowing ratio, pressure loss over the sample, and pressure variation over the transpired surface. As a consequence of the variations in convective heat flux and coolant mass flux over the sample surface, also the cooling efficiency was significantly altered. Reduced values of Θ were found in the sample's front region, while the cooling efficiency recovered to

no-shock-generator values for the aft region. Furthermore, a weak influence on the wake region was detected. In summary, the discussed results demonstrate that the more complex main-flow conditions have a significant effect on transpiration cooling which, however, remains an effective means of cooling.

The numerical simulation results are in reasonable agreement to the experiments. Regarding the no-blowing test case, deviations in the absolute surface-temperature distributions were found for the shock-generator test case which are linked to the modelling of shock-wave/boundary-layer interaction. In contrast, a very good agreement between numerical and experimental pressure distributions was observed for both shock-generator positions. The cooling efficiency has been employed to investigate the effect of the introduced flow-field modifications on transpiration cooling. A fair agreement between numerical and experimental results was found for both shock-generator positions and all investigated blowing ratios. The developed OpenFOAM solver is thus capable of simulating transpiration cooling also in more complex flow fields such as present for the shock-generator test cases.

Lastly, the contoured sample 180° was tested in combination with the shock generator. As found before, the reduced wall thickness in the front region increased the local coolant mass flux. This counteracted the higher heat loads induced by the shock-generator flow field to some extent.

7.6 Double-Wedge Sample - Combined Effects of Geometry and Flow Field

Besides the modelling of transpiration cooling in more complex flow fields, extending the simulation capabilities towards more complex porous structures has been one of the main goals of the here-presented research work. This is important with respect to application cases such as strut and wall injectors within a scramjet combustor or sharp leading edges envisaged for hypersonic vehicles. These non-flat geometries self-induce the formation of shock waves and thus combine the effects of geometry and flow-field variations which have been investigated separately in sections 7.4 and 7.5. To explore the combination of effects, the double-wedge sample which features two inclined surfaces is examined in the following. Again, experimental and numerical results are discussed together to analyse the transpiration-cooling processes. Moreover, the validation of the numerical solver is continued by means of comparisons to the experimental data for the double-wedge test cases.

7.6.1 Non-Uniform Flow Field without Blowing

The non-flat geometry of the porous sample represents a flow obstruction and thus triggers the formation of shock waves. This alters the flow field as well as the distributions of static wall pressure and heat flux. Before analysing the influence of these effects on transpiration cooling, the double-wedge sample without blowing is discussed.

First, the flow field is examined by means of experimental and numerical schlieren images given in figure 7.52. As expected, the non-flat sample geometry induces a system of shock waves and expansion fans which manifests throughout the test section. The first oblique shock wave forms at the leading edge of the double wedge at the channel's top wall. It subsequently impinges onto the bottom wall where the numerical results suggest the occurrence of a recirculation zone ($x \approx 0.21\,\mathrm{m}$). The associated boundary-layer thickening triggers the formation of a new shock wave which merges with the reflected shock before hitting the sample's wake region on the channel's top wall. Additionally, another shock wave impinges slightly downstream in the wake region. It is formed at the bottom wall and originates from the boundary-layer reattachment downstream of the recirculation zone. At the tip of the double-wedge sample, an expansion fan forms due to the widening of the test channel. Comparing numerical and experimental schlieren images, a very good conformity is found.
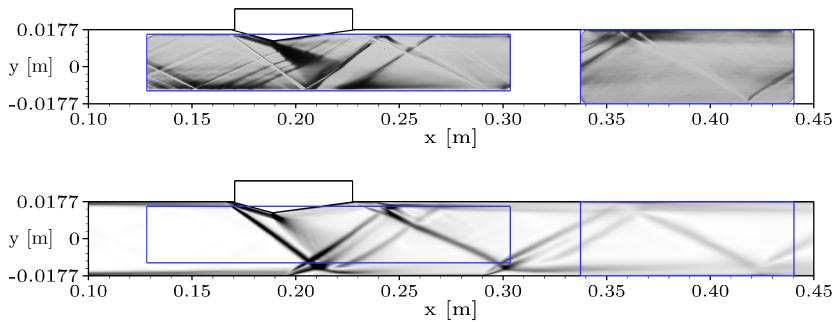
Figure 7.52: Experimental (top) and numerical (bottom) schlieren images for double-wedge sample test case and $F = 0\%$

Figure 7.53 depicts the corresponding wall pressure distribution on the channel's symmetry plane based on experimental and numerical data. As suggested by the schlieren images, a non-uniform distribution with significant pressure variations is found. The oblique shock forming at the first ramp of the double wedge yields a rise of static pressure whereas the expansion fan triggers a pressure drop at the tip of the double-wedge sample. This results in a pressure difference of around 50 kPa between the two inclined surfaces, referred to as front and aft surfaces in the following. Likewise, pressure increases are detected in the sample's wake region and at the channel's bottom wall at the positions of shock impingements. The comparison between simulation results and measurements shows a very good agreement for both top and bottom walls of the test section. Following this, the employed numerical setup is able to accurately reproduce the flow field without boundary-layer blowing.
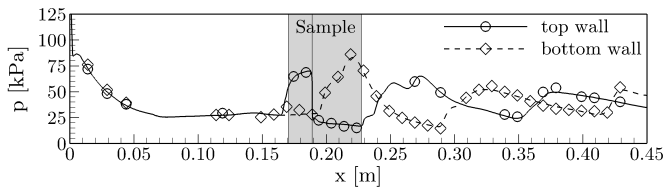
Figure 7.53: Experimental (symbols) and numerical (lines) wall pressure over channel length for the double-wedge sample without blowing

To investigate the effects of shock-wave/boundary-layer interaction for the double-wedge sample in more detail, figure 7.54 visualises the occurrence of recirculation zones based on numerical data. As for the shock-generator test cases, isosurfaces for $u_x = 0$ (black coloured) are employed to roughly mark the regions of flow separation. Additionally, the top-wall temperature distribution is shown. For better visualisation the y-coordinate is inverted in the figure.

Two recirculation zones are indicated for both top and bottom walls of the channel. A small separation zone is observed at the leading edge of the sample, i.e. where the first oblique shock wave forms. The shock wave is reflected at the bottom wall (note the upside-down visualisation) and impinges again in the direct wake of the porous sample. This results in a significant increase in pressure that triggers the occurrence of a second recirculation zone. The numerical results are confirmed by applying the empirical Korkegi criterion, i.e. equation (2.43), on the pressure distribution given in figure 7.53. With respect to the transpiration-cooling test cases, particularly the shock-wave impinging onto the downstream region and the interaction with the coolant film is of interest. The numerical surface temperature distribution without blowing reveals elevated values directly downstream of the formation of shock waves as well as in the zones affected by shock-wave/boundary-layer interaction. The highest temperatures are observed at the reattachment lines downstream of the recirculation zones.
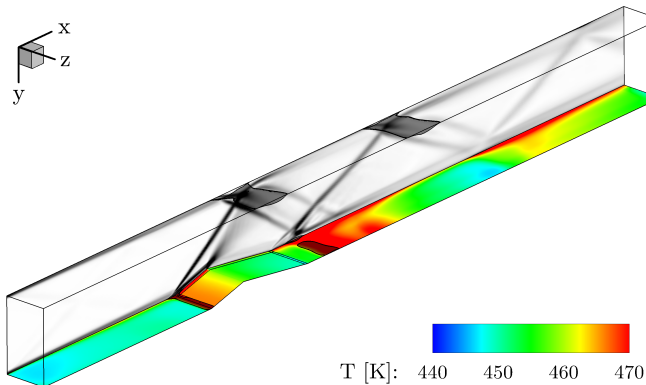
Figure 7.54: Combined visualisation of schlieren image, isosurfaces for $u_x = 0$, and top-wall surface temperature for double-wedge sample without blowing (numerical results, half model)
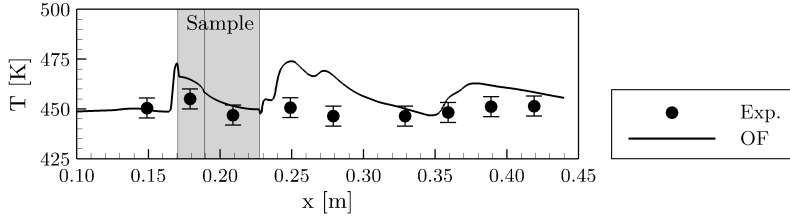
Figure 7.55: Wall temperature distribution for double wedge without blowing

A comparison of numerical and experimental wall temperatures is given in figure 7.55. The diagram depicts spanwise-averaged numerical results (lines) as well as thermocouple measurements (symbols) over channel length for the no-blowing test case. The results confirm the previous analysis and indicate a non-uniform wall temperature distribution due to the formation of shock waves and expansion fans. Comparing front and aft surfaces of the double wedge, significantly elevated temperatures are found on the front surface. This suggests also a higher heat flux in the front region of the sample for a transpiration-cooled test case. The comparison of numerical simulation results to thermocouple data reveals a fair agreement for the surface of the porous sample. Opposed to this, larger deviations are found in the direct wake region (up to $x \approx 0.3\,\mathrm{m}$), where the numerical simulation overpredicts the temperature levels. The numerical values in the wake region exhibit significant temperature variations in regions of shock impingement, whereas the variation in the experimental data is less. As discussed for the shock-generator cases in section 7.5, these deviations are linked to the numerical simulation of shock-wave/boundary-layer interaction.

7.6.2 Influence of Boundary-Layer Blowing on Main Flow Field

A non-uniform main flow field featuring shock waves and expansion fans substantially influences transpiration-cooling processes. This has been demonstrated in section 7.5. However, the effect of boundary-layer blowing on the main flow field (not considering the wall-near region) was found to be weak.

This is now evaluated for the double-wedge sample. Figure 7.56 compares numerical schlieren images at no blowing and for a blowing ratio of $F = 1.00\%$. Additionally, the static wall pressure along the channel's top wall for different blowing ratios is depicted in figure 7.57. Examining the schlieren images, a clear influence of boundary-layer blowing on the wall-near region is found. The large blowing ratio of $F = 1.00\%$ leads to a displacement of the main flow which is particularly distinct for the aft region. Besides, the brighter region
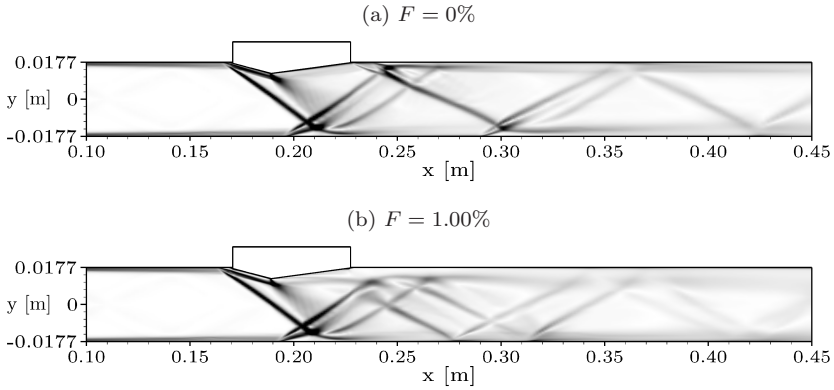
Figure 7.56: Comparison of numerical schlieren images without and with blowing

close to the wall roughly indicates the coolant film in the wake region. These alterations of the wall-near region also influence the formation of the shock waves. The point of shock formation at the front ramp of the double wedge shifts slightly upstream. Moreover, the system of shock waves and expansion fan changes downstream of the sample due to thick coolant film. At the top wall, two oblique shocks are forming ($F = 1.00\%$) instead of a single shock ($F = 0\%$). The absence of distinct recirculation zones at the positions of impingement onto the bottom wall indicates that the two shock waves are mitigated in strength.

The top-wall pressure distribution depicted in figure 7.57 reveals a considerable influence of coolant injection for the aft surface as well as the sample's wake region. In contrast, no influence on the front surface is visible. For boundary-layer blowing the wall pressure on the aft surface of the double wedge is elevated when compared to the no-blowing case. An increase of the blowing ratio inten-
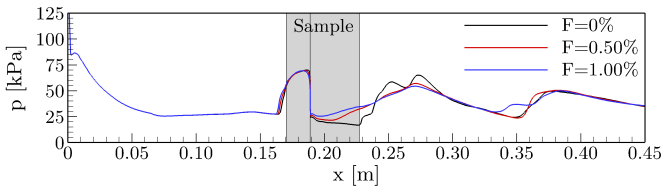
Figure 7.57: Comparison of top-wall pressure over channel length for double-wedge sample at different blowing ratios

sifies the effect. For the no-blowing case, a significant pressure increase is observed at the trailing edge of the sample. This is due to the formation of a shock wave to adjust the direction of the supersonic flow parallel to the channel's top wall. This is not present for the two blowing test cases. Here, the coolant film yields a thick subsonic region close to the wall which prevents the occurrence of a shock wave. As a consequence, a smoother pressure distribution results. However, the wall pressure still shows an oscillating behaviour due to the reflections of the shock waves throughout the test section.

Following the analysis, a substantial effect of boundary-layer blowing on the main flow field has been found for the double-wedge sample test case. This stresses the importance of coupled simulation approaches such as followed within the frame of this thesis.

7.6.3 Geometry and Flow-Field Effects on Transpiration Cooling

In the previous sections, the influences of a variable wall thickness and non-uniform main-flow conditions on transpiration cooling have been demonstrated separately. The double-wedge test cases combines both aspects by means of a non-flat, shock-inducing sample geometry. Figure 7.58 combines an experimental schlieren image with in-situ calibrated IR data and is exemplarily used to introduce the different aspects which are subsequently discussed in more detail. Note that the field of view of the schlieren image is limited and does not reach to the wall. Moreover, the coordinate system has been rotated for better visualisation.

The experimental results reveal a non-uniform surface temperature distribution with elevated temperatures for the front part of the double wedge. This is linked to several effects. First, the shock wave forming at the leading edge of the sample increases the pressure over the front surface. The expansion fan at the tip of the wedge then yields a pressure drop for the aft surface of the double wedge. The substantial pressure difference triggers a non-uniform coolant flow distribution and possibly also coolant cross flow within the sample. The coolant mass flow rate is higher for the aft surface. This is also suggested by the schlieren image as several density-gradient lines are visible. Secondly, also the heat flux is significantly higher for the front surface. In combination with the reduced cooling, this yields elevated temperatures in the front region. The elevated temperature levels in turn affect the through-flow resistance which increases at higher coolant-fluid temperature as shown in section 5.2.3. Lastly, the wall thickness of the sample is largest at the tip of the
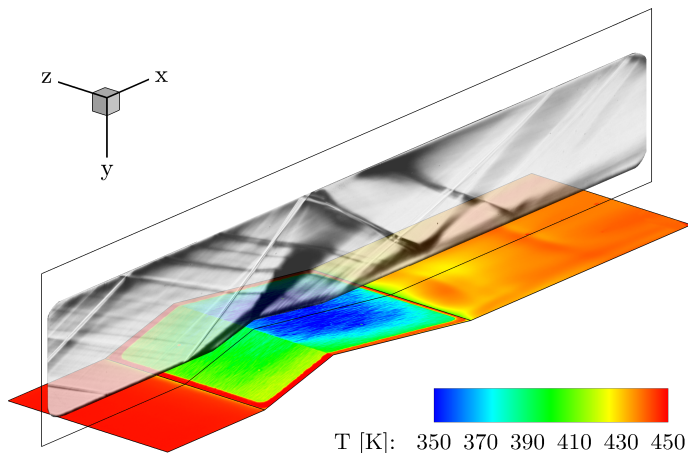
Figure 7.58: Combined experimental schlieren and in-situ calibrated IR images for a blowing ratio of $F = 0.25\%$

double wedge and decreases towards leading and trailing edges. This further modulates the distribution of coolant mass flow as an increased thickness generally leads to reduced coolant mass fluxes.

The shock wave forming at the inclined front surface is reflected on the bottom wall and impinges in the sample's wake region. There, the coolant film interacts with the shock wave which expresses by means of the non-uniform temperature distribution shown in figure 7.58. Higher temperatures are observed in the recirculation zones and at the positions of flow reattachment.

Complementing the experimental results plot, figure 7.59 illustrates the internal temperature distribution obtained through numerical simulation. The isometric plot depicts a half model of the double-wedge sample. The y-coordinate has been reversed to show the symmetry plane. A comparison of OpenFOAM results to internal thermocouple measurements is given later. As found for the IR data, the sample's front surface exhibits elevated temperatures when compared to the aft surface. Although the simulation results show a generally more homogeneous distribution, local hot spots occur which are due to three-dimensional main-flow phenomena. The temperature values decrease towards the coolant-reservoir side. Moreover, the front region exhibits substantially higher temperatures and the isotherms indicate heat transfer by conduction from front to aft region.
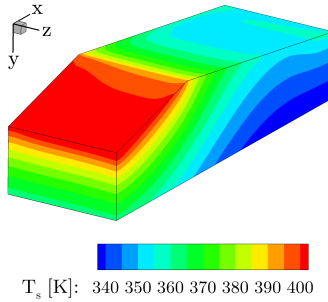
Figure 7.59: Solid-phase temperature distribution for symmetrical half model of double-wedge sample for $F = 0.25\%$

The blowing behaviour and the distribution of the available coolant mass flow has a decisive influence on the temperature levels. To investigate this for the double-wedge sample, the through-flow behaviour is exemplarily discussed for the test case with a blowing ratio of $F = 0.25\%$. Figure 7.60 illustrates several properties on the sample's symmetry plane. These include the Darcy velocity vectors within the sample and on the transpired surface. Additionally, the coolant fluid's pressure distribution p_f over the sample is given by the contour plot and the static wall pressure p at the interface to the main flow is plotted on the diagram axis.

Two effects are expected to affect the coolant-flow behaviour: First, the wall-pressure variation and secondly, the elevated temperature levels in the front region. The wall pressure varies by around $50\,\mathrm{kPa}$ between front surface and aft surface of the porous sample. As previously shown by means of figure 7.57, blowing induces an increase of hot-gas static pressure close to the sample's trailing edge. This is also visible for the here-discussed test case with $F = 0.25\%$. The coloured contour visualises the pressure drop of the coolant over the sample. The distance between isobars reduces towards the hot-gas side which is a consequence of the coolant gases' acceleration within the porous structure. The curved Darcy streamlines indicate coolant-flow in cross direction. Substantially reduced outlet velocities are found for the front region when compared to the aft region. Examining the front surface, a reduction of outflow velocity with increasing distance to the leading edge is depicted. Here, different effects are counteracting. Directly at the leading edge, sample thickness and wall pressure p have their minimum values. Opposed to this, the temperature is at a maximum as illustrated in figure 7.59. The first-mentioned effect apparently outweighs the temperature dependency which leads to a larger Darcy velocity at the leading edge. With respect to the aft surface, an elevated and nearly

194

constant Darcy velocity is found. Variations of pressure, sample thickness, and temperature seem to balance each other out. The direction of the outflow vectors is nearly normal to the transpired surface as the tangential velocity component is small for the complete surface of the double-wedge.

Although the outflow Darcy velocity is substantially higher in the aft region, a conclusion on the distribution of coolant mass flux cannot be drawn directly. This is because of the pressure and temperature variations which yield differing densities at the transpired surface. Figure 7.61 gives the ratio of coolant mass fluxes exiting over front and aft surfaces of the sample in dependence of the blowing ratio. Regarding this, the coolant mass fluxes $(\dot{m}_c/A_c)_{front}$ and $(\dot{m}_c/A_c)_{aft}$ are determined as the averages of the respective surfaces. The diagram reveals a reduced coolant mass flux over the front surface when compared to the aft surface. Moreover, a significant dependency on the blowing ratio is found. For the lowest blowing ratio, i.e. $F = 0.10\%$, the mass flux $(\dot{m}_c/A_c)_{front}$ is reduced by around 35%. With respect to the previously discussed test case at $F = 0.25\%$, the numerical simulation indicates a mass flux reduction of around 20%. This is relatively low when compared to the differences between Darcy velocities for front and aft surfaces. For increasing blowing rates, the ratio diminishes which suggests a more uniform coolant mass
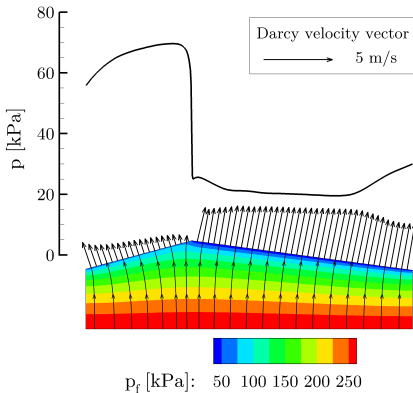
Figure 7.60: Pressure distribution on sample surface, resulting Darcy velocity vectors, and coolant pressure distribution within double-wedge sample for $F = 0.25\%$
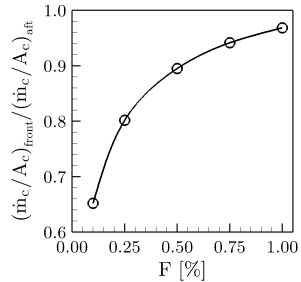
Figure 7.61: Mass flux ratio between the two surfaces of the double-wedge sample

flow distribution. This is a consequence of the rising pressure difference over the sample thickness for elevated blowing ratios. While the pressure difference between front and aft surfaces remains similar for all blowing ratios, the coolant reservoir pressure significantly increases for rising blowing ratios. In fact, also the pressure difference between the two surfaces of the double wedge slightly reduces for increasing blowing ratio as indicated by figure 7.57.

The through-flow behaviour of the double-wedge sample and the non-uniform aerothermal load explain the observed temperature distribution for the example case. Next, the surface temperature is evaluated for different blowing ratios. Simultaneously, the experimental results are compared to the numerical simulations to further validate the developed OpenFOAM solver. Figure 7.62 depicts in-situ calibrated infrared images and numerical results for the transpired surface and the sample's wake region. The temperature distributions confirm the previous findings of higher temperatures for the sample's front surface
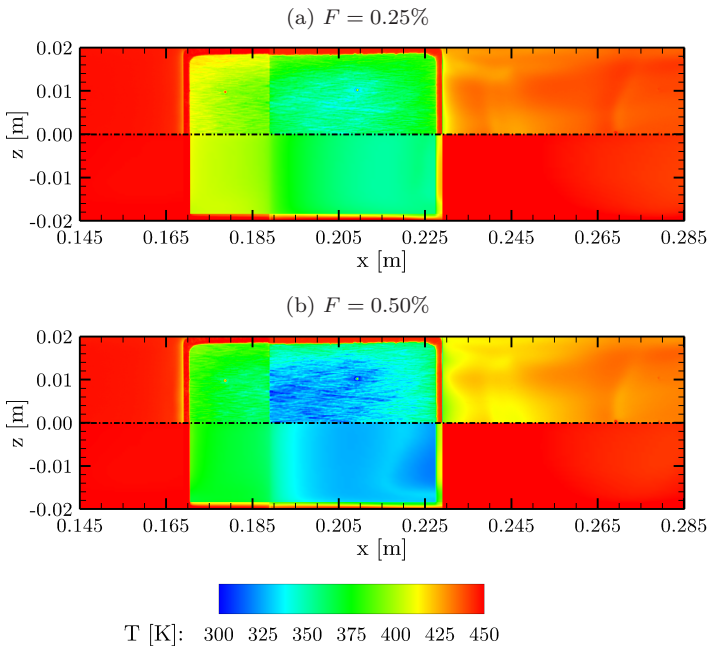
Figure 7.62: Comparison of sample surface and wake region temperatures for double-wedge sample and two blowing ratios - in-situ calibrated infrared thermography (top half) and OpenFOAM simulation (bottom half)

when compared to the aft surface. Here, the coolant mass flux is reduced and the aerothermal load is higher. Besides, a significant increase in temperature is observed at the trailing edge. Generally high temperatures are found for the non-transpired wake region. This is linked to the impingement of the reflected shock wave as visible in the schlieren images given for example by figure 7.52. The effect is discussed in more detail in appendix E.4 where additional results for test cases with the double-wedge sample turned by 180° are given. The comparison between experimental data and simulation results shows a fair agreement of the temperature levels on the transpired surface for both blowing ratios. However, larger deviations are found for the wake region where the simulation indicates higher temperatures. Examining the porous surface more closely, the experimental temperature distribution reflects the C/C fibre structure of the material. This effect has been discussed before and cannot be captured by the numerical simulations. Furthermore, the regions close to the double-wedge sample's boarder exhibit elevated temperatures which can be explained by parasitic lateral heat conduction to some extent (cf. section 7.3.2).

To evaluate the effect of transpiration cooling in more detail, the cooling efficiency which takes into account the uncooled wall temperature as well as the reservoir temperature is employed. Figure 7.63 compares the cooling efficiencies obtained from spanwise-averaged simulation results (lines) and wall thermocouple measurements (symbols). The diagram reveals a general increase of cooling efficiency with blowing ratio and particularly at the transition to the aft surface. This corresponds well to the previously discussed differences in the coolant mass flux between front and aft surfaces, see figure 7.61. A good agreement between simulation results and experimental measurements is found for all blowing ratios and over the complete length observed.
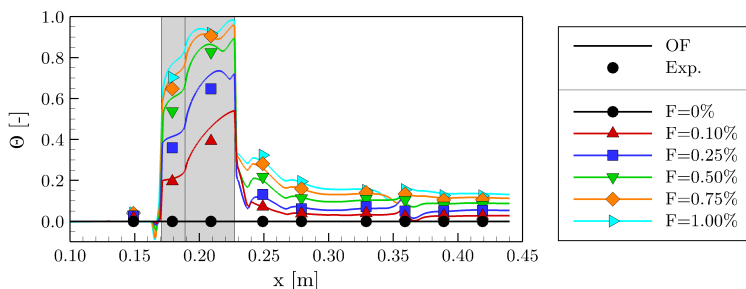
Figure 7.63: Cooling efficiency over axial channel length for double-wedge sample test case at different blowing ratios
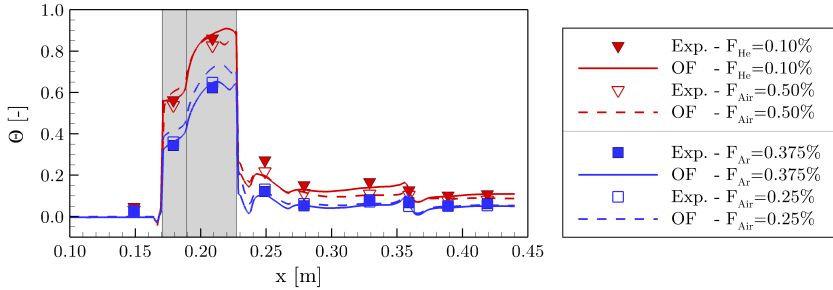
Figure 7.64: Cooling efficiency over axial channel length for double-wedge sample and blowing with helium and argon

The effect of foreign-gas blowing for the double-wedge sample is exemplarily shown for helium and argon transpiration in figure 7.64. As in section 7.3.3, each test case using foreign gas (solid line) is compared to blowing of air at a scaled blowing ratio (dashed line). Moreover, the OpenFOAM results are compared to the corresponding thermocouple measurements. In general, the results for blowing with helium and argon show similar features as discussed for cooling with air. The significant influence of the coolant gas properties on the cooling efficiency is confirmed also for the double-wedge sample. Similar results are obtained for the test cases with $F_{He} = 0.10\%$ and $F_{Air} = 0.50\%$ for which the blowing ratios were scaled by the ratio of specific heat capacities. The superiority of helium in the cooling of the non-transpired wake region (see section 7.3.3) is less pronounced for the double-wedge sample. A generally good agreement between OpenFOAM simulations and experimental data is found for both helium and argon blowing. This validates the OpenFOAM solver's modelling capabilities with respect to foreign-gas injection also for more complex geometries and main-flow conditions.

Having the temperature and cooling efficiency of the external surfaces analysed, the focus is now shifted on the temperatures within the double-wedge sample. Figure 7.65 therefore depicts the temperature distribution over sample thickness for the test cases using air as coolant gas. Foreign-gas test cases are not included here. However, the internal temperatures within the porous sample are comparable to the air test cases at scaled blowing ratios. The analysis is split in two regions, i.e. front (large symbols, solid lines) and aft (small symbols, dashed lines). Thermocouple positions are indicated in figure 3.6c, while the numerical data is obtained from slices through the symmetry plane at $x = 0.179\,\mathrm{m}$ (front) and $x = 0.209\,\mathrm{m}$ (aft). Comparing both regions, the
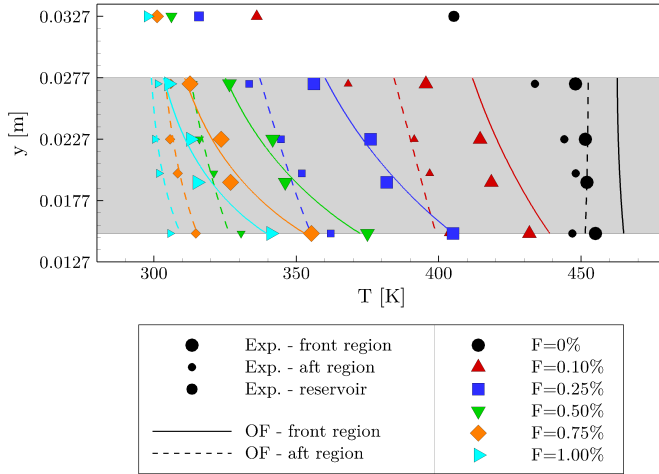
Figure 7.65: Internal solid-phase temperatures for double-wedge sample at different blowing ratios

diagram indicates elevated temperatures for the front region, while the levels are reduced in the aft of the double-wedge sample. Moreover, the temperature gradients at the transpired surface (i.e. Γ_{HG} at $y \approx 0.015\,\mathrm{m}$) are higher for the front region which is in accordance with the increased aerothermal loads. Rising blowing ratios reduce the temperature levels at the sample surface and within the porous wall. However, a significant temperature difference between front and aft regions at the hot-gas side remains visible for all test cases. The comparison between OpenFOAM simulations and internal thermocouple measurements shows a generally good agreement for all blowing ratios as well as both regions of the porous sample.

From the sensitivity study in section 7.2.4, the modified ω boundary condition was found to give best agreement for the reference-sample test case. It has therefore been employed in all numerical simulations thereafter as the boundary condition on transpired surfaces. The good agreement of the simulation results to experimental data for the here-investigated double-wedge confirms this choice and suggests the suitability of $\omega_{F>0,mod}$ also for non-flat transpiration-cooled geometries and more complex flow conditions. To evaluate this in more detail, the sensitivity study on the ω boundary condition is repeated for the
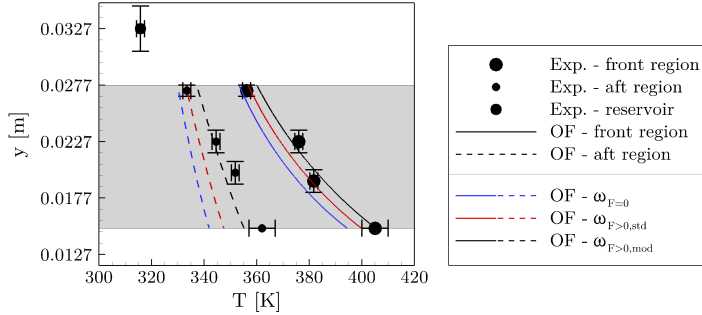
Figure 7.66: Sensitivity analysis on ω-BC for double-wedge sample - internal temperature for F = 0.25%

double-wedge test case. The corresponding results for blowing with air at $F = 0.25\%$ are given in figure 7.66. As for the reference sample and uniform flow conditions, best agreement to the experimental measurement is found for the modified blowing condition $\omega_{F>0,mod}$. This applies to the comparison of both front region and aft region.

7.6.4 Summary

The test cases with the double-wedge sample triggered the formation of shock waves and expansion fans due to the non-flat sample geometry. This combines the previously discussed influences of variable sample thickness and more complex supersonic main flow field. The analysis of the flow field without boundary-layer blowing revealed significant variations of local wall pressure and wall temperature respectively heat flux. Moreover, recirculation zones formed at top and bottom walls as a consequence of shock-wave/boundary-layer interaction.

The non-uniform main flow field has several effects on transpiration cooling. Likewise, a considerable influence of boundary-layer blowing on the main flow field was found for the double-wedge sample test case. This concerned the formation and positions of shock waves as well as the wall pressure distribution. The finding underlines the importance of coupled simulation approaches.

Regarding the transpiration-cooled double wedge, substantially higher temperatures were found for the front surface of the sample when compared to the

aft region. This is a consequence of the higher aerothermal load in this region as well as the reduced coolant mass flux. The latter effect resulted from the higher hot-gas pressure and the elevated temperatures in the front region. The difference between the coolant mass flux for front and aft surfaces depended on the blowing ratio and was found to be less pronounced for high blowing ratios. Moreover, the numerical simulation revealed a multidimensional coolant flow within the porous structure.

A generally good agreement was observed for the comparison between experimental results and numerical simulations. The temperatures within the porous structure are well captured by the numerical solver for front and aft regions and all blowing ratios tested. With respect to the surface temperatures, infrared thermography measurements were compared to the numerical temperature distributions. Deviations were limited to the boarder regions of the porous sample and may be explained by lateral heat fluxes and/or a reduced boarder permeability. Both effects were not considered in the numerical simulations. Moreover, differences in the absolute temperatures were observed in the direct wake region where shock-wave/boundary-layer interaction occurred. The cooling efficiency has been employed to analyse the effect of transpiration cooling. As it takes into account the no-blowing wall temperature, the discrepancies originating from the modelling errors linked to shock-wave/boundary-layer interaction are partially eliminated. Experimental and numerical results are in good agreement for all blowing ratios and over the complete length of the test section. This was additionally demonstrated for the injection of gases other than air by means of test cases using helium and argon as coolants.

Lastly, an exemplary comparison of the simulation results for the three proposed boundary conditions of the specific turbulence dissipation rate ω was performed. The modified boundary condition $\omega_{F>0,mod}$ yielded best agreement to the experimental measurements. This confirms the findings of the sensitivity study for the reference sample and suggests a good suitability of the new boundary condition also for the more complex main flow field and blowing behaviour of the double-wedge test case.

Summarising the comparison of simulation and experiment, the OpenFOAM solver and the applied numerical setup were able to capture the influences of non-uniform main-flow conditions as well as multidimensional coolant flow within the porous sample. The results thus validate the solver's simulation capabilities with respect to non-flat porous geometries under more complex supersonic main-flow conditions.

CHAPTER 8

Conclusion and Outlook

Transpiration cooling offers great potential for thermal protection of future combustion engines as well as hypersonic vehicles. A considerate body of research work has focused on different aspects of the cooling technique. However, the detailed numerical modelling of transpiration cooling as well as the numerical coupling of processes occurring within the porous structure and in the hot-gas main flow field have still not been conclusively investigated. Moreover, reliable and accurate numerical tools for the design and layout of transpiration-cooled structures are lacking. This is of particular importance, since the design of aerospace applications increasingly relies on simulation results.

Within the present thesis, a numerical CFD solver has been developed that allows the simulation of complex transpiration-cooled structures in non-uniform sub- and supersonic hot-gas flows. An integral approach with full coupling of both domains, i.e. hot-gas flow field and porous structure, has been followed. For practical reasons, a volume-averaged method with consideration of local thermal non-equilibrium effects was selected. A three-dimensional Darcy-Forchheimer approach is employed to model coolant through flow. Moreover, the solver is capable of modelling the injection of arbitrary coolant gases in a hot main flow of air. Special attention was put on the consideration of anisotropic material parameters which are characteristic for the investigated fibre-reinforced ceramics, i.e. thermal conductivity and permeability. The OpenFOAM software package was selected as the framework for the development since it allows for

implementation of own models and solver modifications and is additionally free from licensing costs.

The solver has been applied to various test cases and validated by means of comparisons to experimental results. In addition to the solver development, the combined numerical and experimental approach aims to enhance the understanding of transpiration cooling for more complex porous geometries and main-flow situations.

First, the physical processes taking place within a transpiration-cooled porous structure were discussed. Therefore, the internal heat transfer between coolant and solid skeleton of the porous structure was addressed. A theoretical study based on an analytical criterion suggests a non-negligible influence of local thermal non-equilibrium for the later-discussed transpiration-cooling test cases. This motivated the implementation of separate energy equations for the porous domain into the OpenFOAM solver which was validated against an analytical solution.

In a second step, results with respect to the through-flow behaviour of the porous material C/C were presented. The analysis is split in uniform and multi-dimensional coolant flow and combines experimental measurements and numerical simulations. Summarising the permeability investigation for unidirectional flow, the presented measurements confirm the applicability of the Darcy-Forchheimer equation for modelling of pressure loss within C/C structures. Moreover, the experimental data suggests that the permeability coefficients K_D and K_F for C/C are independent of the coolant gas used as well as temperature and pressure levels. Thus, K_D and K_F can be considered as material properties in the measured range. Subsequently, multi-dimensional through-flow behaviour was investigated. A new kind of validation experiment has been performed which employs partial sealing of the outlet surface to evoke coolant cross flow. A generally good agreement between all measurements and the corresponding simulations validates the OpenFOAM solver with respect to isothermal and heated through-flow processes. Moreover, the superposition principle of the multidimensional Darcy-Forchheimer equation could be confirmed for C/C in the parallel-parallel fibre plane.

Besides the internal process, the numerical modelling of boundary-layer injection into a main flow has been investigated. For this, numerical simulations of a subsonic turbulent channel flow with boundary-layer injection have been performed. The selected test case is based on an experiment from literature. By comparison of the results to the available experimental data and correlations, the solver was validated with respect to same and foreign gas transpiration into heated and non-heated main flows. The important effects of boundary-layer

blowing on the main flow such as the thickening of kinematic and thermal boundary layers and the reduction of gradients close to the wall are accurately represented in the simulations. Moreover, the influence of the fluid properties of the injected gas could be well reproduced. The conformance of results validates several aspects of the simulation setup. First, the continuous blowing model may be applied to represent a transpired wall with microscopic pore openings. Secondly, the supplemented models for fluid properties of gas mixtures and diffusion modelling performed well in the simulation of the test cases with foreign-gas injection. Thirdly, the consideration of an additional term in the solver's enthalpy equation that represents energy transport due to species diffusion is confirmed.

The main part of the thesis investigates transpiration-cooled C/C structures in supersonic hot-gas flows. For this purpose, experiments in the institute's supersonic wind tunnel have been conducted using three different porous samples, a shock generator, and various coolants. Several aspects regarding non-flat geometries, pressure variations on the transpired surfaces, and multidimensional coolant flow have been investigated for the first time for C/C.

The new test channel setup features supersonic flow conditions at M = 2.5 and shows smooth wall pressure and wall temperature distributions. Rather modest temperature levels of $T_{tot} = 500\,\mathrm{K}$ have been selected in the experiments to reduce parasitic influences and thus allow for precise measurements. Complementing numerical simulations accurately reproduced the experimental test case without blowing. The no-blowing test case subsequently served as a reference for the conducted transpiration-cooling investigations.

Concerning these, remaining unknown modelling parameters were determined based on sensitivity studies. This includes the internal heat transfer from porous solid to coolant fluid as well as the convective heat transfer at the coolant-reservoir side. Moreover, the choice of the turbulence boundary condition on the transpired surface has been found to have a significant influence on the wall temperature. The proposed modified condition for the turbulent dissipation rate which considers the wall's porosity yielded best agreement to the test data with boundary-layer blowing. Having the numerical setup selected, a combined numerical and experimental investigation on transpiration cooling in supersonic flow was performed for multiple test cases.

Starting with the flat reference sample, significant temperature reductions on the transpired surface, in the wake region, and within the porous wall were found. These depend on the applied blowing ratio as well as the coolant properties. Similar temperature levels as for air were observed for reduced (helium), comparable (CO_2), and increased (argon) coolant mass flow rates. The cooling

efficiency of all test gases coincides for blowing ratios scaled with the specific heat capacity. This indicates a strong internal heat transfer for C/C at the tested conditions. A considerable film-cooling effect was observed for all gases. Due to the differing cooling mechanism, the c_p-scaling yielded less agreement here. Surface temperature distributions obtained by means of IR thermography indicated slight non-homogeneities which are due to the fibre character of C/C and the sample's blowing behaviour. Additionally, slightly higher temperatures were found close to the sample's boarder. Therefore, numerical simulations with an enlarged numerical domain have been performed to determine the influence of non-desired heat fluxes from the uncooled surroundings to the sample. The analysis revealed that the effect is limited to regions close to the boarders and is only significant for the test cases with higher blowing ratios.

Further test cases with a contoured sample in two configurations demonstrated a significant effect of variations in the porous wall thickness. A reduced wall thickness results in locally higher coolant mass fluxes. The effect can be used to adapt the cooling efficiency to locally increased heat loads. As an example, higher temperatures close to the leading edge due to the not-yet-established cooling film could be compensated in the investigated test case. The effect is limited to the transpired surface, no influence of the coolant flow variation on the cooling of the wake region was detected.

The shock-generator test cases introduced variations to the main flow field due to the formation of shock waves and expansion fans. As desired, this caused a significant axial pressure variation over the porous sample. Additionally, the wall-temperature and heat-flux distributions were found to be non-uniform and shock-wave/boundary-layer interaction triggered flow separation. The combination of higher heat fluxes and reduced coolant flow rates led to locally reduced cooling efficiencies for the reference sample with uniform wall thickness. Replacing the reference sample with the contoured sample compensated the effect of the shock generator to some extent and yielded a more uniform temperature distribution.

Lastly, a porous double-wedge sample has been tested. Here, the non-flat sample itself triggers the formation of shock waves and expansion fans in a supersonic flow. The test case thus combines the influences of variable sample thickness and more complex main flow field. Again, a significant influence of the non-uniform distributions in wall pressure and heat flux on transpiration cooling was found. The front surface of the double wedge displayed elevated temperature due to the higher aerothermal load and the reduced coolant flow rate. Numerical simulations revealed that more coolant mass flow is directed to the aft region of the sample where the main-flow pressure is reduced. The

boundary-layer blowing showed to have a considerable influence on the main flow field for this test case which expressed by altered shock-wave positions. This underlines the importance of coupled simulation approaches as presented here.

Concerning the validation of the developed OpenFOAM solver and the applied numerical setup, the simulations of the different test cases captured all relevant effects well. Temperature distributions were found to be in generally good agreement with the experimental data. Deviations were limited to the regions close to the trailing edge, whereas the sample surface and downstream wake region as well as the internal temperature distributions were in good agreement to the thermocouple measurements. This also applied to the test cases with more complex main flow field due to the formation of shock waves. Discrepancies in the absolute surface temperatures are connected to the modelling of shock-wave/boundary-layer interaction and occurred for both blowing and no-blowing cases. However, when regarding the cooling efficiency a good agreement was observed for all test cases. Thus, the effect of transpiration cooling was well captured by the numerical simulations for all blowing ratios and coolant gases tested. The overall good agreement confirms the suitability of the continuous blowing model also for supersonic flow and Carbon/Carbon. Moreover, the employed transition-layer model as well as the proposed modification to the turbulence boundary condition for the transpired wall performed well for all supersonic test cases considered.

In summary, the main objectives of the thesis could be successfully completed. A numerical solver for the fully-coupled simulation of transpiration-cooling processes has been developed in OpenFOAM. Moreover, transpiration-cooling experiments using several porous samples have been performed in the institute's supersonic hot-gas wind tunnel. A combined numerical and experimental approach has then been followed to investigate various aspects of transpiration cooling for porous ceramic materials. In this regard, the focus was on exploring transpiration cooling for more complex geometries featuring multidimensional coolant flow and different coolant gases. Moreover, the test cases exhibited non-uniform main flow fields which included significant pressure variations over the transpired surface induced by high-speed flow phenomena such as shock waves and expansion fans. Comparisons between experimental data and numerical simulation results validated the developed solver for all considered aspects. At the same time, the combined study enhances the understanding of transpiration cooling.

Further work could be centred around the application and validation of the developed solver to test cases at more realistic conditions. This would include

considerable higher aerothermal loads such as occurring in combustion engines. A similar approach as in the current thesis work could be followed by combining experimental testing and corresponding OpenFOAM simulations. Regarding combustion engine applications, it would further be interesting to implement reactive flow modelling into the solver. This would enable the complete simulation of a transpiration-cooled rocket or scramjet engine. As these simulations would imply enormous computational costs, they could benefit from the possibility of massive parallelisation provided by OpenFOAM. Moreover, employing hydrogen as propellant and coolant would represent a step towards real application cases while being interesting from the perspective of transpiration-cooling physics. The coolant with low-density and high specific-heat capacity might shift the thermal situation within a porous wall further towards local thermal non-equilibrium. With respect to this, transient experiments and simulations would be of interest as well, since they might allow the determination of the volumetric heat transfer coefficient of the porous materials used. Finally, the developed OpenFOAM solver can readily be used to optimise the design of porous wall liners for specific application cases featuring transpiration cooling. In this context, also further advances in the manufacturing process of porous CMC materials which enable full control of the material's properties including gradual changes in permeability would be of great value.

Bibliography

[1] Ahn, H. S., Lee, S. W., and Lau, S. C.: Heat Transfer Enhancement for Turbulent Flow Through Blockages With Round and Elongated Holes in a Rectangular Channel. *Journal of Heat Transfer*, 2007, 129 (11), pp. 1611–1615. DOI: 10.1115/1.2764091.

[2] Alazmi, B. and Vafai, K.: Analysis of Variants within the Porous Media Transport Models. *Journal of Heat Transfer*, 1999, 122 (2), pp. 303–326. DOI: 10.1115/1.521468.

[3] Alazmi, B. and Vafai, K.: Constant Wall Heat Flux Boundary Conditions in Porous Media under Local Thermal Non-Equilibrium Conditions. *International Journal of Heat and Mass Transfer*, 2002, 45 (15), pp. 3071–3087. DOI: 10.1016/S0017-9310(02)00044-3.

[4] Amiri, A. and Vafai, K.: Analysis of Dispersion Effects and Non-Thermal Equilibrium, Non-Darcian, Variable Porosity Incompressible Flow through Porous Media. *International Journal of Heat and Mass Transfer*, 1994, 37 (6), pp. 939–954. DOI: 10.1016/0017-9310(94)90219-4.

[5] Amiri, A., Vafai, K., and Kuzay, T. M.: Effects of Boundary Conditions on Non-Darcian Heat Transfer through Porous Media and Experimental Comparisons. *Numerical Heat Transfer, Part A: Applications*, 1995, 27 (6), pp. 651–664. DOI: 10.1080/10407789508913724.

[6] Andersen, P. S., Kays, W. M., and Moffat, R. J.: The Turbulent Boundary Layer on a Porous Plate: An Experimental Study of the Fluid Mechanics for Adverse Free Stream Pressure. NASA Technical Report, NASA-CR-127817, HMT-15. Tech. rep. Dept. of Mechanical Engineering, Stanford Univ., 1972.

Bibliography

[7] Anderson, J. D.: Hypersonic and High Temperature Gas Dynamics. McGraw-Hill, 1989. ISBN: 9780070016729.

[8] Anderson, J. D.: Modern Compressible Flow: With Historical Perspective. McGraw-Hill, 07/01/2002. 784 pp. ISBN: 0072424435.

[9] Arnold, R., Suslov, D., and Haidn, O. J.: Circumferential Film Cooling Effectiveness in a LOX/H2 Subscale Combustion Chamber. *Journal of Propulsion and Power*, 2009, 25 (3), pp. 760–770. DOI: 10.2514/1.40305.

[10] Bachmat, Y. and Bear, J.: Macroscopic Modelling of Transport Phenomena in Porous Media. 1: The Continuum Approach. *Transport in Porous Media*, 1986, 1 (3), pp. 213–240.

[11] Bartle, E. R. and Leadon, B. M.: Experimental Evaluation of Heat Transfer with Transpiration Cooling in a Turbulent Boundary Layer at $M = 3.2$. *Journal of the Aerospace Sciences*, 1960, 27 (1), pp. 78–80. DOI: 10.2514/8.8397.

[12] Bear, J.: Dynamics of Fluids in Porous Media. Courier Corporation, 2013.

[13] Bellettre, J., Bataille, F., Rodet, J.-C., and Lallemand, A.: Thermal Behavior of Porous Plates Subjected to Air Blowing. *Journal of Thermophysics and Heat Transfer*, 2000, 14 (4), pp. 523–532. DOI: 10.2514/2.6575.

[14] Bernhard, F.: Handbuch der Technischen Temperaturmessung. Springer, 2014. DOI: 10.1007/978-3-642-24506-0.

[15] Betchen, L., Straatman, A., and Thompson, B.: A Nonequilibrium Finite-Volume Model for Conjugate Fluid/Porous/Solid Domains. *Numerical Heat Transfer: Part A: Applications*, 2006, 49 (6), pp. 543–565. DOI: 10.1080/10407780500430967.

[16] BIPM, IEC, IFCC, ILAC, ISO, IUPAC, IUPAP, and OIML: Evaluation of Measurement Data - Guide to the Expression of Uncertainty in Measurement. Geneva, ISO, 2008.

[17] BIPM, IEC, IFCC, ILAC, ISO, IUPAC, IUPAP, and OIML: Evaluation of Measurement Data - Supplement 1 to the "Guide to the Expression of Uncertainty in Measurement" - Propagation of Distributions using a Monte Carlo Method. Geneva, ISO, 2008.

[18]   Blackwell, B. F., Kays, W. M., and Moffat, R. J.: The Turbulent Boundary Layer on a Porous Plate: An Experimental Study of the Heat Transfer Behavior with adverse Pressure Gradients. Tech. rep., Report No. HMT-16. Thermosciences Division, Dept. of Mechanical Engineering, Stanford University, 1972.

[19]   Böhrk, H., Piol, O., and Kuhn, M.: Heat Balance of a Transpiration-Cooled Heat Shield. *Journal of Thermophysics and Heat Transfer*, 2010, 24 (3), pp. 581–588. DOI: `10.2514/1.47172`.

[20]   Böhrk, H.: Transpiration-Cooled Hypersonic Flight Experiment: Setup, Flight Measurement, and Reconstruction. *Journal of Spacecraft and Rockets*, 2015, 52 (3), pp. 674–683. DOI: `10.2514/1.A33144`.

[21]   Bouchez, M.: Scramjet Combustor Design in French PREPHA Program - Final Status in 1998. *8th AIAA International Space Planes and Hypersonic Systems and Technologies Conference*. Norfolk, VA, USA, 1998. DOI: `10.2514/6.1998-1534`.

[22]   Bouchez, M. and Beyer, S.: PTAH-SOCAR Fuel-Cooled Composite Materials Structure. *EUCASS Proceedings Series - Advances in AeroSpace Sciences*. Vol. 1. EDP Sciences, 2009, pp. 627–644. DOI: `10.1051/eucass/200901627`.

[23]   Boussinesq, J.: Essai sur la théorie des eaux courantes. Impr. nationale, 1877.

[24]   Brauckmann, D. and von Wolfersdorf, J.: Infrared Thermography With In-Situ Calibration Using Thermochromic Liquid Crystals Applied to Film Cooling. *Volume 3: Turbo Expo 2004*. ASME International, 2004. DOI: `10.1115/GT2004-53855`.

[25]   Brillant, G., Husson, S., Bataille, F., and Ducros, F.: Study of the Blowing Impact on a Hot Turbulent Boundary Layer using Thermal Large Eddy Simulation. *International Journal of Heat and Fluid Flow*, 2008, 29 (6), pp. 1670–1678. DOI: `10.1016/j.ijheatfluidflow.2008.06.011`.

[26]   Bunker, R. S.: A Review of Shaped Hole Turbine Film-Cooling Technology. *Journal of Heat Transfer*, 2005, 127 (4), pp. 441–453. DOI: `10.1115/1.1860562`.

[27]   Burcat, A. and Ruscic, B.: Third Millenium Ideal Gas and Condensed Phase Thermochemical Database for Combustion (with Update from Active Thermochemical Tables). Tech. rep. 2005. DOI: `10.2172/925269`.

[28] Burch, D. M., Allen, R. W., and Peavy, B. A.: Transient Temperature Distributions within Porous Slabs Subjected to Sudden Transpiration Heating. *Journal of Heat Transfer*, 1976, 98 (2). DOI: 10.1115/1.3450522.

[29] Cadafalch, J., Pe'rez-Segarra, C. D., Co'nsul, R., and Oliva, A.: Verification of Finite Volume Computations on Steady-State Fluid Flow and Heat Transfer. *Journal of Fluids Engineering*, 2002, 124 (1). DOI: 10.1115/1.1436092.

[30] Cebeci, T.: Analysis of Turbulent Flows. 2nd edition. Elsevier, 2004. ISBN: 978-0080443508.

[31] Celik, I. B., Ghia, U., Roache, P. J., Freitas, C. J., Coleman, H., and Raad, P. E.: Procedure for Estimation and Reporting of Uncertainty Due to Discretization in CFD Applications. *Journal of Fluids Engineering*, 2008, 130 (7). DOI: 10.1115/1.2960953.

[32] Cerminara, A., Deiterding, R., and Sandham, N.: Direct Numerical Simulation of Hypersonic Flow through Regular and Irregular Porous Surfaces. *7th European Conference on Computational Fluid Dynamics, United Kingdom.* 2018.

[33] Cheuret, F., Steelant, J., Langener, T., and von Wolfersdorf, J.: Transpiration Cooling Modelling for Ceramic Combustion Chambers. *ISABE Conference 2011.* 2011.

[34] Clauser, F. H.: Turbulent Boundary Layers in Adverse Pressure Gradients. *Journal of the Aeronautical Sciences*, 1954, 21 (2), pp. 91–108. DOI: 10.2514/8.2938.

[35] Colladay, R. S. and Stepka, F. S.: Examination of Boundary Conditions for Heat Transfer through a Porous Wall. Tech. rep., NASA TND-6405. 1971.

[36] Curran, E. T.: Scramjet Engines: The First Forty Years. *J. Propul. Power*, 2001, 14 (6), pp. 1138–1148. DOI: 10.2514/2.5875.

[37] Dahmen, W., Müller, S., Rom, M., Schweikert, S., Selzer, M., and von Wolfersdorf, J.: Numerical Boundary Layer Investigations of Transpiration-Cooled Turbulent Channel Flow. *International Journal of Heat and Mass Transfer*, 2015, 86, pp. 90–100. DOI: 10.1016/j.ijheatmasstransfer.2015.02.075.

[38] Darcy, H. P. G.: Les fontaines publiques de la ville de Dijon. Dalamont, 1856.

[39] Dean, D. E. and Stiel, L. I.: The Viscosity of Nonpolar Gas Mixtures at Moderate and High Pressures. *AIChE J.*, 1965, 11 (3), pp. 526–532.

[40] DeBonis, J. R., Oberkampf, W. L., Wolf, R. T., Orkwis, P. D., Turner, M. G., Babinsky, H., and Benek, J. A.: Assessment of Computational Fluid Dynamics and Experimental Data for Shock Boundary-Layer Interactions. *AIAA Journal*, 2012, 50 (4), pp. 891–903. DOI: `10.2514/1.J051341`.

[41] DIN EN 1779: *Non-Destructive Testing - Leak Testing - Criteria for the Method and Technique Selection*.

[42] DIN EN 993-1: *Methods of Test for Dense Shaped Refractory Products - Determination of Bulk Density, Apparent Porosity and True Porosity*.

[43] Dittert, C., Selzer, M., and Böhrk, H.: Flowfield and Pressure Decay Analysis of Porous Cones. *AIAA Journal*, 2017, 55 (3), pp. 874–882. DOI: `10.2514/1.j055298`.

[44] Dolling, D. S.: Fifty Years of Shock-Wave/Boundary-Layer Interaction Research: What Next? *AIAA Journal*, 2001, 39 (8), pp. 1517–1531. DOI: `10.2514/2.1476`.

[45] Dröske, N. C.: Investigation of Thermal Loads onto a Cooled Strut Injector inside a Scramjet Combustion Chamber. PhD Thesis. University of Stuttgart, Germany, 2016. ISBN: 978-3843928328.

[46] Dunbar, D. I. A. and Squire, L. C.: Correlations of Concentration, Temperature and Velocity Profiles in Compressible Turbulent Boundary Layers with Foreign Gas Injection. *International Journal of Heat and Mass Transfer*, 1971, 14 (1), pp. 27–40. DOI: `10.1016/0017-9310(71)90137-2`.

[47] Dupuit, J. E. J.: Études théoriques et pratiques sur le mouvement des eaux dans les canaux découverts et à travers les terrains perméables. Dunod, 1863.

[48] Eckert, E. R. G.: Introduction to the Transfer of Heat and Mass. McGraw-Hill, 1950.

[49] Eckert, E. R. G. and Livingood, N. B.: Comparison of Effectiveness of Convection-, Transpiration-, and Film-Cooling Methods with Air as Coolant. Tech. rep., NACA Technical Note 3010. 1953.

[50] Ergun, S.: Fluid Flow Through Packed Columns. *Chemical Engineering Progress*, 1952, 48, pp. 89–94.

[51] Ferziger, J. H. and Perić, M.: Computational Methods for Fluid Dynamics. Springer, 2002. DOI: `10.1007/978-3-642-56026-2`.

[52] Fick, A.: Über Diffusion. *Ann. Phys.*, 1855, 170 (1), pp. 59–86. DOI: `10.1002/andp.18551700105`.

[53] Florio, J., Henderson, J. B., Test, F. L., and Hariharan, R.: A Study of the Effects of the Assumption of Local-Thermal Equilibrium on the Overall Thermally-Induced Response of a Decomposing, Glass-Filled Polymer Composite. *International Journal of Heat and Mass Transfer*, 1991, 34 (1), pp. 135–147. DOI: `10.1016/0017-9310(91)90181-D`.

[54] Florio, J., Henderson, J. B., Test, F. L., and Hariharan, R.: Characterization of Forced Convection Heat Transfer in Decomposing, Glass-Filled Polymer Composites. *Journal of Composite Materials*, 1991, 25 (11), pp. 1515–1539. DOI: `10.1177/002199839102501108`.

[55] Forchheimer, P.: Wasserbewegung durch Boden. *Zeitschrift des Vereines Deutscher Ingenieure*, 1901, 45.

[56] Frieß, M., Krenkel, W., Kochendörfer, R., Brandt, R., Neuer, G., and Maier, H.-P.: High Temperature Materials and Hot Structures. In: Jacob, D., Sachs, G., and Wagner, S. *Basic Research and Technologies for Two-Stage-to-Orbit Vehicles*. Wiles-VCH, 2005.

[57] Fu, X., Viskanta, R., and Gore, J. P.: Measurement and Correlation of Volumetric Heat Transfer Coefficients of Cellular Ceramics. *Experimental Thermal and Fluid Science*, 1998, 17 (4), pp. 285–293. DOI: `10.1016/S0894-1777(98)10002-X`.

[58] Fuller, E. N. and Giddings, J. C.: A Comparison of Methods for Predicting Gaseous Diffusion Coefficients. *Journal of Chromatographic Science*, 1965, 3 (7), pp. 222–227. DOI: `10.1093/chromsci/3.7.222`.

[59] Fuller, E. N., Schettler, P. D., and Giddings, J. C.: New Method for Prediction of Binary Gas-Phase Diffusion Coefficients. *Industrial & Engineering Chemistry*, 1966, 58 (5), pp. 18–27. DOI: `10.1021/ie50677a007`.

[60] Fuller, E. N., Ensley, K., and Giddings, J. C.: Diffusion of Halogenated Hydrocarbons in Helium. The Effect of Structure on Collision Cross Sections. *The Journal of Physical Chemistry*, 1969, 73 (11), pp. 3679–3685. DOI: `10.1021/j100845a020`.

[61] Gaitonde, D. V.: Progress in Shock Wave/Boundary Layer Interactions. *Progress in Aerospace Sciences*, 2015, 72, pp. 80–99. DOI: `10.1016/j.paerosci.2014.09.002`.

[62] Gerlinger, P.: Numerische Verbrennungssimulation. Springer, 2005. ISBN: 3540233377.

[63] Ghadiani, S. R.: A Multiphasic Continuum Mechanical Model for Design Investigations of an Effusion-Cooled Rocket Thrust Chamber. PhD Thesis. University of Stuttgart, Germany, 2005. ISBN: 978-3843900232.

[64] Glass, D. E., Dilley, A. D., and Kelly, H. N.: Numerical Analysis of Convection / Transpiration Cooling. *Journal of Spacecraft and Rockets*, 2001, 38 (1), pp. 15–20. DOI: `10.2514/2.3666`.

[65] Goldstein, R. J., Eckert, E. R. G., and Wilson, D. J.: Film Cooling With Normal Injection Into a Supersonic Flow. *Journal of Manufacturing Science and Engineering*, 1968, 90 (4), pp. 584–588. ISSN: 1087-1357. DOI: `10.1115/1.3604692`.

[66] Goldstein, R. J.: Film Cooling, 1971, pp. 321–379. DOI: `10.1016/S0065-2717(08)70020-0`.

[67] Greuel, D., Herbertz, A., Haidn, O. J., Ortelt, M., and Hald, H.: Transpiration Cooling Applied to C/C Liners of Cryogenic Liquid Rocket Engines. *40th AIAA/ASME/SAE/ASEE Joint Propulsion Conference and Exhibit*. American Institute of Aeronautics and Astronautics (AIAA), 2004. DOI: `10.2514/6.2004-3682`.

[68] Greuel, D.: Untersuchungen zum Impuls- und Stofftransport in effusiv gekühlten faserkeramischen Raketenbrennkammerwänden. PhD Thesis. RWTH Aachen University, Germany, 2013.

[69] Gutiérrez Marcantonia, L. F., Tamagnoa, J. P., and Elaskara, S. A.: High Speed Flow Simulation using OpenFOAM. *Asoc. Argent. Mec. Comput. 31.* 2012.

[70] Hahn, D. W. and Özisik, M. N.: Heat Conduction. 3rd edition. John Wiley & Sons, 2012. 752 pp. ISBN: 978-0-470-90293-6.

[71] Hald, H., Ortelt, M., Fischer, I., Greuel, D., and Haidn, O. J.: Effusion Cooled CMC Rocket Combustion Chamber. *AIAA/CIRA 13th International Space Planes and Hypersonics Systems and Technologies Conference*. American Institute of Aeronautics and Astronautics (AIAA), 2005. DOI: `10.2514/6.2005-3229`.

[72] Han, J. C., Park, J. S., and Lei, C. K.: Heat Transfer and Pressure Drop in Blade Cooling Channels with Turbulence Promoters. Tech. rep., NASA Contractor Report 3837. 1984.

[73] Han, J.-C.: Recent Studies in Turbine Blade Cooling. *The International Journal of Rotating Machinery*, 2004, 10 (6), pp. 443–457. DOI: `10.1080/10236210490503978`.

[74] Harten, A.: High Resolution Schemes for Hyperbolic Conservation Laws. *Journal of Computational Physics*, 1983, 49 (3), pp. 357–393. DOI: `10.1016/0021-9991(83)90136-5`.

[75] Harten, A., Lax, P. D., and Van Leer, B.: On Upstream Differencing and Godunov-Type Schemes for Hyperbolic Conservation Laws. *SIAM Review*, 1983, 25 (1), pp. 35–61.

[76] Heidenreich, B.: Manufacture and Applications of C/C-SiC and C/SiC Composites, 2012, pp. 183–198. DOI: `10.1002/9781118491867.ch20`.

[77] Herbertz, A. and Selzer, M.: Analysis of Coolant Mass Flow Requirements for Transpiration Cooled Ceramic Thrust Chambers. *Transactions of the Japan Society for Aeronautical and Space Sciences, Aerospace Technology*, 2014, 12, pp. 31–39. DOI: `10.2322/tastj.12.Pa_31`.

[78] Hermann, T. A., McGilvray, M., Ifti, H. S., Hufgard, F., and Löhle, S.: Fluid-Solid Heat Exchange in Porous Media for Transpiration Cooling Systems. *AIAA Scitech 2019 Forum*. American Institute of Aeronautics and Astronautics (AIAA), 2019. DOI: `10.2514/6.2019-0537`.

[79] Holden, M. and Sweet, S.: Studies of Transpiration Cooling with Shock Interaction in Hypersonic Flow. *25th Plasmadynamics and Lasers Conference*. American Institute of Aeronautics and Astronautics (AIAA), 1994. DOI: `10.2514/6.1994-2475`.

[80] Horstman, C. C. and Owen, F. K.: Turbulent Properties of a Compressible Boundary Layer. *AIAA Journal*, 1972, 10 (11), pp. 1418–1424. DOI: `10.2514/3.6640`.

[81] Howard, J. W. and Abel, I. R.: Narcissus: Reflections on Retroreflections in Thermal Imaging Systems. *Applied Optics*, 1982, 21 (18). DOI: `10.1364/AO.21.003393`.

[82] Huang, Z., Zhu, Y. H., Jiang, P. X., and Xiong, Y. B.: Investigation of Transpiration Cooling with Local Thermal Non-Equilibrium Model: Effects of Different Thermal Boundary Conditions at the Porous-Fluid Interface. *5th International Conference on Porous Media and its Applications in Science and Engineering*. 2014.

[83] Huang, Z., Zhu, Y. H., Jiang, P. X., and Xiong, Y. B.: Investigation of a Porous Transpiration-Cooled Strut Injector. *Journal of Propulsion and Power*, 2015, 31 (1), pp. 278–285. DOI: `10.2514/1.B35371`.

[84]   Huang, G., Zhu, Y., Liao, Z., Ouyang, X., and Jiang, P.: Experimental Investigation of Transpiration Cooling with Phase Change for Sintered Porous Plates. *International Journal of Heat and Mass Transfer*, 2017, 114, pp. 1201–1213. DOI: `10.1016/j.ijheatmasstransfer.2017.05.114`.

[85]   Huang, G., Liao, Z., Xu, R., Zhu, Y., and Jiang, P.: Self-Pumping Transpiration Cooling with a Protective Porous Armor. *Applied Thermal Engineering*, 2020, 164. DOI: `10.1016/j.applthermaleng.2019.114485`.

[86]   Ishii, I. and Kubota, H.: Two-dimensional Material Response of a Transpiration-Cooled System in a Radiative/Convective Environment. *AIAA Journal*, 1984, 22 (6), pp. 831–836. DOI: `10.2514/3.8688`.

[87]   Issa, R. I.: Solution of the Implicitly Discretised Fluid Flow Equations by Operator-Splitting. *Journal of Computational Physics*, 1986, 62 (1), pp. 40–65. DOI: `10.1016/0021-9991(86)90099-9`.

[88]   Jasak, H., Jemcov, A., and Tukovic, Z.: OpenFOAM: A C++ Library for Complex Physics Simulations. *International Workshop on Coupled Methods in Numerical Dynamics*. Dubrovnik, Croatia, 2007.

[89]   Jiang, P.-X. and Ren, Z.-P.: Numerical Investigation of Forced Convection Heat Transfer in Porous Media using a Thermal Non-Equilibrium Model. *International Journal of Heat and Fluid Flow*, 2001, 22 (1), pp. 102–110. DOI: `10.1016/S0142-727X(00)00066-7`.

[90]   Jiang, P., Huang, G., Zhu, Y., Liao, Z., and Huang, Z.: Experimental Investigation of Combined Transpiration and Film Cooling for Sintered Metal Porous Struts. *International Journal of Heat and Mass Transfer*, 2017, 108, pp. 232–243. DOI: `10.1016/j.ijheatmasstransfer.2016.12.014`.

[91]   Jiang, P., Huang, G., Zhu, Y., Xu, R., Liao, Z., and Lu, T.: Experimental Investigation of Biomimetic Self-Pumping and Self-Adaptive Transpiration Cooling. *Bioinspiration & Biomimetics*, 2017, 12 (5). DOI: `10.1088/1748-3190/aa753b`.

[92]   Jiang, P., Liao, Z., Huang, Z., Xiong, Y., and Zhu, Y.: Influence of Shock Waves on Supersonic Transpiration Cooling. *International Journal of Heat and Mass Transfer*, 2019, 129, pp. 965–974. DOI: `10.1016/j.ijheatmasstransfer.2018.10.043`.

[93]   Jones, W. P. and Launder, B. E.: The Prediction of Laminarization with a Two-Equation Model of Turbulence. *International Journal of Heat and Mass Transfer*, 1972, 15 (2), pp. 301–314.

[94]   Kaviany, M.: Principles of Heat Transfer in Porous Media. Springer, 2012. ISBN: 978-1-4684-0412-8.

[95]   Kays, W. M.: Turbulent Prandtl Number—Where Are We? *Journal of Heat Transfer*, 1994, 116 (2), pp. 284–295. DOI: `10.1115/1.2911398`.

[96]   Kays, W. M., Crawford, M. E., and Weigand, B.: Convective Heat and Mass Transfer. 4th edition. McGraw-Hill, 2004. ISBN: 978-0071238298.

[97]   Keener, D., Lenertz, J., Bowersox, R., and Bowman, J.: Transpiration Cooling Effects on Nozzle Heat Transfer and Performance. *Journal of Spacecraft and Rockets*, 1995, 32 (6), pp. 981–985. DOI: `10.2514/3.26718`.

[98]   Keller, M. A. and Kloker, M. J.: Effusion Cooling and Flow Tripping in Laminar Supersonic Boundary-Layer Flow. *AIAA Journal*, 2015, 53 (4), pp. 902–919. DOI: `10.2514/1.J053251`.

[99]   Költzsch, K.: Parameter des turbulenten Strömungsfeldes und der Stoffausbreitung in rauhen turbulenten Plattengrenzschichten mit Bezug auf die atmosphärische Grenzschicht. PhD thesis. TU Dresden, Germany, 1999.

[100] Korkegi, R. H.: Comparison of Shock-Induced Two-and Three-Dimensional Incipient Turbulent Seperation. *AIAA Journal*, 1975, 13 (4), pp. 534–535.

[101] Kraposhin, M., Bovtrikova, A., and Strijhak, S.: Adaptation of Kurganov-Tadmor Numerical Scheme for Applying in Combination with the PISO Method in Numerical Simulation of Flows in a Wide Range of Mach Numbers. *Procedia Computer Science*, 2015, 66, pp. 43–52. DOI: `10.1016/j.procs.2015.11.007`.

[102] Kraposhin, M. V., Banholzer, M., Pfitzner, M., and Marchevsky, I. K.: A Hybrid Pressure-Based Solver for Nonideal Single-Phase Fluid Flows at all Speeds. *International Journal for Numerical Methods in Fluids*, 2018, 88 (2), pp. 79–99. DOI: `10.1002/fld.4512`.

[103] Kubota, H.: A Simplified Analytical Solution for Thermal Response of a one-dimensional, steady state Transpiration Cooling System in Radiative and Convective Environment. NASA Technical Note D-8129. Tech. rep. Ames Research Center, Moffett Field, CA, 1976.

[104] Kuhn, M. and Hald, H.: Application of Transpiration Cooling for Hot Structures. RESPACE – Key Technologies for Reusable Space Systems. In: Gülhan, A. *Notes on Numerical Fluid Mechanics and Multidisciplinary Design*. Springer, 2008, pp. 82–103. DOI: `10.1007/978-3-540-77819-6_6`.

[105] Kurganov, A. and Tadmor, E.: New High-Resolution Central Schemes for Nonlinear Conservation Laws and Convection–Diffusion Equations. *Journal of Computational Physics*, 2000, 160 (1), pp. 241–282. DOI: `10.1006/jcph.2000.6459`.

[106] Kurganov, A., Noelle, S., and Petrova, G.: Semidiscrete Central-Upwind Schemes for Hyperbolic Conservation Laws and Hamilton–Jacobi Equations. *SIAM Journal on Scientific Computing*, 2001, 23 (3), pp. 707–740. DOI: `10.1137/S1064827500373413`.

[107] Kutateladze, S. S. and Leont'ev, A. I.: Heat-Mass Transfer and Friction in a Turbulent Boundary Layer. *Energiya Press*, 1972.

[108] Laganelli, A.: A Comparison between Film Cooling and Transpiration Cooling Systems in High Speed Flow. *8th Aerospace Sciences Meeting*. American Institute of Aeronautics and Astronautics (AIAA), 1970. DOI: `10.2514/6.1970-153`.

[109] Lage, J.: The Fundamental Theory of Flow through Permeable Media from Darcy to Turbulence. In: Ingham, D. B. and Pop, I. *Transport Phenomena in Porous Media*. Vol. 1. 1998.

[110] Landis, R. B. and Mills, A. F.: The Calculation of Turbulent Boundary Layers with Foreign Gas Injection. *International Journal of Heat and Mass Transfer*, 1972, 15 (10), pp. 1905–1932. DOI: `10.1016/0017-9310(72)90061-0`.

[111] Langener, T.: A Contribution to Transpiration Cooling for Aerospace Applications using CMC Walls. PhD Thesis. University of Stuttgart, Germany, 2011. ISBN: 978-3843900232.

[112] Langener, T., von Wolfersdorf, J., and Steelant, J.: Experimental Investigations on Transpiration Cooling for Scramjet Applications Using Different Coolants. *AIAA Journal*, 2011, 49 (7), pp. 1409–1419. DOI: `10.2514/1.j050698`.

[113] Lau, A. S.: The Narcissus Effect In Infrared Optical Scanning Systems, 1977. Ed. by John, D. L. and Morrow, H. E. DOI: `10.1117/12.964596`.

[114] Leadon, B. M. and Scott, C. J.: Measurement of Recovery Factors and Heat Transfer Coefficients with Transpiration Cooling in a Turbulent Boundary Layer at $M = 3$ using Air and Helium as Coolants. Research rep., No. RR-126. Minnesota University Rosemount Aeronautical Labs, 1956.

[115] L'Ecuyer, M. R. and Colladay, R. S.: Influence of Porous-Wall Thermal Effectiveness on Turbulent-Boundary-Layer Heat Transfer. Tech. rep., NASA-TN-D-6837, E-6711. 1972.

Bibliography

[116] Lee, D.-Y. and Vafai, K.: Analytical Characterization and Conceptual Assessment of Solid and Fluid Temperature Differentials in Porous Media. *International Journal of Heat and Mass Transfer*, 1999, 42 (3), pp. 423–435. DOI: `10.1016/S0017-9310(98)00185-9`.

[117] Lei, G., Dong, P. C., Mo, S. Y., Yang, S., Wu, Z. S., and Gai, S. H.: Calculation of Full Permeability Tensor for Fractured Anisotropic Media. *Journal of Petroleum Exploration and Production Technology*, 2015, 5 (2), pp. 167–176. DOI: `10.1007/s13202-014-0138-6`.

[118] Lemmon, E. W., Huber, M. L., and McLinden, M. O.: NIST Standard Reference Database 23: Reference Fluid Thermodynamic and Transport Properties-REFPROP, Version 9.1. Natl Std. Ref. Data Series (NIST NSRDS), 2013.

[119] Leontiev, A. I.: Heat and Mass Transfer Problems for Film Cooling. *Journal of Heat Transfer*, 1999, 121 (3), pp. 509–527. DOI: `10.1115/1.2826012`.

[120] Leontiev, A. I. and Polyakov, A. F.: Simulation of Internal Heat Transfer in a Porous Permeable Envelope at low Values of Reynolds Number. *High Temperature*, 2008, 46 (6), pp. 811–826. DOI: `10.1134/s0018151x08060114`.

[121] Ligrani, P. M., Oliveira, M. M., and Blaskovich, T.: Comparison of Heat Transfer Augmentation Techniques. *AIAA Journal*, 2003, 41 (3), pp. 337–362. DOI: `10.2514/2.1964`.

[122] Liu, Y.-Q., Jiang, P.-X., Jin, S.-S., and Sun, J.-G.: Transpiration Cooling of a Nose Cone by Various Foreign Gases. *International Journal of Heat and Mass Transfer*, 2010, 53 (23-24), pp. 5364–5372. DOI: `doi:10.1016/j.ijheatmasstransfer.2010.07.019`.

[123] Liu, Y.-Q., Xiong, Y.-B., Jiang, P.-X., Wang, Y.-P., and Sun, J.-G.: Effects of Local Geometry and Boundary Condition Variations on Transpiration Cooling. *International Journal of Heat and Mass Transfer*, 2013, 62, pp. 362–372. DOI: `10.1016/j.ijheatmasstransfer.2013.02.075`.

[124] Liu, Y., Sun, X., Sethi, V., Nalianda, D., Li, Y.-G., and Wang, L.: Review of Modern Low Emissions Combustion Technologies for Aero Gas Turbine Engines. *Progress in Aerospace Sciences*, 2017, 94, pp. 12–45. DOI: `10.1016/j.paerosci.2017.08.001`.

[125] Maiorov, V. A.: Boundary Conditions for a Forced Transpiration Cooling System. *Journal of Engineering Physics*, 1984, 47 (4), pp. 1170–1176. DOI: `10.1007/bf00869912`.

[126] Martiny, M., Schiele, R., Gritsch, M., Schulz, A., and Wittig, S.: In-Situ Calibration for Quantitative Infrared Thermography. *Proceedings of the 1996 International Conference on Quantitative InfraRed Thermography*. QIRT Council, 1996. DOI: `10.21611/qirt.1996.001`.

[127] Mason, E. A. and Saxena, S. C.: Approximate Formula for the Thermal Conductivity of Gas Mixtures. *Physics of Fluids*, 1958, 1 (5). DOI: `10.1063/1.1724352`.

[128] Matsuo, K., Miyazato, Y., and Kim, H.-D.: Shock Train and Pseudo-shock Phenomena in Internal Gas Flows. *Progress in Aerospace Sciences*, 1999, 35 (1), pp. 33–100. DOI: `10.1016/S0376-0421(98)00011-6`.

[129] Meinert, J.: Haftreibung und Wärmeübergang in einer turbulenten Grenzschicht bei Fremdgastranspiration. PhD thesis. TU Dresden, Germany, 2000. ISBN: 978-3183402076.

[130] Meinert, J., Huhn, J., Serbest, E., and Haidn, O. J.: Turbulent Boundary Layers with Foreign Gas Transpiration. *Journal of Spacecraft and Rockets*, 2001, 38 (2), pp. 191–198. DOI: `10.2514/2.3693`.

[131] Menter, F. R.: Improved Two-Equation κ-ω Turbulence Models for Aerodynamic Flows. Tech. rep., NASA Technical Memorandum 103975. 1992.

[132] Menter, F. R.: Influence of Freestream Values on κ-ω Turbulence Model Predictions. *AIAA Journal*, 1992, 30 (6), pp. 1657–1659. DOI: `10.2514/3.11115`.

[133] Menter, F. R.: Two-Equation Eddy-Viscosity Turbulence Models for Engineering Applications. *AIAA Journal*, 1994, 32 (8), pp. 1598–1605. DOI: `10.2514/3.12149`.

[134] Menter, F. and Esch, T.: Elements of Industrial Heat Transfer Predictions. *16th Brazilian Congress of Mechanical Engineering (COBEM), Uberlandia, Brazil*. 2001.

[135] Menter, F. R., Kuntz, M., and Langtry, R. B.: Ten Years of Industrial Experience with the SST Turbulence Model. *Turbulence, Heat and Mass Transfer IV*. Begell House, 2003, pp. 625–632.

[136] Meola, C. and Carlomagno, G. M.: Recent Advances in the Use of Infrared Thermography. *Measurement Science and Technology*, 2004, 15 (9), pp. 27–58. DOI: `10.1088/0957-0233/15/9/R01`.

[137] Mickley, H. S., Ross, R. C., Squyers, A. L., and Stewart, W. E.: Heat, Mass, and Momentum Transfer for Flow over a Flat Plate with Blowing or Suction. Tech. rep., NACA TN 3208. 1954.

Bibliography

[138] Mickley, H. S. and Davis, R. S.: Momentum Transfer for Flow over a Flat Plate with Blowing. Tech. rep., Technical Report TN 4017. NACA, Massachusetts Institute of Technology, Cambridge, MA., 1957.

[139] Moffat, R. J. and Kays, W. M.: The Turbulent Boundary Layer on a Porous Plate: Experimental Heat Transfer with Uniform Blowing and Suction. *Int. J. Heat Mass Transf.*, 1968, 11 (10), pp. 1547–1566.

[140] Moffat, R. J.: Describing the uncertainties in experimental results. *Experimental Thermal and Fluid Science*, 1988, 1 (1), pp. 3–17. DOI: `10.1016/0894-1777(88)90043-x`.

[141] Nield, D. A. and Bejan, A.: Convection in Porous Media. Springer, 2017. ISBN: 978-3-319-49562-0.

[142] Ortelt, M., Hald, H., Fischer, I., Greuel, D., Haidn, O., and Suslov, D.: Empirical Verification of Effusion Cooled CMC Rocket Thrust Chambers. *41st AIAA/ASME/SAE/ASEE Joint Propulsion Conference & Exhibit.* American Institute of Aeronautics and Astronautics (AIAA), 2005. DOI: `10.2514/6.2005-3569`.

[143] Ortelt, M., Hald, H., and Herbertz, A.: Investigations on Fibre Reinforced Combustion Chamber Structures under Effusion Cooled LOX/LH2 Operation. *45th AIAA/ASME/SAE/ASEE Joint Propulsion Conference & Exhibit.* American Institute of Aeronautics and Astronautics (AIAA), 2009. DOI: `10.2514/6.2009-5475`.

[144] Osher, S. and Sanders, R.: Numerical Approximations to Nonlinear Conservation Laws with Locally Varying Time and Space Grids. *Math. Comput.*, 1983, 41 (164), pp. 321–336. DOI: `10.1090/S0025-5718-1983-0717689-8`.

[145] Pappas, C. C. and Okuno, A. F.: The Relation between Skin Friction and Heat Transfer for the Compressible Turbulent Boundary layer with Gas Injection. Tech. rep., NASA TN D-2857. 1965.

[146] Parnas, R. S. and Salem, A. J.: A Comparison of the Unidirectional and Radial In-Plane Flow of Fluids through Woven Composite Reinforcements. *Polymer Composites*, 1993, 14 (5), pp. 383–394. DOI: `10.1002/pc.750140504`.

[147] Patankar, S. V. and Spalding, D. B.: A Calculation Procedure for Heat, Mass and Momentum Transfer in Three-Dimensional Parabolic Flows. *International Journal of Heat and Mass Transfer*, 1972, 15 (10), pp. 1787–1806. DOI: `10.1016/0017-9310(72)90054-3`.

[148] Polezhaev, Y. V. and Seliverstov, E. M.: A Universal Model of Heat Transfer in Systems with Penetration Cooling. *High Temperature*, 2002, 40 (6), pp. 856–864. ISSN: 1608-3156. DOI: `10.1023/A:1021477217065`.

[149] Poling, B. E., Prausnitz, J. M., and O'Connell, J. P.: The Properties of Gases and Liquids. 5th edition. McGraw-Hill, 2001. ISBN: 0070116822. DOI: `10.1016/b978-0-12-386910-4.00002-0`.

[150] Prokein, D., Böhrk, H., and von Wolfersdorf, J.: Analysis of Anisotropy Effects for Transpiration Cooled CMC Leading Edges using OpenFOAM. *20th AIAA International Space Planes and Hypersonic Systems and Technologies Conference*. American Institute of Aeronautics and Astronautics (AIAA), 2015. DOI: `10.2514/6.2015-3552`.

[151] Prokein, D., Dittert, C., Böhrk, H., and von Wolfersdorf, J.: Numerical Simulation of Transpiration Cooling Experiments in Supersonic Flow using OpenFOAM. *CEAS Space Journal*, 2019. ISSN: 1868-2510. DOI: `10.1007/s12567-019-00292-6`.

[152] Prokein, D. and von Wolfersdorf, J.: Numerical Simulation of Turbulent Boundary Layers with Foreign Gas Transpiration using OpenFOAM. *Acta Astronautica*, 2019, 158, pp. 253–263. DOI: `10.1016/j.actaastro.2019.03.030`.

[153] Quentmeyer, R. J.: Rocket Combustion Chamber Life-Enhancing Design Concepts. Tech. rep., NASA Contractor Report 185257. 1990.

[154] Rannie, W. D., Dunn, L. G., and Millikan, C. B.: A Simplified Theory of Porous Wall Cooling. Tech. rep., Jet Propulsion Laboratory, National Aeronautics and Space Administration. 1947.

[155] Reddy, V. S.: The SpaceX Effect. *New Space*, 2018, 6 (2), pp. 125–134.

[156] Renard, P., Genty, A., and Stauffer, F.: Laboratory Determination of the Full Permeability Tensor. *Journal of Geophysical Research: Solid Earth*, 2001, 106 (B11), pp. 26443–26452.

[157] Richardson, L. F.: The Approximate Arithmetical Solution by Finite Differences of Physical Problems Involving Differential Equations, with an Application to the Stresses in a Masonry Dam. *Philosophical Transactions of the Royal Society A: Mathematical, Physical and Engineering Sciences*, 1911, 210 (459-470), pp. 307–357. DOI: `10.1098/rsta.1911.0009`.

[158] Roache, P. J.: Perspective: A Method for Uniform Reporting of Grid Refinement Studies. *Journal of Fluids Engineering*, 1994, 116 (3), pp. 405–413.

Bibliography

[159] Roe, P. L.: Approximate Riemann Solvers, Parameter Vectors, and Difference Cchemes. *Journal of Computational Physics*, 1981, 43 (2), pp. 357–372. DOI: 10.1016/0021-9991(81)90128-5.

[160] Romanenko, P. N. and Kharchenko, V. N.: The Effect of Transverse Mass Flow on Heat Transfer and Friction Drag in a Turbulent Flow of Compressible Gas along an Arbitrarily Shaped Surface. *International Journal of Heat and Mass Transfer*, 1963, 6 (8), pp. 727–738. DOI: 10.1016/0017-9310(63)90043-7.

[161] Roy, C. J. and Blottner, F. G.: Review and Assessment of Turbulence Models for Hypersonic Flows. *Progress in Aerospace Sciences*, 2006, 42 (7-8), pp. 469–530. DOI: 10.1016/j.paerosci.2006.12.002.

[162] Rubesin, M. W.: An Analytical Estimation of the Effect of Transpiration Cooling on the Heat-Transfer and Skin-Friction Characteristics of a Compressible, Turbulent Boundary Layer. Tech. rep., NACA Technical Note 3341. 1954.

[163] Rubesin, M. W., Pappas, C. C., and Okuno, A. F.: The Effect of Fluid Injection on the Compressible Turbulent Boundary Layer - Preliminary Tests on Transpiration Cooling of a Flat Plate at $M = 2.7$ with Air as the Injected Gas. Tech. rep., NACA RM A55I19. 1955.

[164] Schlichting, H. and Gersten, K.: Boundary-Layer Theory. Springer, 2017. DOI: 10.1007/978-3-662-52919-5.

[165] Schweikert, S.: Ein Beitrag zur Beschreibung der Transpirationskühlung an keramischen Verbundwerkstoffen. PhD Thesis. University of Stuttgart, Germany, 2019. ISBN: 978-3843942638.

[166] Segal, C.: The Scramjet Engine. Processes and Characteristics. Cambridge University Press, 2009. ISBN: 978-0521838153.

[167] Selzer, M., Schweikert, S., Hald, H., and von Wolfersdorf, J.: Through-Flow Characteristics of C/C. Annual Report, SFB / Transregio 40. 2014.

[168] Serbest, E., Haidn, O., Hald, H., Korger, G., and Winkelmann, P.: Effusion Cooling in Rocket Combustors applying Fibre Reinforced Ceramics. *35th Joint Propulsion Conference and Exhibit*. American Institute of Aeronautics and Astronautics (AIAA), 1999. DOI: 10.2514/6.1999-2911.

[169] Shadloo, M. S., Hadjadj, A., and Hussain, F.: Statistical Behavior of Supersonic Turbulent Boundary Layers with Heat Transfer at $M_\infty = 2$. *International Journal of Heat and Fluid Flow*, 2015, 53, pp. 113–134. DOI: 10.1016/j.ijheatfluidflow.2015.02.004.

[170] Shen, L., Wang, J., Dong, W., Pu, J., Peng, J., Qu, D., and Chen, L.: An Experimental Investigation on Transpiration Cooling with Phase Change under Supersonic Condition. *Applied Thermal Engineering*, 2016, 105, pp. 549–556. DOI: 10.1016/j.applthermaleng.2016.03.039.

[171] Simpson, R. L., Moffat, R. J., and Kays, W. M.: The Turbulent Boundary Layer on a Porous Plate: Experimental Skin Friction with Variable Injection and Suction. *International Journal of Heat and Mass Transfer*, 1969, 12 (7), pp. 771–789.

[172] Simpson, R. L., Whitten, D. G., and Moffat, R. J.: An Experimental Study of the Turbulent Prandtl Number of Air with Injection and Suction. *International Journal of Heat and Mass Transfer*, 1970, 13 (1), pp. 125–143. ISSN: 0017-9310. DOI: 10.1016/0017-9310(70)90030-x.

[173] Sommer, T. P., So, R. M. C., and Zhang, H. S.: Supersonic Flow Calculation using a Reynolds-Stress and an Eddy Thermal Diffusivity Turbulence Model. Tech. rep., NASA Contract. Rep. 4515. 1993.

[174] Song, K. D., Choi, S. H., and Scotti, S. J.: Transpiration Cooling Experiment for Scramjet Engine Combustion Chamber by High Heat Fluxes. *Journal of Propulsion and Power*, 2006, 22 (1), pp. 96–102. DOI: 10.2514/1.11300.

[175] Soret, C.: Sur l'état d'équilibre que prend au point de vue de sa concentration une dissolution saline primitivement homohéne dont deux parties sont portées à des températures différentes. *Arch. Sci. Phys. Nat.*, 1879, 2, pp. 48–61.

[176] Steelant, J.: Achievements Obtained for Sustained Hypersonic Flight within the LAPCAT Project. *15th AIAA International Space Planes and Hypersonic Systems and Technologies Conference*. Dayton, OH, USA, 2008. DOI: 10.2514/6.2008-2578.

[177] Steelant, J.: ATLLAS: Aero-Thermal Loaded Material Investigations for High-Speed Vehicles. *15th AIAA International Space Planes and Hypersonic Systems and Technologies Conference*. American Institute of Aeronautics and Astronautics (AIAA), 2008. DOI: 10.2514/6.2008-2582.

[178] Steelant, J.: Sustained Hypersonic Flight in Europe: First Technology Achievements within LAPCAT II. *17th AIAA International Space Planes and Hypersonic Systems and Technologies Conference*. San Francisco, CA, USA, 2011. DOI: 10.2514/6.2011-2243.

[179] Steelant, J., Villace, V., Kallenbach, A., Wagner, A., Andro, J.-Y., di Benedetto, S., Saracoglu, B., Chernyshev, S. L., Gubanov, A. A., Talyzin, V. A., Voevodenko, N. V., Kukshinov, N. V., Prokhorov, A. N., Grigoriev, N. V., Neely, A. J., Verstraete, D., and Buttsworth, D.: Flight Testing Designs in HEXAFLY-INT for High-Speed Transportation. *International Conference on High-Speed Vehicle Science Technology (HiSST), Moscow, Russia.* 2018.

[180] Strauss, F., Wößner, M., Weißwange, M., Manfletti, C., and Schlechtriem, S.: Experiments on Flow Interaction in a Transpiration Cooled Model Scramjet. Eng. *7th Euopean Conference for Aeronautics and Space Science.* 2017. DOI: `10.13009/EUCASS2017-235`.

[181] Strauss, F., Witte, J., Manfletti, C., and Schlechtriem, S.: Experiments on Nitrogen and Hydrogen Transpiration Cooling in Supersonic Combustion Ramjets (Scramjets). *Space Propulsion Conference 2018.* 2018.

[182] Sutherland, W.: The Viscosity of Gases and Molecular Force. *Philos. Mag.* 5th ser., 1893, 36 (223), pp. 507–531. DOI: `10.1080/14786449308620508`.

[183] Thivet, F., Knight, D. D., Zheltovodov, A. A., and Maksimov, A. I.: Insights in Turbulence Modeling for Crossing-Shock-Wave/Boundary-Layer Interactions. *AIAA Journal*, 2001, 39 (6), pp. 985–995. DOI: `10.2514/2.1417`.

[184] Toro, E. F.: Riemann Solvers and Numerical Methods for Fluid Dynamics. Springer, 2009. ISBN: 978-3540252023.

[185] Valler, H. W.: Performance of a Transpiration-Regenerative Cooled Rocket Thrust Chamber. Tech. rep., NASA CR 159742. 1979.

[186] van Foreest, A., Sippel, M., Gülhan, A., Esser, B., Ambrosius, B. A. C., and Sudmeijer, K.: Transpiration Cooling Using Liquid Water. *Journal of Thermophysics and Heat Transfer*, 2009, 23 (4), pp. 693–702. DOI: `10.2514/1.39070`.

[187] Verdicchio, J. A., Chew, J. W., and Hills, N. J.: Coupled Fluid/Solid Heat Transfer Computation for Turbine Discs. *Volume 3: Heat Transfer, Electric Power, Industrial and Cogeneration.* ASME International, 2001. DOI: `10.1115/2001-GT-0205`.

[188] von Wolfersdorf, J.: Effect of Coolant Side Heat Transfer on Transpiration Cooling. *Heat and Mass Transfer*, 2004, 41 (4), pp. 327–337. DOI: `10.1007/s00231-004-0549-x`.

[189] Wagner, A., Kuhn, M., Martinez Schramm, J., and Hannemann, K.: Experiments on Passive Hypersonic Boundary Layer Control using Ultrasonically Absorptive Carbon/Carbon Material with Random Microstructure. *Experiments in Fluids*, 2013, 54 (10). DOI: 10.1007/s00348-013-1606-3.

[190] Wang, X., Thauvin, F., and Mohanty, K. K.: Non-Darcy Flow through Anisotropic Porous Media. *Chemical Engineering Science*, 1999, 54 (12), pp. 1859–1869. DOI: 10.1016/s0009-2509(99)00018-4.

[191] Wang, J. H., Messner, J., and Stetter, H.: An Experimental Investigation of Transpiration Cooling. Part I: Application of an Infrared Measurement Technique. *International Journal of Rotating Machinery*, 2003, 9 (3), pp. 153–161. DOI: 10.1155/s1023621x03000149.

[192] Wang, J. H. and Wang, H. N.: A Discussion of Transpiration Cooling Problems through an Analytical Solution of Local Thermal Nonequilibrium Model. *Journal of Heat Transfer*, 2006, 128 (10). DOI: 10.1115/1.2345434.

[193] Wang, J. and Shi, J.: Discussion of Boundary Conditions of Transpiration Cooling Problems Using Analytical Solution of LTNE Model. *Journal of Heat Transfer*, 2008, 130 (1). DOI: 10.1115/1.2780188.

[194] Wang, J., Zhao, L., Wang, X., Ma, J., and Lin, J.: An Experimental Investigation on Transpiration Cooling of Wedge Shaped Nose Cone with Liquid Coolant. *International Journal of Heat and Mass Transfer*, 2014, 75, pp. 442–449. DOI: 10.1016/j.ijheatmasstransfer.2014.03.076.

[195] Wassiljewa, A.: Wärmeleitung in Gasgemischen. *Phys. Z.*, 1904, 5 (22), pp. 737–742.

[196] Weigand, B., Semmler, K., and von Wolfersdorf, J.: Heat Transfer Technology for Internal Passages of Air-Cooled Blades for Heavy-Duty Gas Turbines. *Annals of the New York Academy of Sciences*, 2006, 934 (1), pp. 179–193. DOI: 10.1111/j.1749-6632.2001.tb05851.x.

[197] Weigand, B. and Gaisbauer, U.: An Overview on the Structure and Work of the DFG Research Training Group GRK 1095: 'Aero-thermodynamic Design of a Scramjet Propulsion System'. *16th AIAA/DLR/DGLR International Space Planes and Hypersonic Systems and Technologies Conference.* Bremen, Germany, 2009. DOI: 10.2514/6.2009-7276.

[198] Weller, H. G., Tabor, G., Jasak, H., and Fureby, C.: A Tensorial Approach to Computational Continuum Mechanics using Object-Oriented Techniques. *Computers in Physics*, 1998, 12 (6). DOI: 10.1063/1.168744.

Bibliography

[199] Werner, D.: Reusable. *Aerospace America*, 2015, (09), pp. 38–43.

[200] Whitaker, S.: Simultaneous Heat, Mass, and Momentum Transfer in Porous Media: A Theory of Drying. *Advances in Heat Transfer*, 1977, 13, pp. 119–203. DOI: `10.1016/S0065-2717(08)70223-5`.

[201] White, F. M.: Viscous Fluid Flow (Int'l Ed). 3rd edition. McGraw-Hill, 2006. ISBN: 978-0071244930.

[202] Wilcox, D. C.: Reassessment of the Scale-Determining Equation for Advanced Turbulence Models. *AIAA Journal*, 1988, 26 (11), pp. 1299–1310. DOI: `10.2514/3.10041`.

[203] Wilcox, D. C.: Turbulence Modeling for CFD. DCW Industries, 1998. ISBN: 978-0963605153.

[204] Wilcox, D. C.: Formulation of the κ-ω Turbulence Model Revisited. *AIAA Journal*, 2008, 46 (11), pp. 2823–2838. DOI: `10.2514/1.36541`.

[205] Wilke, C. R.: A Viscosity Equation for Gas Mixtures. *J. Chem. Phys.*, 1950, 18 (4), pp. 517–519.

[206] Williams, F. A.: Combustion Theory. 2nd edition. CRC Press, 1985. ISBN: 978-0201407778. DOI: `10.1201/9780429494055`.

[207] Woodruff, L. W. and Lorenz, G. C.: Hypersonic Turbulent Transpiration Cooling including Downstream Effects. *AIAA Journal*, 1966, 4 (6), pp. 969–975. DOI: `10.2514/3.3589`.

[208] Wuest, W.: Strömungsmesstechnik. Vieweg+Teubner Verlag, 1969. DOI: `10.1007/978-3-663-04532-8`.

[209] Xiong, Y., Zhu, Y., and Jiang, P.: Numerical Simulation of Transpiration Cooling for Sintered Metal Porous Strut of the Scramjet Combustion Chamber. *Heat Transfer Engineering*, 2014, 35 (6-8), pp. 721–729. DOI: `10.1080/01457632.2013.837790`.

[210] Xu, R., Huang, Y., Jiang, P., and Wang, B.: Internal Heat Transfer Coefficients in Microporous Media with Rarefaction Effects. *Science China Technological Sciences*, 2012, 55 (10), pp. 2869–2876. DOI: `10.1007/s11431-012-4994-3`.

[211] Zhang, H. J., Zou, Z. P., Li, Y., and Ye, J.: Preconditioned Density-Based Algorithm for Conjugate Porous/Fluid/Solid Domains. *Numerical Heat Transfer, Part A: Applications*, 2011, 60 (2), pp. 129–153. DOI: `10.1080/10407782.2011.588567`.

Uncertainty Analysis

A standard uncertainty calculation according to GUM (Guide to the Expression of Uncertainty in Measurement) [16] has been performed for the experimentally determined properties. Regarding an exemplary property R that depends on n separately measured values x_i

$$R = f(x_1, x_2, ... , x_n) \quad , \tag{A.1}$$

a Gaussian error propagation is applied, yielding the uncertainty

$$(\delta R)^2 = \sum_{i=1}^{n} \left(\frac{\partial R}{\partial x_i} \right)^2 \delta x_i^2 \quad . \tag{A.2}$$

Here, the model function for R is partially derived with respect to the single measurands x_i and subsequently multiplied with the uncertainty δx_i.

Table A.1 summarises the accuracies for all relevant properties measured in the transpiration-cooling experiments. The mass flow rate of the applied coolants (Air, He, Ar, CO_2) is controlled by a thermal mass-flow controller. The device is calibrated to air as the reference gas with an accuracy of $\pm 0.5\%$ of the read value (RD) plus $\pm 0.1\%$ of the controller's full-scale value (FS), i.e. the maximum mass flow rate. For other gases than air, it is used with conversion factors which introduce an additional uncertainty (Ar $\pm 3.05\%$ RD, He $\pm 3.06\%$ RD, CO_2 $\pm 2.66\%$ RD). The accuracies specified in table A.1 represent the values for the maximum mass flow rates applied and include all conversion factors.

A Uncertainty Analysis

Thermocouples are employed to measure the channel-wall temperature as well as the internal temperature within the porous wall. All applied sheathed thermocouples are from the same type and production batch for which the accuracy is specified with $\pm 1.5\,\text{K}$ by the manufacturer. Regarding the wall-temperature measurement, the sensors are led through the channel's wall and installed flush with the surface. However, some installation uncertainty remains and the exact position of the sensing element is not clear. Therefore, a higher uncertainty of $\pm 5\,\text{K}$ is assumed for these measurements. Additional information on the locations of the temperature measurements within the porous wall as well as the corresponding positioning uncertainties is given in appendix B.

Based on equation (A.2), the uncertainty for the coolant mass flux $\dot{m}_c/A_c$ is determined from

$$\delta\left(\frac{\dot{m}_c}{A_c}\right) = \sqrt{\left(\frac{1}{A_c}\delta\dot{m}_c\right)^2 + \left(\frac{\dot{m}_c}{A_c^2}\delta A_c\right)^2} \quad , \tag{A.3}$$

which can also be expressed by

$$\left(\frac{\delta\left(\dot{m}_c/A_c\right)}{\left(\dot{m}_c/A_c\right)}\right)^2 = \left(\frac{\delta\dot{m}_c}{\dot{m}_c}\right)^2 + \left(\frac{\delta A_c}{A_c}\right)^2 \quad . \tag{A.4}$$

Table A.1: Overview of most important error sources in measurement equipment

		Symbol	Measured range	Accuracy δx_i
coolant mass flow rate [a]	- Air	$\dot{m}_c$	$0 \ldots 6.5\,\text{g/s}$	$< 0.043\,\text{g/s}$
	- He		$0 \ldots 1.2\,\text{g/s}$	$< 0.044\,\text{g/s}$
	- Ar		$0 \ldots 7.7\,\text{g/s}$	$< 0.285\,\text{g/s}$
	- CO$_2$		$0 \ldots 5.8\,\text{g/s}$	$< 0.195\,\text{g/s}$
main-stream volume-flow rate [b]		$\dot{V}_{hg}$	$\sim 0.096\,\text{m}^3/\text{s}$	$0.001\,\text{m}^3/\text{s}$
main-stream supply pressure [b]		p_{hg}	$\sim 543\,\text{kPa}$	$8\,\text{kPa}$
main-stream supply temperature [b]		T_{hg}	$\sim 416\,\text{K}$	$1.1\,\text{K}$
hot-gas total pressure		$p_{tot,hg}$	$500\,\text{kPa}$	$10\,\text{kPa}$
hot-gas total temperature		$T_{tot,hg}$	$500\,\text{K}$	$1.5\,\text{K}$
channel width/height		B_{hg}, H_{hg}	$35.4/40.0\,\text{mm}$	$0.1\,\text{mm}$
sample width/height		B_c, H_c	$36.8/56.8\,\text{mm}$	$1.0\,\text{mm}$
sample thickness		L	$10 \ldots 40.8\,\text{mm}$	$0.5\,\text{mm}$
ambient pressure		p_{amb}	$90 \ldots 100\,\text{kPa}$	$400\,\text{Pa}$
channel-wall pressure		p	$0 \ldots 500\,\text{kPa}$	$400\,\text{Pa}$
channel-wall temperature		T	$290 \ldots 480\,\text{K}$	$5\,\text{K}$
coolant-reservoir pressure		$p_{tot,c}$	$0 \ldots 650\,\text{kPa}$	$400\,\text{Pa}$
coolant-reservoir temperature		T_c	$290 \ldots 365\,\text{K}$	$1.5\,\text{K}$
porous-sample temperature		T	$290 \ldots 480\,\text{K}$	$1.5\,\text{K}$

[a] accuracy of mass-flow controller depends on coolant gas and varies with read value
[b] measured upstream of heater II

The uncertainty of the measured hot-gas mass flux is calculated in the same way. However, in this case, the main-flow mass flow rate itself is obtained from several parameters.

The blowing ratio combines both mass fluxes with the corresponding cross-sectional areas and is determined from

$$F = \frac{\dot{m}_c R_{hg} T_{hg} A_{hg}}{\dot{V}_{hg} p_{hg} A_c} \quad . \tag{A.5}$$

The related uncertainty is given by

$$\left(\frac{\delta F}{F}\right)^2 = \left(\frac{\delta \dot{m}_c}{\dot{m}_c}\right)^2 + \left(\frac{\delta \dot{V}_{hg}}{\dot{V}_{hg}}\right)^2 + \left(\frac{\delta p_{hg}}{p_{hg}}\right)^2$$
$$+ \left(\frac{\delta T_{hg}}{T_{hg}}\right)^2 + \left(\frac{\delta A_{hg}}{A_{hg}}\right)^2 + \left(\frac{\delta A_c}{A_c}\right)^2 \quad . \tag{A.6}$$

The normalised pressure drop per length $(\Delta p/L)^*$ as introduced by equation (2.57) is employed to describe the through-flow processes of compressible gases in chapter 5. Its uncertainty is determined from

$$\delta \left(\frac{\Delta p}{L}\right)^* = \sqrt{\left(\frac{p_{in}}{p_{ex} L} \delta p_{in}\right)^2 + \left(\frac{p_{in}^2 + p_{ex}^2}{2 p_{ex}^2 L} \delta p_{ex}\right)^2 + \left(\frac{p_{in}^2 - p_{ex}^2}{2 p_{ex} L^2} \delta L\right)^2} \quad . \tag{A.7}$$

The cooling efficiency for the porous sample surface is determined from three measurement values, i.e. the wall temperature at no blowing $T_{F=0}$, the wall temperature for the current blowing ratio T, and the coolant reservoir temperature T_c:

$$\Theta = \frac{T_{F=0} - T}{T_{F=0} - T_c} \quad . \tag{A.8}$$

Regarding this, the surface temperature is recorded by four thermocouples which are subsequently averaged to calculate the cooling efficiency $\bar{\Theta}$. The obtained average value is then compared to the individual thermocouple results, i.e.

$$\Theta_i = \frac{T_{F=0} - T_i}{T_{F=0} - T_c} \quad , \quad \text{for } i = 1 \dots 4 \quad . \tag{A.9}$$

This yields the uncertainty in the cooling efficiency which is defined as

$$\frac{\delta \Theta}{\Theta} = \max \left\{ \frac{\Theta_i - \bar{\Theta}}{\bar{\Theta}} \right\} \quad . \tag{A.10}$$

Regarding the performed experimental tests, the maximum and minimum values of measurement uncertainties are summarised in tables A.2 to A.4 for various parameters. In the frame of the given thesis, the uncertainty is typically displayed by means of error bars in the according diagrams. However, the error bars are omitted in selected plots for reasons of clarity.

The most relevant uncertainties for the through-flow experiments are in the determination of mass flux and pressure loss. The thermal mass-flow controller employed in the tests offers a generally high accuracy which depends on the set mass flow rate $\dot{m}_c$. In the isothermal test cases, the applied coolant mass flow rates include very small values which are below 5% of the maximum mass flow rate tested. This results in a higher uncertainty for these particular measurements, while for all other mass flow rates the relative uncertainty $\delta(\dot{m}_c/A_c)/(\dot{m}_c/A_c)$ is between 4% and 8%. As the applied coolant mass flow rates in the heated wind-tunnel tests were not reduced to values below 5% of the respective maximum value, the uncertainty is in a similar range. Furthermore, also the calculated uncertainties for the blowing ratio F are below 7.5%. The slightly higher values when compared to the uncertainty of $\dot{m}_c/A_c$ are due to the additional measurands used in the determination of F. With respect to the pressure measurements, the analysis yields generally small uncertainties for $(\Delta p/L)^*$ and Δp. This is a consequence of the high accuracy of the employed pressure transducers. Again, the values increase with reduced mass flow rates. Regarding the normalised pressure drop $(\Delta p/L)^*$, the uncertainty

Table A.2: Estimated uncertainties in unidirectional through-flow experiments

	Symbol δx_i	Uncertainty $\delta x_i/x_i$
Mass flux inlet	$\dot{m}_c/A_c$	
- air isothermal		4.5% ... 11.4%
- other gases isothermal		5.7% ... 14.3%
- air heated		4.5% ... 6.0%
- other gases heated		5.6% ... 6.9%
Normalised pressure drop per length	$(\Delta p/L)^*$	
- air isothermal		3.4% ... 4.2%
- other gases isothermal		3.4% ... 4.3%
- air heated		3.5% ... 3.7%
- other gases heated		3.4% ... 5.1%

Table A.3: Estimated uncertainties in multidimensional through-flow experiments

	Symbol δx_i	Uncertainty $\delta x_i/x_i$
Mass flux inlet	$\dot{m}/A_{in}$	4.5% ... 12.3%
Mass flux outlet [a]	$\dot{m}/A_{out}$	5.1% ... 13.1%
Absolute pressure difference	Δp	0.1% ... 3.4%

[a] applicable to partial sealing test cases only

in the measurement of the sample thickness is the dominating influence. With respect to the thermal measurements, temperatures at the wall and within the porous sample were analysed. Moreover, the cooling efficiency Θ is considered which can be determined to an uncertainty ($\delta\Theta/\Theta$) of less than 10%. The wall temperature is measured by surface thermocouples and the adiabatic wall insert as described in section 3.3. Although the installation of thermocouples was carried out with greatest care, a positioning uncertainty remains for the surface thermocouples. Based on this mounting uncertainty, an increased accuracy value of ± 5 K was assumed for the surface thermocouples. This yields relative high uncertainties ($\delta T/T$) between 11.1% and 16.1%. In contrast, the wall insert measurement eliminates the mounting uncertainty and yields values of around 3.4% (using the thermocouple accuracy of ± 1.5 K). In light of the good agreement between the readings of adiabatic wall insert and wall thermocouples (see section 7.1), the uncertainty for the surface thermocouple measurements represents a rather conservative estimate. Using the wall thermocouples' accuracy as specified by the manufacturer, i.e. ± 1.5 K, would result in an uncertainty between 3.4% and 4.8%. This is similar to the values obtained for the temperature measurements in the porous sample.

Table A.4: Estimated uncertainties in supersonic wind-tunnel experiments

	Symbol δx_i	Uncertainty $\delta x_i/x_i$
Blowing ratio	F	
- air		5.1% ... 6.4%
- other gases		6.1% ... 7.3%
Wall temperature	T	11.1% ... 16.1%
Porous sample temperature [a]	T	3.4% ... 5.0%
Cooling efficiency	Θ	4.2% ... 9.3%

[a] only thermocouples within porous structure considered here

Additional Data on Experimental Setup

Within the frame of this thesis, three porous samples have been experimentally investigated. For each of the samples, ten thermocouples are installed within the porous structure to monitor the thermal state of the porous wall. Figure 3.6 indicates the sample geometries as well as the positions of thermocouple measurements, see section 3.2. Tables B.1 and B.2 specify the exact measurement positions in the earlier defined coordinate system (x-y-plane defined by channel's symmetry plane, x-axis coincides with Laval nozzle throat, y-axis pointing towards channel top). Additionally, the corresponding positioning uncertainties of the different thermocouples are given in table B.3. The values depend on the installation location, i.e. internal, surface, or backside, and are assumed to be equal for all samples.

In addition to the thermocouples installed within the porous structure, the fluid temperature in the coolant reservoir as well as the temperature of the stainless-steel mounting frame are recorded for all samples. The latter is measured at two positions on the flat overhang of the mounting frame. Regarding the coolant reservoir temperature, two thermocouples are installed with a distance of 5 mm to the sample's backside. The two measurement positions are located on the symmetry-plane and exhibit an offset of ± 10 mm to the axial centre of the sample, i.e. $z = 0$ and $x \in [189, 209]$ mm. The positioning uncertainty is assumed to be ± 2 mm for all directions.

Table B.1 Thermocouple positions for porous samples - part A

#	Description	Reference sample Position			Contoured sample 0° Position		
		x [m]	y [m]	z [m]	x [m]	y [m]	z [m]
1		0.184	0.0177	0.0100	0.184	0.0177	-0.010
2	hot-gas	0.184	0.0177	0.0100	0.184	0.0177	0.010
3	surface	0.214	0.0177	0.0100	0.214	0.0177	0.010
4		0.214	0.0177	-0.0100	0.214	0.0177	-0.010
5		0.189	0.0227	-0.0050		—	
6	internal	0.209	0.0227	0.0050	0.184	0.0372	0.005
7	positions	0.204	0.0277	0.0025	0.199	0.0290	0.005
8		0.194	0.0277	-0.0025	0.214	0.0274	-0.005
9	sample	0.209	0.0322	-0.0050	0.184	0.0497	0.000
10	backside	0.189	0.0322	0.0050	0.214	0.0347	0.000

Table B.2 Thermocouple positions for porous samples - part B

#	Description	Double-wedge sample Position		
		x [m]	y [m]	z [m]
1		0.179	0.0150	-0.0100
2	hot-gas	0.179	0.0150	0.0100
3	surface	0.209	0.0150	0.0100
4		0.209	0.0150	-0.0100
5		0.182	0.0192	0.0050
6	internal	0.204	0.0199	-0.0050
7	positions	0.179	0.0227	-0.0050
8		0.214	0.0227	0.0050
9	sample	0.179	0.0272	0.0000
10	backside	0.209	0.0272	0.0000

Table B.3 Positioning uncertainty of the porous sample thermocouples

#		Description	Uncertainty		
			δx [mm]	δy [mm]	δz [mm]
1 - 4		hot-gas surface	0.1	0	0.1
5 - 8		internal positions	0.1	1.0	0.1
9 - 10		sample backside	0.1	0.5	0.1

Additional Results on Multi-Dimensional Flow through Porous Media

---

Multidimensional coolant flow in porous media has been discussed in section 5.3 for the parallel-parallel fibre plane of the employed C/C material. This effect is of importance for the supersonic transpiration-cooling test cases investigated which feature coolant flows not aligned with the fibre directions. It was found that the superposition principle as defined by equation (2.62) is applicable to model these multidimensional flows in porous media. However, the cross flow was generally limited to the parallel-parallel fibre plane and did not occur in perpendicular direction. In a more general sense, also the through-flow behaviour in the parallel-perpendicular fibre plane of C/C is of interest. Therefore, two investigations linked to this effect are presented in the following. First, a theoretical study using the superposition principle details the change of permeability and the effect on the coolant-flow field. Secondly, numerical simulations of a cone test case corresponding to an experiment performed at DLR Stuttgart is presented. The test case features three-dimensional internal coolant flow and is employed for the validation of the superposition model as well as the OpenFOAM solver.

C.1 Numerical Pre-Study on Anisotropic Permeability

As a first step to investigate cross flow perpendicular to the C/C fibres, through-flow simulation results based on the superposition principle are discussed.

Therefore, through-flow angle and (in a second step) mass flow rate are varied for a flat-plate sample test case while the coolant-fluid temperature is isothermal.

For the simulations, the reference sample is reproduced by means of the two-dimensional mesh with 15 000 cells which has also been used for the unidirectional through-flow investigation, see figure 5.6. The previously determined permeability coefficients for C/C are employed to construct the orthotropic permeability tensor, see table 5.2. As mentioned before, the permeability coefficients in perpendicular direction $K_{D,\perp}$ and $K_{F,\perp}$ are lower by a factor of 9 and 15 when compared to the values for parallel direction. Since neither a main-flow domain nor internal heat transfer to the solid-phase of the porous structure need to be considered, only the fluid-phase region is modelled by the solver. Figure C.1 illustrates the resulting pressure distributions and streamlines for a mass flow rate of $\dot{m} = 1\,\mathrm{g/s}$ and through-flow angles 0° (i.e. parallel), 30°, 60°, and 90° (i.e. perpendicular). The figure reveals a considerable influence of the angle between fibre and inlet flow direction on the through-flow behaviour. Figure C.1a illustrates the test case discussed in section 5.2 with unidirectional through flow aligned with the fibre direction. Examining figure C.1b, a two-dimensional flow field is found. Due to the reduced permeability perpendicular to the fibre, the coolant flow streamlines are redirected towards the fibre orientation to some extent. Thereby, the flow resistance reduces as the permeability in parallel fibre direction is higher. Opposed to this, the flow path length increases with through-flow angle when compared to the length of the direct path, i.e. the sample thickness. The two effects are counteracting and result in the shown flow fields. Moreover, the pressure loss over the porous sample is increased when compared to parallel coolant-flow situation as indicated by the pressure contour plot. For increasing through-flow angle, the coolant flow vector is turned further and the flow path length increases. This results in a higher total pressure loss over the sample thickness. Finally, figure C.1d illustrates fully perpendicular through-flow behaviour. For this test case, the pressure gradient and the flow direction are normal to the fibre orientation. Although the streamlines are straight and the gas flows along the direct path from inlet to outlet, the minimum permeability in perpendicular direction results in maximum pressure loss. Besides these findings, the illustrated flow fields indicate the need for two-dimensional simulations. If a one-dimensional simulation was applied instead, slightly different results would be obtained due to omitting the effect of the boarder regions.

The relation between fibre orientation and the required pressure difference to induce a certain coolant mass flow is depicted in figure C.2. For the plot, simulations with a constant mass flow rate of $\dot{m} = 1\,\mathrm{g/s}$ and varying fibre orientations were performed. The resulting pressure difference is given on the
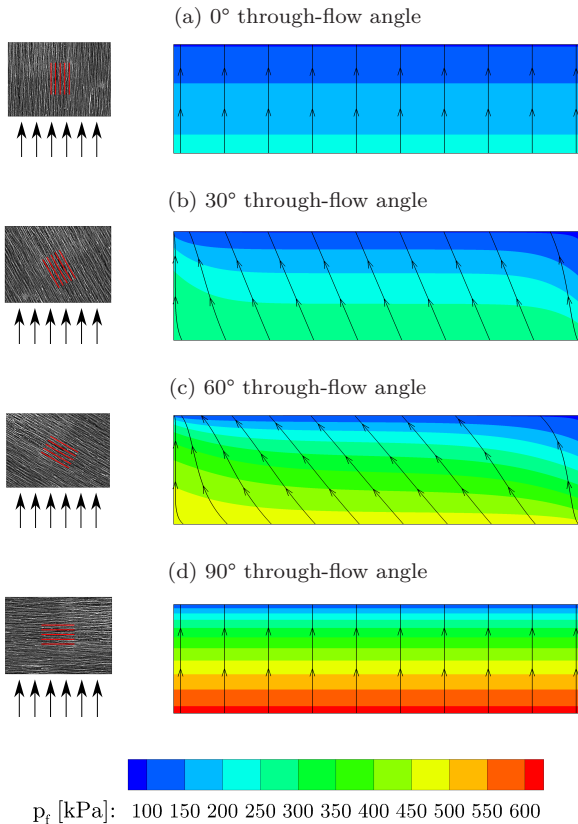
Figure C.1: Internal pressure distribution and coolant streamtraces for different angles between through-flow direction and fibre orientation

radial coordinate of the polar diagram. The pressure loss for the prescribed mass flow rate is minimal for a through-flow angle of 0° which corresponds to flow parallel to the C/C fibre orientation. It increases with through-flow angle up to the maximum at 90° where the coolant flow is perpendicular to the fibre orientation. Following this, the pressure loss decreases again to its minimum value for a through-flow angle of 180°. The behaviour repeats for through-flow angles between 180° and 360° due to the symmetry of the permeability tensor.
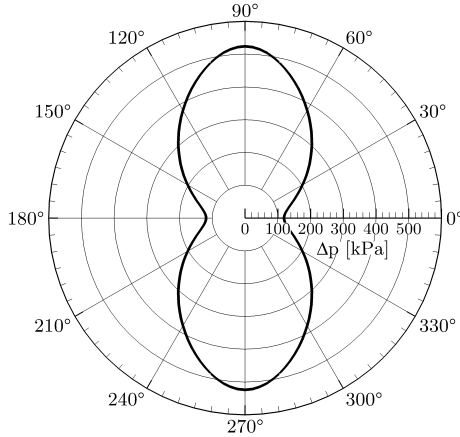
Figure C.2: Pressure loss over angle of fibre orientation for a constant mass flow
rate of $\dot{m} = 1\,\mathrm{g/s}$ (parallel$\hat{=}[0°, 180°]$, perpendicular$\hat{=}[90°, 270°]$)

C.2 Multi-Dimensional Flow in Parallel-Perpendicular Fibre Plane

Besides the presented theoretical studies, numerical simulations of a porous
cone experiment by DLR Stuttgart have been performed to investigate multidi-
mensional coolant flow in the parallel-perpendicular fibre plane. The test case
is designed to feature three-dimensional internal coolant flow and can thus be
employed for the validation of the superposition model and the OpenFOAM
solver.

The experiment explores the through-flow behaviour of a porous cone manu-
factured from C/C material and is presented in detail by Dittert et al. [43].
Figure C.3 depicts the porous cone. The lateral surface of the cone-shaped
part represents the porous outlet, whereas the far end and the exterior of the
cylindrical base are sealed by a galvanised layer. A controlled mass flow rate of
gaseous air is provided to the reservoir, flows through the porous structure, and
is eventually exhausted into ambience ($p_{ex} = 96.2\,\mathrm{kPa}$). The detailed geometry
of the cone structure including the reservoir is shown in the x-ray scan given by
figure C.4. For the here-investigated aspect of the experiment only the pressure
measurements of ambient and reservoir pressure as well as the applied air mass
flow rate are of interest. Additional measurements of the outflow distribution
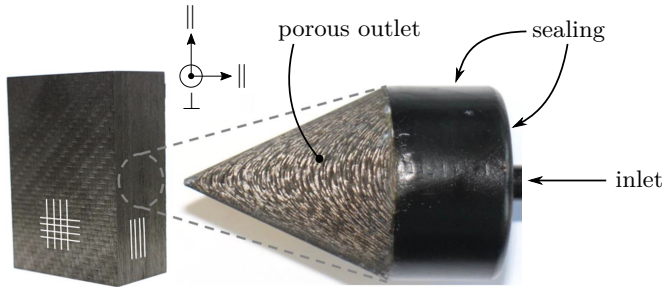using a pitot probe are described in reference [43].

Figure C.3: Porous cone experiment by DLR Stuttgart, adapted from reference [43]

The porous cone is numerically modelled by a three-dimensional, hybrid mesh with around 6.1 million cells. A slice view is provided in figure C.5. As for the experiment, isothermal conditions are assumed in the simulations. Regarding the applied boundary conditions, non-porous walls are modelled by means of no-slip and adiabatic conditions. The air mass flow rate is induced by the modified total pressure boundary condition, i.e. equation (4.33), and enters the porous structure at a temperature of $T_f = 295\,\mathrm{K}$. Permeability coefficients are applied as measured[1] and provided by DLR Stuttgart, i.e. $K_{D,\parallel} = 6.244 \cdot 10^{-13}\,\mathrm{m}^2$, $K_{D,\perp} = 1.734 \cdot 10^{-13}\,\mathrm{m}^2$, $K_{F,\parallel} = 1.175 \cdot 10^{-7}\,\mathrm{m}$, and $K_{F,\perp} = 6.194 \cdot 10^{-9}\,\mathrm{m}$. Similar to the through-flow experiments presented in section 5.2, the pressure difference between reservoir and ambience has been experimentally measured
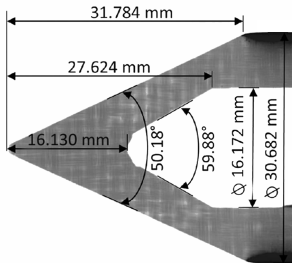
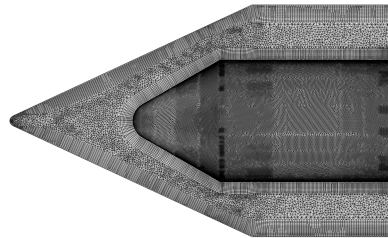Figure C.4: X-ray scan of porous cone, adapted from reference [43]

Figure C.5: Slice through hybrid mesh employed for numerical simulations

---

1 The permeability coefficients for the C/C material of the porous cone have been determined experimentally by means of one-dimensional through-flow measurements similar to those described in chapter 5.

for various air mass flow rates. Corresponding to each mass flow rate applied in the tests, a numerical simulation has been performed using the developed OpenFOAM solver.

Figure C.6 exemplarily illustrates the numerical outflow behaviour for the porous cone structure and an air mass flow rate of $\dot{m} = 1\,\text{g/s}$. The contour plot shows the distribution of the mass flux at the outlet surface. The effect of the orthotropic permeability of the C/C material is clearly visible. The mass flux distribution is significantly differing in circumferential direction with maxima in the parallel-parallel fibre plane and minima in the perpendicular direction. Additionally, a variation over axial length of the cone is found with a minimum outflow velocity at the cone's tip. This is due to the varying wall thickness which is largest for the flow path from reservoir to tip.

Figure C.7 compares numerical and experimental pressure loss over mass flow rate for the porous cone structure. The experimental data included in the figure has been provided by DLR Stuttgart. To demonstrate the sensitivity of coolant flow in the parallel-perpendicular fibre plane regarding the permeability coefficient $K_{D,\perp}$, two additional sets of simulations have been performed for reduced and intensified cross flow. For this purpose, the Darcy permeability in the perpendicular direction $K_{D,\perp}$ has been reduced and increased by a factor of 5, respectively. This yields permeability coefficients $K_{D,\perp}^{*} = \frac{1}{5} \cdot K_{D,\perp}$ and $K_{D,\perp}^{**} = 5 \cdot K_{D,\perp}$. A good agreement between experimental data and the numerical simulations is found for the superposition principle and the reference
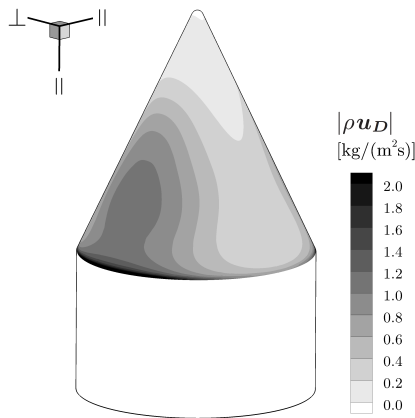

Figure C.6: Isometric contour plot of mass flux at the outlet surface for $\dot{m} = 1\,\text{g/s}$
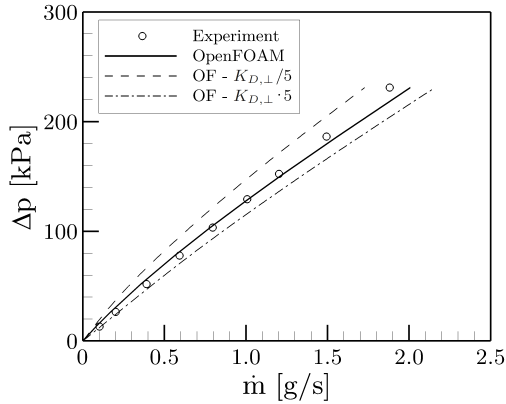
Figure C.7: Comparison of experimental and numerical pressure loss over mass flow rate for porous cone

permeability coefficients measured from one-dimensional through-flow tests. In contrast, the numerical test cases with reduced and intensified cross-flow permeabilities show considerable deviations to the measurements. This confirms that cross flow in the parallel-perpendicular fibre plane occurs and significantly influences the pressure drop behaviour of the porous cone.

In summary, the study on the porous cone suggests that the three-dimensional Darcy-Forchheimer equation and the superposition principle as proposed by equation (2.62) are applicable also for the parallel-perpendicular fibre plane of C/C material. Moreover, the OpenFOAM solver was successfully applied to the simulation of three-dimensional coolant flow in porous media also for the more complex cone geometry.

Modelling of Mass Injection through Porous Walls

Regarding the numerical modelling of mass injection through porous walls, the continuous blowing model as described in section 4.4 has been employed in the present thesis. In addition to this blowing model, a second surface-averaging approach denoted as 'discrete pores model' has been investigated in a previous study by Prokein and von Wolfersdorf [152]. The following section gives a brief comparison of the two injection models which are schematically illustrated in figure D.1.

The numerical work is based on the test case of a subsonic turbulent channel flow as described in chapter 6. The corresponding experiment by Meinert [129] employs a porous wall segment which is manufactured from SIKA-R5 and has a length of 270 mm. The open porosity of the material is 30% and the average pore size is $d_{pore} = 10\,\mu$m. For a two-dimensional model of the channel, this
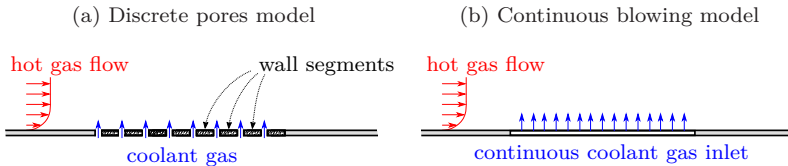

Figure D.1: Macroscale modelling approaches for gas injection through porous walls with microscopic pores

yields around 8100 pores spread over the axial length of the porous sample.

Both numerical approaches do not exactly reproduce the pore resolution but model the injection of coolant gas on a larger scale. For the discrete pores model, the porous wall is represented by a series of enlarged holes and wall segments which are regularly distributed according to the material's porosity. Due to computational costs, the pore resolution cannot be met in the numerical mesh. Instead, two rough representations using 9 and 27 pores have been considered. Openings are numerically treated as inlets with a turbulent intensity of TI $= 2\%$ and turbulent mixing length $L_{t,in} = d_{pore}$, whereas solid segments are modelled as common wall patches with the no-slip condition and standard turbulence boundary condition, i.e. equation (4.24). The continuous blowing model shown in figure D.1b reproduces the transpired surface by a homogeneous patch which combines the properties of fluid inlet and solid wall. It is described in detail in section 4.4 and has been applied for all simulations with boundary-layer injection presented in chapters 6 and 7.

The comparison between the two injection models is based on the test case by Meinert [129] that features air injection with $F = 0.5206\%$ at isothermal conditions. First, the numerical flow field in vicinity of the transpired surface is qualitatively examined. Figure D.2 shows contour plots of the axial velocity for the three injection cases. The detail views illustrate the flow behaviour at the beginning of the porous wall segment up to a wall distance of around 5 mm. A scale factor of five is applied to the y-axis for better illustration. The coolant inlet positions are clearly visible for the discrete pores model, whereas the injection is uniform and at lower velocity magnitude for the continuous blowing model. The jet-like injections for the pore models disturb the boundary-layer development as shown by the wavelike variation of velocity isolines. Although this is visible for both pore resolutions, the increase of pore number has a smoothing effect. This suggests that the effect is less pronounced in the experiment since the 27 pores are still only a rough representation of the porous material SIKA-R5 (i.e. real pore diameter around 300 times smaller). In a second step, the numerical results for both blowing models are compared to the measured boundary-layer profiles in figure D.3. Good agreement is found between experiment and simulation for both injection models. The detail view on the right-hand side of the diagram reveals a smaller deviation for the continuous blowing model close to the wall when compared to the discrete model. Comparing the two pore resolutions for the discrete model, the deviations to the experimental data are marginally smaller for the higher resolution.
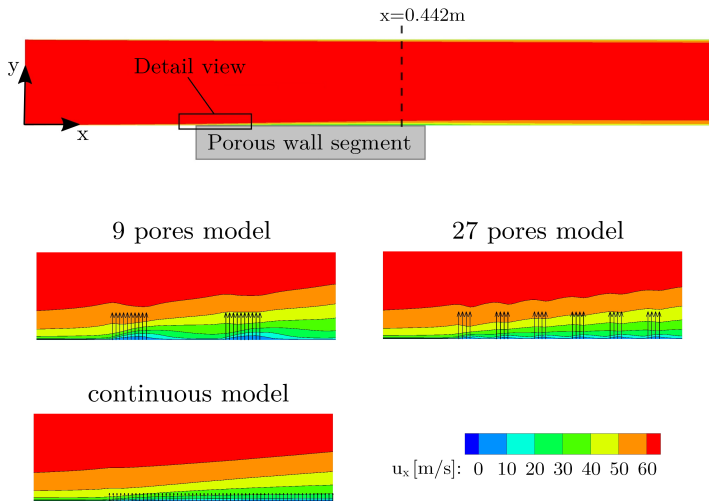
Figure D.2: Detail view of velocity contour plot in injection area, i.e. $0.18\,\mathrm{m} < x < 0.26\,\mathrm{m}$. For the sake of clarity, the detail view's axes size is scaled by a ratio $y : x = 5 : 1$.
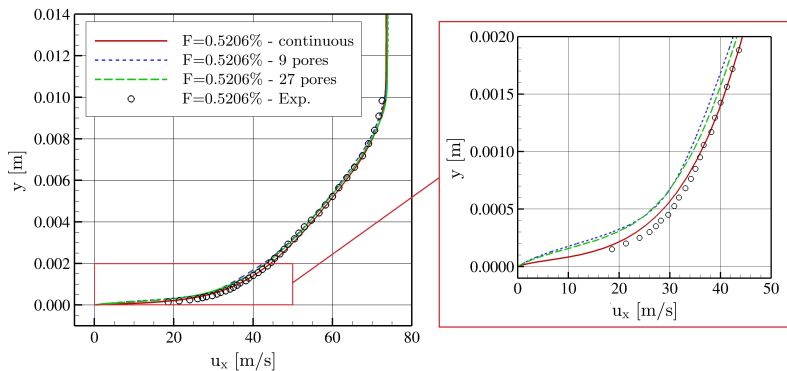

Figure D.3: Velocity distribution over wall distance for discrete pores model (9 and 27 pores) and continuous blowing model at axial position $x = 0.442\,\mathrm{m}$. Right-hand side diagram shows a detail view.

D Modelling of Mass Injection through Porous Walls

In the presented study, two blowing models were successfully applied to the investigated turbulent channel test case. Both showed good agreement to the velocity profile measured at $x = 0.442\,\mathrm{m}$. However, the velocity flow field revealed fluctuations for the discrete pore model which are linked to the rough pore resolution and the jet-like mass injections. The consequent dependency of results on the evaluation position as well as the intricate mesh generation are disadvantages when compared to the continuous blowing model. Based on the discussed results, the continuous blowing model was selected for the simulation of boundary-layer injection in the frame of this thesis.

Additional Numerical and Experimental Results for
Transpiration Cooling in Supersonic Flow

E.1 Selection of Turbulent Prandtl and Turbulent Schmidt Numbers

A common approach regarding turbulence modelling is to employ constant turbulent Prandtl and Schmidt numbers. However, if the simplified assumption of constant values for Sc_t and Pr_t is made, the selection of the actual values is still subject to discussion throughout literature.

With respect to the turbulent Schmidt number, a value of $Sc_t = 0.8$ has been employed within the frame of this thesis for all simulations involving species diffusion. The value gave reasonable agreement in turbulent channel flow experiments of Dunbar and Squire [46] and is also suggested by Landis and Mills [110]. Measurements by Költzsch [99] indicate a relation $Sc_t = f(y/\delta)$. However, averaging Sc_t over the boundary-layer thickness δ yields a value of 0.8 and thus suggests $Sc_t = 0.8$ if a constant value is to be assumed.

Similarly, the choice of the turbulent Prandtl number which governs the heat transport due to turbulent motion is debated. Kays [95] summarises on various investigations in which the reported values of Pr_t range from 0.5 to slightly above 1, depending on the considered region of the boundary layer. Concluding his review, Kays suggests a value of $Pr_t = 0.85$ within the logarithmic part of

boundary layers in flows with high Peclet numbers ($\mathrm{Pe} = \mathrm{Re}\,\mathrm{Pr}$). A slightly
lower average value $\mathrm{Pr}_t = 0.8$ is proposed by Simpson et al. [172], while
Schlichting and Gersten [164] suggest a value of $\mathrm{Pr}_t = 0.87$. The latter value
has also been used by Meinert [129] to analyse his subsonic turbulent channel
flow experiments with foreign-gas blowing. More recently, Shadloo et al. [169]
performed a DNS of a supersonic flow at $\mathrm{M}_\infty = 2$ which is similar to the Mach
number of the supersonic transpiration-cooling test cases considered in this
thesis. In contrast, the flow Reynolds number of the DNS was comparatively
low. The study yields values of Pr_t between 0.65 and 0.85 in the log-layer
region of the boundary layer, whereas Pr_t increases to around 1 directly at the
wall. A mean value of around 0.75 is obtained from averaging Pr_t over the
boundary-layer thickness. Similar values are reported in a numerical study by
Sommer et al. [173] for a flow at $\mathrm{M}_\infty = 2.2$. For even higher Mach numbers,
i.e. $\mathrm{M}_\infty = 7$, Horstman and Owen [80] measured boundary-layer profiles of
Pr_t that decrease from around 0.8 for $y/\delta < 0.4$ to values of around 0.5 at the
outer edge of the boundary layer. Measurements with respect to the influence
of boundary-layer blowing on Pr_t have been performed by Blackwell et al. [18]
and Simpson et al. [172]. However, their results do no indicate a significant
effect of blowing or suction on Pr_t.

Following the above discussion, it becomes evident that the choice of a constant
turbulent Prandtl number is not trivial. With respect to the selection of an
appropriate value of Pr_t for the present work, a sensitivity study is performed
for the supersonic flow test cases discussed in chapter 7.

E.2 Inlet Conditions for Reduced Simulation Domain

As detailed in section 7.1.2, a reduced numerical domain has been used for the
simulation of test cases with transpiration cooling to lower the computational
costs. Therefore, the Laval nozzle and the subsonic upstream part of the
test channel are not included in the reduced mesh. The boundary conditions
at the inlet plane of the reduced numerical domain are extracted from the
converged numerical solution for the supersonic channel flow without boundary-
layer blowing. This simulation test case uses the full three-dimensional
channel domain including Laval nozzle and subsonic upstream part. For the
transpiration-cooling test cases, the obtained distributions are then prescribed
at the inlet boundary. The values for axial velocity u_x, temperature T, turbu-
lent kinetic energy κ, and specific dissipation rate ω at the inlet plane are given
in figure E.1. In the contour slices of the half domain, the boundary layers on
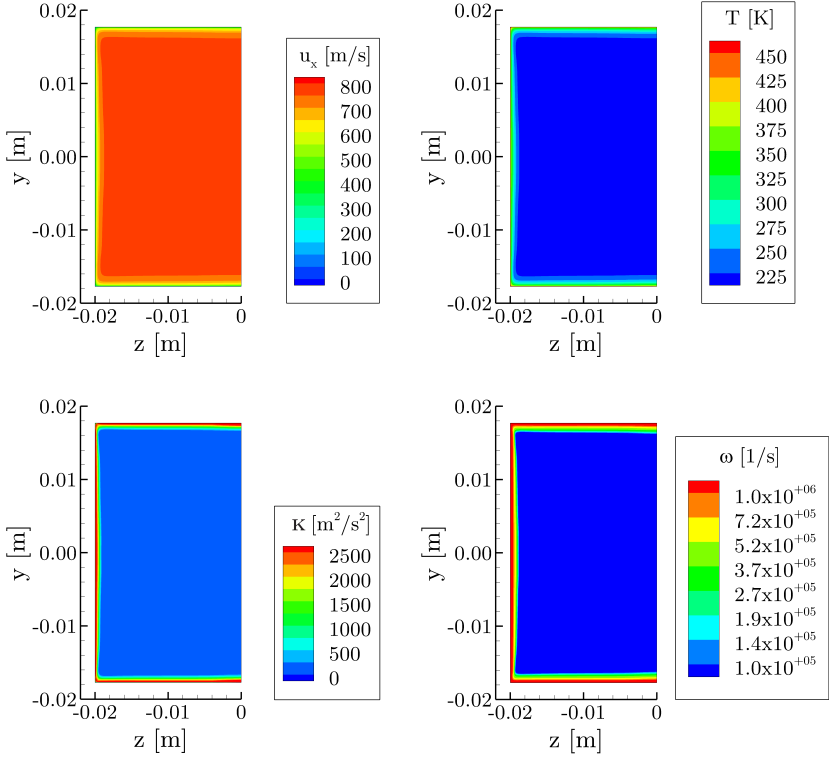top and bottom walls as well as on the side wall are visible.[1]

Figure E.1: Contour plots of boundary conditions at inlet plane of reduced numerical domain - axial velocity u_x, temperature T, turbulent kinetic energy κ, and specific dissipation rate ω

1   The side-wall boundary layer has a moderate influence on pressure and temperature distributions as found for a simplified two-dimensional simulation setup. Additional lateral effects are expected for the transpiration-cooling cases since the transpired surface of the porous sample does not extend over the full channel width. Consequently, a three-dimensional half domain has been employed for all simulations.

E.3 Formation of Shock Waves due to Boundary-Layer Injection

The injection of a coolant gas over a porous wall segment thickens the boundary layer. This corresponds to a reduction of the flow area which results in the formation of an oblique shock wave for supersonic flows. However, for most of the here-discussed test cases the flow deflection is small and thus also the strength of the induced shock wave is weak. The shock formation as well as its influence on the axial pressure distribution is illustrated for the reference sample at an air blowing rate of $F = 0.75\%$ in figures E.2 and E.3. The experimental schlieren image displays the formation of a first shock wave that is triggered by the boundary-layer blowing over the porous sample. Moreover, the following series of weak lines in the figure represents the continuous formation of (weak) shock waves while the boundary-layer thickness continuously increases over the transpired surface. The initial shock wave is reflected at the channel's bottom wall and impinges again on the top wall at $x \approx 0.3$ m. Figure E.3 depicts the corresponding axial pressure distribution on the channel's top wall for the reference-sample test case with and without blowing, i.e. for $F = 0.75\%$ and $F = 0\%$. Experimental measurements are depicted as symbols, whereas the numerical simulation data is represented by solid and dashed lines. The pressure distribution varies slightly for the case with boundary-layer injection. Main deviations are visible over the porous sample and at $x \approx 0.3$ m where the reflected initial shock wave impinges the top wall. At this position, also an influence on the temperature distribution was detected which expresses by means of a small fluctuation, see figure 7.27 as an example. However, the effect is small and only visible for the highest blowing ratios tested. It diminishes further for less intense boundary-layer injection and thickening, respectively.

Regarding the double-wedge test case featuring a non-flat surface, a more significant influence of boundary-layer blowing on the main flow field is found. This is discussed in section 7.6.2.
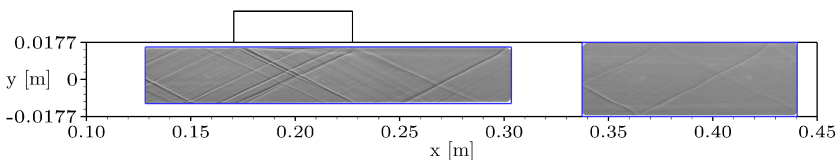

Figure E.2: Experimental schlieren image of supersonic channel flow with boundary-layer blowing at $F = 0.75\%$
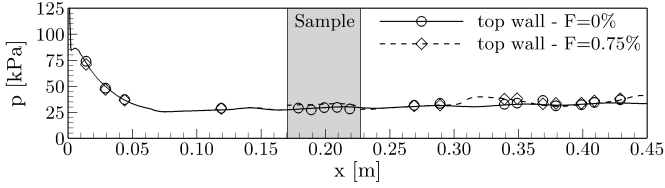
Figure E.3: Experimental (symbols) and numerical (lines) wall pressure over channel length for the reference sample at blowing ratios $F = 0\%$ and $F = 0.75\%$

E.4 Shock-Wave/Coolant-Film Interaction in Wake Region

In section 7.6, test cases with the double-wedge sample were analysed. It was found that the inclined surface of the sample triggers the formation of an oblique shock. The initial shock wave is reflected at the opposed wall and impinges again at the top wall downstream of the sample. Thereby, the cooling efficiency in the non-transpired wake region changes considerably. To further investigate the effect of shock wave impingement on the coolant film, test cases with the double-wedge sample in two configurations and the reference sample (without shock impingement) are compared in the following. The second test configuration for the double wedge is obtained by turning the sample by 180°. This new configuration is denoted as 'double wedge 180°' while the previously analysed configuration is now referred to as 'double wedge 0°', see figure E.4.
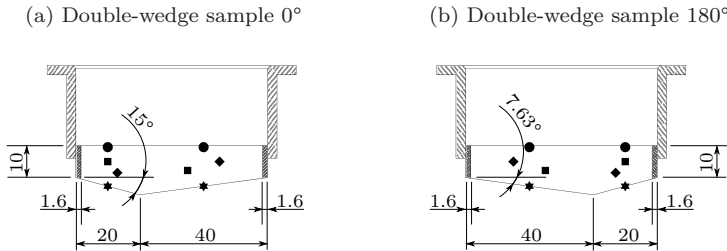
(a) Double-wedge sample 0°   (b) Double-wedge sample 180°

Figure E.4: Test configurations for double-wedge sample (units in mm, main-flow direction from left to right)
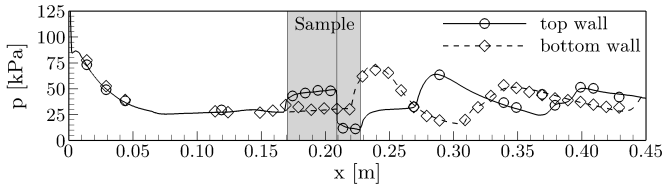
Figure E.5: Experimental (symbols) and numerical (lines) wall pressure over channel length for the double-wedge 180° sample without blowing

Figure E.5 depicts the pressure distribution for the double-wedge 180° test case which reveals fluctuations linked to the presence of shock waves. As the double-wedge 180° sample exhibits a smaller front ramp angle, the oblique shock wave is less intense and the impingement of the shock wave occurs at a more aft position for this configuration. Moreover, the pressure difference between front and aft surfaces of the sample are smaller when compared to the corresponding results for the double-wedge 0° sample in figure 7.53. Again, a very good agreement between simulation and experimental measurements is found for the no-blowing case. Combined visualisations of numerical schlieren images and top-wall surface temperatures for a blowing ratio of $F = 0.25\%$ and the three test cases are given in figure E.6. The schlieren images illustrate the positions of shock waves for the double-wedge test cases. A significant increase in wall temperature occurs downstream of the position where the reflected
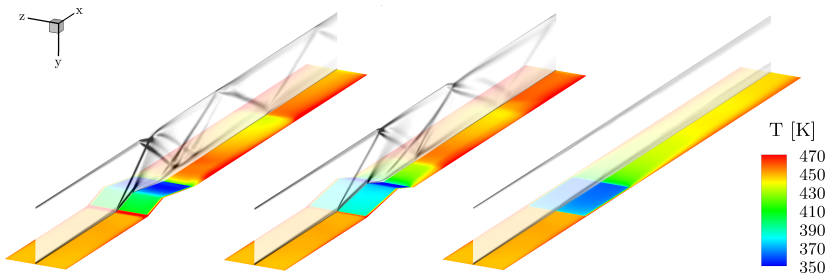

Figure E.6: Combined visualisation of schlieren image and top-wall surface temperature for double-wedge sample in both configurations, i.e. 0° (left) and 180° (centre), and reference sample for $F = 0.25\%$ (numerical results, half domain mirrored for visualisation)

shock wave impinges. In contrast, the reference-sample test case shows a smooth increase of wall temperatures with channel run length as no shock formation occurs. Regarding the sample surface, a less significant temperature difference between front and aft surfaces is visible for the 180° configuration of the double-wedge test case.

This is confirmed by the numerical and experimental distributions of the cooling efficiency depicted in figure E.7. The reference-sample test case features a rather homogeneous cooling efficiency over the transpired surface, whereas the double-wedge sample yields a change at the transition between the two inclined surfaces. This is present for both test configurations. However, the cooling efficiency for the double-wedge 180° sample is higher in the front region due to the less intense initial oblique shock when compared to the double-wedge 0° test case. Again, two effects are superposed: First, the reduced pressure increase results in elevated coolant mass flow rate and secondly, the aerothermal load is smaller. Examining the wake region, similar cooling efficiencies are detected for reference and double-wedge 180° sample, while the stronger shock wave for the double-wedge 0° test case significantly reduces the coolant film effectiveness. Although less pronounced, the effect is also captured in the experimental data.

The discussed results confirm that transpiration cooling remains effective in the wake region, even in more complex flow fields exhibiting shock waves. However, the study suggests that the cooling efficiency downstream of an impinging shock depends on the strength of the associated shock wave.
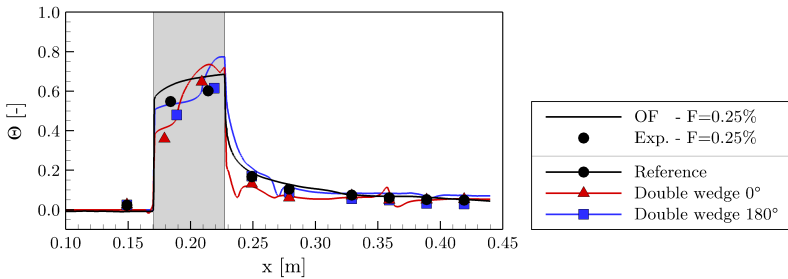

Figure E.7: Cooling efficiency over axial channel length for reference, double-wedge 0°, and double-wedge 180° samples at $F = 0.25\%$

Analytical Solution of Porous Media Energy Equations

In section 2.4.3, the temperature distributions of fluid and solid phases within a porous structure are described by equations (2.63) and (2.64). By assuming a one-dimensional problem and constant thermal properties while additionally neglecting the heat conduction within the porous-fluid phase, they reduce to the following forms:

$$\text{fluid:} \quad \rho_f c_{p,f} u_D \frac{dT_f}{dx} = h_v (T_s - T_f) \tag{F.1}$$

and

$$\text{solid:} \quad k_{s,eff} \frac{d^2 T_s}{d^2 x} = h_v (T_s - T_f) \ , \tag{F.2}$$

where $k_{s,eff} = (1 - \varepsilon) k_s$ is the effective solid thermal conductivity. The boundary conditions employed to validate the internal heat transfer in section 5.1.2 are given by

$$x = L: \quad k_{s,eff} \frac{dT_s}{dx} = \dot{q}_0 \tag{F.3}$$

and

$$x = 0: \quad k_{s,eff} \frac{dT_s}{dx} = h_c \left(T_s - T_c \right) \quad \text{and} \tag{F.4}$$

$$\rho_f u_D c_{p,f} \left(T_f - T_c \right) = k_{s,eff} \frac{dT_s}{dx} \ . \tag{F.5}$$

Using the following dimensionless quantities:

$$X = \frac{x}{L} \ , \quad \Theta_s = \frac{T_s - T_c}{\dot{q}_0 L / k_{s,eff}} \ , \quad \Theta_f = \frac{T_f - T_c}{\dot{q}_0 L / k_{s,eff}} \ , \quad \text{Bi}_c = \frac{h_c L}{k_{s,eff}} \tag{F.6}$$

$$\text{Bi}_v = \frac{h_v L^2}{k_{s,eff}} \ , \quad \text{St}_v = \frac{h_v L}{\rho_f u_D c_{p,f}} \ , \quad \frac{\text{Bi}_v}{\text{St}_v} = \frac{\rho_f u_D c_{p,f} L}{k_{s,eff}} \ , \tag{F.7}$$

the governing equations and boundary conditions can be written as:

$$\text{fluid:} \quad \frac{d\Theta_f}{dX} = \text{St}_v \left(\Theta_s - \Theta_f \right) \ , \tag{F.8}$$

$$\text{solid:} \quad \frac{d^2 \Theta_s}{dX^2} = \text{Bi}_v \left(\Theta_s - \Theta_f \right) \ , \tag{F.9}$$

$$X = 1: \quad \frac{d\Theta_s}{dX} = 1 \tag{F.10}$$

$$X = 0: \quad \frac{d\Theta_s}{dX} = \text{Bi}_c \Theta_s \quad \text{and} \tag{F.11}$$

$$\frac{d\Theta_s}{dX} = \frac{\text{Bi}_v}{\text{St}_v} \Theta_f \ . \tag{F.12}$$

From equations (F.8) and (F.9), a third order ordinary differential equation for the solid matrix temperature is obtained as

$$\frac{d^3 \Theta_s}{dX^3} + \text{St}_v \frac{d^2 \Theta_s}{dX^2} - \text{Bi}_v \frac{d\Theta_s}{dX} = 0 \ , \tag{F.13}$$

with the fluid temperature

$$\Theta_f = \Theta_s - \frac{1}{\mathrm{Bi}_v} \frac{d^2 \Theta_s}{dX^2} \quad . \tag{F.14}$$

The general solution of equation (F.13) is

$$\Theta_s = C_1 e^{z_1 X} + C_2 e^{z_2 X} + C_3 \quad , \tag{F.15}$$

where

$$z_{1,2} = \frac{1}{2} \left(-\mathrm{St}_v \pm \sqrt{\mathrm{St}_v^2 + 4\mathrm{Bi}_v} \right) \quad . \tag{F.16}$$

The integration constants C_1, C_2, and C_3 can be determined from the boundary conditions defined by equations (F.10) to (F.12):

$$C_1 = \frac{1}{z_1 e^{z_1} - \frac{z_1 - \mathrm{Bi}_c}{z_2 - \mathrm{Bi}_c} z_2 e^{z_2}} \quad ,$$

$$C_2 = \frac{1}{z_2 e^{z_2} - \frac{z_2 - \mathrm{Bi}_c}{z_1 - \mathrm{Bi}_c} z_1 e^{z_1}} \quad , \tag{F.17}$$

$$C_3 = 0 \quad .$$